UNIVERSIDAD
DE GRANADA

DOCTORAL THESIS

Design, Modeling and Fabrication of Flexible Sensors for IoE Applications using Emerging Technologies

Francisco J. Romero

Department of Electronics and Computer Technology
Faculty of Sciences

University of Granada, Spain

Programa de Doctorado en Tecnologías de la Información y la Comunicación

Thesis to obtain the International PhD Degree in Information and Communication Technologies at the University of Granada, to be defended publicly in July, 2021.

Thesis Advisors:

Prof. Dr. Noel Rodriguez,	University of Granada
Prof. Dr. Diego P. Morales,	University of Granada

Editor: Universidad de Granada. Tesis Doctorales
Autor: Francisco Javier Romero Maldonado
ISBN: 978-84-1306-963-0
URI: http://hdl.handle.net/10481/69860

Series of dissertations submitted to the
University of Granada

Always walk through life as if you have something new to learn, and you will

Vernon Howard

To my parents

Preface

This thesis is submitted in partial fulfillment of the requirements for the degree of *Philosophiae Doctor* at the University of Granada, Spain. The research presented here was mainly conducted at the University of Granada under the supervision of Prof. Noel Rodriguez and Prof. Diego P. Morales. Some of the results presented in this thesis were also partially carried out during a research stay at the Institute for Nanoelectronics of the Technical University of Munich, Germany, under the supervision of Prof. Markus Becherer. This work was supported by the Spanish Ministry of Science, Innovation and Universities through the predoctoral grant FPU16/01451 and its international mobility program; as well as by the University of Granada by means of its program for junior researchers (project ref. PPJIB2019-05).

The thesis is a collection of different papers presented following a thematic order. The papers are preceded by an introductory chapter that relates them to each other and provides background information and motivation for the work, and by a second chapter describing methodological aspects. Finally, the last chapter summarizes the main conclusions drawn during the course of this thesis.

Acknowledgements

> *If you talk to a man in a language he understands, that goes to his head. If you talk to him in his language, that goes to his heart.*
>
> Nelson Mandela

Definitivamente los grandes logros de cualquier persona dependen de muchas manos, corazones y mentes. Es por ello por lo que las líneas que escribo a continuación las dedico a expresar mi agradecimiento y reconocimiento a todas aquellas personas que han hecho posible que consiga este gran logro que, creedme, es tan mío como vuestro.

En primer lugar, mi eterno agradecimiento a mis directores de tesis, Diego y Noel, por la confianza plena depositada en mí para el desarrollo de este trabajo. Es un gusto trabajar con vosotros y os agradezco de corazón la libertad que me habéis ofrecido a lo largo de la tesis para alcanzar los diferentes objetivos, así como vuestra paciencia, experiencia y tiempo dedicado. Creo que ambos habéis realizado un trabajo encomiable como directores y espero que en el futuro otros tengan la suerte de contar con vosotros para el desarollo de su tesis. Gracias Diego por tus consejos sinceros y por tu trato cercano desde aquella primera

vez que entré a tu despacho para una tutoría de electrónica de potencia, desde entonces has sido una persona clave en mi desarrollo tanto profesional como personal. De igual modo, gracias Noel por tu disposición plena y tu capacidad de trabajo, quiero que sepas que cuentas con toda mi admiración y respeto, espero haber estado a la altura de tus expectativas. Como siempre os digo, recordad que esto no es el final, es solo el principio.

También quiero dar las gracias al resto de compañeros del departamento que me han acompañado durante esta aventura: Encarni, Almudena, Antonio García, Víctor, Fran García, Andrés Godoy y a todos los demás, por hacerme sentir como en casa. De igual modo también agradecer a aquellos compañeros de otros departamentos que han seguido de cerca el desarrollo de esta tesis, en especial a Alfonso Salinas y Antonio Rodríguez. También querría agradecer a Inma del departamento de Química Analítica su disposición y ayuda siempre que la he necesitado.

Ich möchte auch Prof. Markus Becherer für die Gelegenheit danken, am Institut für Nanoelektronik der Technische Universität München zu arbeiten, sowie Marco Bobinger und Josef Mock für ihre Hilfe während meines Forschungsaufenthaltes.

Gracias a todos aquellos familiares y amigos que se han precoupado por mí a lo largo de estos años y se han interesado por el desarrollo de esta tesis, en especial a Fran Cruz, Cristian, Fernando, Celso y Jorge. También querría dar las gracias a Antonio Escobar, Fernando Moreno, Henry Hinz, Alberto Segura y Álvaro (aka *Ramoncillo Saltabalates*) por hacer mis estancias en Múnich más amenas, así como al grupo de estudiantes de eesy-innovation e Infineon. Por último, no quiero olvidarme de Juan Antonio Enríquez y Víctor Unai y nuestras charlas de arreglar el mundo a través de un grupo de whatsapp.

Agradecer a mi familia por su apoyo incondicional. A mis padres, Encarni y Francisco, por enseñarme que nada regalan en la vida, que la suerte no existe, solo el esfuerzo y el trabajo. Gracias por todo lo que me habéis dado y me seguís dando. A mis hermanos, Iván y Rául, porque sé que siempre puedo contar con vosotros. Así como a mis abuelos, Encarnación y José, y a mis suegros, Elena y José Antonio, por tratarme como a un hijo.

Por último, y no por ellos menos importante, quiero dar las gracias a Elena, mi compañera en este viaje que es la vida, por aceptarme con mis virtudes y defectos y por su apoyo incondicional en cualquier circunstancia.

A todos, hoy y siempre: GRACIAS.

Francisco J. Romero
Granada, May 2021

Abstract

Flexible and stretchable electronics is one of the most promising fields for diverse scientific and industrial areas such as electronic skin, wearables devices or biosensing. In this way, there is a big emerging effort focused on the synthesis of flexible conductive materials as an alternative to the conventional rigid silicon-based technology to satisfy the requirements of this kind of applications (flexibility, lightness, transparency, etc.).

Since Andre Geim and Konstantin Novoselov were awarded with the Nobel Prize in Physics in 2010 for their groundbreaking experiments regarding the two-dimensional material graphene, it has attracted the interest of many researchers due to its unique electrochemical, mechanical and optical properties. However, although it is a perfect candidate to be used in flexible and stretchable electronics, these expectations have not been yet materialized into end-user applications since its current synthesis methods remain costly and unscalable. For these reasons, the interest of some research activities around graphene is shifting to the graphene-derived materials which, even though they do not present a pristine monolayer structure, capitalize part of the unique graphene's properties and are paired with synthesis processes suitable for a mass-production of samples.

In this context, the main objective of this thesis is the study of promising graphene-derived materials, such as graphene oxide (GO), reduced-graphene oxide (rGO) and laser-induced graphene (LIG), for their use in flexible electronics devices. In particular, the work carried out during this doctoral thesis includes from the synthesis and study of these materials to the exploitation of their properties to develop end-user devices and applications.

Regarding the fabrication processes, this thesis is focused on a scalable method based on laser assisted photothermal processes to obtain conductive graphene-derived patterns on flexible substrates, specifically, laser-induced graphene and laser-reduced graphene oxide (LrGO). In addition to the laser-synthesis of these nanomaterials, this work also addresses other fabrication techniques for the mass-production of flexible electronics over large area substrates, such screen and inkjet printing.

Apart from the description of these fabrication techniques and the characterization of the different materials synthesized, this thesis presents different kinds of sensors and devices based on these materials, including temperature and humidity sensors, heaters, supercapacitors and electrocardiogram (ECG) electrodes. Furthermore, some of these devices have been studied in final applications. Thus, the LrGO-based temperature sensors were integrated in an IoT sensing platform with Bluetooth Low Energy capability, whereas the ECG electrodes were tested in combination with a commercial wearable and custom processing techniques in order to be used for the ubiquitous and long-term monitoring of the heart rate.

Abstract

Furthermore, this work also reports a pioneering research on the fabrication of laser-lithographed graphene oxide memristors. Finally, the use of memristors for the implementation of memcapacitor and meminductor emulators has also been addressed.

The eleven articles published in indexed journals and the contribution to a conference of international relevance reflect the success of results achieved during this thesis.

Keywords: flexible electronics, graphene oxide, heater, laser-induced graphene, laser fabrication, memristor, nanomaterials, printed electronics, reduced-graphene oxide, sensor, supercapacitor.

Resumen

La electrónica flexible y deformable es uno de los campos más prometedores para diversas áreas científicas e industriales, como la piel electrónica, los dispositivos vestibles o los biosensores. Es por ello por lo que existe un gran esfuerzo científico dirigido a la síntesis de materiales flexibles y conductores eléctricos que permitan constituir una alternativa a la electrónica rígida convencional basada en silicio para así satisfacer las necesidades de este tipo de aplicaciones (por ejemplo, flexibilidad, ligereza, transparencia, etc.).

Desde que Andre Geim y Konstantin Novoselov fueron galardonados con el Premio Nobel de Física en 2010 por sus innovadores experimentos sobre el material bidimensional grafeno, este ha atraído el interés de muchos investigadores por sus singulares propiedades electroquímicas, mecánicas y ópticas. Sin embargo, aunque es un candidato perfecto para ser usado en el desarrollo de electrónica flexible y estirable, estas expectativas aún no se han materializado en aplicaciones para el usuario final, ya que sus métodos de síntesis actuales siguen siendo costosos y poco escalables. Por ello, el interés de algunas actividades de investigación en torno al grafeno se está desplazando hacia materiales derivados del grafeno que, aunque no presentan una estructura monocapa prístina, sí que cuentan con una parte de las propiedades que hacen al grafeno un material único, con la adicional ventaja de que estar asociados con procesos de síntesis que permiten una producción masiva de muestras de una forma más simple y menos costosa.

En este contexto, el objetivo principal de esta tesis es el estudio de materiales derivados del grafeno, como el óxido de grafeno (GO), el óxido de grafeno reducido (rGO) y el grafeno inducido por láser (LIG), para su uso en dispositivos electrónicos flexibles. En concreto, el trabajo realizado durante esta tesis doctoral incluye desde la síntesis y el estudio de estos materiales hasta la explotación de sus propiedades para el desarrollo de dispositivos y aplicaciones para el usuario final.

En lo que respecta a los procesos de fabricación, esta tesis se centra en un método escalable basado en procesos fototérmicos asistidos por láser para obtener patrones conductores derivados del grafeno sobre sustratos flexibles, en concreto, grafeno inducido por láser y óxido de grafeno reducido por láser (LrGO). Además de la síntesis por láser de estos nanomateriales, este trabajo también aborda otras técnicas de fabricación para la producción masiva de electrónica flexible sobre sustratos de gran superficie, como la serigrafía (*screen-printing*) y la inyección de tinta (*inkjet printing*).

Además de la descripción de estas técnicas de fabricación y la caracterización de los diferentes materiales sintetizados, esta tesis presenta diferentes tipos de sensores y dispositivos basados en estos materiales, incluyendo sensores de temperatura y humedad, calentadores (*heaters*), supercondensadores y electrodos

para electrocardiografía (ECG). Además, algunos de estos dispositivos han sido estudiados en aplicaciones finales. Así, los sensores de temperatura basados en LrGO se integraron en un nodo sensor IoT con capacidad de transmisión Bluetooth Low Energy, mientras que los electrodos de ECG se probaron en combinación con un *wearable* comercial y técnicas de procesamiento personalizadas con el fin de ser utilizados para la monitorización ubicua y a largo plazo de la frecuencia cardíaca. Además, este trabajo también presenta una investigación pionera sobre la fabricación de memristores de óxido de grafeno litografiados por láser. Por último, también se ha abordado el uso de memristores para la implementación de emuladores de memcondensadores y meminductores.

Los once artículos publicados en revistas indexadas y la contribución a una conferencia de relevancia internacional reflejan el éxito de los resultados obtenidos durante esta tesis.

Palabras clave: electrónica flexible, óxido de grafeno, *heaters*, grafeno inducido por láser, fabricación por láser, memristor, nanomateriales, electrónica impresa, óxido de grafeno reducido, sensor, supercondensador.

Contents

List of Figures

List of Tables

Chapter 1

Introduction

In recent years, our society is demanding smart-solutions to meet the increasing and novel needs of diverse strategic fields, such as transportation, energy and health. So far, decades of nanotechnology research have enabled ultra-small formats and low-cost sensors and devices, which have led us to the Internet of Things (IoT) era in which we are immersed nowadays. Thanks to the IoT, we count on a wide range of interconnected electronics devices that are making the impact of the Internet more pervasive and ubiquitous in our daily life [1]. However, despite the technology is evolving rapidly, a large part of the current electronics devices that tries to improve our quality of life are still devices that have to be operated in specific environments or by a specialist. In addition, the scope of the IoT is still closely linked to just machine-to-machine communications (M2M). That is why, in order to meet the expected requirements of the tomorrow's applications, the IoT must evolve to surpass these limitations and extend its scope to the so-called Internet of Everything (IoE) [2]. The concept IoE was introduced by Cisco as a paradigm beyond IoT. It is built not only upon things, but also upon people, process and data. This networked connection of people, process, data and things is intended to bring intelligence and interactivity to our environment, trying to provide an immersive and integrated experience in a new digitally monitored and connected world. Thus, the IoE expands the M2M communication to machine-to-people (M2P) and people-to-people (P2P) communication, bringing unprecedented opportunities for business, individuals and countries [3], [4].

Flexible and strechable electronics is one of the most promising fields for some of the emerging IoE applications, such as electronic skin, robotics or wearable biosensors and health-monitoring devices [5]–[14]. Many of the advances in this context came with the emergence of new conductive and flexible materials as alternative to the traditional silicon-based electronics to address the requirements of this kind of applications (i.e., flexibility, lightness, transparency or bio-compatibility, among others) [15]. This led to intensive studies on different kinds of flexible materials with promising results in terms of electrical conduction and integration, examples of them are some semiconducting metal oxides (e.g., SnO_2, TiO_2, ZnO_2 or ITO [16]–[18]) or the poly-crystalline silicon (poly-Si) [19], [20]. More recently, the graphene also emerged as a key player for the development of flexible electronics devices. Without any doubt, the unique physical, electronic, optical, mechanical and chemical properties of this 2D material make it a perfect candidate to cause a disruption in the field of flexible electronics as well as in many other areas of technology [21], [22]. However, factors such as high volume manufacturing, reliability and performance per cost difficult the cost-effective circuit integration of these materials and therefore the

wide commercialization of electronics devices based on them [23]–[25].

Because of this, many researchers are still seeking alternative materials and fabrication technologies that allow the inexpensive mass-production of sensors and electronics devices over flexible substrates. The efforts in this direction have been mainly focused on the use of several classes of nanomaterials with different conductivity and sensing capabilities, including carbon nanotubes (CNT) [26]–[28], graphene-derived materials [29]–[33], metal-based inks [34]–[38] and conductive polymers [39]–[42]. One of the greatest advantages of these materials relies on their compatibility with printing techniques (e.g., ink-jet or screen printing), spray deposition and/or laser-processing, which allow their economical and efficient processing on diverse flexible substrates, thereby providing a commercially attractive possibility to obtain multifunctional electronics over large areas [43], [44]. In addition, some of these materials are also fully biodegradable so, in combination with certain biodegradable substrates (e.g., paper or some polymers), printing techniques can be oriented for a sustainable and eco-friendly production of biodegradable electronics devices [45].

For all these reasons, flexible electronics and their associated production methods are expected to "transform the way we make and use electronic devices" [46]. Therefore, although they do not yet provide the level of integration and performance achieved by the silicon chips, the investigation on flexible and conductive materials as well as on their inexpensive and large-scale fabrication are key factors to pave the way for many IoE applications.

1.1 Motivation

As introduced before, graphene is expected to be used to develop an unprecedented generation of flexible electronics devices due to its outstanding properties. Nevertheless, these expectations have not been yet materialized into end-user applications since their current synthesis methods remain costly and unscalable. Because of this, in recent years many research groups have focused its interest on studying those graphene-derived materials that, despite not having all the unique properties of pristine graphene, do posses convincing features to satisfy certain application-dependent requirements [47]. Some of the most promising graphene derivatives in the context of flexible electronics are the graphene oxide (GO), the reduced-graphene-oxide (rGO) and the laser-induced graphene (LIG) [48]–[51]. These materials have in common a simpler and cheaper synthesis process when compared with 2D graphene. In the case of GO, it has become of high interest within the graphene research community given that it can be easily synthesized from the chemical oxidation and sonic exfoliation of bare graphite powder [52]. Despite its low electrical conductivity as a consequence of a structure composed mainly of sp^3 carbon domains, GO offers excellent properties that could be of high interest in many applications, ranging from biosensors to optical devices [53]–[55]. Moreover, the most attractive property of GO in the scope of flexible electronics is that it can be reduced to graphene-like sheets by removing the oxygen-containing functional groups from their

structure, hence recovering, at least partially, a conjugated sp^2 carbon-based structure. Despite none of the current reduction methods is able to obtain rGO with properties comparable to that obtained with the mechanical exfoliation of individual layers of graphite [21], it has been demonstrated that rGO presents some of the interesting properties of graphene, such as electrical and thermal conductivity and flexibility, among others [56]. Until recently, the reduction of GO has been carried out by means of either thermal or chemical processes [57], [58], however it has been recently proved the feasibility of the laser-assisted photolithography for the fabrication rGO patterns by the direct and selective patterning of GO films [59]. The laser reduction of GO offers the advantages of being *i*) able to obtain rGO patterns in various geometries with micrometer resolution (without the use of lithography masks), *ii*) environmental friendly and *iii*) able to modulate the electrical conductivity of the resulting rGO sheets [25]. The laser-synthesis of graphene-based nanomaterials opened up a wide range of possibilities for the development of flexible electronics devices, given its suitability for a straightforward synthesis in a scalable approach. The results on the LrGO led to exploit the laser-assisted processes for the synthesis of other laser-induced graphene (LIG) materials on diverse carbon-based precursors, such as polyimides, cloth, paper or even food [60].

Therefore, the GO and both LrGO and LIG are perfect candidates for being studied in the scope of flexible electronics for IoE applications. In addition, the focus of this work is based not only on the mere synthesis of these graphene-based materials on flexible substrates, but also on the study of their properties to be exploited for the fabrication of transducers and other electronics devices to contribute to the further development of the IoE.

1.2 Objectives

The prime objective of this thesis was the design, modeling and fabrication of flexible sensors and devices by means of emerging materials and technologies with special interest in graphene-derived materials and their laser-assisted fabrication. Other emerging techniques for the fabrication of cost-effective flexible electronics, such as ink-jet and screen printing, were also employed for the development of some of the devices presented in this work. As it was introduced before, the scope of this thesis is not limited to the synthesis of conductive materials over flexible substrates, but also covers the study of their properties for their deployment in final applications. For that, the main objective could be divided into the followings items:

- Fabrication of laser-synthesized materials and printed conductive patterns on flexible substrates.
- Study and modeling of the materials synthesized in order to exploit their physical and electrical properties for the fabrication of sensors and other kind of electronic devices.

- Integration of the transducers in end-user applications for their deployment in the IoE paradigm.

1.3 Outline

The present document constitutes a thesis by compendium of publications. This means that it is based on a collection of the most relevant scientific papers published as a result of the research carried out during the doctoral period. After this introduction, Chapter 2 summarizes the methodology followed for the attainment of the different results and the fulfillment of the aforementioned objectives. After that, the different research papers as a result of this thesis are presented. These results include eleven articles in indexed scientific journals and one contribution to an international conference, as listed in List of Papers. A brief description of the results of each one of these contributions is provided below. Finally, the main conclusions of this work are presented in the last chapter.

Paper I presents the design guidelines for the fabrication of flexible temperature sensors based on LrGO. It covers from the synthesis of the GO colloid to the integration of the flexible temperature sensors in a wireless Bluetooth-Low Energy (BLE) node. This work demonstrates the successful reduction of GO by means of a low-power laser diode ($\lambda = 405$ nm) as well as the possibility to modulate the sheet resistance of the resulting LrGO patterns by adjusting both laser power and speed. Taking advantage of the semiconducting properties of the LrGO patterns, which produces that as the temperature increases so does the charge carriers, hence reducing its resistance; the LrGO-based flexible sensors were modeled and characterized as a function of the temperature. Finally, the flexible sensors were integrated in a reconfigurable wireless node for the the long-term monitoring of the ambient temperature via BLE.

Paper II presents the synthesis and characterization of LIG by the photothermal ablation of flexible Kapton® polyimide films using a low-power laser diode ($\lambda = 405$ nm). The electrical and structural properties of the LIG patterns were characterized in detail for different laser powers. It was also studied the contact resistance of the LIG sheets synthesized for different printed electrodes, demonstrating that the porous nature of the LIG patterns contributes to reduce the contact resistance when compared with other graphene-derived sheets.

Paper III addresses the characterization and comparison of flexible humidity sensors fabricated following the laser-assisted synthesis of LrGO and LIG presented in Paper I and Paper II, respectively. These two methods were used to fabricate planar interdigitated electrodes (IDE) on flexible Kapton® HN polyimide films. Thanks to the inherent capacitance of the

IDE structure and the sensitivity of the Kapton®'s dielectric constant to the relative humidity (RH), the capacitance of these structures can be modeled as a function of the RH, and therefore, be used as humidity sensors. The sensors developed were characterized in terms of sensitivity to humidity, linearity, losses and thermal drift. In addition, the results obtained for the graphene-based sensors were compared with those obtained for ink-jet printed IDEs of silver nanoparticles (AgNPs) on the same substrate.

Paper IV presents a further study of the GO for the cost-effective fabrication of high-sensitivity humidity sensors on flexible substrates. Paper III illustrated the outstanding sensitivity of the GO's dielectric constant to humidity changes, which makes it a perfect candidate to be used in flexible humidity sensors. However, this work also demonstrated that the use of LrGO-based IDEs results in an increase of the thermal drift because of the sensitivity of the LrGO to the temperature. To avoid this drawback, the sensors presented in this work are based on Ag-based IDE structures screen-printed on PET films. These structures were characterized using GO and GO/PEDOT:PSS composites at different concentrations as sensitive materials. It is demonstrated that the functionalization of GO with PEDOT:PSS helps to increase their sensitivity to humidity as as a consequence of the combination of the active region of both GO and PEDOT:PSS.

Paper V demonstrates the potential of the LIG for the cost-effective fabrication of flexible heaters. The performance of the heaters was studied in terms of steady-state temperature, power consumption, time response and mechanical stability, among other parameters. Given the feasibility of the Kapton® for high-temperature applications, the heaters fabricated can operate up to 400 ^{o}C and present a very stable response up to 225 ^{o}C with a heat transfer coefficient of 131 ^{o}C cm^2/W, even while bending them.

Paper VI also addresses the use of LrGO for the fabrication of flexible heaters. Contrary to the previous papers, in this work the synthesis of the LrGO patterns was carried out using a CO_2 laser ($\lambda = 10.6$ μm) instead of a laser diode. It is demonstrated that the use of a high power CO_2 laser beam is able to achieve a greater level of reduction than the laser diode, obtaining a sheet resistance comparable to those reported for Ag-doped LrGO or electrochemically exfoliated graphite. In this case, the maximum operation temperature of the heaters is lower than the case of the LIG heaters, however, the LrGO ones posses a higher heat transfer coefficient (up to 400 ^{o}C cm^2/W), which implies less power consumption to achieve the same temperature.

Paper VII is focused on the use of carbon-based materials as electrodes for flexible supercapacitors, in particular, this work presents a novel approach for the fabrication of electrochemical capacitors (ECs) based on the screen-printing of a commercial carbon-based conductive ink on a flexible

substrate. Using PVA/H_3PO_4 as electrolyte, the devices are characterized as electrochemical double layer capacitors by means of cyclic voltammetry, charge-discharge experiments at constant current and electrochemical impedance spectroscopy.

Paper VIII exploits the one-step synthesis process of LIG for the fabrication of flexible electrodes for medical devices. It is demonstrated that, thanks to the porous nature of the LIG, this approach constitutes an inexpensive alternative to the commercial ECG electrodes, leading to a lower and much more stable skin–electrode contact resistance. The feasibility of the LIG electrodes within the IoE paradigm is proved by their use in combination with a commercial wearable device and a clustering algorithm for the heart rate monitoring.

Paper IX presents a low-cost approach for the mass-production of memristors based on LrGO. Given the possibility of modulating the level of reduction of the LrGO by adjusting the laser irradiation power, it is possible to obtain LrGO sheets with an intermediate level of reduction between the GO and the highly reduced GO. Here we demonstrate that these LrGO sheets exhibit memristive behavior under bipolar excitation signals as a consequence of a bulk phenomenon involving the drift of the remaining oxygen ions and oxygen-containing groups, hence inducing local changes in the level of reduction of the GO.

Paper X provides the guidelines to design and implement an elemental memcapacitor emulator based on a flux-controlled memristor such as the presented in Paper IX. Contrary to memristors, solid-state demonstrators of memcapacitors still need to be found, and that is why their study is limited to circuital emulators that enable the assessment of their properties and applications in actual circuits. In this context, this work proposes a circuit mutator (i.e., a circuit which turns the constitutive equations of memristors into the constitutive equations of memcapacitors) based on the relation between memcapacitance and the Miller effect in voltage amplifiers.

Paper XI presents, in a similar way, the design and simulation of a meminductor emulator based on a modified version of the Antoniou's gyrator, typically used to emulate inductors. In this case, the constitutive equations of the memristor are turned into the constitutive equations of flux-controlled meminductors. It is also demonstrated the feasibility of this emulator for the emulation of the long-term memory in biological systems with a long-term potentiation (LTP) and a long-term depression (LTD) example.

Paper XII demonstrates that the flux-controlled memristors can also be used for the implementation of simple floating meminductor emulators. Following a similar approach than the followed in Paper XI, this work presents the design, simulation and implementation of a floating meminductor emulator not limited to grounded configurations. In particular, the

emulator proposed in this work is also an electrical mutator built upon the Riordan gyrator in which the memristive device has been implemented by means of a resistive optocoupler.

References

[1] Miraz, M. H., Ali, M., Excell, P. S., and Picking, R., "A review on internet of things (IoT), internet of everything (IoE) and internet of nano things (IoNT)," in *2015 Internet Technologies and Applications (ITA)*, IEEE, Sep. 2015.

[2] Snyder, T. and Byrd, G., "The internet of everything," *Computer*, vol. 50, no. 6, pp. 8–9, 2017.

[3] (2013). "The internet of everything - global private sector economic analysis," Cisco Systems Inc.

[4] (2013). "The internet of everything - cisco ioe value index study," Cisco Systems Inc.

[5] Wang, X., Liu, Z., and Zhang, T., "Flexible sensing electronics for wearable/attachable health monitoring," *Small*, vol. 13, no. 25, p. 1 602 790, Mar. 2017.

[6] Yang, Y. and Gao, W., "Wearable and flexible electronics for continuous molecular monitoring," *Chemical Society Reviews*, vol. 48, no. 6, pp. 1465–1491, 2019.

[7] Jang, H., Park, Y. J., Chen, X., Das, T., Kim, M.-S., and Ahn, J.-H., "Graphene-based flexible and stretchable electronics," *Advanced Materials*, vol. 28, no. 22, pp. 4184–4202, Jan. 2016.

[8] Liu, Y., Pharr, M., and Salvatore, G. A., "Lab-on-skin: A review of flexible and stretchable electronics for wearable health monitoring," *ACS Nano*, vol. 11, no. 10, pp. 9614–9635, Sep. 2017.

[9] Son, D., Kang, J., Vardoulis, O., Kim, Y., Matsuhisa, N., Oh, J. Y., To, J. W., Mun, J., Katsumata, T., Liu, Y., McGuire, A. F., Krason, M., Molina-Lopez, F., Ham, J., Kraft, U., Lee, Y., Yun, Y., Tok, J. B.-H., and Bao, Z., "An integrated self-healable electronic skin system fabricated via dynamic reconstruction of a nanostructured conducting network," *Nature Nanotechnology*, vol. 13, no. 11, pp. 1057–1065, Aug. 2018.

[10] Rich, S. I., Wood, R. J., and Majidi, C., "Untethered soft robotics," *Nature Electronics*, vol. 1, no. 2, pp. 102–112, Feb. 2018.

[11] Xie, M., Hisano, K., Zhu, M., Toyoshi, T., Pan, M., Okada, S., Tsutsumi, O., Kawamura, S., and Bowen, C., "Flexible multifunctional sensors for wearable and robotic applications," *Advanced Materials Technologies*, vol. 4, no. 3, p. 1 800 626, Jan. 2019.

[12] Dahiya, R., Akinwande, D., and Chang, J. S., "Flexible electronic skin: From humanoids to humans [scanning the issue]," *Proceedings of the IEEE*, vol. 107, no. 10, pp. 2011–2015, Oct. 2019.

[13] Huang, S., Liu, Y., Zhao, Y., Ren, Z., and Guo, C. F., "Flexible electronics: Stretchable electrodes and their future," *Advanced Functional Materials*, vol. 29, no. 6, p. 1 805 924, Nov. 2018.

[14] Wang, S., Xu, J., Wang, W., Wang, G.-J. N., Rastak, R., Molina-Lopez, F., Chung, J. W., Niu, S., Feig, V. R., Lopez, J., Lei, T., Kwon, S.-K., Kim, Y., Foudeh, A. M., Ehrlich, A., Gasperini, A., Yun, Y., Murmann, B., Tok, J. B.-H., and Bao, Z., "Skin electronics from scalable fabrication of an intrinsically stretchable transistor array," *Nature*, vol. 555, no. 7694, pp. 83–88, Feb. 2018.

[15] Sun, D.-M., Liu, C., Ren, W.-C., and Cheng, H.-M., "A review of carbon nanotube- and graphene-based flexible thin-film transistors," *Small*, vol. 9, no. 8, pp. 1188–1205, Mar. 2013.

[16] Zhao, J., Zhang, M., Wan, S., Yang, Z., and Hwang, C. S., "Highly flexible resistive switching memory based on the electronic switching mechanism in the al/TiO2/al/polyimide structure," *ACS Applied Materials & Interfaces*, vol. 10, no. 2, pp. 1828–1835, Jan. 2018.

[17] Subbiah, A. S., Mathews, N., Mhaisalkar, S., and Sarkar, S. K., "Novel plasma-assisted low-temperature-processed SnO2 thin films for efficient flexible perovskite photovoltaics," *ACS Energy Letters*, vol. 3, no. 7, pp. 1482–1491, May 2018.

[18] Wang, W., Ai, T., and Yu, Q., "Electrical and photocatalytic properties of boron-doped ZnO nanostructure grown on PET–ITO flexible substrates by hydrothermal method," *Scientific Reports*, vol. 7, no. 1, Feb. 2017.

[19] Trifunovic, M., Sberna, P. M., Shimoda, T., and Ishihara, R., "Solution-based polycrystalline silicon transistors produced on a paper substrate," *npj Flexible Electronics*, vol. 1, no. 1, Dec. 2017.

[20] Chang, T.-C., Tsao, Y.-C., Chen, P.-H., Tai, M.-C., Huang, S.-P., Su, W.-C., and Chen, G.-F., "Flexible low-temperature polycrystalline silicon thin-film transistors," *Materials Today Advances*, vol. 5, p. 100 040, Mar. 2020.

[21] Geim, A. K. and Novoselov, K. S., "The rise of graphene," *Nature Materials*, vol. 6, no. 3, pp. 183–191, Mar. 2007.

[22] Vargas-Quesada, B., Chinchilla-Rodriguez, Z., and Rodriguez, N., "Identification and visualization of the intellectual structure in graphene research," *Frontiers in Research Metrics and Analytics*, vol. 2, Oct. 2017.

[23] Hussain, A. M. and Hussain, M. M., "CMOS-technology-enabled flexible and stretchable electronics for internet of everything applications," *Advanced Materials*, vol. 28, no. 22, pp. 4219–4249, Nov. 2015.

[24] Yu, W., Sisi, L., Haiyan, Y., and Jie, L., "Progress in the functional modification of graphene/graphene oxide: A review," *RSC Advances*, vol. 10, no. 26, pp. 15 328–15 345, 2020.

[25] Marquez, C., Rodriguez, N., Ruiz, R., and Gamiz, F., "Electrical characterization and conductivity optimization of laser reduced graphene oxide on insulator using point-contact methods," *RSC Advances*, vol. 6, no. 52, pp. 46 231–46 237, 2016.

[26] Molina-Lopez, F., Gao, T. Z., Kraft, U., Zhu, C., Öhlund, T., Pfattner, R., Feig, V. R., Kim, Y., Wang, S., Yun, Y., and Bao, Z., "Inkjet-printed stretchable and low voltage synaptic transistor array," *Nature Communications*, vol. 10, no. 1, Jun. 2019.

[27] Huang, S., Zhao, C., Pan, W., Cui, Y., and Wu, H., "Direct writing of half-meter long CNT based fiber for flexible electronics," *Nano Letters*, vol. 15, no. 3, pp. 1609–1614, Feb. 2015.

[28] Xiang, L., Zhang, H., Hu, Y., and Peng, L.-M., "Carbon nanotube-based flexible electronics," *Journal of Materials Chemistry C*, vol. 6, no. 29, pp. 7714–7727, 2018.

[29] Wan, Z., Streed, E. W., Lobino, M., Wang, S., Sang, R. T., Cole, I. S., Thiel, D. V., and Li, Q., "Laser-reduced graphene: Synthesis, properties, and applications," *Advanced Materials Technologies*, vol. 3, no. 4, p. 1 700 315, Feb. 2018.

[30] Xue, Y., Zhu, L., Chen, H., Qu, J., and Dai, L., "Multiscale patterning of graphene oxide and reduced graphene oxide for flexible supercapacitors," *Carbon*, vol. 92, pp. 305–310, Oct. 2015.

[31] Eda, G., Fanchini, G., and Chhowalla, M., "Large-area ultrathin films of reduced graphene oxide as a transparent and flexible electronic material," *Nature Nanotechnology*, vol. 3, no. 5, pp. 270–274, Apr. 2008.

[32] Secor, E. B., Prabhumirashi, P. L., Puntambekar, K., Geier, M. L., and Hersam, M. C., "Inkjet printing of high conductivity, flexible graphene patterns," *The Journal of Physical Chemistry Letters*, vol. 4, no. 8, pp. 1347–1351, Apr. 2013.

[33] Ye, R., James, D. K., and Tour, J. M., "Laser-induced graphene: From discovery to translation," *Advanced Materials*, vol. 31, no. 1, p. 1 803 621, Oct. 2018.

[34] Shen, W., Zhang, X., Huang, Q., Xu, Q., and Song, W., "Preparation of solid silver nanoparticles for inkjet printed flexible electronics with high conductivity," *Nanoscale*, vol. 6, no. 3, pp. 1622–1628, 2014.

[35] Albrecht, A., Rivadeneyra, A., Abdellah, A., Lugli, P., and Salmerón, J. F., "Inkjet printing and photonic sintering of silver and copper oxide nanoparticles for ultra-low-cost conductive patterns," *Journal of Materials Chemistry C*, vol. 4, no. 16, pp. 3546–3554, 2016.

[36] Kell, A. J., Paquet, C., Mozenson, O., Djavani-Tabrizi, I., Deore, B., Liu, X., Lopinski, G. P., James, R., Hettak, K., Shaker, J., Momciu, A., Ferrigno, J., Ferrand, O., Hu, J. X., Lafrenière, S., and Malenfant, P. R. L., "Versatile molecular silver ink platform for printed flexible electronics," *ACS Applied Materials & Interfaces*, vol. 9, no. 20, pp. 17 226–17 237, May 2017.

[37] Nayak, L., Mohanty, S., Nayak, S. K., and Ramadoss, A., "A review on inkjet printing of nanoparticle inks for flexible electronics," *Journal of Materials Chemistry C*, vol. 7, no. 29, pp. 8771–8795, 2019.

[38] Li, W., Zhang, H., Shi, S., Xu, J., Qin, X., He, Q., Yang, K., Dai, W., Liu, G., Zhou, Q., Yu, H., Silva, S. R. P., and Fahlman, M., "Recent progress in silver nanowire networks for flexible organic electronics," *Journal of Materials Chemistry C*, vol. 8, no. 14, pp. 4636–4674, 2020.

[39] Wang, Y., Zhu, C., Pfattner, R., Yan, H., Jin, L., Chen, S., Molina-Lopez, F., Lissel, F., Liu, J., Rabiah, N. I., Chen, Z., Chung, J. W., Linder, C., Toney, M. F., Murmann, B., and Bao, Z., "A highly stretchable, transparent, and conductive polymer," *Science Advances*, vol. 3, no. 3, e1602076, Mar. 2017.

[40] Gu, X., Zhou, Y., Gu, K., Kurosawa, T., Guo, Y., Li, Y., Lin, H., Schroeder, B. C., Yan, H., Molina-Lopez, F., Tassone, C. J., Wang, C., Mannsfeld, S. C. B., Yan, H., Zhao, D., Toney, M. F., and Bao, Z., "Roll-to-roll printed large-area all-polymer solar cells with 5% efficiency based on a low crystallinity conjugated polymer blend," *Advanced Energy Materials*, vol. 7, no. 14, p. 1 602 742, Mar. 2017.

[41] Fan, X., Nie, W., Tsai, H., Wang, N., Huang, H., Cheng, Y., Wen, R., Ma, L., Yan, F., and Xia, Y., "PEDOT:PSS for flexible and stretchable electronics: Modifications, strategies, and applications," *Advanced Science*, vol. 6, no. 19, p. 1 900 813, Jul. 2019.

[42] Kraft, U., Molina-Lopez, F., Son, D., Bao, Z., and Murmann, B., "Ink development and printing of conducting polymers for intrinsically stretchable interconnects and circuits," *Advanced Electronic Materials*, vol. 6, no. 1, p. 1 900 681, Nov. 2019.

[43] Khan, S., Lorenzelli, L., and Dahiya, R. S., "Technologies for printing sensors and electronics over large flexible substrates: A review," *IEEE Sensors Journal*, vol. 15, no. 6, pp. 3164–3185, Jun. 2015.

[44] Huang, Q. and Zhu, Y., "Printing conductive nanomaterials for flexible and stretchable electronics: A review of materials, processes, and applications," *Advanced Materials Technologies*, vol. 4, no. 5, p. 1 800 546, Jan. 2019.

[45] Irimia-Vladu, M., Głowacki, E. D., Voss, G., Bauer, S., and Sariciftci, N. S., "Green and biodegradable electronics," *Materials Today*, vol. 15, no. 7-8, pp. 340–346, Jul. 2012.

[46] Brown, A. S. (Apr. 2021). "Flexible electronics could transform the way we make and use electronic devices," Penn State News.

[47] Lin, L., Peng, H., and Liu, Z., "Synthesis challenges for graphene industry," *Nature Materials*, vol. 18, no. 6, pp. 520–524, May 2019.

[48] Tan, R. K. L., Reeves, S. P., Hashemi, N., Thomas, D. G., Kavak, E., Montazami, R., and Hashemi, N. N., "Graphene as a flexible electrode: Review of fabrication approaches," *Journal of Materials Chemistry A*, vol. 5, no. 34, pp. 17 777–17 803, 2017.

[49] Tarcan, R., Todor-Boer, O., Petrovai, I., Leordean, C., Astilean, S., and Botiz, I., "Reduced graphene oxide today," *Journal of Materials Chemistry C*, vol. 8, no. 4, pp. 1198–1224, 2020.

[50] Ye, R., James, D. K., and Tour, J. M., "Laser-induced graphene," *Accounts of Chemical Research*, vol. 51, no. 7, pp. 1609–1620, Jun. 2018.

[51] Kaidarova, A. and Kosel, J., "Physical sensors based on laser-induced graphene: A review," *IEEE Sensors Journal*, pp. 1–1, 2020.

[52] Hummers, W. S. and Offeman, R. E., "Preparation of graphitic oxide," *Journal of the American Chemical Society*, vol. 80, no. 6, pp. 1339–1339, Mar. 1958.

[53] Chung, C., Kim, Y.-K., Shin, D., Ryoo, S.-R., Hong, B. H., and Min, D.-H., "Biomedical applications of graphene and graphene oxide," *Accounts of Chemical Research*, vol. 46, no. 10, pp. 2211–2224, Mar. 2013.

[54] Rodriguez, R. D., Bing, M., Ruban, A., Pavlov, S., Hamry, A. A., Prakash, V., Khan, M., Murastov, G., Mukherjee, A., Khan, Z., Shah, S., Lipovka, A., Kanoun, O., Mehta, S. K., and Sheremet, E., "Reduced graphene oxide nanostructures by light: Going beyond the diffraction limit," *Journal of Physics: Conference Series*, vol. 1092, p. 012 124, Sep. 2018.

[55] Loh, K. P., Bao, Q., Eda, G., and Chhowalla, M., "Graphene oxide as a chemically tunable platform for optical applications," *Nature Chemistry*, vol. 2, no. 12, pp. 1015–1024, Nov. 2010.

[56] Pei, S. and Cheng, H.-M., "The reduction of graphene oxide," *Carbon*, vol. 50, no. 9, pp. 3210–3228, Aug. 2012.

[57] Ju, H.-M., Huh, S. H., Choi, S.-H., and Lee, H.-L., "Structures of thermally and chemically reduced graphene," *Materials Letters*, vol. 64, no. 3, pp. 357–360, Feb. 2010.

[58] Stankovich, S., Dikin, D. A., Piner, R. D., Kohlhaas, K. A., Kleinhammes, A., Jia, Y., Wu, Y., Nguyen, S. T., and Ruoff, R. S., "Synthesis of graphene-based nanosheets via chemical reduction of exfoliated graphite oxide," *Carbon*, vol. 45, no. 7, pp. 1558–1565, Jun. 2007.

[59] Zhang, Y., Guo, L., Wei, S., He, Y., Xia, H., Chen, Q., Sun, H.-B., and Xiao, F.-S., "Direct imprinting of microcircuits on graphene oxides film by femtosecond laser reduction," *Nano Today*, vol. 5, no. 1, pp. 15–20, Feb. 2010.

[60] Chyan, Y., Ye, R., Li, Y., Singh, S. P., Arnusch, C. J., and Tour, J. M., "Laser-induced graphene by multiple lasing: Toward electronics on cloth, paper, and food," *ACS Nano*, vol. 12, no. 3, pp. 2176–2183, Feb. 2018.

Chapter 2

Methodology

This chapter describes the methodological aspects associated with the development of the different results achieved in this thesis. The first part includes a description of the materials and fabrication techniques employed for the fabrication of the different devices, whereas the second part presents the main equipments and methods used for the characterization of these devices.

2.1 Materials

The two main flexible substrates used in this work were polyethylene terephthalate (PET) and Kapton® HN films. PET films were acquired from 3M (St. Paul, MN, USA) and from ColorGATE Digital Output Solutions GmbH (Hannover, Germany), while the Kapton® HN films were purchased from DuPont de Nemours, Inc. (Constantine, MI, USA). For the characterization of the LrGO heaters, we also used mica sheets with a thickness of ∼1.5 mm as supporting substrate (model HP5M5-1 from ZT Mica, Hubei, China). In some experiments the LIG sheets were isolated using the laminating pouches Capture125, acquired from Fellowes Inc (Itasca, IL,USA). Regarding the GO, two different approaches were followed. On one hand, we synthesized GO following a modified version of the Hummers and Offerman's method (refer to Paper I for more details). This method required the use of sulfuric acid (H_2SO4), sodium nitrate ($NaNO_3$), and potassium permanganate ($KMnO_4$) as functionalization and oxidizing reagents of graphite powder (from Sigma-Aldrich Corp., St. Louis, MO, USA). On the other hand, commercial GO with a concentration of 4 mg/mL was also directly acquired from Graphenea (Gipuzkoa, Spain). The poly(3,4-ethylenedioxythiophene)/polystyrene sulfonate (PEDOT:PSS) dispersion was obtained from Heraeus Holding GmbH (Hanau, Germany, product name: CLEVIOS™ P VP AI 4083). For the fabrication of the printable contacting electrodes we used a Ag-based conductive paint from RS (Corby, UK), two different carbon-based pastes, the C-220 model from Applied Ink Solutions (Westborough, MA, USA) and the Bare Conductive® electrical paint (London, UK); as well as the LOCTITE® ECI 1010 Ag-based screen printable ink from Henkel AG (Düsseldorf, Germany). Both LOCTITE® ECI 1010 and C-220 pastes were also used for the fabrication of the IDEs structures presented in Paper IV and Paper VII, respectively. The inkjet-printed patterns presented in Paper III were made of DGP 40LT-15C silver ink (from ANP USA Inc, Pleasanton, CA, USA). Finally, both Poly(vinyl alcohol) (PVA, Mw 31,000-50,000, 98-99% hydrolyzed) and phosphoric acid (H_3PO_4, product name: 1005731000) used for the fabrication of the electrochemical capacitors were acquired from Sigma-Aldrich (St. Louis, MO, USA).

2.2 Fabrication Techniques

2.2.1 Laser-synthesis of graphene-derived materials

The laser photothermal process was carried out using two different kinds of laser, a CO_2 laser with a wavelength of 10.6 μm, and a diode laser with a wavelength of 405 nm. In particular, we used the laser Rayjet 50 from Trotec Ltd (Marchtrenk, Austria), and the diode lasers Automatic K5 from KKmoon SA and DIY 300 mW Mini Laser from Benbox (China). These lasers, shown in Figure 2.1, count with both adjustable power and speed. In the case of the LIG-based patterns, the laser photothermal ablation is carried out directly on the surface of the Kapton® HN films, as shown in Figure 2.2a(1-2). Moreover, for the synthesis of the LrGO patterns the substrate is firstly covered with a previously sonicated GO layer (drop-casted and/or 3D shaked) and, once the sample is dried at ambient conditions, the GO is turned into rGO through the laser photothermal process, as depicted in Figure 2.2b(1-3). Finally, the laser-synthesized patterns are usually contacted by means of screen-printed electrodes, as shown in Figure 2.2a(3) and Figure 2.2b(4).

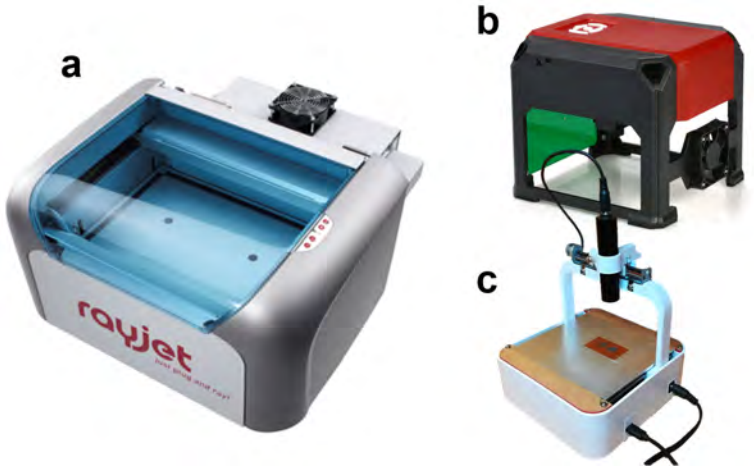

Figure 2.1: (a) Rayjet-50 (image from lhtech.com.my), (b) Automatic K5 (image from greddington.top) and (c) DIY 300 mW Benbox Mini Laser.

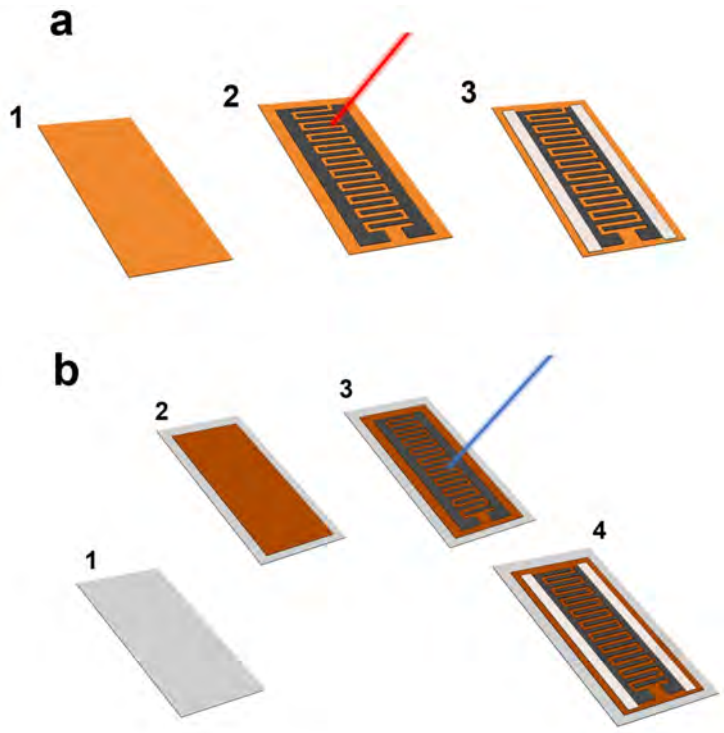

Figure 2.2: Schematic representation of the laser-synthesis of both graphene-derived materials [1]. (a) Laser-Induced Graphene (LIG) patterns: (1) Kapton® polyimide film, (2) laser-scribing process to induce graphene-derived patterns on the surface of the polyimide (this case shows the CO_2 laser beam), (3) silver electrical contacts printed on each electrode. (b) Laser-reduced Graphene Oxide (rGO) (LrGO) patterns: (1) flexible substrate (e.g., PET film), (2) GO deposited onto the PET substrate, (3) laser-scribing process to reduce the GO (this case shows the UV laser beam), (4) silver electrical contacts printed on each electrode.

2.2.2 Screen-printing of conductive inks

The screen-printing process was carried out using the manual screen printer FLAT-DX 200 from Siebdruck-Versand (Magdeburg, Germany). It consists of a 62×52 cm^2 printing table and a holder with a counterweight for mounting screens and holding them while exchanging the substrate, as shown in Figure 2.3a. The screens used in this work were made of nylon with a mesh of 90 threads per centimeter (T/cm). Using a manual rubber squeegee, the different inks and pastes can be transferred through the screen on the flexible substrates. For that it is important to maintain a constant pressure and a defined angle of about 45° to 75° to press the sharp edge of the rubber onto the screen [2]. Once the desired

patterns were transferred to the substrates, the curing of the different pastes was carried out in an applicable lab oven (such as the one shown in Figure 2.3b) following the recommendations provided by each manufacturer.

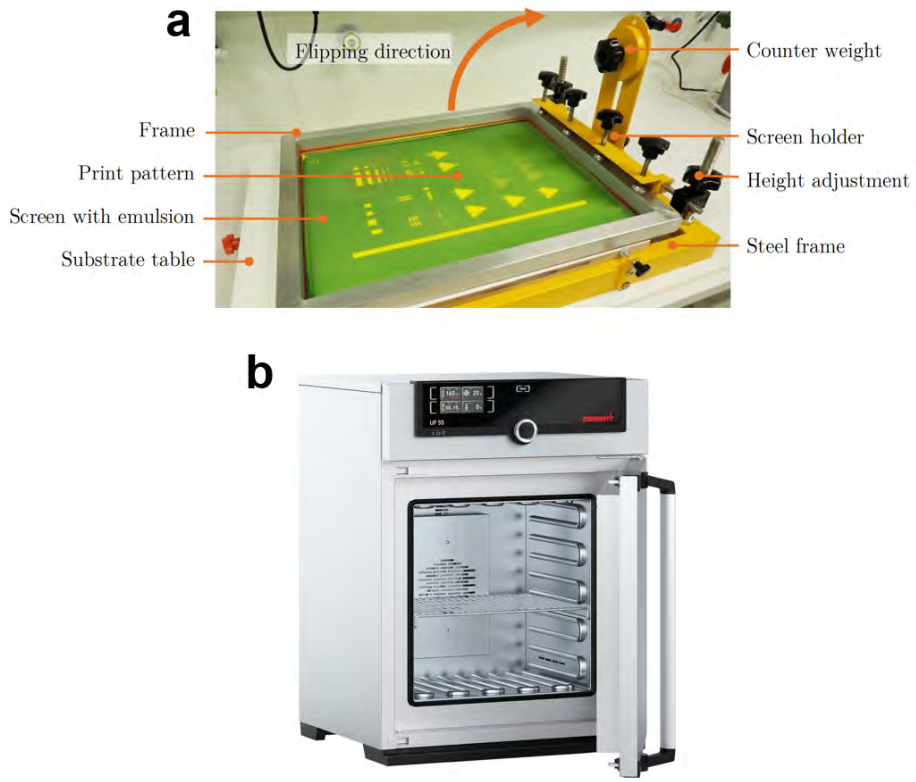

Figure 2.3: (a) Manual screen-printing machine FLAT-DX 200 [2], (b) UF55 oven from Memmert GmbH + Co. KG (Schwabach, Germany).

2.2.3 Inkjet printing of conductive inks

The inkjet printed patterns were defined with a DMP-2831^{TM} Dimatix inkjet printer from Fujifilm Dimatix Inc. (Santa Clara, CA, USA). The printing of the Ag ink layout over the Kapton® polyimide surface was performed with a drop-to-drop distance of 50 μm (resulting in a landing diameter of $\sim$100 μm) and a printing temperature of 60 °C. The drying process was carried out by a photonic sintering step with a Sinteron 2010-S from Xenon Corporation (Wilmington, MA, US) with 5 pulses of an energy of 2.5 kV and a time lapse of 500 μs.

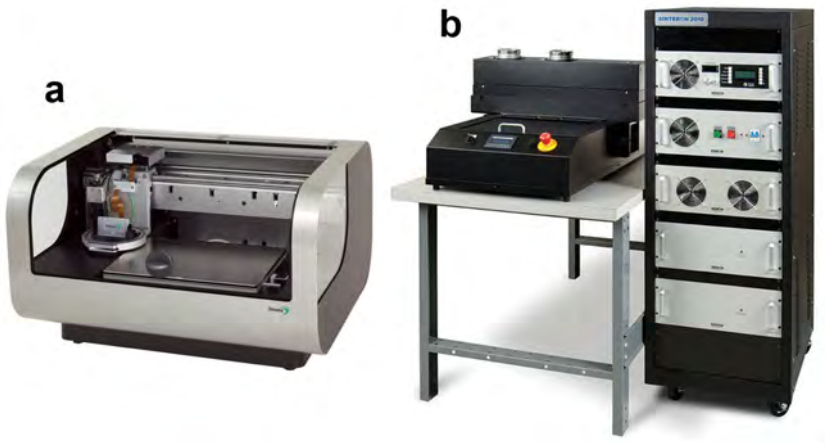

Figure 2.4: (a) DMP-2831^{TM} Dimatix inkjet printer (image from fujifilm.com), (b) Sinteron 2010-S (image from warsash.com).

2.3 Characterization

2.3.1 Material characterization

Optical microscope images were obtained with a ZEISS Axioscope 5 microscope and analyzed with the ZEN Core software, both from Carl Zeiss AG (Oberkochen, Germany). The Scanning Electron Microcospy (SEM) images were extracted using a NVision40 electron microscope from Carl Zeiss (Oberkochen, Germany). X-ray Photoelectron Spectroscopy (XPS) experiments were carried out using an Axis Ultra-DLD X-ray photoelectron spectrometer from Kratos Analytical Ltd (Manchester, UK). Raman spectra were acquired with a JASCO 108 NRS-5100 dispersive micro-Raman spectrometer from JASCO Inc (Tokio, Japan) using an excitation wavelength of λ= 532 nm. For the Diffuse Reflectance Infrared Fourier Transform (DRIFT) experiments ∼2 mg of the material to study were mixed with ∼200 mg of anhydrous KBr powder and pressed into 7 mm diameter discs for its analysis on a Tensor 27 spectrometer from Bruker Corp (Billerica, MA, USA). Those Fourier-Transform Infrared Spectroscopy (FTIR) experiments performed at the University of Munich were carried out using an ALPHA II FTIR spectrophotometer, also from Bruker Corp. The thickness of the samples was acquired using a DekTak XT contact profilometer from Bruker Corp. Finally, two different techniques were used in order to obtain the sheet resistance of the conductive patterns. On one side, the four-point method at constant current with a probe head from Jandel connected to a B2901A source measuring unit (SMU) from Keysight Technologies Inc. (St. Rose, CA, USA) and, on the other side, the transmission line method (TLM) using printed electrodes (refer to Paper II for more details).

2.3.2 Devices characterization

Both temperature and humidity measurements were carried out using the climate chamber VCL 4006 from Vötsch Industrietechnik GmbH (Balingen, Germany) in combination with the impedance analyzer 4294A from Keysight Technologies Inc (St. Rose, CA, USA). The connection between the devices and the impedance analyzer was done by means of the impedance probe kit 42941A, also from Keysight Technologies. The setup to range both humidity and temperature as well as to control the impedance analyzer was automatized with LabVIEW 2016 from National Instruments Corporation (Austin, TX, USA). These two equipments are shown in Figure 2.5.

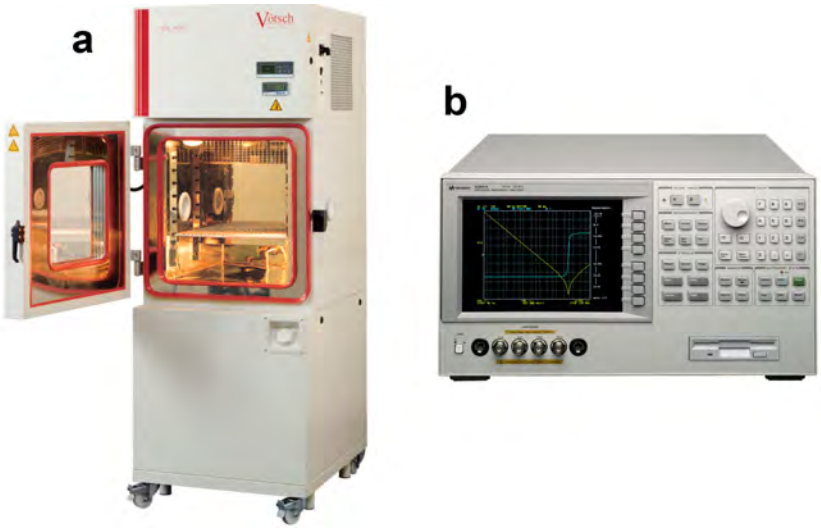

Figure 2.5: (a) VCL 4006 climate chamber (image from directindustry.es), (b) 4294A precision impedance analyzer (image from keysight.com).

For the characterization of the LIG heaters, the input power was applied and monitored using a LabVIEW-controlled DC power supply 2200-30-5 from Keithley Instruments (Cleveland, OH, USA), whereas the thermal images were recorded using a 640×480 px infrared camera Testo890 from Testo SE & Co. KGaA (Titisee-Neustadt, Germany). Using the software IRSoft, also from Testo, and a MATLAB script (from MathWorks Inc., Portola Valley, CA, USA), the temperature transients were extracted from processing the IR images. The same procedure was followed for the characterization of the rGO heaters, but using a B2912A precision SMU from Keysight Technologies Inc controlled by the Quick IV Measurement Software, also from Keysight, and the Fluke TiS75 infrared camera from Fluke Corporation (Everett, WA, USA). In that case, the images were acquired at a sampling rate of 9 Hz and processed with the SmartView 4.3 software from Fluke and a MATLAB script. All these instruments are shown in Figure 2.6.

Figure 2.6: (a) 2200-30-5 power supply (image from mouser.com), (b) Testo890 infrared camera (image from testo.com), (c) B2912A SMU (image from transcat.com) and (d) Fluke TiS75 infrared camera (image from fluke.com).

The electrical characterization of the screen-printed electrochemical capacitors presented in Paper VII were carried out with a 2602B SMU from Tektronix Inc (Beaverton, OR, USA). Bending tests experiments were carried out using a stepper motor (PD4-N5918M4204) equipped with a precision planetary gear (GPLE60) from Nanotec (Feldkirchen, Germany) that slides a movable clamp along an aluminum rail, as shown in Figure 2.7a. The resistance of the samples over time as a function of the bending state was monitored using a Keithley 2700 multimeter (Figure 2.7b) and a LabVIEW program.

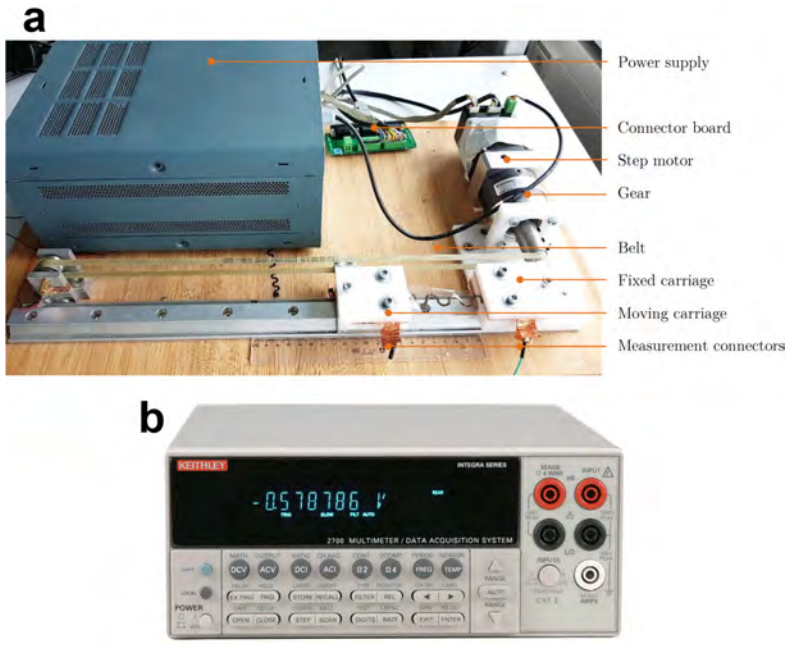

Figure 2.7: (a) Bending Setup [2], (b) Keithley 2700 multimeter (image from testequipmentconnection.com).

2.4 Other equipment and software

The printed circuit board (PCB) was designed using Altium Designer, from Altium Ltd. (La Jolla, CA, USA), and programmed using the PSoC® Creator™ Integrated Design Environment (IDE) from Cypress Semiconductor Corporation (San Jose, CA, USA). The smartphone application was developed using the Android Studio IDE from Google (Mountain View, CA, USA). The reconfigurable Field Programmable Analog Array (FPAA) AN221E04 from Anadigm Inc (Paso Robles, CA, USA) was used for obtaining the contact resistance of the LIG-based electrodes (Paper VIII) and for the implementation of the memcapacitor emulator proposed in Paper X. ECG signals were acquired using the wearable body sensing platform Biosignals Researcher Kit (Figure 2.8) from PLUX wireless biosignals S.A. (Lisboa, Portugal). Finally, LTspice® software was used for the simulation of the different electrical circuits.

Figure 2.8: BiosignalsPlux (image from plux.info).

References

[1] Romero, F. J., Gerardo, D., Romero, R., Ortiz-Gomez, I., Salinas-Castillo, A., Moraila-Martinez, C. L., Rodriguez, N., and Morales, D. P., "Comparison of laser-synthetized nanographene-based electrodes for flexible supercapacitors," *Micromachines*, vol. 11, no. 6, p. 555, May 2020.

[2] Albrecht, A., "Printed sensors for the internet of things," Ph.D. dissertation, Technical University of Munich, 2018.

List of Papers

Paper I

Francisco J. Romero, Almudena Rivadeneyra, Victor Toral, Encarnacion Castillo, Francisco Garcia-Ruiz, Diego P. Morales and Noel Rodriguez. "Design guidelines of laser reduced graphene oxide conformal thermistor for IoT applications". In: *Sensors and Actuators A: Physical*, Vol. 274, pp. 148–154 (2018) DOI: 10.1016/j.sna.2018.03.014. Impact Factor: 2.739, JCR Rank: 19/61 (Q2) in *Instruments & Instrumentation* and 107/266 (Q2) in *Engineering, Electrical & Electronic*.

Paper II

Francisco J. Romero, Alfonso Salinas-Castillo, Almudena Rivadeneyra, Andreas Albrecht, Andres Godoy, Diego P. Morales, Noel Rodriguez. "In-Depth Study of Laser Diode Ablation of Kapton Polyimide for Flexible Conductive Substrates". In: *Nanomaterials*, Vol. 8(7), 517 (2018). DOI: 10.3390/nano8070517. Impact Factor: 4.034, JCR Rank: 71/293 (Q1) in *Materials Science, Multidisciplinary* and 39/94 (Q2) in *Nanoscience & Nanotechnology*

Paper III

Francisco J.Romero, Almudena Rivadeneyra, Alfonso Salinas-Castillo, Akiko Ohata, Diego P.Morales, Markus Becherer and Noel Rodriguez. "Design, fabrication and characterization of capacitive humidity sensors based on emerging flexible technologies". In: *Sensors and Actuators B: Chemical*, Vol. 287, pp. 459–467 (2019) DOI: 10.1016/j.snb.2019.02.043. Impact Factor: 7.100, JCR Rank: 2/64 (Q1) in *Instruments & Instrumentation*, 4/27 (Q1) in *Electrochemistry* and 4/86 (Q1) in *Chemistry, Analytical*.

Paper IV

Francisco J. Romero, Almudena Rivadeneyra, Markus Becherer, Diego P. Morales and Noel Rodríguez. "Fabrication and Characterization of Humidity Sensors Based on Graphene Oxide–PEDOT:PSS Composites on a Flexible Substrate". In: *Micromachines*, Vol. 11(2), 148 (2020). DOI: 10.3390/mi11020148. Impact Factor: 2.523, JCR Rank: 24/64 (Q2) in *Instruments & Instrumentation* and 65/103 (Q3) in *Nanoscience & Nanotechnology*.

Paper V

Marco Bobinger, **Francisco J. Romero**, Alfonso Salinas-Castillo, Markus Becherer, Paolo Lugli, Diego P. Morales and Noel Rodriguez, Almudena Rivadeneyra. "Flexible and robust laser-induced graphene heaters photothermallyscribed on bare polyimide substrates". In: *Carbon*, Vol. 144, pp. 116–126 (2019). DOI: 10.1016/j.carbon.2018.12.010. Impact Factor: 8.821, JCR Rank: 32/314 (Q1) in *Materials Science, Multidisciplinary* and 26/159 (Q1) in *Chemistry, Physical*.

Paper VI

Francisco J. Romero, Almudena Rivadeneyra, Inmaculada Ortiz-Gomez, Alfonso Salinas-Castillo, Andres Godoy, Diego P. Morales and Noel Rodriguez. "Inexpensive Graphene Oxide Heaters Lithographed by Laser". In: *Nanomaterials*, Vol. 9(9), 1184 (2019). DOI: 10.3390/nano9091184. Impact Factor: 4.324, JCR Rank: 42/103 (Q2) in *Nanoscience & Nanotechnology* and 89/314 (Q1) in *Materials Science, Multidisciplinary*.

Paper VII

Francisco J. Romero, Diego P. Morales, Markus Becherer, Almudena Rivadeneyra and Noel Rodriguez. "Screen Printable Electrochemical Capacitors on Flexible Substrates". In: *The Fifth International Conference on Advances in Sensors, Actuators, Metering and Sensing (ALLSENSORS 2020), Valencia, Spain*, Nov. 2020, pp. 3–7. ISBN: 978-1-61208-766-5.

Paper VIII

Francisco J. Romero, Encarnacion Castillo, Almudena Rivadeneyra, Alejandro Toral-Lopez, Markus Becherer, Francisco G. Ruiz, Noel Rodriguez and Diego P. Morales. "Inexpensive and flexible nanographene-based electrodes for ubiquitous electrocardiogram monitoring". In: *npj Flexible Electronics*, Vol. 3, 12 (2019). DOI: 10.1038/s41528-019-0056-2.

Paper IX

Francisco J. Romero, Alejandro Toral-Lopez, Akiko Ohata, Diego P. Morales, Francisco G. Ruiz, Andres Godoy and Noel Rodriguez. "Laser-Fabricated Reduced Graphene Oxide Memristors". In: *Nanomaterials*, Vol. 9(6), 897 (2019). DOI: 10.3390/nano9060897. Impact Factor: 4.324, JCR Rank: 42/103 (Q2) in *Nanoscience & Nanotechnology* and 89/314 (Q1) in *Materials Science, Multidisciplinary*.

Paper X

Francisco J. Romero, Diego P. Morales, Andres Godoy, Francisco G. Ruiz, Isabel M. Tienda-Luna, Akiko Ohata and Noel Rodriguez. "Memcapacitor emulator based on the Miller effect". In: *International Journal of Circuit Theory and Applications*, Vol. 47(4), pp. 572–579 (2019). DOI: 10.1002/cta.2604. Impact Factor: 1.581, JCR Rank: 174/266 (Q3) in *Engineering, Electrical & Electronics*.

Paper XI

Francisco J. Romero, Manuel Escudero, Alfredo Medina-Garcia, Diego P. Morales and Noel Rodriguez. "Meminductor Emulator Based on a Modified Antoniou's Gyrator Circuit". In: *Electronics*, Vol. 9(9), 1407 (2020). DOI: 10.3390/electronics9091407. Impact Factor: 2.412, JCR Rank: 125/266 (Q2) in *Engineering, Electrical & Electronic*.

Paper XII

Francisco J. Romero, Alfredo Medina-Garcia, Manuel Escudero, Diego P. Morales and Noel Rodriguez. "Design and implementation of a floating meminductor emulator upon Riordan gyrator", Vol. 133, 153671 (2021). DOI: 10.1016/j.aeue.2021.153671. Impact Factor: 2.924, JCR Rank: 99/266 (Q2) in *Engineering, Electrical & Electronic* and 38/90 (Q2) in *Telecommunications*.

Results

I

Paper I

Design guidelines of Laser Reduced Graphene Oxide Conformal Thermistor for IoT applications

Francisco J. Romero [1,3,*], Almudena Rivadeneyra [4], Victor Toral [2,3], Encarnacion Castillo [2,3], Francisco Garcia-Ruiz [1,3], Diego P. Morales [2,3], Noel Rodriguez [1,3]

[1] Pervasive Electronics Advanced Research Laboratory. University of Granada, Spain.
[2] Electronic Devices Research Group. University of Granada, Spain.
[3] Department of Electronics and Computer Technology. University of Granada, Granada 18072, Spain.
[4] Technische Universität München, Munich 80333, Germany.
* Corresponding author: franromero@ugr.es

Published in *Sensors and Actuators A: Physical*, May 2018, volume 274, pp. 148–154. DOI: 10.1016/j.sna.2018.03.014. Impact Factor: 2.739. JCR Rank: 19/61 (Q2) in *Instruments & Instrumentation* and 107/266 (Q2) in *Engineering, Electrical & Electronic*.

Abstract

This work presents a complete temperature sensing solution based on a conformal laser-reduced graphene-oxide temperature transducer acting as thermistor. The process to implement the temperature–sensitive element is described in detail; from the raw material to the optimum laser scribing conditions used to define the resistive component. The final transducer is fabricated on a flexible plastic substrate and can be attached to any surface as a conformal patch. To provide a full demonstrator of the potential of this technology, the thermistor is integrated in an IoT sensing platform with wireless data transmission capability using a reconfigurable ultra-low power System-on-Chip.

Keywords: Graphene, reduced-Graphene-Oxide, rGO, sensors, SoC, thermistor.

I.1 Introduction

Since in 2010 the Nobel Prize was awarded to A. Geim and K. Noveselov "for the groundbreaking experiments regarding the two-dimensional material", graphene has become one of the most studied materials in all the fields of technology [1]. Its unique properties combining outstanding electrical conductivity, transparency, toughness and biochemical functionalization capabilities have exponentially attracted the interest of not only fundamental research fields, such as Physics or Chemistry, but also more applied lines, like energy storage or transducers [2]. However, despite graphene's potential is undeniable, the actual end-user applications are still far from achieving the aroused expectations, mostly due to the difficulties associated with the mass production of high quality graphene sheets capable of matching its theoretical properties. The broad spectrum of production approaches has opened the term graphene to a set of materials including not only the ideal sp^2 honeycomb and monoatomic carbon structure, but also multilayer polycrystalline graphene aggregates. One of these graphene-like materials is the so-called reduced-graphene-oxide (rGO) [3]. Notwithstanding that rGO does not feature the superlative properties of monolayer crystalline graphene, it capitalizes part of its unique features (e.g., flexibility or electrical and thermal conductivity), with the great advantage of a much easier and technologically simpler synthesis process. In addition, rGO's conductivity presents a very linear dependence with temperature above 200 K as a consequence of its polycrystalline structure [4]. This latter physical characteristic is exploited in this work to develop a temperature transducer (thermistor), taking advantage of the pliancy and low thermal inertia of the rGO [5], and incorporating an application oriented to a photothermal reduction technique [6]. Some of these properties, such as its ductility, make this kind of sensors a pertinent choice for Internet of Things (IoT) applications or even healthcare implantable systems. In this way, the use of graphene or graphene-like based sensors and devices aims to facilitate the interconnectivity that the future Internet of Every-thing (IoE) environment will need, such as flexible and pervasive devices that shrink the power consumption and enable faster data transmission [7]. In this context, this work presents as a final outcome, a full custom wearable temperature measurement system that illustrates the advantages that this technology brings up to the IoT ecosystem. The manuscript is divided in five parts. After this introduction, Section I.2 introduces the production of rGO from the raw GO colloid. Section I.3 provides guidelines for the design of the transducers based on the laser assisted photothermal lithography, and results from their electrothermal characterization. Section I.4 describes a complete sensor application adopting the rGO transducer in an ultra-low power platform based on Cypress® 5LP System-on-Chip (SoC). Finally, the main conclusions are drawn in Section I.5.

I.2 Laser scribing of reduced-graphene oxide

The starting point for the proposed rGO-based thermistors is the production of the raw material: the Graphene Oxide colloid(GOc). The GOc is synthesized by the oxidation and sonic exfoliation of graphite powder. In our samples, we follow a modified version of the Hummers and Offerman's method [8], schematized in Fig. I.1. For about two hours the graphite is oxidized, in an ice bath, using strong oxidizing reagents like concentrated sulfuric acid (H_2SO_4), sodium nitrate ($NaNO_3$), and potassium permanganate ($KMnO_4$). The temperature should be maintained low to avoid any risk of explosion(Fig. I.1, ice bath). Compared to pristine graphite, GO is strongly oxygenated through functional hydroxyl (-OH) and epoxide (C-O-C) groups in the basal plane of the atoms with sp^3 and sp^2 hybridized planes [9]. After the oxidation, the graphite is filtered (HCl) and washed (H_2O) to remove remaining ions. After that, the hydrophilic nature of GO and the increased interlayer distance caused by the introduction of these functional groups allow the easy penetration of water molecules and hence the layer splitting through sonication (or continuous stirring) in a water dispersion. We sonicated the dispersion (4 mg mL^{-1}) for 30 min taking care of keeping the temperature low enough to avoid the thermal reduction of the GO. Surface charges on the GO are highly negative when dispersed in water due to the carboxylic acid ionization and phenolic-hydroxyl groups, which leads to an electrostatic repulsion that avoids the aggregation of the GOc [3].

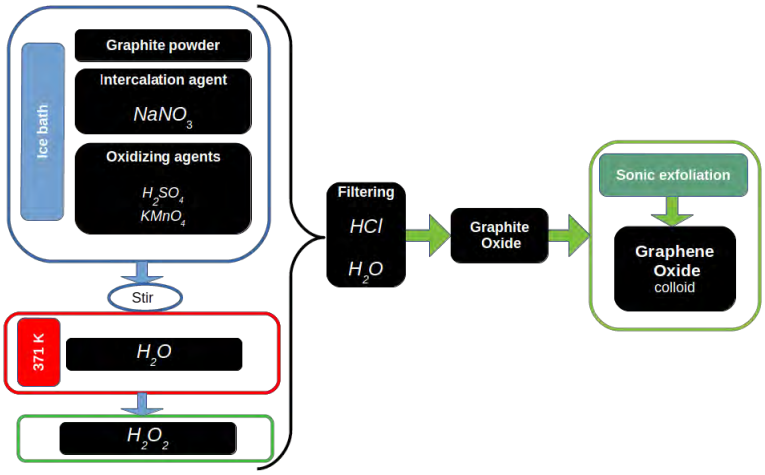

Figure I.1: Schematic diagram summarizing the procedure followed to obtain GO.

I. Design guidelines of Laser Reduced Graphene Oxide Conformal Thermistor for IoT applications

The GOc can be deposited as a thin and uniform film (spin-coated, vortex shaker, etc.) on any non-porous surface (structurally flexible or not) and turned into rGO through a reduction process. GO is an electrical insulator due to the disruption of the crystallographic network of carbon atoms during the oxidation process. However, the electrical conductivity is restored during the reduction by the removal of the functional groups and the partial healing of the crystallographic structure [10]. Among all the existing reduction procedures, we selected the laser photothermal reduction [6] as the best alternative since: *i*) it is environmental friendly, *ii*) it allows the precise patterning of conductive elements without the use of hard masks, and *iii*) the conductivity of the resulting rGO can be modulated by the laser photothermal power. As confirmed by Raman spectroscopy, the 405 nm (up to 300 mW) laser used in this work is able to reduce effectively the GO. The reduction process manifests itself through the change in the intensity ratio of the two main peaks: D and G, located at 1352 cm^{-1} and 1600 cm^{-1}, respectively. The G peak is related to the relative movement of sp^2 pairs of atoms, whereas the D peak is associated with the distortions in the structure [11]. Moreover, the 2D peak (2700 cm^{-1}) is the result of a second order resonant process. In general, the larger the ratio between the 2D and D peaks, the better the quality of the graphene sample obtained [12]. In Fig. I.2, the 2D peak is almost non-existent before the photothermal treatment. But once the laser healing is applied, the 2D peak rises with a large intensity as a consequence of the restoration of the crystallographic structure and the reduction of the number of defects.

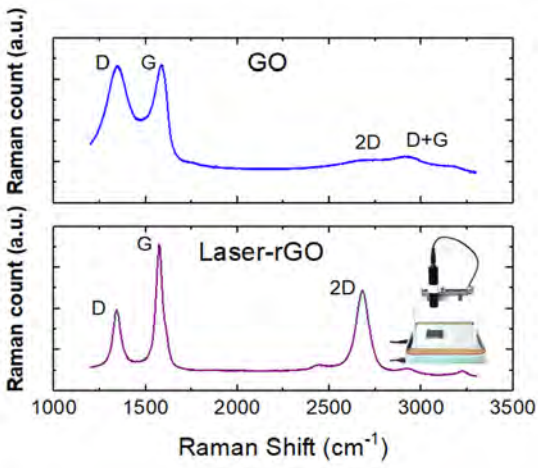

Figure I.2: Raman spectra of GO and laser-reduced GO spin-coated on a PET film at a concentration of 400 μg cm^{-2}. A confocal micro-Raman spectrometer with a 532 nm (green) excitation laser was used. The reduction of GO was achieved by a 405 nm laser, with a photothermal power of 100 mW at an excursion rate of 3 min cm^{-2} and a continuous laser spot. An actual picture of the laser setup is shown at the bottom left-side of the figure.

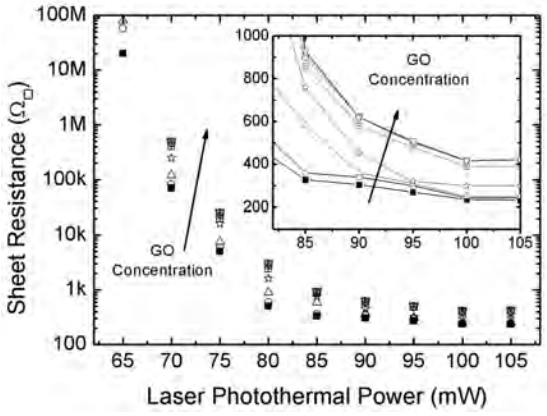

Figure I.3: Laser-rGO sheet resistance extracted from Kelvin measurements as a function of the laser photothermal power (405 nm laser) for different values of GO concentration (50, 70, 100, 130, 150, 160, 180, 200 μg cm^{-2}). Inset shows a magnification in the range of 80-105 mW for an excursion rate of 3 min cm^{-2} with a continuous laser spot. The laser power was limited to 120 mW since greater values can overheat the PET container substrate.

We studied the dependence of the sheet resistance of the laser-rGO as a function of the photothermal power and the initial concentration of GO deposited on the surface before the reduction process. The measurements were conducted by means of the four-point-contact Kelvin method [13]. Results summarized in Fig. I.3 show that, independently of the GO concentration, the increase of the photothermal power decreases dramatically the sheet resistance of the sample, ranging from over-MΩ/sq to sub-kΩ/sq values in a relatively narrow power window. Nevertheless, we observed that the decrease in the sheet resistance tends to saturate for a photothermal power above 90 mW. In addition, a further increase in the laser power does not benefit the conductivity, but rather it can compromise the integrity of the substrate, especially for flexible organic substrates (PET in this case). The initial concentration of the GO before the reduction also plays a role in the resultant conductivity obtained. According to our measurements, the lower the concentration, the better the conductivity obtained, with saturation above 90 μg cm^{-2}. Below 50 μg cm^{-2}, it is more difficult to control the homogeneity of the deposited GO, leading to non-conductive areas. For concentrations above 150 μg cm^{-2}, the increase in the sheet resistance (decrease in conductivity after the reduction) also tends to saturate since, only the surface of the deposited GO is effectively reduced, whereas the layers beneath remain unreduced (as corroborated by Scotch tape exfoliation). In order to achieve the utmost reliability and simultaneously, to minimize the variability in the resistance of the manufactured thermistor prototypes, we tried to mitigate the effect of the synthesis variables, controlling the total resistance of the transductive element only from its physical dimensions. To do so, we set the photothermal

power to 100 mW (where any shift of the power has minor effect according to Fig. I.3, and the integrity of the substrate is guaranteed in terms of local heat dissipation) and the concentration of GO to 70 μg cm^{-2} (where the conductivity of the laser-rGO is very stable).

I.3 Design of rGO thermal transducers

The conductivity of single GO/rGO flakes has been already studied in detail [14]; however, the number of works which exploit the conduction mechanism in large deposited polycrystalline films of rGO is more reduced. In this regard, we have focused our attention on studying the behavior of the conductivity with respect to temperature, rather than analyzing the ultimate physical mechanisms responsible for its conduction. The design of the transducer is dimension-based being its total resistance (R_T) determined by the sheet resistance of the laser-rGO (ρ_s), and both width (W) and length (L) of the patterned resistive element ($R_T = \rho_s L/W$). For our prototypes (Figure I.4 inset), the access to the transducer is implemented by thin copper electrodes. The contact surface between the rGO and copper is coated with conductive silver ink (Merck Dyesol® DYAG350) to decrease the contact resistance and ensure permanent electrical connection. The contact resistance obtained using this method is between 100 Ω and 150 Ω, even for transducers designed for a nominal resistance over the kΩ range. Once the GO is deposited on the polyethylene terephthalate (PET) film, laser-reduced, patterned and contacted, the exposed surface is vacuum sealed with another PET film to prevent direct contact with the atmosphere, thus avoiding the progressive passivation of the functional groups remaining on the GO surface, which may cause a slight time drift on the nominal resistance.

Figure I.4 depicts the calibration curve of one of the developed prototypes (L = 25 cm, W = 0.5 cm). The transducer has been heated and cooled with the aid of a climate chamber (Votsch, Model VCL 4003) at two relative humidity levels (RH = 0% and RH = 50%) while the temperature was being monitored. As observed, the resistance shows a perfectly linear dependence with temperature, facilitating the definition of a calibration curve. However it is worth to mention that this linear law, with RH independence, can only be obtained when the transducer is fully sealed. As shown in Figure I.4, the transducer resistance ranges between [140, 100] kΩ inside the temperature window [243, 308] K, though this resistance could be adjusted by changing the photothermal lithography pattern. The absolute sensitivity for this particular geometry (Figure I.4 inset) is -599.3 Ω/K, which results in a relative sensitivity $[(\Delta R/R_{273K})/(T-273K) = ((R-R_{273K})/R_{273K})/(T-273K)]$ of 0.489 %/K in the range of temperature studied (243-308 K). It is worth mentioning that this value is virtually independent of the rGO lithographed pattern. Only for very long serpentine patterns we corroborated a fluctuation in the sensitivity (up to 0.12 %) attributed to an increase/decrease of the physical dimensions of the transducer with the temperature change.

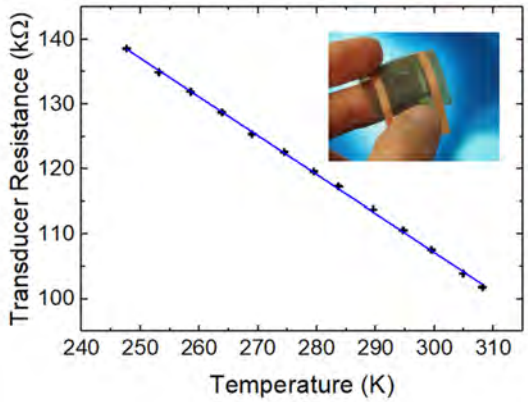

Figure I.4: Total resistance of a thermistive transducer fabricated on laser-rGO as a function of temperature. The values of resistance are obtained at RH=0% and RH=50% showing no difference if the transducer is sealed. Inset shows an example of a flexible thermistive transducer sandwiched between two PET films and connected through copper electrodes.

This resultant sensitivity is similar to that obtained with other non-graphene-based flexible temperature sensors whose synthesis process is technologically more complex [15], [16]. Inside the field of the graphene research applications, Sahoo *et al.* [5] also presented a rGO-based transducer, reduced on an Al_2O_3 substrate, with a sensitivity of 0.195 %/K, about a half of the obtained with the photothermal reduction presented in this work. Another example of flexible temperature sensor based on graphene is the presented by Zhao *et al.* [17]. In that case, a brash mess was used for the Chemical Vapor Deposition (CVD) growth of Graphene Woven Fabrics (GWFs) and transferred afterwards onto a PET substrate, obtaining a sensitivity almost three times higher than the presented in this work. However, this method is significantly less cost-effective for the mass production of transducers. As summary, Table I.1 presents a comparison between the transducer sensitivity presented in this work and others graphene-based as well as non-graphene-based flexible temperature sensors.

	Sensitive Layer	Substrate	Temperature Range	Sensitivity (%/K)
Zhao *et al.* [17]	GWF	PDMS	296 - 328	1.343
Harada *et al.* [15]	PEDOT:PSS-CNT	PET	299 - 326	0.63
Honda *et al.* [16]	PEDOT:PSS-CNT	Kapton	295 - 326	0.61
Sahoo *et al.* [5]	rGO	Al_2O_3	80 - 375	0.195
Xue *et al.* [18]	ZnO NW	PET	283 - 383	[0.98, 3.05]
This work	rGO	PET	243 - 308	0.488

Table I.1: Comparison among close related temperature sensors.

Two aspects should be considered regarding the operation range of these rGO-based transducers. On one hand, if the transducer is laser lithographed maintaining unreduced areas (like in the serpentine pattern), those regions could be progressively reduced if the sensor is maintained at high temperature. The ratio of reduction depends on both temperature and time, but as a general rule to avoid resistance drift, the sensor should be kept below 400 K. This is not a limitation for a fully reduced surface (like a rectangle). On the other hand, at very low temperature (< 200 K) (not tested here), the characteristic may become non-linear, requiring a more sophisticated calibration law [4].

Finally, the impedance of one of the prototype transducers has been analyzed as a function of the frequency. Results evidence a purely resistive behavior up to the 10 kHz of excitation frequency (see Figure I.5), thus ensuring a fast electrical response, whereas beyond 10 kHz the phase of the impedance turns negative, displaying a parasitic parallel capacitive contribution ($Z_T = R_T \ / \ (1 + j2\pi f R_T C)$). From the results shown in Figure I.5, the parasitic capacitance of the transducer can be considered very low (∼95 pF for this particular case), so it does not compromise the fast electrical response.

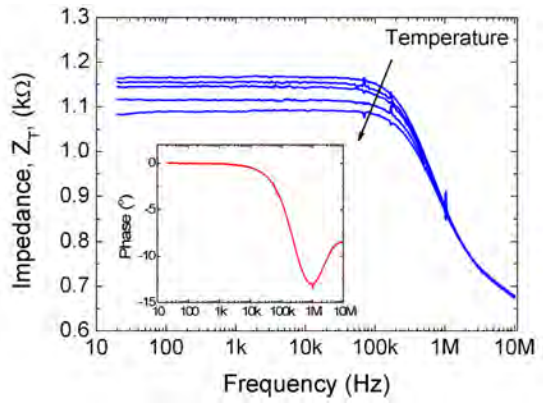

Figure I.5: Impedance plot of a rectangular ($L = 2$ cm, $W = 0.5$cm) laser-rGO thermistor. The impedance presents a resistive signature even beyond 10 kHz, however, at high frequencies the phase turns negative reflecting the appearance of a capacitive behaviour.

I.4 Ultra-Low Power sensor application

The use of any temperature sensor prototype is intimately related to the design of the conditioning interface that provides its information to the final user. Furthermore, in the IoT era [19], the electronic instrumentation designed for an emerging sensor prototype must underline the advantages of this technology and envision the myriads of environments where this device could be employed, especially enhancing the sensor instrumentation symbiosis inside the IoT context.

The main characteristics of an IoT sensor system can be sum up as small size, low-power consumption and wireless communication capability [20]. With these features, the sensor device can be integrated in quite a lot of different systems. In general terms of analog sensors, the design of an instrumentation interface for a sensor node must cope with far different scenarios because of the inherent variability in the output from one to another physical sensor prototype. For this reason, the use of reconfigurable electronic systems is a powerful solution. This alternative might seem unsuitable and uncompetitive for a commercial final version, but the recent advances in the development of programmable Systems-on-Chip (SoC) for IoT applications make this choice as powerful as the full-custom designs [21], [22]. In addition, the solutions based on SoCs help to reduce the time-to-market as well as to make easier the design of sensor-based systems thanks to their programmable Analog Front Ends (AFE). In fact, previous works already show the versatility of this approach for the development of sensor instrumentation applications [23]–[25].

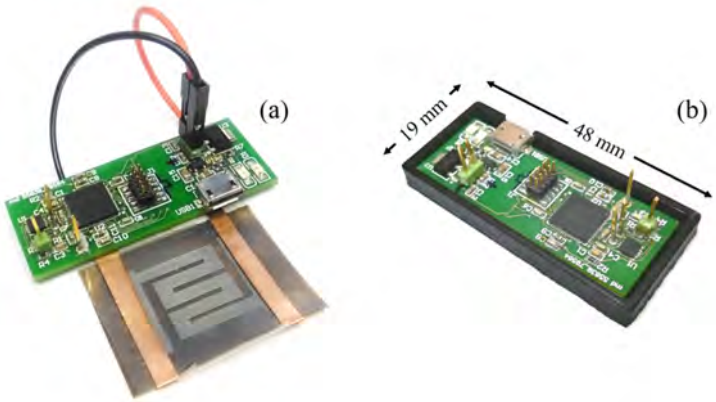

Figure I.6: Real view (sensor connected (a), and inside a housing (b)), of the electronic portable device developed for temperature measurements using the laser-rGO thermistor.

Following this direction, the prototype developed in this work makes use of the Programmable SoC (PSoC) model V from Cypress®, specifically the low-power version [26]. The PSoC 5LP offers numerous advantages over the older versions, specifically in terms of performance, quality and low-power operation, being ideal for IoT applications. The philosophy of this approach is to ensure that all the analog and digital resources that could be necessary for an IoT sensor design are in the same silicon die, thus enabling the design of a miniaturized sensor system that can be attached or integrated in almost any object, such as wearables or even implantable medical devices. On this basis, the prototype shown in Figure I.6 was developed to monitor the ambient temperature using the rGO thermal transducer presented previously. The obtained temperature is sent afterwards by Bluetooth Low Energy (BLE, or Bluetooth 4.0) to a master

device, e.g., a smartphone. For this latter, together with the PSoC 5LP, this device incorporates a BLE module based on the CC2541 transceiver by Texas Instruments [27].

For rGO thermistors, the resistance decreases lineally as the temperature increases in the temperature range studied (Figure I.4). In this case, and in order to minimize the voltage reference dependencies, a ratiometric resistor divider method has been implemented to measure the thermistor resistance. As detailed before, the fact of using a PSoC-based device reduces the signal conditioning complexity since only one external reference resistor is needed (see Figure I.7). The value of the selected R_{ref} should be as similar as possible to the thermistor resistance at the central value of temperature to take advantage of both temperature range and Analog-to-Digital Converter (ADC) dynamic range. The full hardware configuration of the PSoC is shown in Figure I.7. This design has been implemented using the PSoC Creator Integrated Design Environment (IDE), which makes possible the design of both concurrent hardware and application firmware. As seen in Figure I.7, the simplest way to supply power the external circuit would be using the voltage of the battery as V_{hi}, which would also reduce the resolution required for the ADC. However, for ultra-low power consumption, the current through the resistor divider must be as low as possible. In this way, there should be a compromise between V_{hi} (responsible of the current across the resistors) and the resolution of the ADC (temperature resolution). In addition, the Voltage Digital-to-Analog Converter (VDAC) helps to limit the current consumption of the resistor divider, since it can be turned on only when a measurement is taken. Moreover, the PSoC pin used to measure V_{therm} must be set to High-Z to avoid current leakages. This configuration, together with the variation ΔR_T in the range of interest, provides a temperature resolution of $\pm$ 0.001 K.

Once the temperature is measured, the device update the temperature value of the temperature service. From the BLE communication point of view, the device performs a peripheral role. The interface with the BLE module is carried out by means of a full-duplex Universal Asynchronous Receiver Transmitter (UART) component. Due to the standardization of the Bluetooth 4.0 services, any device that incorporates this kind of communication protocol could serve as the master device. In this work, a smartphone has been chosen to widen its potential use.

One of the critical issues in instrumentation is the power efficiency, directly related with the battery lifetime. The consumption of the presented prototype is mainly associated with the software execution, and hence with the SoC hardware peripherals involved on it. Therefore, the program execution cycle must be optimized to minimize the power consumption. SoCs offer the possibility of turning off its peripherals when are not being used, which implies a substantial energy saving without compromising its functionality. In this case, the sensor device has been set to be in idle state until a timer timeout triggers the process to carry out a measurement, then the VDAC is turned on only the time required for an ADC single-shot conversion. Once the temperature is computed and registered, the device returns back to low-power mode (idle). The power supply

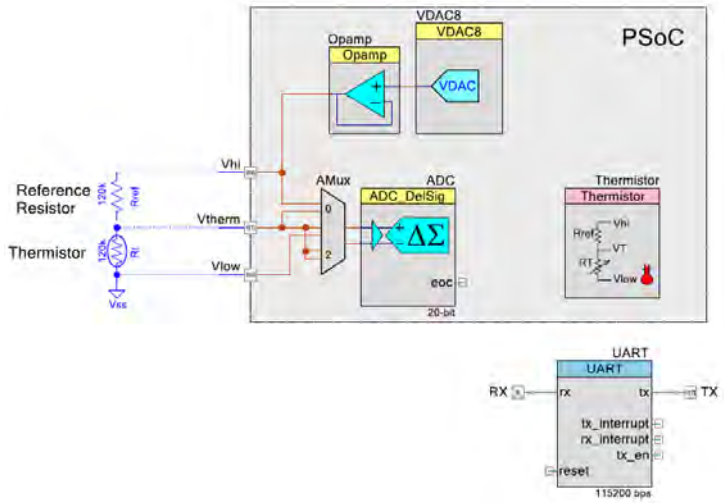

Figure I.7: Laser-rGO thermistor measurement circuit for the prototype shown in Figure 6. This design is a custom modification of the project CE210514 from Cypress [28].

can be provided by an external battery or by a MicroUSB connector depending on the specific application. However, most ultra-low power sensor applications require the use of batteries. Therefore, it is also important to estimate in advance the battery life-time, which depends on the frequency of the measurement. For example, in a room temperature monitoring application which measures the temperature every five minutes, the average current of this device is assessed to be below 10 μA (sensor current included). Thus, the estimation of the battery life-time would be, using the most common coin cell battery (CR2032), of about 2 years.

As an illustrative example of end user application, we present a car outdoor thermometer (Figure I.8). The transducer was attached as a conformal patch to the right rear-view mirror of the car, and the wireless device was located inside it to monitor the ambient temperature. The graph inset in Figure I.8 presents the recorded temperature during 24 hours. Finally, we advocate that once the SoC systems become available on flexible substrates, rGO-based sensors will take a big step forward expanding to multiple ubiquitous applications. For example, the combination of this technology, which is compatible with the human tissue, with self-powered or passively-powered microcontrollers and transceivers would make the medical implants smarter, more accurate, human-friendly and inexpensive.

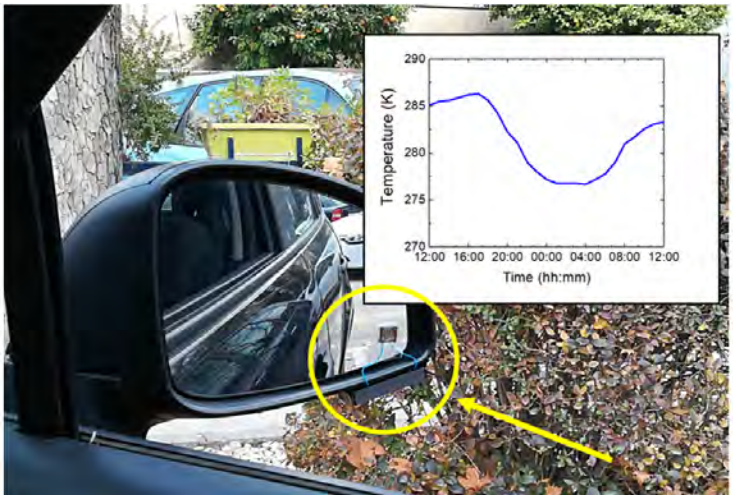

Figure I.8: Temperature sensing solution integrated in the side-view mirror of a car. Inset shows the temperature recorded during one day.

I.5 Conclusions

Graphene Oxide has been suited as a sensing platform ready to be exported to certain end-user applications. We have presented a prototype of temperature monitoring solution, covering aspects from the production of the raw material to its design and integration with a SoC deivce. Once the GO is deposited on the supporting substrate, a simple process is followed to create the transducer: a CNC-laser scribes the desire pattern, yielding a conductivity that can be easily predicted and controlled by the dimensional aspects of the pattern as well as the concentration of GO and laser photothermal power. The final transducer is fabricated on a flexible PET substrate and can be attached to any surface as a conformal patch throwing a very competitive sensitivity when compared with other flexible transducers at a lower production cost. The final complete wireless SoC-based sensing solution presented constitutes an actual demonstrator of the potential of the GO for the implementation of versatile and flexible sensing solutions.

Acknowledgements. Thanks are due to the Center of Scientific Instrumentation of the University of Granada (CIC-UGR) for Raman Spectroscopy experiments. This work has been partially supported by the Spanish Ministry of Education, Culture and Sport (MECD), the European Union and the University of Granada through the project TEC2017-89955-P, the pre-doctoral grant FPU16/01451, the fellowship H2020-MSCA-IF-2017 794885-SELFSENS and the grant “Initiation to Research”. The authors would like to thank Prof. A. Palma for the climate chamber support.

References

[1] Geim, A. K. and Novoselov, K. S., "The rise of graphene," *Nature Materials*, vol. 6, no. 3, pp. 183–191, Mar. 2007.

[2] Vargas-Quesada, B., Chinchilla-Rodriguez, Z., and Rodriguez, N., "Identification and visualization of the intellectual structure in graphene research," *Frontiers in Research Metrics and Analytics*, vol. 2, Oct. 2017.

[3] Dimiev, A. M. and Eigler, S., *Graphene Oxide: Fundamentals and Applications*. WILEY, Nov. 14, 2016, 464 pp.

[4] Neustroev, E. P., Nogovitsyna, M. V., Solovyova, Y. S., Alexandrov, G. N., and Burtseva, E. K., "STUDY OF ELECTRICAL CONDUCTIVITY OF THERMALLY REDUCED GRAPHENE OXIDE," *Radioelectronics. Nanosystems. Information Technologies.*, vol. 7, no. 2, pp. 162–167, Dec. 2015.

[5] Sahoo, S., Barik, S. K., Sharma, G. L., Khurana, G., Scott, J. F., and Katiyar, R. S., "Reduced graphene oxide as ultra fast temperature sensor," *ArXiv*, Apr. 9, 2012. arXiv: 1204.1928.

[6] Kymakis, E., Petridis, C., Anthopoulos, T. D., and Stratakis, E., "Laser-assisted reduction of graphene oxide for flexible, large-area optoelectronics," *IEEE Journal of Selected Topics in Quantum Electronics*, vol. 20, no. 1, pp. 106–115, Jan. 2014.

[7] Alahi, M. E. E., Nag, A., Mukhopadhyay, S. C., and Burkitt, L., "A temperature-compensated graphene sensor for nitrate monitoring in real-time application," *Sensors and Actuators A: Physical*, vol. 269, pp. 79–90, Jan. 2018.

[8] Hummers, W. S. and Offeman, R. E., "Preparation of graphitic oxide," *Journal of the American Chemical Society*, vol. 80, no. 6, pp. 1339–1339, Mar. 1958.

[9] Dreyer, D. R., Park, S., Bielawski, C. W., and Ruoff, R. S., "The chemistry of graphene oxide," *Chem. Soc. Rev.*, vol. 39, no. 1, pp. 228–240, 2010.

[10] Pei, S. and Cheng, H.-M., "The reduction of graphene oxide," *Carbon*, vol. 50, no. 9, pp. 3210–3228, Aug. 2012.

[11] Tuinstra, F. and Koenig, J. L., "Raman spectrum of graphite," *The Journal of Chemical Physics*, vol. 53, no. 3, pp. 1126–1130, Aug. 1970.

[12] Ferrari, A. C., Meyer, J. C., Scardaci, V., Casiraghi, C., Lazzeri, M., Mauri, F., Piscanec, S., Jiang, D., Novoselov, K. S., Roth, S., and Geim, A. K., "Raman spectrum of graphene and graphene layers," *Physical Review Letters*, vol. 97, no. 18, Oct. 2006.

[13] Schroder, *Semiconductor Material 3 Ed.* John Wiley and Sons, Jan. 11, 2006, 800 pp.

[14] Joung, D. and Khondaker, S. I., "Efros-shklovskii variable-range hopping in reduced graphene oxide sheets of varying carbonsp2fraction," *Physical Review B*, vol. 86, no. 23, Dec. 2012.

[15] Harada, S., Honda, W., Arie, T., Akita, S., and Takei, K., "Fully printed, highly sensitive multifunctional artificial electronic whisker arrays integrated with strain and temperature sensors," *ACS Nano*, vol. 8, no. 4, pp. 3921–3927, Mar. 2014.

[16] Honda, W., Harada, S., Arie, T., Akita, S., and Takei, K., "Wearable, human-interactive, health-monitoring, wireless devices fabricated by macroscale printing techniques," *Advanced Functional Materials*, vol. 24, no. 22, pp. 3299–3304, Feb. 2014.

[17] Zhao, X., Long, Y., Yang, T., Li, J., and Zhu, H., "Simultaneous high sensitivity sensing of temperature and humidity with graphene woven fabrics," *ACS Applied Materials & Interfaces*, vol. 9, no. 35, pp. 30 171–30 176, Aug. 2017.

[18] Xue, F., Zhang, L., Tang, W., Zhang, C., Du, W., and Wang, Z. L., "Piezotronic effect on ZnO nanowire film based temperature sensor," *ACS Applied Materials & Interfaces*, vol. 6, no. 8, pp. 5955–5961, Apr. 2014.

[19] Miorandi, D., Sicari, S., Pellegrini, F. D., and Chlamtac, I., "Internet of things: Vision, applications and research challenges," *Ad Hoc Networks*, vol. 10, no. 7, pp. 1497–1516, Sep. 2012.

[20] Gubbi, J., Buyya, R., Marusic, S., and Palaniswami, M., "Internet of things (IoT): A vision, architectural elements, and future directions," *Future Generation Computer Systems*, vol. 29, no. 7, pp. 1645–1660, Sep. 2013.

[21] Aitken, R., Chandra, V., Myers, J., Sandhu, B., Shifren, L., and Yeric, G., "Device and technology implications of the internet of things," in *2014 Symposium on VLSI Technology (VLSI-Technology): Digest of Technical Papers*, IEEE, Jun. 2014.

[22] Semiconductor, C. (2015). "Wearables solutions catalog," Cypress Semiconductor, [Online]. Available: https://www.cypress.com/file/180136/download.

[23] Salinas-Castillo, A., Morales, D. P., Lapresta-Fernandez, A., Ariza-Avidad, M., Castillo, E., Martinez-Olmos, A., Palma, A. J., and Capitan-Vallvey, L. F., "Evaluation of a reconfigurable portable instrument for copper determination based on luminescent carbon dots," *Analytical and Bioanalytical Chemistry*, vol. 408, no. 11, pp. 3013–3020, Feb. 2016.

[24] Morales, D., Lopez-Ruiz, N., Castillo, E., Garcia, A., and Martinez-Olmos, A., "Adaptative ECT system based on reconfigurable electronics," *Measurement*, vol. 74, pp. 238–245, Oct. 2015.

[25] Morales, D. P., Garcia, A., Olmos, A. M., Banqueri, J., and Palma, A. J., "Digital and analog reconfiguration techniques for rapid smart sensor system prototyping," *Sensor Letters*, vol. 7, no. 6, pp. 1113–1118, Dec. 2009.

[26] Semiconductor, C. (2018). ""psoc® 5lp: Cy8c52lp family datasheet," Cypress Semiconductor, [Online]. Available: https://www.cypress.com/file/45916/download.

[27] Instruments, T. (2013). "2.4-ghz bluetooth™ low energy and proprietary system-on-chip," Texas Instruments, [Online]. Available: https%3A%2F%2Fwww.google.com%2F.

[28] "Ce210514 - psoc® 3, psoc 4 and psoc 5lp temperature sensing with a thermistor," Cypress Semiconductor, Tech. Rep., 2018.

Paper II

II

In-Depth Study of Laser Diode Ablation of Kapton Polyimide for Flexible Conductive Substrates

Francisco J. Romero [1,*], Alfonso Salinas-Castillo [2], Almudena Rivadeneyra [3], Andreas Albrecht [3], Andres Godoy [1], Diego P. Morales [1], Noel Rodriguez [1]

[1] Department of Electronics and Computer Technology, University of Granada, 18071 Granada, Spain.
[2] Department of Analytical Chemistry, University of Granada, 18071 Granada, Spain.
[3] Institute for Nanoelectronics, Technical University of Munich, 80333 Munich, Germany.
* Corresponding author: franromero@ugr.es

Published in *Nanomaterials*, Jul 2018, volume 8, 517. DOI: 10.3390/nano8070517. Impact Factor: 4.034. JCR Rank: 71/293 (Q1) in *Materials Science, Multidisciplinary* and 39/94 (Q2) in *Nanoscience & Nanotechnology*.

Abstract

This work presents a detailed study of the photothermal ablation of Kapton® polyimide by a laser diode targeting its electrical conductivity enhancement. Laser-treated samples were structurally characterized using Scanning Electron Microscopy (SEM), Raman spectroscopy, X-ray Photoelectron Spectroscopy (XPS), as well as Diffuse Reflectance Infrared Fourier Transform (DRIFT) spectroscopy. The results show that the laser-assisted ablation constitutes a simple one-step and environmental friendly method to induce graphene-derived structures on the surface of polyimide films. The laser-modified surface was also electrically characterized through the Transmission Line Method (TLM) aiming at the improvement of the conductivity of the samples by tuning the laser power and at the extraction of the contact resistance of the electrodes. Once the laser-ablation process is optimized, the samples increase their conductivity up to six orders of magnitude, being comparable to that of graphene obtained by chemical vapor deposition or by the reduction of graphene-oxide. Additionally, we

show that the contact resistance can be decreased down to promising values of ∼2 Ω when using printed silver-based electrodes.

Keywords: Laser-induced graphene, polyimide, flexible electronics, laser-scribing, sheet resistance, contact resistance

II.1 Introduction

Carbon nanostructures and graphene-derived sheets are auspicious materials for different areas in science and technology, such as healthcare, flexible electronics or energy storage [1], [2]. Nevertheless, reproducible cost-effective methods for the mass production of samples, which would allow introducing them into the market, are still being sought. The difficulties associated with the current production methods have raised researchers' interest in a wide spectrum of techniques to synthesize graphene-based materials. Some of those techniques, such as the epitaxial growth on Silicon Carbide or the Chemical Vapor Deposition (CVD), follow a bottom-up approach pursuing the synthesis of high-quality graphene from a physico-chemical assembly of elemental carbon sources [3]–[5]. However, up to date, they suffer from relatively low yield and high production costs as compared with certain top-down approaches [6], [7]. In this work, we revisited one of those top-down production approaches by proposing the carbon-rich aromatic polyimides, such as Kapton® films, as raw-material to obtain inexpensive graphene-derived sheets which, regardless of their lower crystallographic quality, are capturing growing niches of interest [8].

Since its commercialization, Kapton® films have been used in an impressive wide range of applications, highlighting their use as substrate for flexible electronics [9]–[11]. Previous works have reported that the carbon bonds which constitute Kapton®'s structure can be partially isolated using charged-particle excitation [12], ultraviolet (UV) laser radiation [13], pyrolysis processes [14] or heat-treatments [15]. However, although all these techniques report a substantial increase of the electrical conductivity, they do not fully satisfy the requirements for a cost-effective production of samples due to their poor spatial resolution or the need for using masks to pattern the polyimide surface [16], [17].

The laser assisted production of graphene-derived sheets has been previously applied to materials such as graphene oxide (GO) [18], [19], but also to Kapton® polyimide [20]–[22]. This approach offers the advantage of defining high-precision laser-induced graphene (LIG) patterns on the polyimide surface without affecting the unexposed areas, and, therefore, without the need of lithographic masks. This technique is also compatible with roll-to-roll methods, enabling an inexpensive mass-production of samples. In the present work, we further explore the possibilities of this procedure conducting an exhaustive study covering both the structural and electrical characterization. In contrast to previous works, we used a low-power continuous laser diode driven by a Computer Numerical Control (CNC) unit, rather than CO_2 lasers, for the photothermal ablation of

Kapton® polyimide. The feasibility of this system to induce porous graphene from the bare polyimide substrate has been demonstrated by Scanning Electron Microscopy (SEM), as well as Raman and X-ray Photoelectron Spectroscopy (XPS). In addition, Diffuse Reflectance Infrared Fourier Transform (DRIFT) results confirm that the carbon atoms that compose the 3D structure of the LIG layer result mainly from the removal of carbonyl, phenyl ether and imide bonds from the carbon aromatic rings of the pre-ablated chemical structure of the Kapton® polyimide. The changes in the structure have also been studied as a function of the level of ablation (laser power), seeking the enhancement of the electrical conductivity of the samples. Finally, the contact resistance for different electrode materials has been studied as a key parameter for electronics applications.

II.2 Materials and Methods

II.2.1 Materials

Kapton® HN polyimide films with a thickness of 125 μm from DuPont^{TM} were used as raw material in these experiments. This polyimide, which is produced from the condensation of pyromellitic dianhydride with 4,4-Oxydianiline as cross-linking agent, exhibits an excellent balance of physical, chemical and electrical properties over a wide range of temperature [23]. Ag-loaded conductive paint (from RS, Corby, UK), carbon-based resistive paste (from Henkel, Dusseldorf, Germany), screen printable AgCl paste (from Henkel) and Graphene Oxide, GO, (from Graphenea, Gipuzkoa, Spain) were also employed as printable contacting electrodes for the electrical characterization of the treated surface.

II.2.2 Exposure Source

The laser-ablation experiments were performed using an in-house developed CNC-driven continuous laser diode (from Q-BAIHETM, model 405ML-300-2290, Shenzhen, China). This system, shown in Figure II.1, allows for patterning the polyimide surface, located in an horizontal holder at a distance of 6 cm from the laser head, with a spatial resolution of about 20 μm (given by the mechanical setup) at a fixed wavelength of 405 nm. Furthermore, the laser power can be modulated from 15 mW up to 300 mW.

II.2.3 Structural Characterization

The laser-ablated surfaces were structurally characterized by Scanning Electron Microscopy (SEM), Micro-Raman spectroscopy, X-ray Photoelectron Spectroscopy (XPS) and Infrared (IR) spectroscopy. SEM-images were recorded with a field-emission scanning electron microscope (NVision40 from Carl Zeiss, Oberkochen, Germany) at an extraction and acceleration voltage of 5 kV. A dispersive micro-Raman spectrometer (JASCO NRS-5100, Easton, PA, USA) with a green diode (Elforlight G4-30; Nd:YAG, $\lambda = 532$ nm) as excitation source

Figure II.1: Experimental setup for the laser irradiation of the polyimide surface. The inset displays a sample with two patterned areas of 1 cm^2 on the surface scribed at two different values of the laser power: 50 mW (lighter one) and 100 mW (darker one).

was used for the Raman spectra acquisition. The XPS experiments were carried out on a Kratos Axis Ultra-DLD (Manchester, UK), using an X-ray (Al Kα, hν =1486.6 eV) power of 450W in a vacuum chamber where the pressure was kept below 10^{-10} Torr. On the other hand, the standard IR transmission spectroscopy is not sensitive enough for our purpose due to the thickness of the Kapton® samples, as reported by previous works [24]. For this reason, we selected the DRIFT spectroscopy, which is well-known for its high sensitivity [25]. Thus, the ablated Kapton® foil was scratched using a scalpel, obtaining a powder (∼2 mg) that was mixed with ∼200 mg of anhydrous KBr powder and pressed into 7 mm diameter discs for its analysis on a Bruker Tensor 27 spectrometer (Billerica, MA, USA).

II.2.4 Electrical Characterization

The second objective of this work is the study of the modification of the electrical conductivity of the laser-ablated area. One of the fastest and technologically simplest ways to obtain the electrical characterization of the modified Kapton® films is the Transmission Line Method (TLM) [26]. Therefore, once the Kapton® surface was laser ablated, electrical contacts were printed on the polyimide surface at a distance d_i from each other, as shown in Figure II.2a. The total resistance, R_T, between two consecutive pads is defined by the following expression [27]:

$$R_T = \frac{R_s \cdot d_i}{W} + 2R_c \tag{II.1}$$

being R_s the sheet resistance of the sample and W the contact width. The

relationship of Equation II.1 for a generic sample is plotted in Figure II.2a (inset), illustrating that the sheet resistance, R_s, can be obtained from the slope of the linear fit of the total resistance between contacts (measured in our experiments with a Keysight 34461A Digital Multimeter, Santa Rosa, CA, USA) as a function of their interspacing. The contact resistance, R_c, is evaluated from the residual resistance (d=0, interception of the plot with the total resistance axis), being independent of the contacts' separation [28], [29].

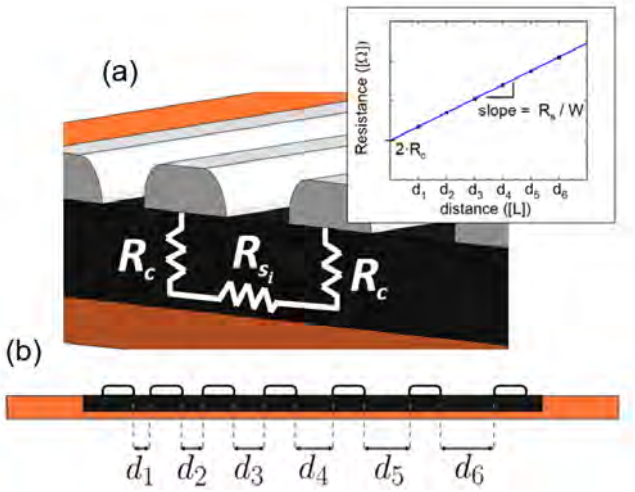

Figure II.2: (a) Equivalent Transmission Line Method (TLM) electrical circuit under two consecutive printed electrodes (R_c: contact resistance, R_{si}: total resistance between contacts i and $i+1$). The inset shows a model of the total resistance (R_T) as a function of the distance between consecutive lines and its relation with the ablated Kapton® sheet resistance (R_S) and contact resistance (R_c); (b) printed contacts are positioned over the modified Kapton® surface at a distance d_i from each other, where d_i ranges from $d_1 = 1$ mm to $d_6 = 3.5$ mm in 0.5 mm steps.

The sheet resistance was evaluated as a function of the laser-ablation level on the Kapton® surface. Accordingly, the samples were prepared following the setup illustrated in Figure 2b, where d_i ranges from $d_1 = 1$ mm to $d_6 = 3.5$ mm in 0.5 mm steps. The laser power was increased from 65 mW to 100 mW (λ = 405 nm, continuous wave) at a fixed excursion rate of 3 min/cm^2.

II.3 Results and Discussion

II.3.1 Structural Characterization of Ablated Kapton

Two SEM micrographs of the irradiated Kapton® surface using a laser power of 100 mW are shown in Figure II.3. Irradiated and unirradiated areas can be

clearly distinguished: the bright ones correspond to the non-ablated Kapton® (yellow box in Figure II.3a), while the dark ones are areas resulting of the laser ablation (red box in Figure II.3a and corresponding magnification in Figure II.3b). The reticulated pattern of the scribing process shown in Figure II.3a is a direct consequence of the mechanical step of our CNC unit, which is larger than the laser spot focused on the surface. The sample is laser-scribed in two passes (one for x-axis and one for y-axis). This fact limits the effective LIG surface of the ablated area, and therefore the minimum value of sheet resistance that can be achieved. The alteration of the color of the Kapton® is visible at a glance: the initial orange tone becomes darker when the laser power is increased, as shown in Figure II.1. Furthermore, as seen in Figure II.3b, the ablated region exhibits a homogeneously porous foam-like appearance, which indicates a drastic increase in the atomic percentage of carbon [30]. This 3D foam-like morphology is also present in other graphene-based materials with high electrical conductivity such as the CVD-grown graphene foams (GFs) presented by Chen *et al.* [31] or the pure-rGO foams obtained from GO-coated-PU-foams proposed by Samad *et al.* [32]. This kind of structure makes the ablated layer easily peelable; however, this could be solved by using a thin lacquer-like layer of polymer to cover it, as it is done for Printed Circuit Boards (PCBs).

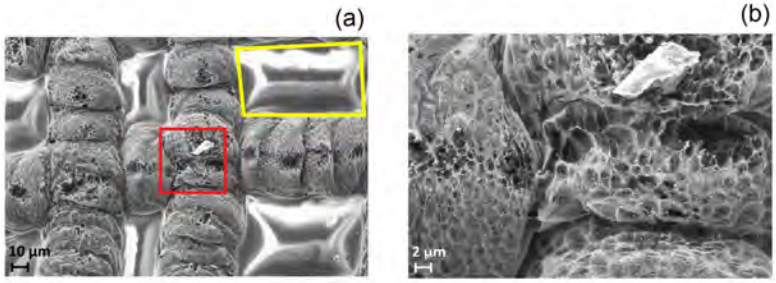

Figure II.3: (a) SEM image of Kapton® polyimide (scale: 10 μm, extraction and acceleration voltage: 5 kV, working distance: 6.0 mm) ablated using a laser power of 100 mW. The bright areas (such as the one framed in yellow) correspond to the non-irradiated surfaces; (b) SEM image (scale: 2 μm, extraction and acceleration voltage: 5 kV, working distance: 6.0 mm) of the red framed area in (a) where the porous structure resulting from the laser ablation process can be appreciated.

Raman spectroscopy is a very helpful technique for the characterization of these kind of samples in a non-invasive way. The Raman spectrum of the treated surface provides a large amount of information about its structure, as well as a quantification of the disorders and defects introduced by the ablation process [33]. Figure II.4 presents the Raman spectra of the laser-ablated surface using different laser photothermal powers in the range from 50 mW to 100 mW. From our experiments, 50 mW was the minimum power to ensure surpassing the ablation threshold for the selected excursion rate (3 min/cm^2) [34]. The laser incidence on

the Kapton® surface creates two main peaks in the Raman spectra, the so-called D and G peaks, located at ∼1350 cm^{-1} and ∼1580 cm^{-1}, respectively. These peaks are present in disordered graphitic materials. In particular, the D peak reveals the presence of defects in sp^2-hybridized carbonous systems [35], while the G peak indicates a graphite-derived structure. The 2D peak (∼2700 cm^{-1}) is due to a second-order resonance, and gives information about the number of layers of the graphite structure [36]. As observed in Figure II.4, the ratio $I_D/I_G \cong 1$ for a laser power below 100 mW confirms the crystalline nature of the ablated surface [37], whereas the increase of the I_{2D}/I_G ratio indicates a reduction of the number of graphene layers [38].

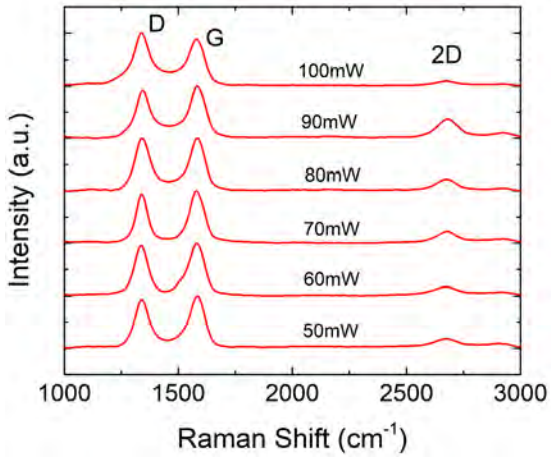

Figure II.4: Raman spectra acquired from the laser-treated Kapton® for different laser powers (wavelength: 532 nm, data interval: 1 cm^{-1}, exposure time: 15 s, accumulations: 5, center number: 1469.99 cm^{-1}).

The resulting Raman spectra of the LIG for the higher laser powers (70-90) mW are similar to the one in nanographene [33]. However, once the laser power exceeds 90 mW, the surface begins to deteriorate and then both I_{2D}/I_G and I_G/I_D ratios decay. At this point, the surface is mainly composed of sp^2 amorphous carbon [39]. The laser-treated films were further characterized by XPS analysis. The XPS data demostrate that the ablated surface is mainly composed of carbon, oxygen and nitrogen, whose atomic contents as a function of the laser power are illustrated in Figure II.5a. The results obtained show that the laser is able to break the C-N, C-O-C and C=O bonds of the untreated Kapton® films, entailing a drastic increase in the atomic content of carbon, while both oxygen and nitrogen are released as gases as a consequence of the laser irradiation [40]. The lower decay of nitrogen ratio suggests the formation of intermediate nitrile groups (-C≡N) [25]. As a result of the rapid removal of some sp^2 carbon atoms from the plane, as well as a great part of the bonds of carbon with both nitrogen and oxygen, the ablated surface adopts the porous

morphology that can be appreciated in Figure II.3, which is a characteristic of the LIG.

Figure II.5b shows the high resolution XPS C1s spectra for different laser powers using a Gaussian decomposition resolved with the CasaXPS software (version 2.3.15, Casa Software Ltd, Teignmouth, UK). All of the spectra are calibrated with respect to the carbon peak (284.6 eV). The spectrum of the Kapton® film presents mainly four functional groups: carbon in the aromatic rings (C-C), C-O-C bonds, carbon bonded to nitrogen (C-N) and carbonyls (C=O) [41]–[43]. As expected, the photothermal process implies significant modifications in the C1s peak intensity and its shape. These results confirm that, as the laser power increases, the number of C=O, C-O-C and C-N bonds decreases, while the C-C peak increases, which is in agreement with the atomic percentages obtained.

DRIFT spectroscopy also indicates the removal of these bonds. Figure II.6 shows the spectra of the unablated and ablated areas of the Kapton® polyimide with its characteristic absorption bands, whose assignment is given in Table II.1. To establish an appropriate comparison, both curves are baseline calibrated with respect to the intensity of the spectrum acquired in the range (1800-2500) cm^{-1}, which is the least influenced by the laser diode ablation [24]. As can be seen, the spectrum of the ablated area presents a significant reduction of the aromatic C-H stretching modes, the imide C-N peaks as well as the phenyl ether linkage (C-O-C), whereas the intensities of the 1500 cm^{-1} and 1600 cm^{-1} peaks reveal an increase in the aromaticity of the ablated surface.

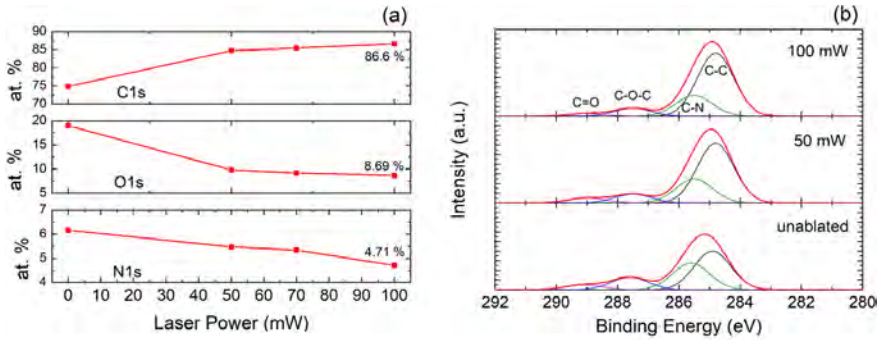

Figure II.5: (a) Atomic percentage of carbon, oxygen and nitrogen in the laser-ablated area as a function of the laser power; (b) comparison of the C1s peaks (black: C-C, green: C-N, blue: C-O-C, purple: C = O) from the XPS spectrum of the laser-ablated Kapton® surface using different laser powers (scanned area: 300 × 700 μm^2, pass energy: 40 eV, sampling depth: 10 nm, step: 1 eV).

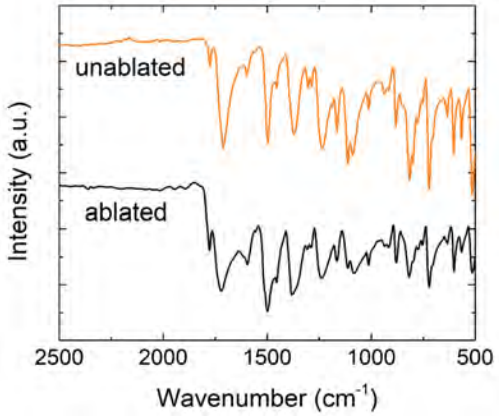

Figure II.6: Diffuse Reflectance Infrared Fourier Transform (DRIFT) spectra of Kapton polyimide before and after the laser irradiation (number of scans: 1024, resolution: 1 cm^{-1}).

Bond	Wavenumber (cm^{-1})
C=O (Carbonyl)	1775, 1712, 1165
C-C (Aromatic)	1600, 1500
C-N (Imide)	1371, 1305, 1285, 1112, 1088
C-O-C (Aromatic)	1235
C-H (Aromatic)	1012, 937, 880, 815
C-H or C-N	721

Table II.1: Infrared absorption bands' identification [44].

II.3.2 Electrical Characterization of Ablated Kapton

The experimental values of the total resistance between contacts using Ag electrodes, and extracted from a TLM structure for different values of the laser ablation power, are presented in Figure II.7a. As expected, the total resistance exhibits a linear dependence with respect to the electrodes' separation [45]. Additionally, all curves converge to the same point ($\pm 14\ \Omega$) in the ordinate axis, indicating that the contact resistance is almost independent of the laser power. The sheet resistance of the LIG, extracted from the slope of the linear fit, is plotted in Figure II.7b as a function of the laser power. The boost of the conductivity is correlated with the ablation level of the surface, and therefore with the aromaticity of the samples. In the same way that the atomic percentages of carbon change, the sheet resistance presents a nonlinear behavior with respect to the laser power. As observed, the decrease of the sheet resistance tends to saturate at $\sim 250\ \Omega\ sq^{-1}$; a value that could be lowered by uniformly patterning the ablated area (instead of using a reticulated ablation mesh as shown in Figure II.3) [20]. Even so, as detailed in Table II.2, this value is very competitive

with respect to the obtained from other graphene-based sheets whose synthesis process is technologically more complex, such as occurs in chemical methods.

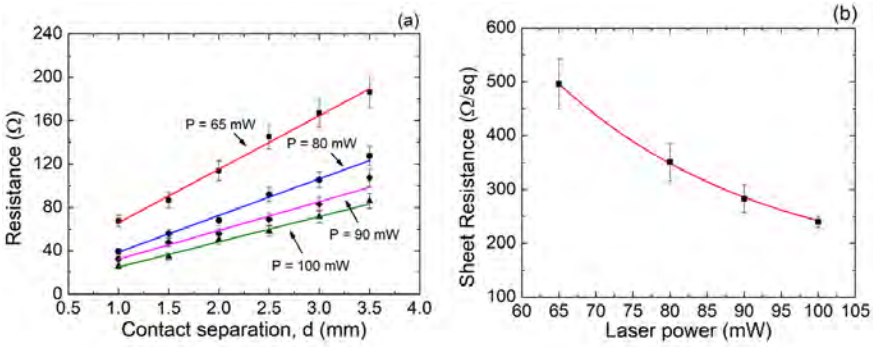

Figure II.7: (a) Total resistance extracted from the Transmission Line Method (TLM) using Ag electrodes; (b) sheet resistance as a function of the laser power at an excursion rate of 3 min cm^{-2}.

	Sample	R_s (Ω/sq.)	Method
Kim *et al.* [46]	Graphene/PET	280	CVD
Li *et al.* [47]	Graphene/SiO_2	350	CVD
Zhao *et al.* [48]	rGO/PET	840	Chemical reduction
Romero *et al.* [49]	rGO/PET	226	Laser diode
Lin *et al.* [20]	LIG/Kapton	<35	CO_2 laser
This work	LIG/Kapton	[242, 295]	Laser diode

Table II.2: Comparison of the sheet resistance, R_s, extracted from close related graphene-derived samples.

In addition to the sheet resistance, the quality of the electrical contact between the ablated surface and the access electrodes is a crucial aspect for the development of high-performance devices [50]. The contact resistance was measured by the TLM method for different electrode materials (Ag, AgCl, rGO and a carbon-based paste). The results obtained are presented in Table II.3. Silver and carbon-based contacts were printed on the ablated surface with the pattern presented in Figure II.7b, while the rGO contacts were fabricated from the laser-assisted reduction of a GO electrode over the Kapton® ablated surface [49]. We report promissing contact-resistance values, R_c, as low as 2 Ω for the Ag and AgCl electrodes, while the reduced-GO and the carbon resistive paste ones yield a contact resistance of ∼75 Ω and ∼125 Ω, respectively. These contact resistance values are much lower than the obtained for others' graphene-derived sheets [51]; this fact might be correlated with the great porosity of the laser-ablated Kapton®, which enhances the specific contact area of the printed electrodes.

Electrode Material	Contact Resistance (Ω)
Ag, AgCl	2 (±6.5%)
Laser-rGO)	75 (±30%)
Carbon-based paste	125 (±20%)

Table II.3: Values of the contact resistance, R_c, extracted from different material-based electrodes.

The results obtained from both sheet resistance and contact resistance reflect the great potential of the laser diode ablation of Kapton® polyimide films, since it constitutes an inexpensive, simple and environmentally friendly method to generate conductive graphene-derived patterns on flexible substrates, anticipating applications in the field of biosensors [52], [53] and energy storage [19].

II.4 Conclusions

The laser diode ablation of Kapton® polyimide has been demonstrated as a high-precision method to modify its surface-structure and electrical properties. The laser-treated surface has been structurally characterized by SEM, Raman, XPS and DRIFT spectroscopy. The results obtained validate the capability of the laser diode photothermal process to induce porous graphene on the polyimide surface. Furthermore, the electrical conductivity has been studied as a function of the laser power aiming at the optimization of the resistivity of the samples. The experiments have shown promising values of electrical conductivity (R_s $\sim$250 Ω sq^{-1}), once the laser-assisted photothermal process has been tuned. The results have also shown independence of the contact resistance with the laser power, presenting values as low as 2 Ω for Ag-based electrodes. These outcomes pave the way for the application of this eco-friendly and low-power manufacturing technology in the flexible electronics field.

Acknowledgements. This work has been partially supported by the Spanish Ministry of Education, Culture and Sport (MECD), the European Union and the University of Granada through the project TEC2017-89955-P, the pre-doctoral grant FPU16/01451, the fellowship H2020-MSCA-IF-2017 794885-SELFSENS and the grant "Initiation to Research". Additionally, this work was supported by the German Research Foundation (DFG) and the Technical University of Munich within the Open Access Publishing Funding Programme.

References

[1] Nathan, A., Ahnood, A., Cole, M. T., Lee, S., Suzuki, Y., Hiralal, P., Bonaccorso, F., Hasan, T., Garcia-Gancedo, L., Dyadyusha, A., Haque, S., Andrew, P., Hofmann, S., Moultrie, J., Chu, D., Flewitt, A. J., Ferrari, A. C., Kelly, M. J., Robertson, J., Amaratunga, G. A. J., and Milne, W. I.,

"Flexible electronics: The next ubiquitous platform," *Proceedings of the IEEE*, vol. 100, no. Special Centennial Issue, pp. 1486–1517, May 2012.

[2] Vargas-Quesada, B., Chinchilla-Rodriguez, Z., and Rodriguez, N., "Identification and visualization of the intellectual structure in graphene research," *Frontiers in Research Metrics and Analytics*, vol. 2, Oct. 2017.

[3] Edwards, R. S. and Coleman, K. S., "Graphene synthesis: Relationship to applications," *Nanoscale*, vol. 5, no. 1, pp. 38–51, 2013.

[4] Zurutuza, A. and Marinelli, C., "Challenges and opportunities in graphene commercialization," *Nature Nanotechnology*, vol. 9, no. 10, pp. 730–734, Oct. 2014.

[5] Shi, X., Li, X., Jiang, L., Qu, L., Zhao, Y., Ran, P., Wang, Q., Cao, Q., Ma, T., and Lu, Y., "Femtosecond laser rapid fabrication of large-area rose-like micropatterns on freestanding flexible graphene films," *Scientific Reports*, vol. 5, no. 1, Nov. 2015.

[6] Zhong, Y. L., Tian, Z., Simon, G. P., and Li, D., "Scalable production of graphene via wet chemistry: Progress and challenges," *Materials Today*, vol. 18, no. 2, pp. 73–78, Mar. 2015.

[7] Warner, J., *Graphene : fundamentals and emergent applications*. Amsterdam: Elsevier, 2013.

[8] Jijun, Z., Liu, L., Li, F., and Zhao, J., *Graphene Oxide: Physics and Applications*. Springer-Verlag GmbH, Dec. 5, 2014.

[9] Rivadeneyra, A., Fernandez-Salmeron, J., Agudo-Acemel, M., Lopez-Villanueva, J. A., Capitan-Vallvey, L. F., and Palma, A. J., "Printed electrodes structures as capacitive humidity sensors: A comparison," *Sensors and Actuators A: Physical*, vol. 244, pp. 56–65, Jun. 2016.

[10] Virtanen, J., Ukkonen, L., Bjorninen, T., Elsherbeni, A. Z., and Sydänheimo, L., "Inkjet-printed humidity sensor for passive UHF RFID systems," *IEEE Transactions on Instrumentation and Measurement*, vol. 60, no. 8, pp. 2768–2777, Aug. 2011.

[11] Chahadih, A., Cresson, P. Y., Hamouda, Z., Gu, S., Mismer, C., and Lasri, T., "Microwave/microfluidic sensor fabricated on a flexible kapton substrate for complex permittivity characterization of liquids," *Sensors and Actuators A: Physical*, vol. 229, pp. 128–135, Jun. 2015.

[12] Venkatesan, T., Forrest, S. R., Kaplan, M. L., Murray, C. A., Schmidt, P. H., and Wilkens, B. J., "Ion-beam-induced conductivity in polymer films," *Journal of Applied Physics*, vol. 54, no. 6, pp. 3150–3153, Jun. 1983.

[13] Schumann, M., Sauerbrey, R., and Smayling, M. C., "Permanent increase of the electrical conductivity of polymers induced by ultraviolet laser radiation," *Applied Physics Letters*, vol. 58, no. 4, pp. 428–430, Jan. 1991.

[14] Bruck, S., "Thermal degradation of an aromatic polypyromellitimide in air and vacuum III—pyrolytic conversion into a semiconductor," *Polymer*, vol. 6, no. 6, pp. 319–332, Jun. 1965.

[15] Venkatachalam, S., Depriester, M., Sahraoui, A. H., Capoen, B., Ammar, M., and Hourlier, D., "Thermal conductivity of kapton-derived carbon," *Carbon*, vol. 114, pp. 134–140, Apr. 2017.

[16] Phillips, H., Smayling, M., and Sauerbrey, R., "Modification of electrical conductivity and surface structure in polymers using ultraviolet laser radiation," *Microelectronic Engineering*, vol. 20, no. 1-2, pp. 73–88, Mar. 1993.

[17] Feurer, T., Sauerbrey, R., Smayling, M. C., and Story, B. J., "Ultraviolet-laser-induced permanent electrical conductivity in polyimide," *Applied Physics A Solids and Surfaces*, vol. 56, no. 3, pp. 275–281, Mar. 1993.

[18] Yung, W. K. C., Li, G., Liem, H. M., Choy, H. S., and Cai, Z., "Eye-friendly reduced graphene oxide circuits with nonlinear optical transparency on flexible poly(ethylene terephthalate) substrates," *Journal of Materials Chemistry C*, vol. 3, no. 43, pp. 11 294–11 299, 2015.

[19] El-Kady, M. F., Strong, V., Dubin, S., and Kaner, R. B., "Laser scribing of high-performance and flexible graphene-based electrochemical capacitors," *Science*, vol. 335, no. 6074, pp. 1326–1330, Mar. 2012.

[20] Lin, J., Peng, Z., Liu, Y., Ruiz-Zepeda, F., Ye, R., Samuel, E. L. G., Yacaman, M. J., Yakobson, B. I., and Tour, J. M., "Laser-induced porous graphene films from commercial polymers," *Nature Communications*, vol. 5, no. 1, Dec. 2014.

[21] Chyan, Y., Ye, R., Li, Y., Singh, S. P., Arnusch, C. J., and Tour, J. M., "Laser-induced graphene by multiple lasing: Toward electronics on cloth, paper, and food," *ACS Nano*, vol. 12, no. 3, pp. 2176–2183, Feb. 2018.

[22] Lamberti, A., Perrucci, F., Caprioli, M., Serrapede, M., Fontana, M., Bianco, S., Ferrero, S., and Tresso, E., "New insights on laser-induced graphene electrodes for flexible supercapacitors: Tunable morphology and physical properties," *Nanotechnology*, vol. 28, no. 17, p. 174 002, Apr. 2017.

[23] "Dupont™ kapton® summary of properties," DuPont, Inc., Tech. Rep., 2017.

[24] Ortelli, E. E., Geiger, F., Lippert, T., Wei, J., and Wokaun, A., "UV-laser-induced decomposition of kapton studied by infrared spectroscopy," *Macromolecules*, vol. 33, no. 14, pp. 5090–5097, Jul. 2000.

[25] Ortelli, E. E., Geiger, F., Lippert, T., and Wokaun, A., "Pyrolysis of kapton® in air: An in situ DRIFT study," *Applied Spectroscopy*, vol. 55, no. 4, pp. 412–419, Apr. 2001.

[26] Reeves, G. and Harrison, H., "Obtaining the specific contact resistance from transmission line model measurements," *IEEE Electron Device Letters*, vol. 3, no. 5, pp. 111–113, May 1982.

[27] Watanabe, E., Conwill, A., Tsuya, D., and Koide, Y., "Low contact resistance metals for graphene based devices," *Diamond and Related Materials*, vol. 24, pp. 171–174, Apr. 2012.

[28] Nagashio, K., Nishimura, T., Kita, K., and Toriumi, A., "Contact resistivity and current flow path at metal/graphene contact," *Applied Physics Letters*, vol. 97, no. 14, p. 143 514, Oct. 2010.

[29] Vinod, P. N., "Specific contact resistance measurements of the screen-printed ag thick film contacts in the silicon solar cells by three-point probe methodology and TLM method," *Journal of Materials Science: Materials in Electronics*, vol. 22, no. 9, pp. 1248–1257, Jan. 2011.

[30] In, J. B., Hsia, B., Yoo, J.-H., Hyun, S., Carraro, C., Maboudian, R., and Grigoropoulos, C. P., "Facile fabrication of flexible all solid-state micro-supercapacitor by direct laser writing of porous carbon in polyimide," *Carbon*, vol. 83, pp. 144–151, Mar. 2015.

[31] Chen, Z., Ren, W., Gao, L., Liu, B., Pei, S., and Cheng, H.-M., "Three-dimensional flexible and conductive interconnected graphene networks grown by chemical vapour deposition," *Nature Materials*, vol. 10, no. 6, pp. 424–428, Apr. 2011.

[32] Samad, Y. A., Li, Y., Schiffer, A., Alhassan, S. M., and Liao, K., "Graphene foam developed with a novel two-step technique for low and high strains and pressure-sensing applications," *Small*, vol. 11, no. 20, pp. 2380–2385, Jan. 2015.

[33] Wu, J.-B., Lin, M.-L., Cong, X., Liu, H.-N., and Tan, P.-H., "Raman spectroscopy of graphene-based materials and its applications in related devices," *Chemical Society Reviews*, vol. 47, no. 5, pp. 1822–1873, 2018.

[34] Kuper, S., Brannon, J., and Brannon, K., "Threshold behavior in polyimide photoablation: Single-shot rate measurements and surface-temperature modeling," *Applied Physics A Solids and Surfaces*, vol. 56, no. 1, pp. 43–50, Jan. 1993.

[35] Venkatachalam, S., Bertin, D., Ducournau, G., Lampin, J., and Hourlier, D., "Kapton-derived carbon as efficient terahertz absorbers," *Carbon*, vol. 100, pp. 158–164, Apr. 2016.

[36] Thomsen, C. and Reich, S., "Double resonant raman scattering in graphite," *Physical Review Letters*, vol. 85, no. 24, pp. 5214–5217, Dec. 2000.

[37] Cancado, L. G., Takai, K., Enoki, T., Endo, M., Kim, Y. A., Mizusaki, H., Jorio, A., Coelho, L. N., Magalhães-Paniago, R., and Pimenta, M. A., "General equation for the determination of the crystallite size la of nanographite by raman spectroscopy," *Applied Physics Letters*, vol. 88, no. 16, p. 163 106, Apr. 2006.

[38] Hao, Y., Wang, Y., Wang, L., Ni, Z., Wang, Z., Wang, R., Koo, C. K., Shen, Z., and Thong, J. T. L., "Probing layer number and stacking order of few-layer graphene by raman spectroscopy," *Small*, vol. 6, no. 2, pp. 195–200, Jan. 2010.

[39] Childres, I., Jauregui, L. A., Park, W., Cao, H., and Chen, Y. P., "Raman spectroscopy of graphene and related materials," *New developments in photon and materials research*, 2013.

[40] Zeng, D., Yung, K., and Xie, C., "XPS investigation of the chemical characteristics of kapton films ablated by a pulsed TEA CO2 laser," *Surface and Coatings Technology*, vol. 153, no. 2-3, pp. 210–216, Apr. 2002.

[41] Yung, K., Zeng, D., and Yue, T., "XPS investigation of upilex-s polyimide ablated by 355 nm nd:YAG laser irradiation," *Applied Surface Science*, vol. 173, no. 3-4, pp. 193–202, Mar. 2001.

[42] Hu, C., Feng, L., and Andrade, J., "Surface structure of pyrolyzed polyimide," *Carbon*, vol. 26, no. 4, pp. 543–545, 1988.

[43] Yumitori, S., "Correlation of c1s chemical state intensities with the o1s intensity in the xps analysis of anodically oxidized glass-like carbon samples," *Journal of Materials Science*, vol. 35, no. 1, pp. 139–146, 2000.

[44] Ferl, J. E. and Long, E. R., "Infrared spectroscopic analysis of the effects of simulated space radiation on a polyimide," *IEEE Transactions on Nuclear Science*, vol. 28, no. 6, pp. 4119–4124, 1981.

[45] Russo, S., Craciun, M., Yamamoto, M., Morpurgo, A., and Tarucha, S., "Contact resistance in graphene-based devices," *Physica E: Low-dimensional Systems and Nanostructures*, vol. 42, no. 4, pp. 677–679, Feb. 2010.

[46] Kim, K. S., Zhao, Y., Jang, H., Lee, S. Y., Kim, J. M., Kim, K. S., Ahn, J.-H., Kim, P., Choi, J.-Y., and Hong, B. H., "Large-scale pattern growth of graphene films for stretchable transparent electrodes," *Nature*, vol. 457, no. 7230, pp. 706–710, Jan. 2009.

[47] Li, X., Zhu, Y., Cai, W., Borysiak, M., Han, B., Chen, D., Piner, R. D., Colombo, L., and Ruoff, R. S., "Transfer of large-area graphene films for high-performance transparent conductive electrodes," *Nano Letters*, vol. 9, no. 12, pp. 4359–4363, Dec. 2009.

[48] Zhao, J., Pei, S., Ren, W., Gao, L., and Cheng, H.-M., "Efficient preparation of large-area graphene oxide sheets for transparent conductive films," *ACS Nano*, vol. 4, no. 9, pp. 5245–5252, Sep. 2010.

[49] Romero, F. J., Rivadeneyra, A., Toral, V., Castillo, E., Garcia-Ruiz, F., Morales, D. P., and Rodriguez, N., "Design guidelines of laser reduced graphene oxide conformal thermistor for IoT applications," *Sensors and Actuators A: Physical*, vol. 274, pp. 148–154, May 2018.

[50] Xia, F., Perebeinos, V., Lin, Y.-m., Wu, Y., and Avouris, P., "The origins and limits of metal–graphene junction resistance," *Nature Nanotechnology*, vol. 6, no. 3, pp. 179–184, Feb. 2011.

[51] Hsu, A., Wang, H., Kim, K. K., Kong, J., and Palacios, T., "Impact of graphene interface quality on contact resistance and RF device performance," *IEEE Electron Device Letters*, vol. 32, no. 8, pp. 1008–1010, Aug. 2011.

[52] Vanegas, D., Patiño, L., Mendez, C., Oliveira, D., Torres, A., Gomes, C., and McLamore, E., "Laser scribed graphene biosensor for detection of biogenic amines in food samples using locally sourced materials," *Biosensors*, vol. 8, no. 2, p. 42, Apr. 2018.

[53] Tehrani, F. and Bavarian, B., "Facile and scalable disposable sensor based on laser engraved graphene for electrochemical detection of glucose," *Scientific Reports*, vol. 6, no. 1, Jun. 2016.

Paper III

Design, Fabrication and Characterization of Capacitive Humidity Sensors based on Emerging Flexible Technologies

III

Francisco J. Romero [1,*], Almudena Rivadeneyra [2], Alfonso Salinas-Castillo [3], Akiko Ohata [4], Diego P. Morales [1], Markus Becherer [2], Noel Rodriguez [1]

[1] Department of Electronics and Computer Technology, University of Granada, 18071 Granada, Spain.
[2] Institute for Nanoelectronics, Technical University of Munich, 80333 Munich, Germany.
[3] Department of Analytical Chemistry, University of Granada, 18071 Granada, Spain.
[4] Institute of Space and Astronautical Science (ISAS), Japan Aerospace Exploration Agency (JAXA), Kanagawa, Japan.
* Corresponding author: franromero@ugr.es

Published in *Sensors and Actuators B: Chemical*, Feb 2019, volume 287, pp. 459–467. DOI: 10.1016/j.snb.2019.02.043. Impact Factor: 7.100. JCR Rank: 2/64 (Q1) in *Instruments & Instrumentation*, 4/27 (Q1) in *Electrochemistry* and 4/86 (Q1) in *Chemistry, Analytical*.

Abstract

This work presents a case-based comparison between two emerging fabrication techniques for the development of conductive patterns for flexible electronics: inkjet-printing and nanographene production by laser-scribing. In particular, these two methods are used to fabricate planar interdigitated electrode (IDE) capacitors with Kapton® HN polyimide as supporting flexible substrate. Silver-based electrodes are manufactured by inkjet-printing, while a laser-scribing technique is used to obtain laser-reduced graphene oxide (laser-rGO) patterns from deposited graphene oxide (GO) and laser-induced graphene (LIG) layouts from the bare polyimide substrate. The comparison is focused on the application of these IDE capacitors as relative humidity (RH) sensors. The different sensors are benchmarked in

terms of sensitivities to RH as well as thermal drift and linearity considering frequency dependencies. The results show that the manufactured capacitors exhibit a very competitive performance as capacitive structures when compared with other similar capacitive sensors from the literature. Furthermore, inkjet-printed and LIG-based capacitors stand out for its thermal stability and linearity.

Keywords: Capacitive sensor, inkjet-printing, laser-induced graphene, laser-reduced graphene oxide, nanographene laser-scribing, relative humidity.

III.1 Introduction

Flexible thin-film electronics is called to be one of the main actor in the more-than-moore domain, targeting auspicious applications for several areas in science and technology [1]. The rising interest in this field lies on its inherent advantages such as lightweight, flexibility and long-lasting durability, combined with cost-effective manufacturing processes [2]. Two basic approaches can be considered for the development of flexible electronics: One of them is the transfer-and-bond procedure, which consists of transferring complete circuits to flexible substrates. This technique, although intended for the development of flexible high-performance devices, requires sophisticated fabrication processes and suffers from low scalability [3]. The other alternative is the direct production of the circuit on the flexible substrate, which bears the manufacturing of large-area electronics and yields to simpler technological processes. This approach, in turn, includes different manufacturing technologies, such as conductive inkjet-printing and nanographene laser-scribing [4]–[7], which are the alternatives followed in the present work.

These technologies have the advantage of being compatible with roll-to-roll techniques, enabling an inexpensive mass-production of samples. In addition, as an asset over other printing techniques, the inkjet printing and laser-scribing processes do not precise of the use of lithographic masks or screens to define the desired layout on the substrate surface; being both contact-less: the process is carried out without physical contact between the nozzle (inkjet-printing) or the laser head (laser-scribing) and the substrate. Another point in favor of these technologies is the high resolution and small thickness that can be achieved when compared with other techniques such as screen printing [8]. Previous studies have already opted for these procedures to fabricate capacitive structures. Examples of that can found in the literature, where the direct laser writing technique is used to develop graphene-based flexible supercapacitors [9], [10], or where supercapacitors on cloth fabrics and flexible substrates are manufactured by inkjet-printing [11].

The present work addresses the design, fabrication and characterization of different capacitive relative humidity (RH) sensors based on interdigitated

electrodes (IDEs) and manufactured by both of these methods on a commercial polyimide thin-film substrate. The same capacitive IDE structure has been defined with the different proposed techniques: one made by inkjet printing of silver nanoparticles, another one by laser-reduction of graphene oxide (laser-rGO) and the third one by laser-induction of porous graphene (LIG) directly on the substrate [12]–[14]. We have characterized these capacitive structures as RH sensors using a climate chamber for different environmental conditions (ranging the temperature at a fixed value of humidity and vice versa), as well as for different working frequencies to evaluate and to compare their performance. This work is structured as follows: after this introduction, Section III.2 summarizes the different materials used in our experiments as well as the methodologies followed for the fabrication and characterization of the samples. Section III.3 presents the results of both structural and electrical characterization of the inkjet-printed and laser-scribed layers, together with a discussion of the capacitive sensors' performance in terms of sensitivity to humidity, linearity, losses and thermal drift. Finally, the main conclusions are drawn in Section III.4.

III.2 Materials and methods

III.2.1 Materials

Kapton® HN films with a thickness of 125 μm were used as a flexible substrate for the implementation of the designed capacitors. The inkjet-printed patterns were made of DGP 40LT-15C silver ink (from ANP USA Inc.) with an average content of 30% silver nanoparticles (NPs) dissolved in triethylene glycol monoethyl ether (TGME). The graphene-oxide was obtained by in-house oxidation and sonic exfoliation of graphite powder (from Sigma-Aldrich) following a modified version of the Hummers and Offerman's method [15]. First, the graphite was oxidized in an ice bath with sulfuric acid (H_2SO_4), sodium nitrate ($NaNO_3$) and potassium permanganate ($KMnO_4$). Then, the resulting aqueous solution was filtered with hydrochloric acid (HCl) and washed (H_2O) to remove the remaining ions. Finally, the dispersion was sonicated in a concentration of 4 mg mL^{-1} for 30 min, which causes its layer splitting [16].

III.2.2 Fabrication processes

The inkjet-printed patterns were defined with a DMP-2831^{TM} Dimatix printer (from Fujifilm Dimatix Inc.), which has already been used for this kind of applications [17]. The printing of the Ag ink layout over the Kapton® polyimide surface was performed under the following conditions: drop-to-drop distance of 50 μm (being the landing diameter of 100 μm), temperature of 60 °C while printing followed, after drying, by a photonic sintering step (Sinteron 2010 from Xenon) with 5 pulses of an energy of 2.5 kV and a time lapse of 500 μs. Only one layer was needed to define the IDE structure. The laser-scribing was performed using an in-house developed Computerized Numeric Control (CNC)

driven laser diode, bypassing the use of lithographic masks. The laser head is able to modulate its power in the range from 15 to 300 mW at a fixed wavelength of 405 nm; while the engraving spatial resolution of 20 μm is given by the motors' mechanical step. Two different experimental approaches were considered for the preparation of the samples using this setup. First, the laser was used for the photothermal reduction of a graphene oxide (GO) film, prepared by drop coating on the Kapton® HN polyimide surface and dried in a vortex shaker (about 24 h). Secondly, for the direct laser photothermal ablation of the Kapton® HN polyimide, which induces on its surface graphene-derived patterns with high electrical conductivity [18].

III.2.3 Capacitive sensor design

The previous fabrication processes were employed to develop planar IDE capacitive RH sensors [19]–[21]. The intrinsic properties of polyimides, such as its effectiveness to absorb moisture and its stability at a wide range of temperatures, make this substrate a perfect choice for the manufacturing of inexpensive RH sensors. These sensors, schematized in Fig. III.1a and photographed in Fig. III.1b, were designed following the IDE layout dimensions summarized in Table III.1. Capacitive-type transducers offer several advantages over the resistive-type ones, such as linear humidity-capacitance relationship for a given frequency, which makes easier the definition of a calibration curve, and a wider RH range of operation [22]. The capacitance of these structures is intimately related to the relative dielectric constant (ε_r) of the insulators which, in the case of the Kapton® HN polyimide, increases with respect to the relative humidity (RH(%)) and decreases as the frequency (f) increases [23]:

$$\varepsilon_r = F(\varepsilon_{o,r}, RH(\%), f) \tag{III.1}$$

being $\varepsilon_{o,r}$ dependent on the polyimide substrate. Moreover, although planar capacitors might have lower performance than parallel plate ones, the interest in planar IDE structures lies on its compactness and low thickness, which is particularly useful when the sensor is used as a conformal patch [24].

In this study, the performance of these RH sensors is evaluated as a function of the technology of the electrodes and the material between them, since they share the same flexible substrate and layout but different resolutions and thicknesses.

Parameter	Value
Number of fingers	13
Fingers length	10 mm
Fingers width	1 mm
Fingers interspacing	0.5 mm
Electrodes separation	0.5 mm

Table III.1: Planar IDE capacitors layout description.

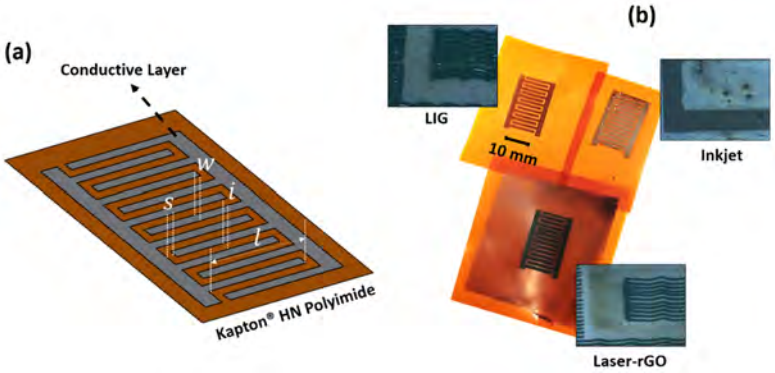

Figure III.1: (a) Planar IDE capacitor on Kapton® HN polyimide substrate (w: finger width; s: electrode separation; i: finger interspacing; l: finger length). (b) Actual photographs and microscope images of an Ag-ink printed electrode, a laser-induced graphene electrode and a laser-rGO electrode.

III.2.4 Electrodes characterization

The structural and electrical characterization of the electrodes of the capacitors are key aspects for the assessment of their performance, especially, for the laser-rGO and LIG ones. As reported by previous works, the electrical conductivity of the laser-derived graphene aggregates presents a strong dependence with the level of photothermal ablation of the raw material, which in turn depends on the power used during the scribing process [18], [25]. Therefore, the analytical structure and conductivity of the electrodes were studied as a function of the laser power with the purpose of optimizing the laser photoablation process. First, both rGO and LIG patterns were electrically characterized using the Transmission Line Model (TLM) method [26]. Once the sheet resistance of the samples was optimized as a function of the laser power, the resulting layer constituting the electrodes was structurally characterized by Scanning Electron Microcospy (SEM), Infrared (IR) spectroscopy, Raman spectroscopy, and X-ray Photoelectron Spectroscopy (XPS).

SEM images were acquired at an extraction and acceleration voltage of 5 kV using the field-emission scanning electron microscope NVision40 from Carl Zeiss. A Kratos X-ray photoelectron spectrometer model Axis Ultra-DLD was used for the XPS experiments. The samples were characterized in a vacuum chamber at a pressure 10^{-10} Torr using an X-ray power of 450 W. The Raman spectra acquisition was carried out in a JASCO NRS-5100 dispersive micro-Raman spectrometer with an excitation source of $\lambda = 532$ nm (Elforlight G4-30; Nd:YAG). Finally, two different techniques were used for the IR spectroscopy, the rGObased electrodes spectra were obtained using attenuated total reflectance Fourier transform infrared (ATR-FTIR) spectroscopy, while Diffuse Reflectance Infrared Fourier Transform (DRIFT) was used for the LIG-based electrodes since

the ATR-FTIR is not sensitive enough in this case [27]. Both techniques were carried out using a Bruker Tensor 27 spectrometer.

III.2.5 Capacitive sensor characterization

The capacitance and parasitic resistance of the fabricated capacitors were measured as a function of the relative humidity and temperature using the four-wires measurement technique with the impedance analyzer 4294A and the impedance probe kit 42941A (from Keysight). The connection between the analyzer and the electrodes was done through a mini-SMA (SubMiniature version A) connector glued to each electrode using silver-filled epoxy EPO-TEK® H20E (from EpoxyTechnology, Inc.). The measurements were performed using a sinusoidal excitation signal of 0.5 V of amplitude. Furthermore, the samples were also characterized as a function of the frequency, ranging from 1 kHz to 10 MHz. The climate chamber VCL 4006 (from VötschIndustrietechnik GmbH) was used for the characterization of the capacitive sensors under different environmental (humidity and temperature) conditions. In our experiments, the humidity was ranged between 30% and 90%, while the interval of temperature was varied from 15 °C to 65 °C. The whole characterization setup was automatized using the Labview 2016 software (from National Instruments Corporation).

III.3 Results and Discussion

III.3.1 Electrodes characterization

The equivalent circuit of the capacitors is a critical factor influencing their performance. An IDE planar capacitor can be modeled as an $R_s + R_p \| Z_c$ association, being R_s the equivalent series resistance, R_p the equivalent parallel resistance and Z_c its reactance. Then, aiming to maximize the power density and to minimize the self-discharge of the capacitive structure, R_s should be reduced to the minimum value possible while R_p should be as large as possible [28]. In our case, the series resistance is related to the sheet resistance of the electrodes, and therefore, the manufacturing processes must be optimized to minimize the resistivity of the conductive patterns.

In the case of the Ag-loaded electrodes, the sheet resistance is strongly related to the sintering method; while the conductivity of the nanographene-based ones depends on the laser photothermal power. In our experiments, we selected the photonic sintering since, as reported by a previous work [29], it can decrease the sheet resistance of the Ag ink down to 55 mΩ sq^{-1} within a few milliseconds, whereas the sheet resistance of the graphene-derived patterns was studied as a function of the laser ablation level. For that purpose, the laser power was ranged from 65 mW to 100 mW at an excursion rate of 3 min cm^{-2} to ensure surpassing the ablation threshold-power [30]. As observed in Fig. III.2, the sheet resistance of both LIG and rGO patterns presents a strong dependence with the laser power. On one hand, when the laser power is increased the sheet resistance of the rGO decreases exponentially from over-MΩ to sub-kΩ. On the other hand,

the LIG presents a softer decay. In both cases, the sheet resistance is reduced down to the value of ∼250 Ω sq^{-1}. According to these results, a laser power of 100 mW was selected to minimize the resistance of both type of electrodes.

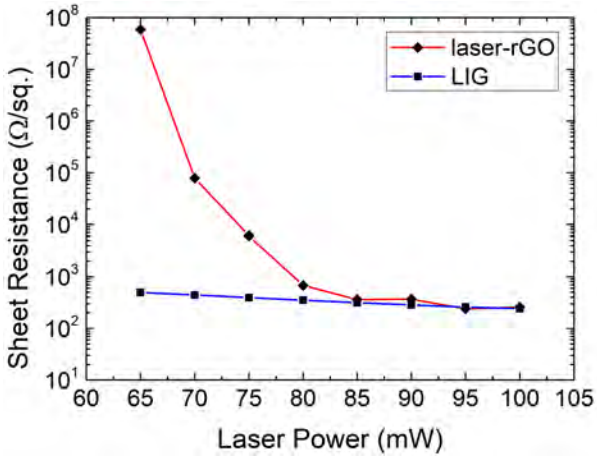

Figure III.2: Sheet resistance of the LIG and laser-rGO as a function of the laser power used for the photoablation of the polyimide surface and the graphene oxide, respectively. The laser excursion rate was set to 3 min cm^{-2}.

SEM images of Fig. III.3 show the morphology of the Ag-ink layer and both nanographene-derived patterns. As seen in Fig. III.3a, the rGO shows a plate-shape structure with multiple cracks as a result of the photothermal reduction of the GO, indicating that the laser is able to restore, at least partially, the crystallographic structure of the carbon bonds disrupted during the oxidation process [31]. In the case of the ablated Kapton® (Fig. III.3b), the irradiated regions show a foam-like morphology which is a defining feature of the LIG [9]citeLin2014. Besides, it can be appreciated that for the rGO sheets the reduction process supposes a thickness decrease of the original thickness of the GO film and an increase of the thickness for the LIG patterns over the Kapton® film, which is consistent with what was reported in previous works [13], [32]. It can also be seen that the engraving resolution limits the effective area of the conductive layers in both laser-treated materials. This makes the sheet resistance higher than that obtained for the Ag-ink layer since this latter, as observed in Fig. III.3c, despite presenting some porosity, it is much more uniform.

Raman spectroscopy and X-ray photoelectron spectroscopy confirm the graphene-derived nature of the rGO and LIG electrodes. On one hand, as observed in Fig. III.4a, the Raman spectra are dominated by three peaks: the D-peak (∼1350 cm^{-1}), the G-peak (∼1580 cm^{-1}) and the 2D-peak (∼2700 cm^{-1}). These peaks are often present in disordered graphene-based materials and its ratio gives a quantification of the disorders and defects of its structure [33]. The G-peak is characteristic in sp^2-hybridized carbon networks, whereas the

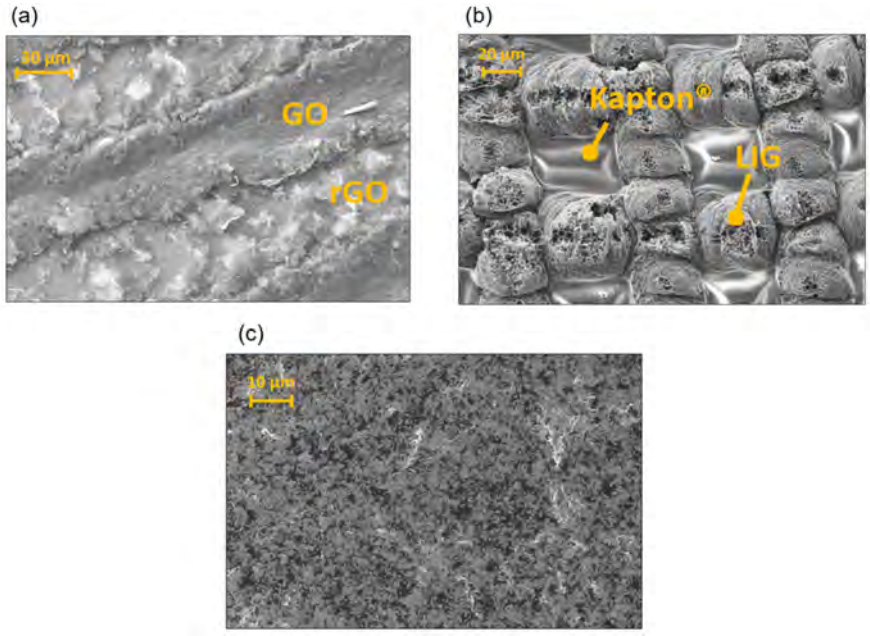

Figure III.3: (a) SEM image of a laser-reduced GO sample (scale: 30 μm, extraction and acceleration voltage: 5 kV, working distance: 6.0 mm). (b) SEM image of a laser-ablated Kapton® sample (scale: 20 μm, extraction and acceleration voltage: 5 kV, working distance: 6.0 mm). (c) SEM image of an Ag-ink sample (scale: 10 μm, extraction and acceleration voltage: 5 kV, working distance 6.0 mm).

D-peak comes from the structural imperfections [34]. Therefore, an estimation for the degree of disorder can be obtained from the ratio I_D/I_G. In this case, this ratio ($I_D/I_G \simeq 1$) points out a larger disorder in the structure of the LIG than in its rGO counterpart. The 2D-peak gives information about the number of layers of the graphitic structure; its intensity increases as the number of layers decreases. Besides, there is no appreciable shift in D and 2D peaks position in both materials, while the G peak of the LIG presents a slight deviation, which might be associated to its larger number of defects [33]. In this way, according to the Raman spectroscopy results, we can infer that the LIG structure presents a lower crystallographic quality with respect to the rGO one.

On the other hand, the XPS spectrum helps to identify the remaining non-desirable bonds after the processing of the raw materials. Fig. III.4b shows the high resolution C1s peak of the XPS spectra for both LIG and laser-rGO electrodes. The Gaussian decomposition was resolved using the CasaXPS software (from Casa Software Ltd). As can be seen, the laser irradiation is able to break most of the C-N, C-O-C and C=O bonds which compose the Kapton® HN polyimide film and the C-OH, C=O and O=C-O bonds of the GO structure

[35]–[37]. The resulting graphene-based materials are basically composed by carbon configurations, with prevalence of the sp^2 carbon aromatic rings (C-C), which is in agreement with the Raman spectroscopy results. In the case of Ag NPs patterns, XPS experiments of Fig. III.4c reveal the dominance of metallic silver, as confirmed by the $3d_{5/2}$ and $3d_{3/2}$ components (located at 368.1 eV and 374.1 eV, respectively) [38], [39]. These results also present a small content of carbon which remains from the TGME solvent after the drying and sintering steps, as observed in inset of Fig. III.4c.

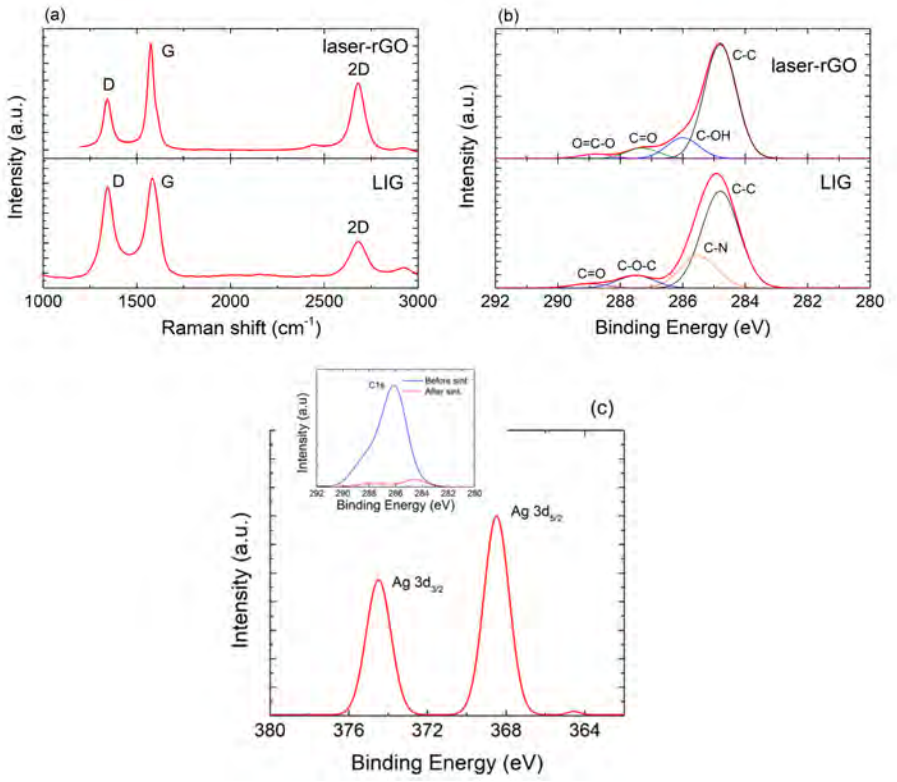

Figure III.4: (a) Comparison of the Raman spectra obtained from the laser-rGO and LIG sheets. The laser power used to produce the samples was 100 mW at an excursion rate of 3 min cm^{-2}. (b) Comparison of the C1s peaks from the XPS spectrum of LIG and laser-rGO. The laser excursion rate was set to 3 min cm^{-2} for a laser power of 100 mW. (c) XPS spectrum of Ag 3d core level of Ag-ink patterns after both drying and sintering steps. Inset shows a comparison of the C1s peaks before and after these steps.

IR spectroscopy also supports these results, Fig. III.5a shows how the reduction process of the GO significantly reduces the stretching vibrations of the hydroxyl groups (-OH) and water molecules presented in the range 3700-2800 cm^{-1} as well as at ∼1614 cm^{-1} and 1347 cm^{-1}. In addition, the broad peak in the range 966-1090 cm^{-1} presented in the GO due to the epoxy groups (C-O-C) is also significantly reduced, while the peak at 1580 cm^{-1} indicates that the C=C band was restored [40]–[42]. As seen, the laser is able to remove various oxygen containing functional groups, although some carbonyl and epoxy groups (C-O-C) still remain after the reduction process. In the case of the Kapton® polyimide (Fig. III.5b), the aromatic C-H stretching modes, the imide C-N groups as well as the phenyl ether linkages (C-O-C) which compose its chemical structure present a significant reduction, whereas the change in the intensity of peaks at 1500 cm^{-1} and 1600 cm^{-1} reveals an increase in the aromaticity of the irradiated surface III.5.

The resolution of the printing and scribing processes is also an important aspect for the performance of the capacitors [20], [21]. Therefore, we analyzed the real physical dimensions of the printed and laser-scribed electrodes under the microscope (see Fig. III.1) to establish a comparison between the designed layout (Table III.1) and the experimental one. Thus,Table III.2 presents the resolution achieved by both methods, where uncertainties were calculated as the standard deviation of the experimental data. As seen, the inkjet patterns have better precision (for the experimental setup considered), especially for the smallest features. Moreover, as it can be seen in Fig. III.1b, the inkjet-printed electrodes are more uniform than the obtained by laser-scribing, which present an appreciable mesh pattern because of the laser-CNC mechanical steps.

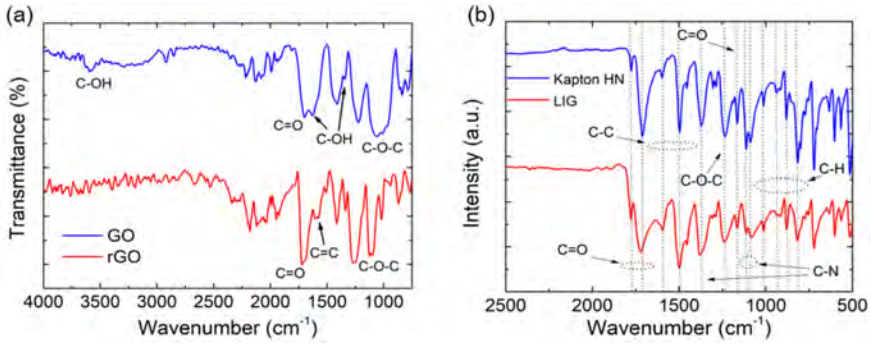

Figure III.5: (a) ATR-FTIR spectroscopy of the GO before and after the reduction. (b) DRIFT spectra of the Kapton® polyimide before and after the laser irradiation. (number of scans: 1024, resolution 1 cm^{-1}).

Parameter	Model (mm)	L-rGO & LIG	Ink-jet Printing (mm)
Fingers length (l)	10	10.4 ± 0.5	9.8 ± 0.2
Fingers width (w)	1	1.32 ± 0.13	1.02 ± 0.05
Fingers interspacing (i)	0.5	0.55 ± 0.02	0.47 ± 0.04
Electrodes separation (s)	0.5	0.54 ± 0.02	0.51 ± 0.05

Table III.2: Planar IDE capacitors: theoretical and experimental dimensions.

III.3.2 Capacitive sensors characterization

Once the electrodes have been structurally and electrically characterized, hereinafter a characterization of the sensors capacitance as a function of the RH(%) and working frequency is presented. The capacitance and equivalent parallel resistance of the capacitors depicted in Fig. III.1 was measured for different values of RH(%) as a function of the frequency and at a constant temperature of 40 °C to be able to cover a broad range of RH. As expected, in all cases the capacitance decreases as the frequency increases. For the LIG electrodes (Fig. III.6a), the capacitance decays half its value, from about 8.5 pF at 1 kHz down to 4 pF at 10 MHz, whereas the response of the Ag-based electrodes (Fig. III.6c) shows a lower dependency on the working frequency with a mean value of 5 pF in the whole range of frequencies analyzed. These values are consequent with the different theoretical models of a coplanar IDE capacitor, such as the proposed by Qin *et al.* [43]. Moreover, for the rGO-based capacitors (Fig. III.6b), the capacitance at 1 kHz is about 40 pF with an exponential decay in frequency down to 5 pF at 10 MHz. As seen, the rGO capacitors present a much higher capacitance at low frequencies due to the high dielectric constant of the GO which remains between the coplanar IDE structure (as can be observed in Fig. III.1b). However, the capacitance reaches a similar value to the previous ones at high frequencies since the dielectric constant of the GO decreases abruptly when the frequency increases [44].

The calibration curves of each sensor, for an excitation source with a frequency of 1 kHz, 10 kHz and 100 kHz, are represented in Fig. III.7. The study was also carried out for different frequencies due to the interest in fast readout sensors [45], [46]. The sensitivity of the sensor, S, which can be obtained from Eq. III.2, gives information about its behavior to humidity changes [47]. Paired in importance, the linearity of the response is defined as the maximum deviation from its linear approximation (Eq. III.3) [48]. Also, the hysteresis is calculated from Eq. III.4, as the maximum difference of capacitance while performing the characterization by increasing and decreasing RH cyclically.

$$S = |\frac{\Delta C}{\Delta RH_i(\%)}|_{T=const} \tag{III.2}$$

$$NonLinearity = \frac{max(C_i - C_{lf})}{C_{max}} \tag{III.3}$$

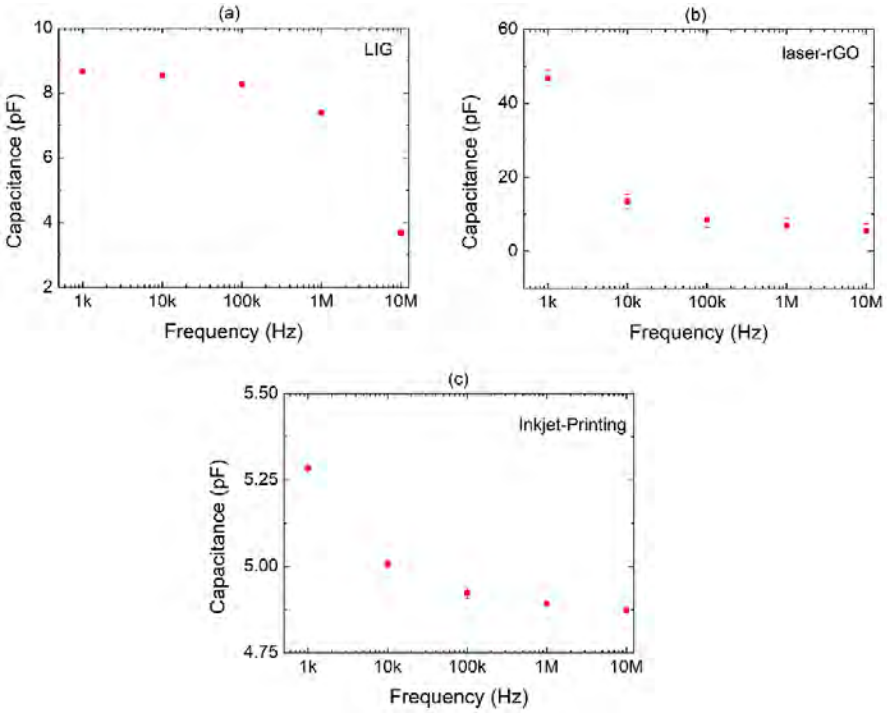

Figure III.6: Capacitance as a function of the frequency at 70%RH, and a fixed temperature of 40 °C for the capacitors with LIG-based electrodes (a), laser-rGO-basedelectrodes (b) and inkjet-printed ones (c). Error bars according to the hysteresis loop due to the increase/decrease of RH are shown.

$$Hysteresis = \frac{max(C_{i,increasing} - C_{i,decreasing})}{C_i} \tag{III.4}$$

being C_i the experimental capacitance measured at $RH_i(\%)$, C_{lf} its linear approximation and C_{max} the maximum capacitance. C_i, increasing and C_i, decreasing are the measured capacitance at $RH_i(\%)$ while increasing and decreasing steps of RH, respectively.

The thermal drift is obtained as the sensitivity of the developed sensors to temperature changes, considering the range from 15 °C to 65 °C (ΔT) at a constant relative humidity of 50%RH, see Eq. III.5.

$$ThermalDrift = |\frac{\Delta C}{\Delta T}|_{RH=CONST} \tag{III.5}$$

A benchmarking of the parameters described above, corresponding to our transducers, is summarized in Table III.3. These results are the average of several measurements carried out on different days, presenting negligible changes from day to day. As can be observed, the LIG-based capacitors present higher linearity

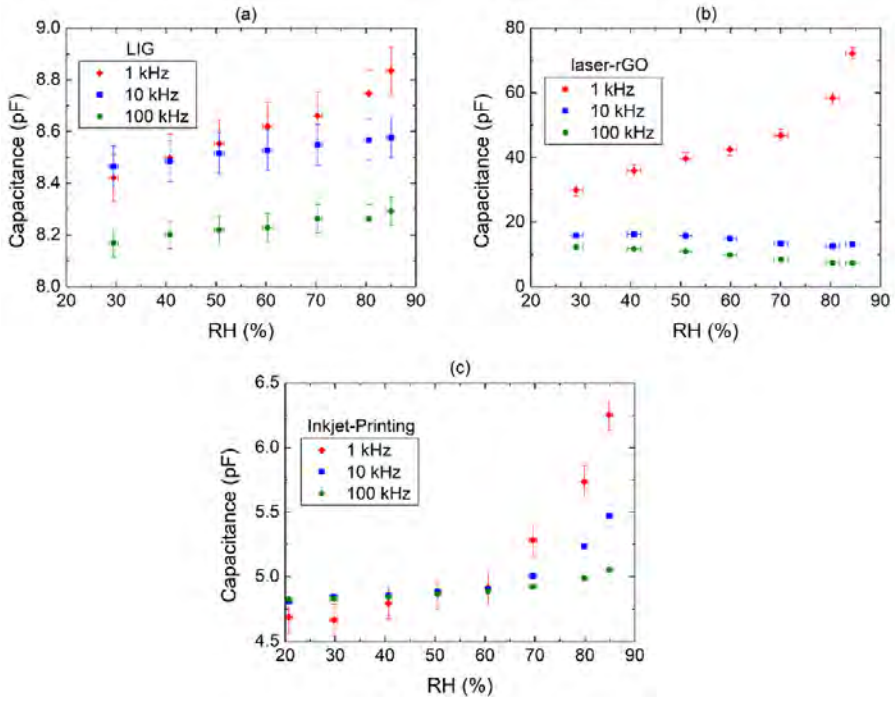

Figure III.7: Response of the humidity sensors: capacitance as a function of the relative humidity, RH(%), for three frequencies at a fixed temperature of 40 °C. Error bars according to the hysteresis loop due to the increase/decrease of RH are shown.

and thermal stability at the expense of a lower sensitivity. This sensitivity, which ranges from 2.0 fF/%RH to 7.44 fF/%RH as a function of the frequency, is comparable to the reported in previous works. For example, Molina-Lopez *et al.* reported a sensitivity of 2.3 fF/%RH with an IDE structure using cellulose acetate butyrate (CAB) as sensing layer and Ag/Ni as electrode material [20], a similar structure with poly(ether urethane) (PEUT) as sensing layer and a sensitivity of 2.03 fF/%RH at 100 kHz was proposed by Altenberend *et al.* [49]. In the same way, comparable sensitivities can be found in the literature for sensors based on more complex technologies [50]–[52]. Besides, as it has been already demonstrated in other works, the sensitivity of these capacitive sensors might be improved using different geometrical layouts [53].

Moreover, the inkjet-printed electrodes present a sensitivity up to 5 times higher than LIG-based capacitors at low frequencies, however, the sensitivity decays with the frequency while their linearity and thermal drift increase. In the case of the rGO-based electrodes, the GO layer between them makes these sensors the most sensitive, although the calibration curve fits better to a second order function. These capacitors also suffer from a low thermal stability since,

Parameter	LIG	Laser-rGO	Inkjet
Sensitivity (fF/%RH)	7.44 at 1 kHz 2.00 at 10 kHz 2.20 at 100 kHz	764 at 1 kHz 66.28 at 10 kHz 89.32 at 100 kHz	24.71 at 1 kHz 10.28 at 10 kHz 3.57 at 100 kHz
Nonlinearity	0.50% at 1 kHz 0.29% at 10 kHz 0.33% at 100 kHz	4.81% at 1 kHz 64.76% 10 kHz 5.41% at 100 kHz	7.07% at 1 kHz 1.43% at 10 kHz 1.04% at 100 kHz
Thermal drift (fF/°C)	< 1 at 1 kHz 5.88 at 10 kHz 4.47 at 100 kHz	218.63 at 1 kHz 60.01 at 10 kHz 73.06 at 100 kHz	17.20 at 1 kHz 23.81 at 10 kHz 26.24 at 100 kHz
Equivalent parallel resistance (MΩ) at 50%RH	678 at 1 kHz 123 at 10 kHz 3.72 at 100 kHzz	0.100 at 1 kHz 0.097 at 10 kHz 0.086 at 100 kHz	2100 at 1 kHz 385 at 10 kHz 110 at 100 kHz

Table III.3: Comparison among the three different flexible capacitive humidity sensors.

as it is well known, the GO is also an outstanding thermal conductor [54]. In any case, the modeling of these calibration curves results easier than the ones from the resistive-type IDE structures, that follow logarithmic or exponential functions [55], [56].

Furthermore, the equivalent parallel resistance of each capacitor is plotted as a function of the frequency in Figure III.8. The change in the parallel resistance with respect to the frequency is due to the leakage current between the electrodes as a result of the dielectric losses when the frequency increases [56]. Because of it, the self-discharge resistance decreases with respect to the frequency in all cases. The best performance in terms of resistivity for the whole range of frequency is achieved by the inkjet-printed capacitors followed by the LIG ones, whose higher leakage current could be directly related to the less uniformity of its electrodes. The laser-rGO-based capacitors are the worst structures in this context since the remaining GO layer between the electrodes facilitates the flow of the leakage current. In any case, these results are very competitive when we compare them with the obtained for other very similar capacitive structures from the literature, such as the presented by Li *et al.* [57], where R_p ranges from ∼10 MΩ (at 1 kHz) to ∼0.1 MΩ (at 100 kHz). These differences in the parallel resistance are also related to the different capacitance values illustrated in Figure III.6. It can be noted that the higher the losses are (lower R_p), the higher the measured capacitance is.

Regarding to the fabrication technologies, inkjet-printing provides the lower value of capacitance, but better performance as capacitive structure (higher R_p, less losses). In addition, this performance is even better for smaller sizes, as it has been already demonstrated [21], [53]. However, this process is more expensive, non-environmentally friendly and slower than the LIG one since it requires of a sintering step. Moreover, the LIG is the simplest method since it can be carried out directly over the substrate without requiring other material or any extra fabrication steps (no previous depositions or sintering processes needed). Thus, this technology allows obtaining humidity sensors with a sensitivity comparable to the reported in the literature combining a high linearity with a low thermal drift. In addition, the performance of these sensors would be enhanced using

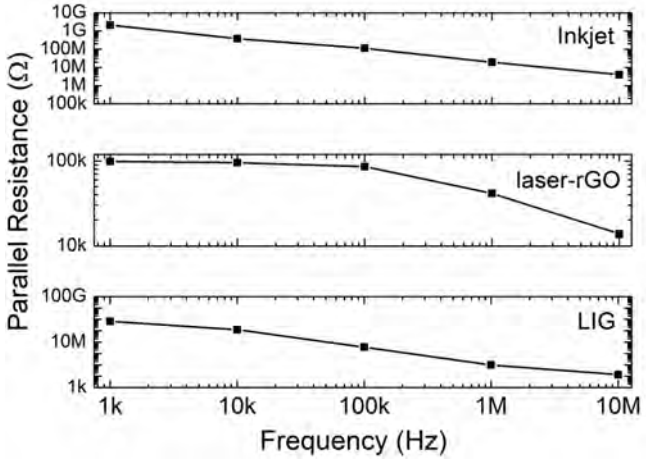

Figure III.8: Equivalent parallel resistance, R_p, of the capacitive structures as a function of the frequency measured at the fixed conditions of 50%RH and 40 °C.

a higher resolution engraving, which would make the LIG layer more uniform, reducing the leakage current (losses), increasing the effective area and, therefore, their sensitivity. Finally, the laser-rGO based capacitors provide much higher capacitance values from the same layout and more sensitivity. Nevertheless, these ones also present the highest losses (lowest R_p values), non-linearity and thermal drift so a rGO-based solution does not result the best choice as capacitive humidity sensors. In fact, this technology is usually better suited for the development of resistive thermistors [25], [58].

Summarizing, the main difference between the graphene-based capacitors and the Ag-ink ones lies on the sheet resistance and uniformity of the conductive layer. Besides, the rGO-based sensor presents the singularity of having a remaining layer of unreduced GO in-between its electrodes. On one hand, this latter feature makes the rGO-based capacitors much more sensitive than both LIG and Ag-ink ones, since the GO dielectric constant is very sensitive to humidity and temperature changes (in contrast to air). Therefore, this also makes the rGO-based sensor thermally less stable and facilitates the current leakage between electrodes. On the other hand, the LIG electrode is less uniform and less conductive that the Ag-ink one, which increase the losses and make these sensors less sensitive.

Finally, as an example of how fast the developed sensors are, the dynamic response of the Ag-based capacitor is depicted in Figure III.9. It can be note that our flexible humidity sensor presents a higher response time (∼3.5 times slower) than the widely-used rigid sensor SHT31 (from Sensirion AG). Besides, this time is intimately related to the sheet resistance of the conductive patterns, being greater as the sheet resistance increases [59], and to the thickness of the sensitive layer [60].

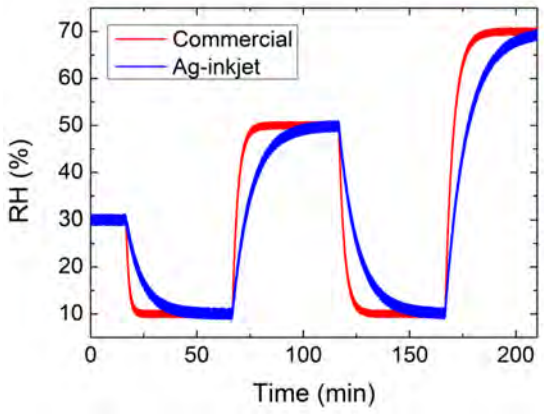

Figure III.9: Transient response of the Ag-ink IDE capacitor.

III.4 Conclusions

Flexible planar IDE capacitive humidity sensors have been compared as a function of the materials and techniques used for its fabrication. Inkjet-printing and laser-scribing techniques have been used to fabricate three different capacitors (Ag-ink, laser-rGO and LIG) over a Kapton® polyimide substrate with the same IDE layout. The structures have been characterized in terms of RH sensitivity, linearity, thermal drift, losses and frequency response. The results obtained have demonstrated that the LIG-based capacitors present a higher linearity response to humidity changes (0.5% of non-linearity at 10 kHz) and the best thermal stability (3.26 fF/°C at 10 kHz) with a sensitivity (ranging from 2 fF/%RH to 7.44 fF/%RH) very competitive when compared with other similar sensor from the literature. On the contrary, the laser-rGO and inkjet-printing based capacitors are much more sensitive to humidity changes (up to 100 and 5 times higher, respectively), keeping a competitive value of sensitivity when the frequency is increased but presenting a higher thermal drift. The inkjet-printed capacitors also stand out for their low losses and the possibility of operating at higher frequencies, while the thermal drift and a higher non-linearity coefficient of the rGO capacitors are their main disadvantages in comparison to the other two structures studied.

Acknowledgements. This research was funded by the Spanish Ministry of Education, Culture and Sport (MECD), the European Union and the University of Granada through the project TEC2017-89955-P, the pre-doctoral grant FPU16/01451, the fellowship H2020-MSCA-IF-2017794885-SELFSENS and the grant "Initiation to Research". The authors would like to thank the support of the JSPS KAKENHI through the grant number JP18K04275 and the support of the Institute for Cognitive Systems from the Technical University of Munich for the use of the inkjet printer.

References

[1] Nathan, A., Ahnood, A., Cole, M. T., Lee, S., Suzuki, Y., Hiralal, P., Bonaccorso, F., Hasan, T., Garcia-Gancedo, L., Dyadyusha, A., Haque, S., Andrew, P., Hofmann, S., Moultrie, J., Chu, D., Flewitt, A. J., Ferrari, A. C., Kelly, M. J., Robertson, J., Amaratunga, G. A. J., and Milne, W. I., "Flexible electronics: The next ubiquitous platform," *Proceedings of the IEEE*, vol. 100, no. Special Centennial Issue, pp. 1486–1517, May 2012.

[2] Zeng, W., Shu, L., Li, Q., Chen, S., Wang, F., and Tao, X.-M., "Fiber-based wearable electronics: A review of materials, fabrication, devices, and applications," *Advanced Materials*, vol. 26, no. 31, pp. 5310–5336, Jun. 2014.

[3] Cheng, I.-C. and Wagner, S., "Overview of flexible electronics technology," in *Flexible Electronics*, Springer US, 2009, pp. 1–28.

[4] Cummins, G. and Desmulliez, M. P., "Inkjet printing of conductive materials: A review," *Circuit World*, vol. 38, no. 4, pp. 193–213, Nov. 2012.

[5] Gans, B.-J. de, Duineveld, P., and Schubert, U., "Inkjet printing of polymers: State of the art and future developments," *Advanced Materials*, vol. 16, no. 3, pp. 203–213, Feb. 2004.

[6] El-Kady, M. F., Strong, V., Dubin, S., and Kaner, R. B., "Laser scribing of high-performance and flexible graphene-based electrochemical capacitors," *Science*, vol. 335, no. 6074, pp. 1326–1330, Mar. 2012.

[7] In, J. B., Hsia, B., Yoo, J.-H., Hyun, S., Carraro, C., Maboudian, R., and Grigoropoulos, C. P., "Facile fabrication of flexible all solid-state micro-supercapacitor by direct laser writing of porous carbon in polyimide," *Carbon*, vol. 83, pp. 144–151, Mar. 2015.

[8] Sondergaard, R., Hosel, M., Angmo, D., Larsen-Olsen, T. T., and Krebs, F. C., "Roll-to-roll fabrication of polymer solar cells," *Materials Today*, vol. 15, no. 1-2, pp. 36–49, Jan. 2012.

[9] Peng, Z., Lin, J., Ye, R., Samuel, E. L. G., and Tour, J. M., "Flexible and stackable laser-induced graphene supercapacitors," *ACS Applied Materials & Interfaces*, vol. 7, no. 5, pp. 3414–3419, Jan. 2015.

[10] Gao, W., Singh, N., Song, L., Liu, Z., Reddy, A. L. M., Ci, L., Vajtai, R., Zhang, Q., Wei, B., and Ajayan, P. M., "Direct laser writing of micro-supercapacitors on hydrated graphite oxide films," *Nature Nanotechnology*, vol. 6, no. 8, pp. 496–500, Jul. 2011.

[11] Chen, P., Chen, H., Qiu, J., and Zhou, C., "Inkjet printing of single-walled carbon nanotube/RuO2 nanowire supercapacitors on cloth fabrics and flexible substrates," *Nano Research*, vol. 3, no. 8, pp. 594–603, Jul. 2010.

[12] Ye, R., James, D. K., and Tour, J. M., "Laser-induced graphene: From discovery to translation," *Advanced Materials*, vol. 31, no. 1, p. 1 803 621, Oct. 2018.

[13] Lin, J., Peng, Z., Liu, Y., Ruiz-Zepeda, F., Ye, R., Samuel, E. L. G., Yacaman, M. J., Yakobson, B. I., and Tour, J. M., "Laser-induced porous graphene films from commercial polymers," *Nature Communications*, vol. 5, no. 1, Dec. 2014.

[14] Lamberti, A., Perrucci, F., Caprioli, M., Serrapede, M., Fontana, M., Bianco, S., Ferrero, S., and Tresso, E., "New insights on laser-induced graphene electrodes for flexible supercapacitors: Tunable morphology and physical properties," *Nanotechnology*, vol. 28, no. 17, p. 174 002, Apr. 2017.

[15] Hummers, W. S. and Offeman, R. E., "Preparation of graphitic oxide," *Journal of the American Chemical Society*, vol. 80, no. 6, pp. 1339–1339, Mar. 1958.

[16] Ayrat M. Dimiev, S. E., *Graphene Oxide: Fundamentals and Applications*. WILEY, Nov. 14, 2016, 464 pp.

[17] Falco, A., Salmerón, J., Loghin, F., Lugli, P., and Rivadeneyra, A., "Fully printed flexible single-chip RFID tag with light detection capabilities," *Sensors*, vol. 17, no. 3, p. 534, Mar. 2017.

[18] Romero, F., Salinas-Castillo, A., Rivadeneyra, A., Albrecht, A., Godoy, A., Morales, D., and Rodriguez, N., "In-depth study of laser diode ablation of kapton polyimide for flexible conductive substrates," *Nanomaterials*, vol. 8, no. 7, p. 517, Jul. 2018.

[19] Yang, T., Yu, Y., Zhu, L., Wu, X., Wang, X., and Zhang, J., "Fabrication of silver interdigitated electrodes on polyimide films via surface modification and ion-exchange technique and its flexible humidity sensor application," *Sensors and Actuators B: Chemical*, vol. 208, pp. 327–333, Mar. 2015.

[20] Molina-Lopez, F., Briand, D., and Rooij, N. de, "All additive inkjet printed humidity sensors on plastic substrate," *Sensors and Actuators B: Chemical*, vol. 166-167, pp. 212–222, May 2012.

[21] Rivadeneyra, A., Fernández-Salmerón, J., Agudo, M., López-Villanueva, J. A., Capitan-Vallvey, L. F., and Palma, A. J., "Design and characterization of a low thermal drift capacitive humidity sensor by inkjet-printing," *Sensors and Actuators B: Chemical*, vol. 195, pp. 123–131, May 2014.

[22] Harrey, P., Ramsey, B., Evans, P., and Harrison, D., "Capacitive-type humidity sensors fabricated using the offset lithographic printing process," *Sensors and Actuators B: Chemical*, vol. 87, no. 2, pp. 226–232, Dec. 2002.

[23] "Dupont™ kapton® summary of properties," DuPont, Inc., Tech. Rep., 2017.

[24] Amendola, S., Lodato, R., Manzari, S., Occhiuzzi, C., and Marrocco, G., "RFID technology for IoT-based personal healthcare in smart spaces," *IEEE Internet of Things Journal*, vol. 1, no. 2, pp. 144–152, Apr. 2014.

[25] Romero, F. J., Rivadeneyra, A., Toral, V., Castillo, E., Garcia-Ruiz, F., Morales, D. P., and Rodriguez, N., "Design guidelines of laser reduced graphene oxide conformal thermistor for IoT applications," *Sensors and Actuators A: Physical*, vol. 274, pp. 148–154, May 2018.

[26] Reeves, G. and Harrison, H., "Obtaining the specific contact resistance from transmission line model measurements," *IEEE Electron Device Letters*, vol. 3, no. 5, pp. 111–113, May 1982.

[27] Ortelli, E. E., Geiger, F., Lippert, T., Wei, J., and Wokaun, A., "UV-laser-induced decomposition of kapton studied by infrared spectroscopy," *Macromolecules*, vol. 33, no. 14, pp. 5090–5097, Jul. 2000.

[28] Frackowiak, E. and Béguin, F., "Carbon materials for the electrochemical storage of energy in capacitors," *Carbon*, vol. 39, no. 6, pp. 937–950, May 2001.

[29] Albrecht, A., Rivadeneyra, A., Abdellah, A., Lugli, P., and Salmerón, J. F., "Inkjet printing and photonic sintering of silver and copper oxide nanoparticles for ultra-low-cost conductive patterns," *Journal of Materials Chemistry C*, vol. 4, no. 16, pp. 3546–3554, 2016.

[30] Kuper, S., Brannon, J., and Brannon, K., "Threshold behavior in polyimide photoablation: Single-shot rate measurements and surface-temperature modeling," *Applied Physics A Solids and Surfaces*, vol. 56, no. 1, pp. 43–50, Jan. 1993.

[31] Neustroev, E. P., Nogovitsyna, M. V., Solovyova, Y. S., Alexandrov, G. N., and Burtseva, E. K., "STUDY OF ELECTRICAL CONDUCTIVITY OF THERMALLY REDUCED GRAPHENE OXIDE," *Radioelectronics. Nanosystems. Information Technologies.*, vol. 7, no. 2, pp. 162–167, Dec. 2015.

[32] Wan, Z., Wang, S., Haylock, B., Kaur, J., Tanner, P., Thiel, D., Sang, R., Cole, I. S., Li, X., Lobino, M., and Li, Q., "Tuning the sub-processes in laser reduction of graphene oxide by adjusting the power and scanning speed of laser," *Carbon*, vol. 141, pp. 83–91, Jan. 2019.

[33] Wu, J.-B., Lin, M.-L., Cong, X., Liu, H.-N., and Tan, P.-H., "Raman spectroscopy of graphene-based materials and its applications in related devices," *Chemical Society Reviews*, vol. 47, no. 5, pp. 1822–1873, 2018.

[34] Venkatachalam, S., Bertin, D., Ducournau, G., Lampin, J., and Hourlier, D., "Kapton-derived carbon as efficient terahertz absorbers," *Carbon*, vol. 100, pp. 158–164, Apr. 2016.

[35] Yung, K., Zeng, D., and Yue, T., "XPS investigation of upilex-s polyimide ablated by 355 nm nd:YAG laser irradiation," *Applied Surface Science*, vol. 173, no. 3-4, pp. 193–202, Mar. 2001.

[36] Hu, C., Feng, L., and Andrade, J., "Surface structure of pyrolyzed polyimide," *Carbon*, vol. 26, no. 4, pp. 543–545, 1988.

[37] Yumitori, S., "Correlation of c1s chemical state intensities with the o1s intensity in the xps analysis of anodically oxidized glass-like carbon samples," *Journal of Materials Science*, vol. 35, no. 1, pp. 139–146, 2000.

[38] Xu, X., Zhuang, J., Du, Y., Feng, H., Zhang, N., Liu, C., Lei, T., Wang, J., Spencer, M., Morishita, T., Wang, X., and Dou, S. X., "Effects of oxygen adsorption on the surface state of epitaxial silicene on ag(111)," *Scientific Reports*, vol. 4, no. 1, Dec. 2014.

[39] Jayabharathi, J., Sundari, G. A., Thanikachalam, V., Jeeva, P., and Panimozhi, S., "A dodecanethiol-functionalized ag nanoparticle-modified ITO anode for efficient performance of organic light-emitting devices," *RSC Advances*, vol. 7, no. 62, pp. 38 923–38 934, 2017.

[40] Piovesan, J. V., Santana, E. R., and Spinelli, A., "Reduced graphene oxide/gold nanoparticles nanocomposite-modified glassy carbon electrode for determination of endocrine disruptor methylparaben," *Journal of Electroanalytical Chemistry*, vol. 813, pp. 163–170, Mar. 2018.

[41] Ciszewski, M., Mianowski, A., Szatkowski, P., Nawrat, G., and Adamek, J., "Reduced graphene oxide–bismuth oxide composite as electrode material for supercapacitors," *Ionics*, vol. 21, no. 2, pp. 557–563, Jun. 2014.

[42] Aragaw, B. A., Su, W.-N., Rick, J., and Hwang, B.-J., "Highly efficient synthesis of reduced graphene oxide–nafion nanocomposites with strong coupling for enhanced proton and electron conduction," *RSC Advances*, vol. 3, no. 45, p. 23 212, 2013.

[43] Qin, H., Cai, Y., Dong, J., and Lee, Y.-S., "Direct printing of capacitive touch sensors on flexible substrates by additive e-jet printing with silver nanoinks," *Journal of Manufacturing Science and Engineering*, vol. 139, no. 3, Oct. 2016.

[44] Kumar, K. S., Pittala, S., Sanyadanam, S., and Paik, P., "A new single/few-layered graphene oxide with a high dielectric constant of 106: Contribution of defects and functional groups," *RSC Advances*, vol. 5, no. 19, pp. 14 768–14 779, 2015.

[45] Zhang, X., Liu, M., Wang, B., Chen, H., and Wang, Z., "A wide measurement range and fast update rate integrated interface for capacitive sensors array," *IEEE Transactions on Circuits and Systems I: Regular Papers*, vol. 61, no. 1, pp. 2–11, Jan. 2014.

[46] Gaisser, A., Geiger, W., Link, T., Merz, J., Steigmajer, S., Hauser, A., Sandmaier, H., Lang, W., and Niklasch, N., "New digital readout electronics for capacitive sensors by the example of micro-machined gyroscopes," *Sensors and Actuators A: Physical*, vol. 97-98, pp. 557–562, Apr. 2002.

[47] Wang, Y., Park, S., Yeow, J. T., Langner, A., and Müller, F., "A capacitive humidity sensor based on ordered macroporous silicon with thin film surface coating," *Sensors and Actuators B: Chemical*, vol. 149, no. 1, pp. 136–142, Aug. 2010.

[48] Kim, K. S., Zhao, Y., Jang, H., Lee, S. Y., Kim, J. M., Kim, K. S., Ahn, J.-H., Kim, P., Choi, J.-Y., and Hong, B. H., "Large-scale pattern growth of graphene films for stretchable transparent electrodes," *Nature*, vol. 457, no. 7230, pp. 706–710, Jan. 2009.

[49] Altenberend, U., Molina-Lopez, F., Oprea, A., Briand, D., Bârsan, N., Rooij, N. F. D., and Weimar, U., "Towards fully printed capacitive gas sensors on flexible PET substrates based on ag interdigitated transducers with increased stability," *Sensors and Actuators B: Chemical*, vol. 187, pp. 280–287, Oct. 2013.

[50] Quintero, A. V., Frolet, N., Marki, D., Marette, A., Mattana, G., Briand, D., and Rooij, N. F. de, "Printing and encapsulation of electrical conductors on polylactic acid (PLA) for sensing applications," in *2014 IEEE 27th International Conference on Micro Electro Mechanical Systems (MEMS)*, IEEE, Jan. 2014.

[51] Rivadeneyra, A., Salmeron, J. F., Capitan-Vallvey, L. F., and Palma, A. J., "Characterization of an interdigitated capacitive structure with branches for relative humidity sensing," *IEEE Sensors Letters*, vol. 1, no. 5, pp. 1–4, Oct. 2017.

[52] Mattana, G., Kinkeldei, T., Leuenberger, D., Ataman, C., Ruan, J. J., Molina-Lopez, F., Quintero, A. V., Nisato, G., Troster, G., Briand, D., and Rooij, N. F. de, "Woven temperature and humidity sensors on flexible plastic substrates for e-textile applications," *IEEE Sensors Journal*, vol. 13, no. 10, pp. 3901–3909, Oct. 2013.

[53] Rivadeneyra, A., Fernandez-Salmeron, J., Agudo-Acemel, M., Lopez-Villanueva, J. A., Capitan-Vallvey, L. F., and Palma, A. J., "Printed electrodes structures as capacitive humidity sensors: A comparison," *Sensors and Actuators A: Physical*, vol. 244, pp. 56–65, Jun. 2016.

[54] Zhu, Y., Murali, S., Cai, W., Li, X., Suk, J. W., Potts, J. R., and Ruoff, R. S., "Graphene and graphene oxide: Synthesis, properties, and applications," *Advanced Materials*, vol. 22, no. 35, pp. 3906–3924, Jun. 2010.

[55] Su, P.-G. and Shiu, C.-C., "Electrical and sensing properties of a flexible humidity sensor made of polyamidoamine dendrimer-au nanoparticles," *Sensors and Actuators B: Chemical*, vol. 165, no. 1, pp. 151–156, Apr. 2012.

[56] Ruiz, V., Fernández, I., Carrasco, P., Cabañero, G., Grande, H. J., and Herrán, J., "Graphene quantum dots as a novel sensing material for low-cost resistive and fast-response humidity sensors," *Sensors and Actuators B: Chemical*, vol. 218, pp. 73–77, Oct. 2015.

[57] Li, Y., Torah, R., Beeby, S., and Tudor, J., "An all-inkjet printed flexible capacitor on a textile using a new poly(4-vinylphenol) dielectric ink for wearable applications," in *2012 IEEE Sensors*, IEEE, Oct. 2012.

[58] Davaji, B., Cho, H. D., Malakoutian, M., Lee, J.-K., Panin, G., Kang, T. W., and Lee, C. H., "A patterned single layer graphene resistance temperature sensor," *Scientific Reports*, vol. 7, no. 1, Aug. 2017.

[59] Oprea, A., Barsan, N., Weimar, U., Bauersfeld, M.-L., Ebling, D., and Wollenstein, J., "Capacitive humidity sensors on flexible RFID labels," *Sensors and Actuators B: Chemical*, vol. 132, no. 2, pp. 404–410, Jun. 2008.

[60] Borini, S., White, R., Wei, D., Astley, M., Haque, S., Spigone, E., Harris, N., Kivioja, J., and Ryhänen, T., "Ultrafast graphene oxide humidity sensors," *ACS Nano*, vol. 7, no. 12, pp. 11 166–11 173, Nov. 2013.

Paper IV

Fabrication and Characterization of Humidity Sensors Based on Graphene Oxide-PEDOT:PSS Composites on a Flexible Substrate

IV

Francisco J. Romero [1,2,*], Almudena Rivadeneyra [1,2], Markus Becherer [3], Diego P. Morales [2,4], Noel Rodriguez [1,2,*]

[1] Pervasive Electronics Advanced Research Laboratory, University of Granada, 18071 Granada, Spain.
[2] Department of Electronics and Computer Technology, University of Granada, 18071 Granada, Spain.
[3] Institute for Nanoelectronics, Technical University of Munich, 80333 Munich, Germany.
[4] Biochemistry and Electronics as Sensing Technologies Group, University of Granada, 18071 Granada, Spain
* Corresponding authors: franromero@ugr.es (F.J.R.), noel@ugr.es (N.R.)

Published in *Micromachines*, Jan 2020, volume 11(2), 148. DOI: 10.3390/mi11020148. Impact Factor: 2.523. JCR Rank: 24/64 (Q2) in *Instruments & Instrumentation*, 65/103 (Q3) in *Nanoscience & Nanotechnology*.

Abstract

In this paper, we present a simple, fast, and cost-effective method for the large-scale fabrication of high-sensitivity humidity sensors on flexible substrates. These sensors consist of a micro screen-printed capacitive structure upon which a sensitive layer is deposited. We studied two different structures and three different sensing materials by modifying the concentration of poly(3,4-ethylenedioxythiophene)/polystyrene sulfonate (PEDOT:PSS) in a graphene oxide (GO) solution. The results show that the aggregation of the PEDOT:PSS to the GO can modify its electrical properties, boosting the performance of the capacitive sensors in terms of both resistive losses and sensitivity to relative humidity (RH) changes. Thus, in an area less than 30 mm^2, the GO/PEDOT:PSS-based sensors

can achieve a sensitivity much higher (1.22 nF/%RH at 1 kHz) than other similar sensors presented in the literature which, together with their good thermal stability, time response and performance over bending, demonstrates that the manufacturing approach described in this work paves the way for the mass production of flexible humidity sensors in an inexpensive way.

Keywords: flexible electronics, graphene oxide, humidity, PEDOT:PSS, screen-printing, sensor.

IV.1 Introduction

Over the last few years, flexible electronics attracted more and more interest in diverse fields of science and technology. Thus, it is now a rapidly developing field of research boosted by the recent advances in two transversal fields: materials for flexible electronics and the compatible fabrication technologies [1]. This interest comes up in response to the challenges imposed by the new electronic applications of the Internet of things (IoT) era, where a trend toward ubiquitous sensing is becoming increasingly clear [2]. In this context, the number of sensing variables, whether environmental or biological, as well as the different ways they can be addressed, resulted in a wide range of studies among which relative humidity (RH) sensors attracted notable attention given their importance for diverse processes and industries, such as food, biomedicine, and the living environment [3]–[6]. Numerous materials have been considered for the manufacturing of flexible RH sensors, such as carbon nanotubes (CNTs) [7], silicon nanosheets (SiNSs) [8], metal–organic frameworks (MOFs) [9], polymers [10], or oxides [11], [12]. However, although some of these sensors reported auspicious results, a technology that enables a cost-effective manufacturing of small flexible RH sensors with a full range of sensitivity, low thermal drift and fast response is still being sought [13].

In this work, we studied two promising materials for this purpose, graphene oxide (GO) and poly(3,4-ethylenedioxythiophene)/polystyrene sulfonate (PEDOT:PSS). On one hand, GO is a perfect candidate to act as a sensing material in RH sensors since, due to its high hydrophilicity, it absorbs the water molecules into its structure, thereby modifying some of its properties, such as the electrical conductivity or the dielectric behavior [14]. On the other hand, PEDOT:PSS is widely used in combination with a large variety of organic materials in order to tune its inherent properties, such as conductivity, dielectric constant, or flexibility [15], [16]. Following this direction, we present a cost-effective approach for the fabrication of flexible RH sensors using a GO/PEDOT:PSS composite as a sensitive layer. We opted for an in-plane capacitive structure consisting of several Ag printed interdigitated electrodes (IDEs), since this configuration allows the fabrication of sensors with lower thickness and smaller distances between electrodes than other conventional technologies [17]. Moreover, we explored not only

the influence of the PEDOT:PSS concentration, but also the capacitive structure itself in terms of sensitivity to humidity changes, frequency response, and losses. Additionally, we also performed tests of thermal stability, time response, and mechanical stress. This work is structured as follows: following this introduction, Section IV.2 summarizes the materials used for the fabrication of the sensors, together with the methodologies for their characterization. Section IV.3 presents both structural and electrical results for two different IDE structures using GO and a hybrid GO/PEDOT:PSS composite as a sensitive layer. Finally, the main conclusions are drawn in Section IV.4.

IV.2 Materials and Methods

IV.2.1 Materials

Transparent and flexible films intended for water-based inks with a thickness of 160 μm (from ColorGATE Digital Output Solutions GmbH, Hannover, Germany) were used as substrate for the fabrication of the RH capacitive sensors. GO colloid with a concentration of 4 mg/mL (0.4 wt%) was prepared following a modified version of the Hummers and Offerman's method [18]. The PEDOT:PSS dispersion used in this work was obtained from Heraeus Holding GmbH (Hanau, Germany, product name: CLEVIOS™ P VP AI 4083). Conductive patterns were achieved using a silver-based screen printable ink (LOCTITE® ECI 1010 E& C from Henkel AG, Düsseldorf, Germany).

IV.2.2 Fabrication of the RH Sensors

The manufacturing procedure of the capacitive humidity sensors presented in this work is schematized in Figure IV.1. Firstly, two interdigitally arranged electrodes (IDE) were printed on the flexible substrate (Figure IV.1a) using a manual screen-printer (from Siebdruck-Versand, Magdeburg, Germany) with a mesh of 90 nylon threads per centimeter (T/cm). Two different IDE structures were considered, as shown in Figure IV.1b. Both of them share a similar area (23 mm^2 and 27 mm^2) but different dimensions. Each one of these capacitive structures follows the pattern indicated in Figure IV.1c, where W is the width of finger, i is the interspacing between fingers, S is the spacing between electrodes, and L is the length of the finger excluding the separation; each one of these electrodes consists of N fingers ($2N$ electrodes in the complete sensing structure). The specific dimensions used for each capacitive structure can be found in Table IV.1.

After the screen-printing process, the samples were dried using a UF55 oven (from Memmert GmbH + Co. KG, Schwabach, Germany) at 120 ^{o}C for 15 min, as recommended by the manufacturer. Then, three different sensitive layers were considered: GO and GO/PEDOT:PSS at two different concentrations of PEDOT:PSS (10% and 20%). For that, 50 μL of these three different solutions were drop-casted using a micropipette on the IDE structures as shown in Figure IV.1d. Finally, the samples were left standing overnight to remove the excess

of water. A real view of one of these sensors can be seen in Figure IV.10 (Supplementary Materials).

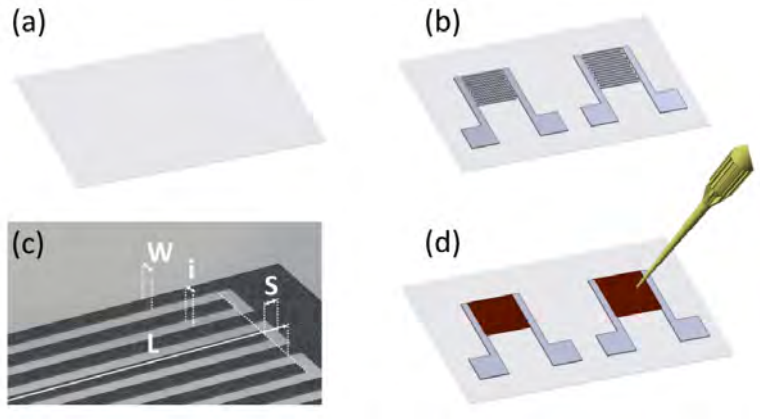

Figure IV.1: Schematic representation of the fabrication process of the relative humidity (RH) sensors. (a) Flexible transparent substrate (thickness: 160 μm). (b) Capacitive interdigitated electrode (IDE) structure screen-printed on the substrate. (c) Dimensions of the interdigitally arranged electrodes (W: width, i: interspacing, L: length, S: spacing). (d) Sensitive layer drop-casted on top of the IDE structure.

Parameter	Layout 1	Layout 2
W (μm)	200	115
i (μm)	200	225
S (μm)	250	250
l (mm)	4.6	4.55
$2N$ (mm)	12	14

Table IV.1: Planar IDE capacitor layout description.

IV.3 Characterization

Fourier-transform infrared spectroscopy (FTIR) was performed using an ALPHA II FTIR spectrophotometer (from Bruker Corporation, Billerica, MA, USA). Optical microscope images were obtained with a ZEISS Axioscope 5 microscope and analyzed with the ZEN Core software (both from Carl Zeiss AG, Oberkochen, Germany). Scanning electron microscope (SEM) images were recorded using an Auriga FIB-FESEM microscope (from Carl Zeiss AG, Oberkochen, Germany). The thickness of the samples was acquired using a DekTak XT contact profilometer (from Bruker Corporation, Billerica, MA, USA) at a stylus force and a scan resolution of 1 μg and 0.33 μm, respectively. The sheet resistances

were measured using the four-point method at a constant current of 100 μA with a probe head from Jandel connected to a B2901A source measuring unit (from Keysight Technologies, Inc., St. Rose, CA, USA). The performance of the capacitive humidity sensors was studied using the climate chamber VCL4006 (from Vötsch Industrietechnik GmbH, Balingen, Germany), together with the impedance analyzer 4294A (from Keysight Technologies, Inc., St. Rose, CA, USA). The impedance of the samples as a function of the frequency was measured for each value of temperature and humidity using an excitation signal of 500 mV. A custom bending set-up was employed to perform the mechanical stress tests using a PD4-N5918M420 stepper motor, together with a GPLE60 precision planetary gear (from Nanotec Electronic GmbH & Co. KG, Feldkirchen, Germany). The whole measurement set-up was automated using the software LabView 2017 (from National Instruments Corporation, Austin, TX, USA).

IV.4 Results and Discussion

IV.4.1 Structural Properties

Before the deposition of the sensitive layer, both capacitive IDE structures were analyzed under the microscope with the purpose of determining whether the pattern was properly transferred to the thin-film substrate without any short-circuit, as well as to establish a comparison between the desired dimensions of the IDE structure and those achieved with the screen-printing process.

Figures IV.2a,b show a partial view of the two different patterns used in this work, so-called layout 1 and 2 in Table IV.1, respectively. At a glance it can be noted that smaller fingers resulted in worse resolution, since this was limited by the mesh of the screen mask [19]. Specifically, the real dimensions for both layouts are specified in Table IV.2, where errors represent the standard deviation of the measurements obtained for different fingers and samples. An image at higher magnification of one of these silver-based patterns is shown in Figure IV.2c, where the sandy texture as a consequence of the irregular flake structure of the Ag-ink can be noticed [20]. The average thickness of these patterns obtained through stylus profilometry was $\sim$3 μm and their sheet resistance was 114 $\pm$ 11 mΩ/sq.

Parameter	Layout 1	Layout 2
W (μm)	197.81 $\pm$ 13.12	148.54 $\pm$ 14.59
i (μm)	201.76 $\pm$ 8.53	233.55 $\pm$ 22.68
S (μm)	260.01 $\pm$ 35.88	277.15 $\pm$ 25.26

Table IV.2: Experimental dimensions of the planar IDE capacitors.

On the other hand, once the sensitive layers were deposited and dried on top of the IDE structures, they were also analyzed under microscope. In the case of the GO (Figure IV.2d), optical images show an uniform layer with a smooth surface and a few craters, which preserved the brown color of the aqueous

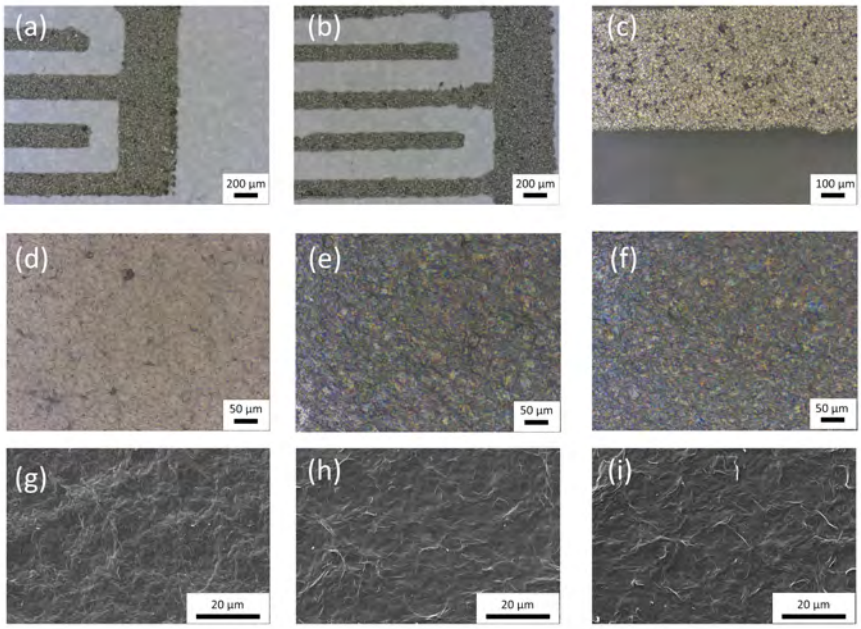

Figure IV.2: Optical microscope images: (a) screen-printed layout 1 (scale bar: 200 μm); (b) screen-printed layout 2 (scale bar: 200 μm); (c) Ag-based conductive ink screen-printed on the flexible substrate (scale bar: 100 μm); (d) graphene oxide (GO) sensitive layer (scale bar: 50 μm); (e) GO/poly(3,4-ethylenedioxythiophene)/polystyrene sulfonate (PEDOT:PSS) sensitive layer at 10% concentration (scale bar: 50 μm); (f) GO/PEDOT:PSS sensitive layer at 20% concentration (scale bar: 50 μm). SEM images: (g) GO sensitive layer (scale bar: 20 μm); (h) GO/PEDOT:PSS sensitive layer at 10% concentration (scale bar: 20 μm); (i) GO/PEDOT:PSS sensitive layer at 20% concentration (scale bar: 20 μm).

solution of GO [21]–[23]. However, when the PEDOT:PSS was added to the GO solution, the dispersion turned dark blue, as seen in Figures IV.2e,f, since this is the hallmark color of PEDOT [24]. Moreover, as observed in SEM images (Figures IV.2g–i), the increase in PEDOT:PSS concentration yielded an increase of the roughness of the surface as a consequence of the PEDOT:PSS structure [25]–[27]. Experiments of the surface profilometry indicated an average sensitive layer thickness of around 3.5 μm.

To further study the changes in the hybrid GO/PEDOT:PSS composites, the three sensitive layers were investigated using FTIR spectroscopy, whose results are presented in Figure IV.3. Firstly, starting with the GO spectrum (Figure IV.3a), three main peaks with a similar intensity could be clearly identified. These peaks indicated the high degree of oxidation of the carbon bonds, since they were associated with ether (C-O-C, 1095 cm^{-1}), epoxy or alkoxy bonds (ν(C-O),

1238 cm^{-1}), and carbonyl groups (C=O, 1715 cm^{-1}) [28]–[30]. Moreover, a peak arising from the C-H stretching vibration at 2876 cm^{-1} was also present [31], [32]. Furthermore, the addition of the PEDOT:PSS intensified the bands associated with the sulfur-containing groups remaining in the GO as a consequence of the H_2SO_4 oxidizing agent [18]. As it can be seen in Figure IV.3b, these peaks were located at 1409 cm^{-1}, 1042 cm^{-1}, and 1018 cm^{-1} and were associated with the S=O links [33], [34]. Moreover, two new bands started appearing at 1173 cm^{-1} and 1124 cm^{-1}, increasing with the content of PEDOT:PSS due to the SO_3 stretching bands of the PSS structure [35]. Additionally, this increase in concentration also increased the ratio of the ν(C-O) bonds with respect the C=O ones, as seen in Figure IV.3c, since the first ones had a pervasive presence in the PEDOT structure.

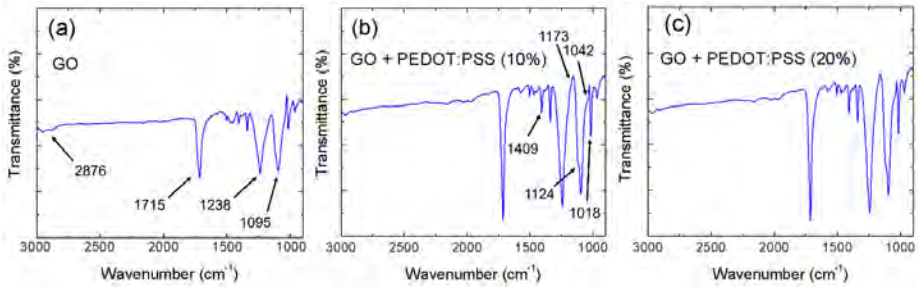

Figure IV.3: Fourier-transform infrared (FTIR) characterizations: (a) GO; (b) GO/PEDOT:PSS (10%); (c) GO/PEDOT:PSS (20%).

IV.4.2 Capacitive Humidity Sensor Characterization

Firstly, the impedance of the flexible RH sensors (both real and imaginary parts) was measured as a function of the frequency modifying the relative humidity. The measurements were carried out at a constant temperature of 40 ^oC, since this operation point of the climate chamber allowed making use of the whole range of RH. Results of the absolute value of the impedance (|Z|) obtained for the different sensitive layers and IDE structures are collected in Figure IV.4.

It can be noticed that the impedance modulus decreased as the frequency increased in all cases. Specifically, GO (Figures IV.4a,b) suffered a logarithmic decrease as a function of the frequency, as widely demonstrated in the literature. This indicates that, although both resistive and capacitive paths for the current-flow existed in the GO sensitive layer, the latter had a predominant role [36]–[38], as proven later. Moreover, the smaller width of electrodes and higher distance between them resulted in an increase in impedance modulus as a consequence of both a reduction of the interface between the GO film and the Ag electrode and an increase in equivalent resistance between electrodes.

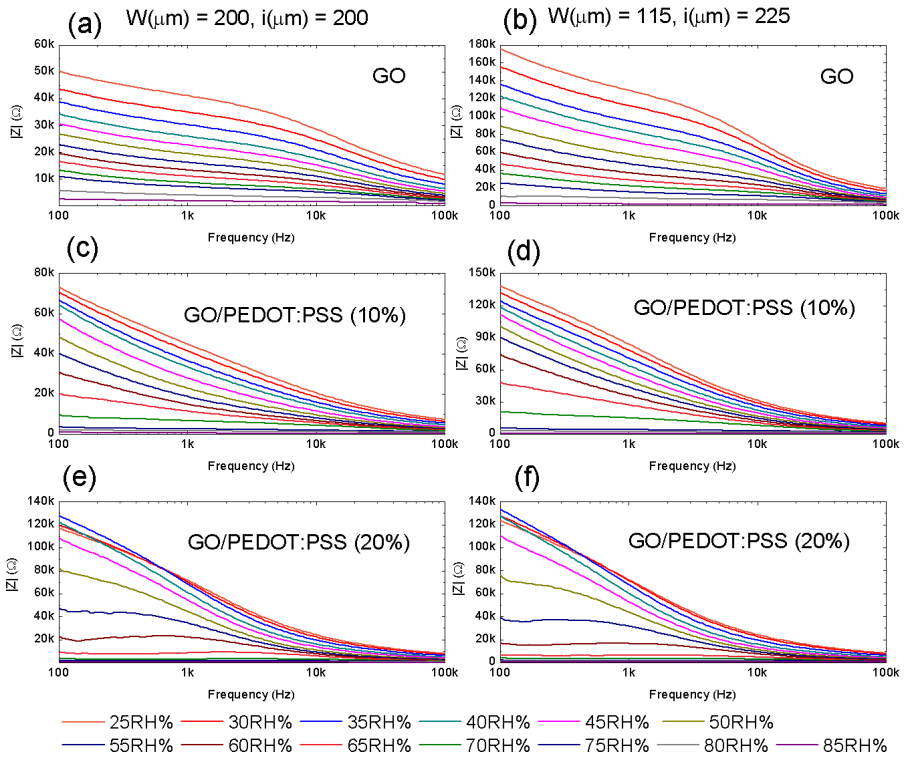

Figure IV.4: Absolute value of the impedance as a function of the frequency for the different values of RH. The left column presents the results obtained for layout 1 using the three different sensitive layers: (a) GO; (c) GO/PEDOT:PSS (10%); (e) GO/PEDOT:PSS (20%). Likewise, the right column presents the result of layout 2 for the same sensitive layers: (b) GO; (d) GO/PEDOT:PSS (10%); (f) GO/PEDOT:PSS (20%).

In the case of the hybrid GO/PEDOT:PSS composites, the decrease in impedance modulus with respect to the frequency was more abrupt, as can be observed for both concentrations of PEDOT:PSS and layouts (from Figures IV.4c–f). This effect is attributed to the high ratio of change of the PEDOT:PSS impedance when the frequency increases [39], which results in a double layer capacitance behavior [40]. However, it can also be observed that, in addition to changes in the frequency response of the capacitive sensors, the aggregation of PEDOT:PSS also induced changes in the response of the impedance to the RH.

To study this effect, the impedance modulus is plotted as a function of the RH at a fixed frequency for both IDE structures in Figure IV.5. Firstly, it can be noted that, as the content of PEDOT:PSS increased, the resistance of the sensitive layer became more influential than that corresponding to the interface between the sensitive layer and the Ag electrodes, which made the impedance

of the wider fingers similar to that obtained with the $W = 115$ μm structure (blue curves in Figure IV.5). This might have been a consequence of the rougher surface morphology of the GO/PEDOT:PSS hybrid films, which contributed to a better contact at the interface electrode-sensitive film [41].

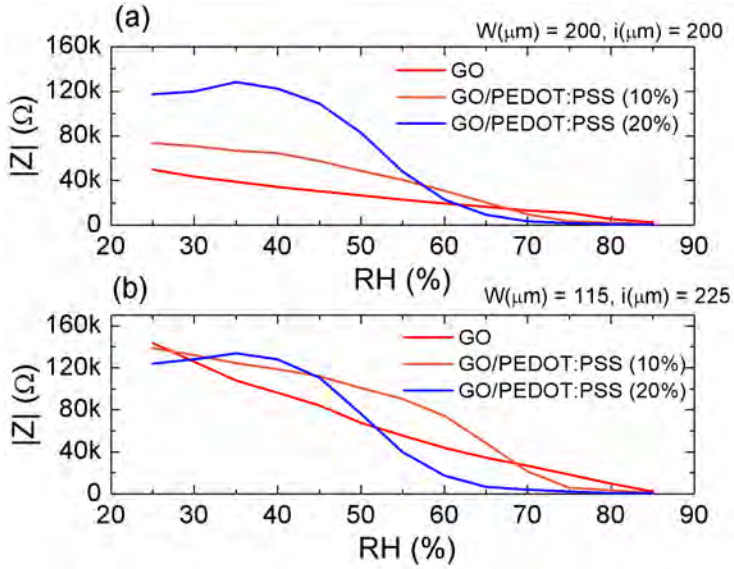

Figure IV.5: Absolute value of the impedance as a function of the relative humidity at a frequency of 100 Hz for both layout 1 (a) and layout 2 (b) using GO and the hybrid GO/PEDOT:PSS composites as sensitive layers.

In any case, the impedance of both IDE structures using the same sensitive layer presented a similar behavior when measured as a function of the RH. On one hand, the GO sensitive films presented a highly linear decrease in impedance modulus for increasing values of RH. This sensitivity to humidity changes was due to the interaction of the hydrogen bonds of the water molecules with the surface of GO. With the increase in RH, a larger number of water molecules were physically adsorbed onto the GO film. These molecules, due to the electrostatic field, were ionized, forming hydronium ions (H_3O^+), thereby promoting the ionic conduction between fingers [11], [38].

On the other hand, these results demonstrate that the aggregation of the PEDOT:PSS introduced changes in the impedance behavior. Thus, it can be noticed that, for the highest concentration of PEDOT:PSS (20%), at low levels of RH (<40%), the impedance modulus of the sensors suffered a slight increase, which indicated that the sensing effect of the PEDOT:PSS dominated the overall film impedance in this region. In this case, the increase in impedance modulus came from the interaction of both water and HSO_3 molecules of the PSS chains. As the PSS absorbed the water molecules, the distance between adjacent PEDOT chains increased, leading to a decrease in electrical conduction [42]. Once the

absorption of water molecules by the PSS chains saturated, the impedance decreased drastically due to the physisorption of the water molecules, which facilitated the ionic current and provides better current flow paths within the PEDOT structure [43]. This occurred up to ∼70% RH, where the impedance modulus started decreasing more softly, since this point is defined as a maximum detection limit of the PEDOT [13]. Furthermore, a lower concentration of PEDOT:PSS led to a softer transition between these three different states, as can be observed in Figure IV.5. The linearity of the impedance modulus changes with respect to RH could also be partially restored by means of an increase in frequency at the cost of a lower ratio of change (see Figure IV.11, Supplementary Materials).

Once we demonstrated that the PEDOT:PSS was capable of modifying the impedance response of the sensors, we studied how these changes were translated into variations on its equivalent electrical circuit. An IDE planar capacitor, such as the ones presented in this work, can be modeled as an $R_p \| Z_c$ association, where R_p is the equivalent parallel resistance between electrodes (resistance of both electrode-sensitive layer interface and sensitive layer itself) and Z_c is its reactance [13], [38], [44]. Following this model, we extracted the equivalent parallel resistance and capacitance as a function of the relative humidity at different frequencies. Figure IV.6 shows the results obtained for the sensors with dimensions $W = 200$ μm, $i = 200$ μm, while the results for the other layout can be consulted in Figure IV.12 (Supplementary Materials).

As analyzed before, the changes in the impedance were ruled by the resistance behavior (see Figure IV.5). It can also be noticed that the increase in PEDOT:PSS involved lower losses due to the increase in equivalent R_p (less shelf-discharge current) [45]. On the other hand, the capacitance increased as RH increased in all cases, which indicated that the water molecules adsorbed within the sensitive layer induced an increase in resulting dielectric permittivity [13]. Moreover, this increase also depended on the content of PEDOT:PSS, as seen in Figures IV.6b,d,f. While the capacitance of the only GO-based sensors did not present significant changes for high values of RH (>75%), as already reported in previous works [13], the presence of PEDOT:PSS led to a considerable increase of the capacitance in this region. This effect was a consequence of the water molecules absorbed by the PSS, which formed a water meniscus layer once the saturation point was achieved [42]. In addition, both equivalent resistance and capacitance decreased when the frequency was increased as a result of the boost of the dielectric losses in the sensitive layer, mostly linked to the effect of the frequency on the dielectric constant of the GO [46]. This effect caused, on one hand, a reduction in equivalent capacitance between electrodes and, on the other hand, an increase in leakage current between them [47].

We summarize in Table IV.3 the results of both equivalent resistance at medium RH (50%) and sensitivity obtained for the different sensors at two different frequencies (100 Hz and 1 kHz). Furthermore, the sensitivity of the sensors as a function of the frequency can be found in Figure IV.13 (Supplementary Materials). It is important to note that the layout with thinner fingers actually helped to increase the parallel resistance of the sensors, but

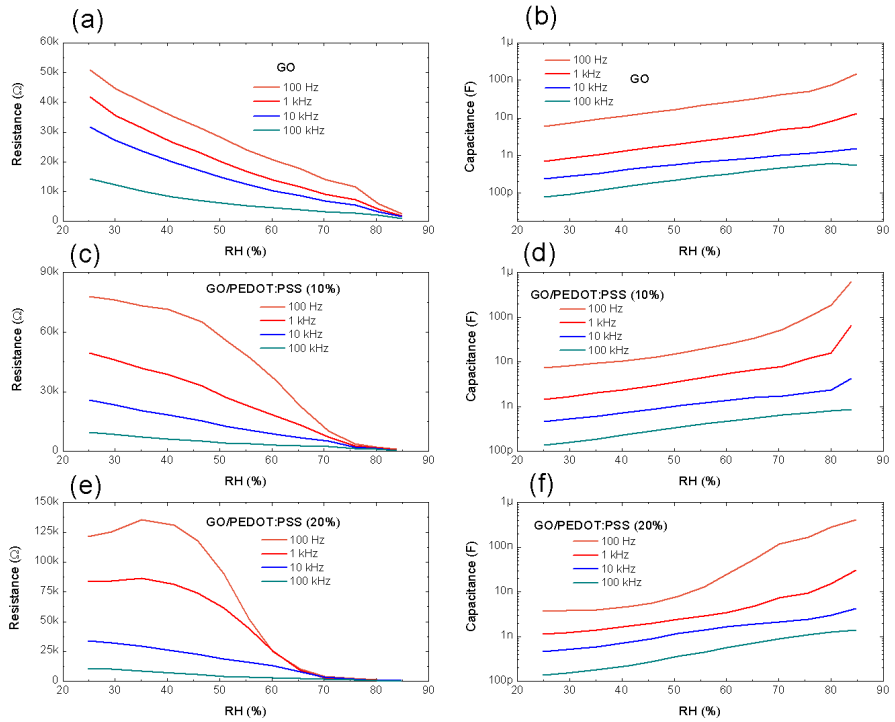

Figure IV.6: Equivalent parallel resistance and capacitance for layout 1 (W = 200 μm, i = 200 μm) at different frequencies using GO and the hybrid GO/PEDOT:PSS composites as sensitive layers; being (a,b) the results obtained for the GO layer, while (c,d) and (e,f) are the results associated to the GO/PEDOT:PSS (10%) and GO/PEDOT:PSS (20%) layers, respectively.

minimally modified their sensitivity. Moreover, as occurred with the capacitance of the sensors, in all cases, their sensitivity decreased as the frequency increased, due to the decrease in dielectric constant for both GO and PEDOT:PSS with respect to increasing frequency [46], [48]. Furthermore, the highest sensitivity was obtained for an intermediate concentration of PEDOT:PSS since, although it helped to improve the sensitivity at higher RH values, if the concentration was too high, the performance of the sensors at low RH values worsened (see Figure IV.6), resulting in an reduction of the overall sensitivity. However, this fact changed when the frequency was increased above 10 kHz since, in that case, the sensitivity of the sensors increased with the concentration of PEDOT:PSS (as illustrated in Figure IV.13, Supplementary Materials). This was due to the fact that, above 10 kHz, the change in dielectric constant of GO and, therefore, its effect on the capacitance vanished rapidly for increasing frequencies and, consequently, the sensitivity relied mainly on the PEDOT:PSS.

Figure of Merit	Sensing Layer	Layout 1	Layout 2
Equivalent parallel resistance (kΩ) at 50% RH	GO	28.11 at 100 Hz	93.09 at 100 Hz
		20.06 at 1 kHz	60.28 at 1 kHz
	GO/PEDOT:PSS (10%)	55.97 at 100 Hz	113.21 at 100 Hz
		27.35 at 1 kHz	60.76 at 1 kHz
	GO/PEDOT:PSS (20%)	90.45 at 100 Hz	84.22 at 100 Hz
		61.43 at 1 kHz	59.72 at 1 kHz
Sensitivity (nF/% RH)	GO	2.39 at 100 Hz	2.09 at 100 Hz
		0.21 at 1 kHz	0.23 at 1 kHz
	GO/PEDOT:PSS (10%)	10.45 at 100 Hz	11.53 at 100 Hz
		1.06 at 1 kHz	1.22 at 1 kHz
	GO/PEDOT:PSS (20%)	6.78 at 100 Hz	4.81 at 100 Hz
		0.49 at 1 kHz	0.37 at 1 kHz

Table IV.3: Comparison of the equivalent parallel resistance and capacitance among the flexible capacitive humidity sensors presented in this work.

Based on these results, the sensor which exhibited a better performance in terms of equivalent parallel resistance and sensitivity was that obtained with layout 2 ($W = 115$ μm, $i = 225$ μm) using GO/PEDOT:PSS (10%) as the sensitive layer. This sensitivity was more than four orders of magnitude higher than that one reported with an Ag-printed IDE structure with almost 10 times more area using polyimide as sensing layer (at the same frequency) [44], as well as much higher or comparing well with other similar sensors presented in the literature, as depicted in Table IV.4.

Sensing Material	Sensitivity (pF/% RH)	Area (mm2)	Reference
GO/PEDOT:PSS	1220@1kHz	27	This work
Polyimide (PI)	0.025@1kHz	270	[44]
Cellulose acetate butyrate (CAB)	0.0023@100kHz	64	[49]
Processed PI	144.2@1kHz	100	[50]
Multi-walled CNTs/PI	0.65@20kHz	0.625	[51]
Reduced GO/SnO2	1604@10kHz	25	[52]
GO	46.25@1kHz	–	[12]

Table IV.4: Comparison among related sensors presented in the literature. CNT—carbon nanotube.

Moreover, the thermal drift of the sensors, i.e., their sensitivity to temperature variations, is also an important parameter. Therefore, we measured the dependence of the capacitance of the sensors with layout 2 as a function of the temperature for an intermediate value of RH (40%). The results obtained for the three sensitive layers are shown in Figure IV.7.

As seen, the capacitance was quite stable to temperature variations. In all cases, it increased as the temperature increased as a consequence of a slight increase in the dielectric constant. This effect was attributed to the highly oxidized nature of the sensitive layers and the effect of the temperature in the charge transfer from the carbon atoms to the oxygen atoms [53]. The thermal drift also decreased with increasing frequency since the changes in the dielectric constant of GO became negligible at high frequencies [54]. Nevertheless, the thermal drift of the sensors did not compromise their performance since, e.g.,

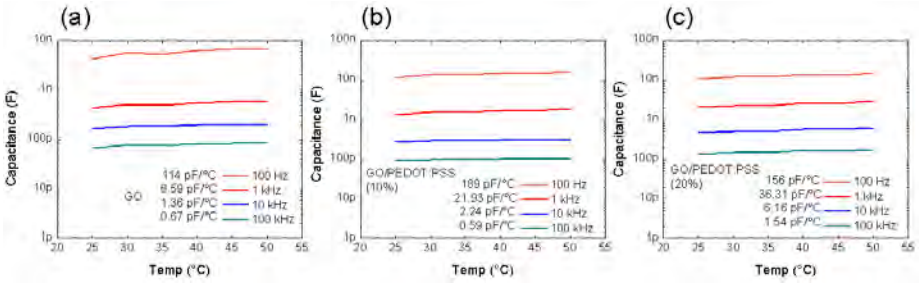

Figure IV.7: Effect of the thermal drift in the capacitance for the sensor with layout 2 (W = 115 μm, i = 225 μm) at different frequencies for the GO (a), GO/PEDOT:PSS (10%) (b), and GO/PEDOT:PSS (20%) (c) sensitive layers.

for the GO/PEDOT:PSS (10%) film, the thermal drift supposed less than 10% of the sensitivity value for any frequency.

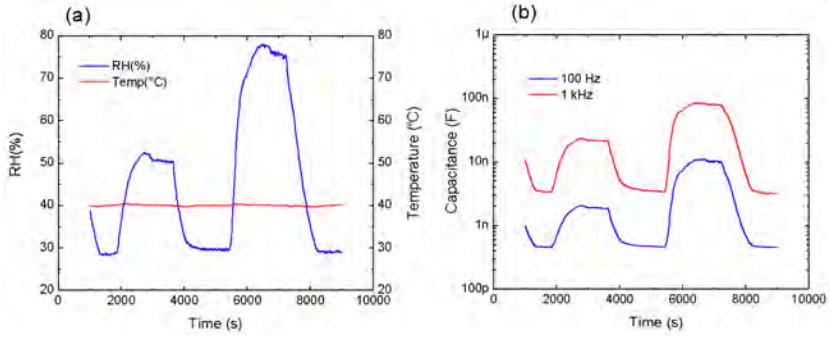

Figure IV.8: Transient response of the GO/PEDOT:PSS (10%) sensitive layer (W = 115 μm, i = 225 μm). (a) Values of temperature and RH obtained from the sensor incorporated in the climate chamber over time. (b) Capacitance response of the sensor at two different frequencies over time.

The response time of the sensors was also studied. GO was already demonstrated as a ultrafast material for humidity sensing [11]; therefore, we analyzed the sensor with the best overall performance (GO/PEDOT:PSS (10%) composite on layout 2) in order to assure that the GO/PEDOT:PSS-based sensors also provide good response and recovery times. For that, this sensor was tested applying two steps of different RH values (50% RH and 75% RH), as depicted in Figure IV.8.

On one hand, Figure IV.8a shows both temperature and relative humidity changes in the climate chamber itself. As seen, the chamber needed a certain time to increase and decrease the RH. For this RH profile, the climate chamber presented the following response times: $t_{30\%RH \rightarrow 50\%RH}$ = 544 s, $t_{50\%RH \rightarrow 30\%RH}$

= 391 s, $t_{30\%RH\rightarrow75\%RH}$ = 562 s, and $t_{75\%RH\rightarrow30\%RH}$ = 752 s. Hence, the response time of the climate chamber was pretty stable for the humidification process; however, the dehumidification took quite longer depending on the RH range. We measured the time response of our sensors below this same RH profile, and the times obtained at a frequency of 1 kHz were as follows: $t_{30\%RH\rightarrow50\%RH}$ = 610 s, $t_{50\%RH\rightarrow30\%RH}$ = 398 s, $t_{30\%RH\rightarrow75\%RH}$ = 701 s, and $t_{75\%RH\rightarrow30\%RH}$ = 496 s. Then, our capacitive sensor had a time response around 10% slower than that incorporated in the climate chamber and a similar recovery time for low values of RH, where the sensitive mechanism was mainly associated with the GO. At low RH, the response of the sensor was faster since the water molecules were physisorbed onto the available active sites (hydrophilic groups and vacancies) of the GO surface, without penetrating the GO layers. However, at high RH levels, the increase in both capacitance and sensitivity occurred due to the permeation of the water molecules within the GO layers, as well as due to their interaction with the PEDOT:PSS chains, which took a longer time [11], [55]. For that, the response was ∼25% slower than that obtained with the sensor incorporated in the climate chamber for high values of RH. Furthermore, it can also be noticed that our sensor presented a recovery time faster than its response time in the whole range of RH indicating that the time of the desorption process was faster than required for the adsorption process [56].

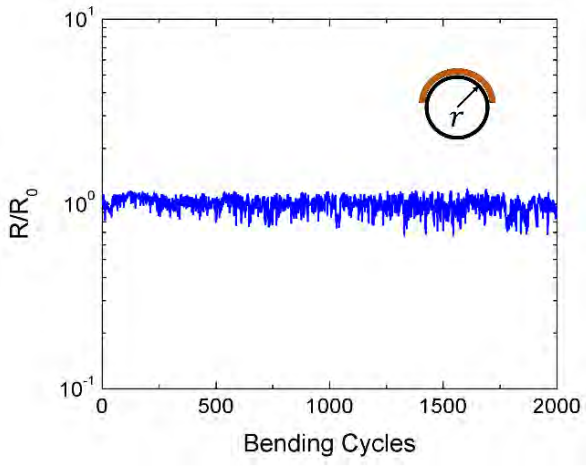

Figure IV.9: Change in resistance R with respect to the initial resistance R_0 for an increasing number of bending cycles. Inset diagram depicts the definition of bending radius (r).

Finally, we further studied the changes in resistance of this latter sensor under mechanical stress. For that, the flexibility of the presented devices was analyzed for subsequent bending cycles with a minimum bending radius of 1.5 mm (see Figure IV.9). Thus, it can be recognized that, even after 2000 bending cycles, the change in the normalized resistance was below 15%, which indicated

that the presented sensors also exhibit good stability and reversibility under bending cycles.

IV.5 Conclusions

In summary, we reported the fabrication of thin-film capacitive sensors through the screen-printing of Ag-based planar IDE structures on flexible substrates. Using both GO and GO/PEDOT:PSS composites as sensitive layers, we studied the performance of the capacitors as humidity sensors. The results showed that the presence of the PEDOT:PSS within the GO structure was able to modify the electrical properties of the sensitive film, improving the overall performance of the sensors. We studied different IDE structures, as well as the influence of the PEDOT:PSS concentration on the sensitive layer. The experiments using hybrid GO/PEDOT:PSS composites as sensitive layer showed promising results regarding the increase in sensitivity to humidity changes when compared with other similar capacitive sensors from the literature as a consequence of the combination of the active region of both GO and PEDOT:PSS materials. The authors believe that this technology is a big step forward in the cost-effective fabrication of high-performance small flexible sensors, which could be expanded to a wide range of applications.

Acknowledgements. This work was supported by the Spanish Ministry of Education, Culture, and Sport (MECD)/FEDER-EU through the project TEC2017-89955-P; the predoctoral grant FPU16/01451 and its international mobility program; the European Commission through the fellowship H2020-MSCA-IF-2017-794885-SELFSENS; and the University of Granada through its projects for junior researchers.

References

[1] Cheng, I.-C. and Wagner, S., "Overview of flexible electronics technology," in *Flexible Electronics*, Springer US, 2009, pp. 1–28.

[2] Alioto, M. and Shahghasemi, M., "The internet of things on its edge: Trends toward its tipping point," *IEEE Consumer Electronics Magazine*, vol. 7, no. 1, pp. 77–87, Jan. 2018.

[3] Bridgeman, D., Corral, J., Quach, A., Xian, X., and Forzani, E., "Colorimetric humidity sensor based on liquid composite materials for the monitoring of food and pharmaceuticals," *Langmuir*, vol. 30, no. 35, pp. 10 785–10 791, Aug. 2014.

[4] Bibi, F., Guillaume, C., Gontard, N., and Sorli, B., "A review: RFID technology having sensing aptitudes for food industry and their contribution to tracking and monitoring of food products," *Trends in Food Science & Technology*, vol. 62, pp. 91–103, Apr. 2017.

[5] Trung, T. Q., Duy, L. T., Ramasundaram, S., and Lee, N.-E., "Transparent, stretchable, and rapid-response humidity sensor for body-attachable wearable electronics," *Nano Research*, vol. 10, no. 6, pp. 2021–2033, Mar. 2017.

[6] Salvo, P., Francesco, F. D., Costanzo, D., Ferrari, C., Trivella, M. G., and Rossi, D. D., "A wearable sensor for measuring sweat rate," *IEEE Sensors Journal*, vol. 10, no. 10, pp. 1557–1558, Oct. 2010.

[7] Falco, A., Loghin, F. C., Becherer, M., Lugli, P., Salmerón, J. F., and Rivadeneyra, A., "Low-cost gas sensing: Dynamic self-compensation of humidity in CNT-based devices," *ACS Sensors*, vol. 4, no. 12, pp. 3141–3146, Nov. 2019.

[8] Lyuleeva, A., Helbich, T., Bobinger, M., Rieger, B., Becherer, M., Lugli, P., and Rivadeneyra, A., "Functionalized and oxidized silicon nanosheets: Customized design for enhanced sensitivity towards relative humidity," *Sensors and Actuators B: Chemical*, vol. 283, pp. 451–457, Mar. 2019.

[9] Seco, J. M., Sebastián, E. S., Cepeda, J., Biel, B., Salinas-Castillo, A., Fernández, B., Morales, D. P., Bobinger, M., Gómez-Ruiz, S., Loghin, F. C., Rivadeneyra, A., and Rodriguez-Diéguez, A., "A potassium metal-organic framework based on perylene-3,4,9,10-tetracarboxylate as sensing layer for humidity actuators," *Scientific Reports*, vol. 8, no. 1, Sep. 2018.

[10] Fernandez-Salmeron, J., Rivadeneyra, A., Rodriguez, M. A. C., Capitan-Vallvey, L. F., and Palma, A. J., "HF RFID tag as humidity sensor: Two different approaches," *IEEE Sensors Journal*, vol. 15, no. 10, pp. 5726–5733, Oct. 2015.

[11] Borini, S., White, R., Wei, D., Astley, M., Haque, S., Spigone, E., Harris, N., Kivioja, J., and Ryhänen, T., "Ultrafast graphene oxide humidity sensors," *ACS Nano*, vol. 7, no. 12, pp. 11 166–11 173, Nov. 2013.

[12] Bi, H., Yin, K., Xie, X., Ji, J., Wan, S., Sun, L., Terrones, M., and Dresselhaus, M. S., "Ultrahigh humidity sensitivity of graphene oxide," *Scientific Reports*, vol. 3, no. 1, Sep. 2013.

[13] Hassan, G., Sajid, M., and Choi, C., "Highly sensitive and full range detectable humidity sensor using PEDOT:PSS, methyl red and graphene oxide materials," *Scientific Reports*, vol. 9, no. 1, Oct. 2019.

[14] Huang, S., Liu, Y., Zhao, Y., Ren, Z., and Guo, C. F., "Flexible electronics: Stretchable electrodes and their future," *Advanced Functional Materials*, vol. 29, no. 6, p. 1 805 924, Nov. 2018.

[15] Yang, C.-T., Hsiang, H.-I., Huang, T.-S., Huang, P.-C., and Han, Y.-K., "Thermal conductivity and dielectric properties of PEDOT:PSS-AlN filler reinforced water-soluble polymer composites," *Ceramics International*, vol. 43, S710–S716, Aug. 2017.

[16] Popov, V. I., Kotin, I. A., Nebogatikova, N. A., Smagulova, S. A., and Antonova, I. V., "Graphene-PEDOT: PSS humidity sensors for high sensitive, low-cost, highly-reliable, flexible, and printed electronics," *Materials*, vol. 12, no. 21, p. 3477, Oct. 2019.

[17] Beidaghi, M. and Gogotsi, Y., "Capacitive energy storage in micro-scale devices: Recent advances in design and fabrication of micro-supercapacitors," *Energy & Environmental Science*, vol. 7, no. 3, p. 867, 2014.

[18] Romero, F. J., Rivadeneyra, A., Toral, V., Castillo, E., Garcia-Ruiz, F., Morales, D. P., and Rodriguez, N., "Design guidelines of laser reduced graphene oxide conformal thermistor for IoT applications," *Sensors and Actuators A: Physical*, vol. 274, pp. 148–154, May 2018.

[19] Hyun, W. J., Secor, E. B., Hersam, M. C., Frisbie, C. D., and Francis, L. F., "High-resolution patterning of graphene by screen printing with a silicon stencil for highly flexible printed electronics," *Advanced Materials*, vol. 27, no. 1, pp. 109–115, Nov. 2014.

[20] Albrecht, A., "Printed sensors for the internet of things," Ph.D. dissertation, Technical University of Munich, 2018.

[21] Fan, Z., Wang, K., Wei, T., Yan, J., Song, L., and Shao, B., "An environmentally friendly and efficient route for the reduction of graphene oxide by aluminum powder," *Carbon*, vol. 48, no. 5, pp. 1686–1689, Apr. 2010.

[22] Dutta, S., Sarkar, S., Ray, C., and Pal, T., "Benzoin derived reduced graphene oxide (rGO) and its nanocomposite: Application in dye removal and peroxidase-like activity," *RSC Advances*, vol. 3, no. 44, p. 21 475, 2013.

[23] Teklu, A., Barry, C., Palumbo, M., Weiwadel, C., Kuthirummal, N., and Flagg, J., "Mechanical characterization of reduced graphene oxide using AFM," *Advances in Condensed Matter Physics*, vol. 2019, pp. 1–13, Jan. 2019.

[24] Zajdel, T. J., Baruch, M., Méhes, G., Stavrinidou, E., Berggren, M., Maharbiz, M. M., Simon, D. T., and Ajo-Franklin, C. M., "PEDOT:PSS-based multilayer bacterial-composite films for bioelectronics," *Scientific Reports*, vol. 8, no. 1, Oct. 2018.

[25] Silva, W. J. da, Mohd Yusoff, A. R. b., and Jang, J., "GO:PEDOT:PSS for high-performance green phosphorescent organic light-emitting diode," *IEEE Electron Device Letters*, vol. 34, no. 12, pp. 1566–1568, Dec. 2013.

[26] Zhou, J., Anjum, D. H., Chen, L., Xu, X., Ventura, I. A., Jiang, L., and Lubineau, G., "The temperature-dependent microstructure of PEDOT/PSS films: Insights from morphological, mechanical and electrical analyses," *J. Mater. Chem. C*, vol. 2, no. 46, pp. 9903–9910, 2014.

[27] Wu, X., Lian, L., Yang, S., and He, G., "Highly conductive PEDOT:PSS and graphene oxide hybrid film from a dipping treatment with hydroiodic acid for organic light emitting diodes," *Journal of Materials Chemistry C*, vol. 4, no. 36, pp. 8528–8534, 2016.

[28] Aragaw, B. A., Su, W.-N., Rick, J., and Hwang, B.-J., "Highly efficient synthesis of reduced graphene oxide–nafion nanocomposites with strong coupling for enhanced proton and electron conduction," *RSC Advances*, vol. 3, no. 45, p. 23 212, 2013.

[29] Zhang, X., Liu, M., Wang, B., Chen, H., and Wang, Z., "A wide measurement range and fast update rate integrated interface for capacitive sensors array," *IEEE Transactions on Circuits and Systems I: Regular Papers*, vol. 61, no. 1, pp. 2–11, Jan. 2014.

[30] Sudesh, Kumar, N., Das, S., Bernhard, C., and Varma, G. D., "Effect of graphene oxide doping on superconducting properties of bulk MgB2," *Superconductor Science and Technology*, vol. 26, no. 9, p. 095 008, Jul. 2013.

[31] Valencia, C., Valencia, C., Zuluaga, F., Valencia, M., Mina, J., and Grande-Tovar, C., "Synthesis and application of scaffolds of chitosan-graphene oxide by the freeze-drying method for tissue regeneration," *Molecules*, vol. 23, no. 10, p. 2651, Oct. 2018.

[32] Habte, A. T. and Ayele, D. W., "Synthesis and characterization of reduced graphene oxide (rGO) started from graphene oxide (GO) using the tour method with different parameters," *Advances in Materials Science and Engineering*, vol. 2019, pp. 1–9, Aug. 2019.

[33] Manoilova, O. V., Olindo, R., Areán, C. O., and Lercher, J. A., "Variable temperature FTIR study on the surface acidity of variously treated sulfated zirconias," *Catalysis Communications*, vol. 8, no. 6, pp. 865–870, Jun. 2007.

[34] Ren, Y.-K., Liu, S.-D., Duan, B., Xu, Y.-F., Li, Z.-Q., Huang, Y., Hu, L.-H., Zhu, J., and Dai, S.-Y., "Controllable intermediates by molecular self-assembly for optimizing the fabrication of large-grain perovskite films via one-step spin-coating," *Journal of Alloys and Compounds*, vol. 705, pp. 205–210, May 2017.

[35] Su, N., Li, H., Huang, Y., and Zhang, X., "Synthesis of salt responsive spherical polymer brushes," *Journal of Nanomaterials*, vol. 2015, pp. 1–7, 2015.

[36] Yoon, Y., Jo, J., Kim, S., Lee, I., Cho, B., Shin, M., and Hwang, W., "Impedance spectroscopy analysis and equivalent circuit modeling of graphene oxide solutions," *Nanomaterials*, vol. 7, no. 12, p. 446, Dec. 2017.

[37] Bonanni, A. and Pumera, M., "High-resolution impedance spectroscopy for graphene characterization," *Electrochemistry Communications*, vol. 26, pp. 52–54, Jan. 2013.

[38] An, J., Le, T.-S. D., Huang, Y., Zhan, Z., Li, Y., Zheng, L., Huang, W., Sun, G., and Kim, Y.-J., "All-graphene-based highly flexible noncontact electronic skin," *ACS Applied Materials & Interfaces*, vol. 9, no. 51, pp. 44 593–44 601, Dec. 2017.

[39] Ganji, M., Kaestner, E., Hermiz, J., Rogers, N., Tanaka, A., Cleary, D., Lee, S. H., Snider, J., Halgren, M., Cosgrove, G. R., Carter, B. S., Barba, D., Uguz, I., Malliaras, G. G., Cash, S. S., Gilja, V., Halgren, E., and Dayeh, S. A., "Development and translation of PEDOT:PSS microelectrodes for intraoperative monitoring," *Advanced Functional Materials*, vol. 28, no. 12, p. 1 700 232, May 2017.

[40] Mamouni, J. and Yang, L., "Interdigitated microelectrode-based microchip for electrical impedance spectroscopic study of oral cancer cells," *Biomedical Microdevices*, vol. 13, no. 6, pp. 1075–1088, Aug. 2011.

[41] Yang, W., Broski, A., Wu, J., Fan, Q. H., and Li, W., "Characteristics of transparent, PEDOT:PSS-coated indium-tin-oxide (ITO) microelectrodes," *IEEE Transactions on Nanotechnology*, vol. 17, no. 4, pp. 701–704, Jul. 2018.

[42] Benchirouf, A., Palaniyappan, S., Ramalingame, R., Raghunandan, P., Jagemann, T., Müller, C., Hietschold, M., and Kanoun, O., "Electrical properties of multi-walled carbon nanotubes/PEDOT:PSS nanocomposites thin films under temperature and humidity effects," *Sensors and Actuators B: Chemical*, vol. 224, pp. 344–350, Mar. 2016.

[43] Siddiqui, G. U., Sajid, M., Ali, J., Kim, S. W., Doh, Y. H., and Choi, K. H., "Wide range highly sensitive relative humidity sensor based on series combination of MoS2 and PEDOT:PSS sensors array," *Sensors and Actuators B: Chemical*, vol. 266, pp. 354–363, Aug. 2018.

[44] Romero, F. J., Rivadeneyra, A., Salinas-Castillo, A., Ohata, A., Morales, D. P., Becherer, M., and Rodriguez, N., "Design, fabrication and characterization of capacitive humidity sensors based on emerging flexible technologies," *Sensors and Actuators B: Chemical*, vol. 287, pp. 459–467, May 2019.

[45] Frackowiak, E. and Béguin, F., "Carbon materials for the electrochemical storage of energy in capacitors," *Carbon*, vol. 39, no. 6, pp. 937–950, May 2001.

[46] Hong, X., Yu, W., and Chung, D., "Electric permittivity of reduced graphite oxide," *Carbon*, vol. 111, pp. 182–190, Jan. 2017.

[47] Li, Y., Torah, R., Beeby, S., and Tudor, J., "An all-inkjet printed flexible capacitor on a textile using a new poly(4-vinylphenol) dielectric ink for wearable applications," in *2012 IEEE Sensors*, IEEE, Oct. 2012.

[48] Pasha, A., Khasim, S., Al-Hartomy, O. A., Lakshmi, M., and Manjunatha, K. G., "Highly sensitive ethylene glycol-doped PEDOT–PSS organic thin films for LPG sensing," *RSC Advances*, vol. 8, no. 32, pp. 18 074–18 083, 2018.

[49] Molina-Lopez, F., Briand, D., and Rooij, N. de, "All additive inkjet printed humidity sensors on plastic substrate," *Sensors and Actuators B: Chemical*, vol. 166-167, pp. 212–222, May 2012.

[50] Yang, T., Yu, Y., Zhu, L., Wu, X., Wang, X., and Zhang, J., "Fabrication of silver interdigitated electrodes on polyimide films via surface modification and ion-exchange technique and its flexible humidity sensor application," *Sensors and Actuators B: Chemical*, vol. 208, pp. 327–333, Mar. 2015.

[51] Hong, H. P., Jung, K. H., Kim, J. H., Kwon, K. H., Lee, C. J., Yun, K. N., and Min, N. K., "Percolated pore networks of oxygen plasma-activated multi-walled carbon nanotubes for fast response, high sensitivity capacitive humidity sensors," *Nanotechnology*, vol. 24, no. 8, p. 085 501, Feb. 2013.

[52] Zhang, D., Chang, H., Li, P., Liu, R., and Xue, Q., "Fabrication and characterization of an ultrasensitive humidity sensor based on metal oxide/graphene hybrid nanocomposite," *Sensors and Actuators B: Chemical*, vol. 225, pp. 233–240, Mar. 2016.

[53] Lee, D. W., Seo, J. W., Jelbert, G. R., Los Santos, L. de, Cole, J. M., Panagopoulos, C., and Barnes, C. H. W., "Transparent and flexible polymerized graphite oxide thin film with frequency-dependent dielectric constant," *Applied Physics Letters*, vol. 95, no. 17, p. 172 901, Oct. 2009.

[54] Kumar, K. S., Pittala, S., Sanyadanam, S., and Paik, P., "A new single/few-layered graphene oxide with a high dielectric constant of 106: Contribution of defects and functional groups," *RSC Advances*, vol. 5, no. 19, pp. 14 768–14 779, 2015.

[55] Li, Y., Zhang, M., Long, S., Teng, J., Liu, Q., Lv, H., Miranda, E., Suñé, J., and Liu, M., "Investigation on the conductive filament growth dynamics in resistive switching memory via a universal monte carlo simulator," *Scientific Reports*, vol. 7, no. 1, Sep. 2017.

[56] Chen, W.-P., Zhao, Z.-G., Liu, X.-W., Zhang, Z.-X., and Suo, C.-G., "A capacitive humidity sensor based on multi-wall carbon nanotubes (MWCNTs)," *Sensors*, vol. 9, no. 9, pp. 7431–7444, Sep. 2009.

IV.6 Supplementary Materials

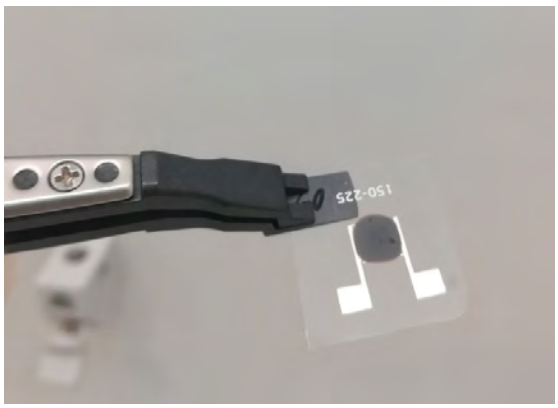

Figure IV.10: Actual view of one of the flexible RH sensors presented in this work.

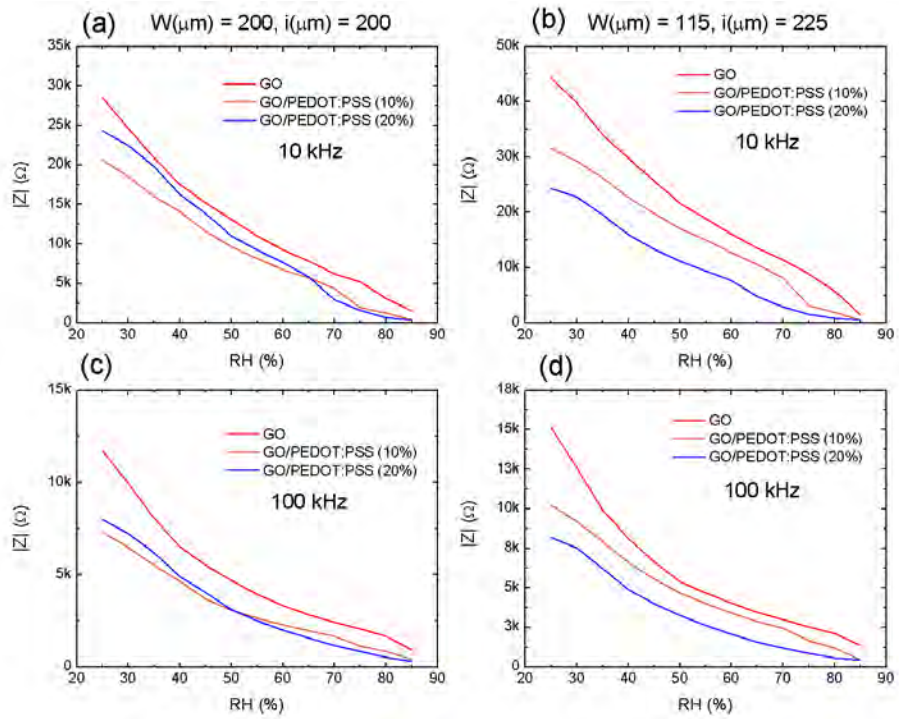

Figure IV.11: Absolute value of the impedance as a function of the relative humidity measured at different frequencies for both layout 1 (10 kHz (a) and 100 kHz (c)) and layout 2 (10 kHz (b) and 100 kHz (d)) using GO and the hybrid GO/PEDOT:PSS composites as sensitive layers.

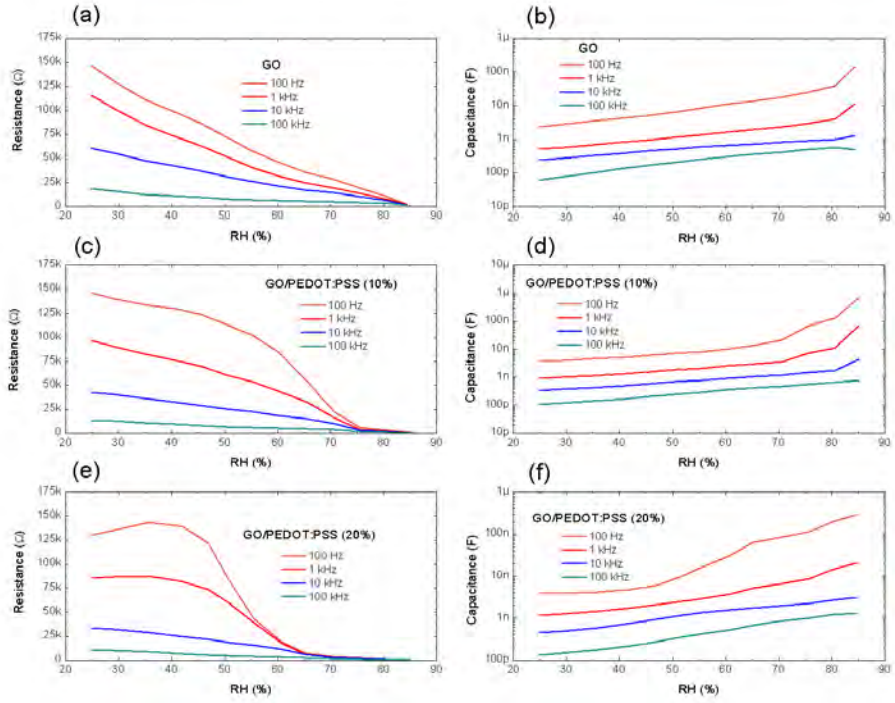

Figure IV.12: Equivalent parallel resistance and capacitance for layout 1 (W = 115 μm, i = 225 μm) at different frequencies using GO and the hybrid GO/PEDOT:PSS composites as sensitive layers.

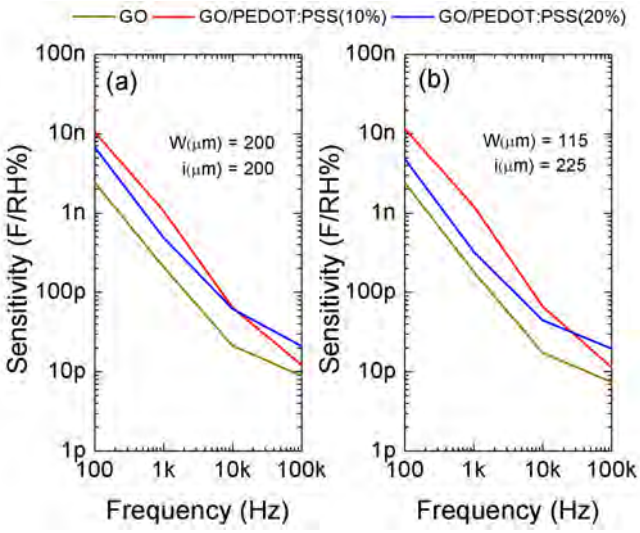

Figure IV.13: Sensitivity as a function of the frequency for the two layouts considered in this work as well as the three different sensitive layer.

Paper V

Flexible and robust laser-induced graphene heaters photothermally scribed on bare polyimide substrates

V

Marco R. Bobinger [1,*], Francisco J. Romero [2], Alfonso Salinas-Castillo [3], Markus Becherer [1], Paolo Lugli [4], Diego P. Morales [2], Noel Rodriguez [2], Almudena Rivadeneyra [1,*]

[1] Institute for Nanoelectronics, Technical University of Munich, 80333, Munich, Germany.
[2] Department of Electronics and Computer Technology, University of Granada, 18071 Granada, Spain.
[3] Department of Analytical Chemistry, University of Granada, 18071 Granada, Spain.
[4] Faculty of Science and Technology, Free University of Bolzano, 39100, Bolzano-Bozen, Italy.
* Corresponding authors: marco.bobinger@tum.de (M.R.B.) and almudena.rivadeneyra@tum.de (A.R.)

Published in *Carbon*, Apr 2019, volume 144, pp. 116–126. DOI: 10.1016/j.carbon.2018.12.010. Impact Factor: 8.821. JCR Rank: 32/314 (Q1) in *Materials Science, Multidisciplinary* and 26/159 (Q1) in *Chemistry, Physical*.

Abstract

We demonstrate the feasibility of fabricating cost-effective and robust laser-induced graphene (LIG) flexible heaters with an innovative technique based on the photothermal production of graphene with a foam-like morphology. The produced devices are precisely defined on a bare polyimide substrate without the need of photomasks by employing a computer numerical control (CNC) driven laser diode. The electrical properties of the LIG-based heaters can be tailored by adjusting the laser power. The resulting conductive material exhibits electrical and chemical properties which are similar to the ones for graphene such as a negative temperature coefficient of -0.46 m $^{o}C^{-1}$ and a maximum operating temperature of

around 400 ^{o}C. The developed heaters can outperform the existing emerging technologies showing a very rapid and stable response up to 225 ^{o}C with the extra features of flexibility, biocompatibility, and environmental friendliness.

Keywords: flexible graphene film heater, laser-induced graphene, laser ablation, micro-hotplate, polyimide

V.1 Introduction

Heaters are resistive structures operating under the principle of Joule's heating that results in a self-heating effect. Tailor-made heating devices that are thin,flexible, mechanically or chemically robust are employed in many different applications ranging from gas sensing to microfluidics. In the former case, many gas sensors require high operating temperatures [1], [2] or they need to be actively recovered after being exposed to the target gas [3], [4]. For the active recovery, the heater is placed under the sensing element to achieve the required temperature to drive or to recover the sensor. One example of application can be found for microfluidic systems that carry out a polymerase chain reaction (PCR) on nucleotides of interest within microfluidic channels: a certain and precise temperature is needed to cultivate the biological samples to detect those nucleotides [5].

Such devices have been conventionally fabricated based on silicon (Si) micromachining technologies [6], [7]. Also, there are examples where heaters have been integrated on porous silicon and glass substrates [8], [9]. In the last decades, the interest inflexible electronics has substantially been aroused [10]. In the case of the fabrication of heaters on flexible substrates, there are unique properties, i.e., mechanical flexibility and lower thermal conductivity, which cannot be found for devices based on rigid Si wafers [11]–[13]. For this kind of substrates, printing techniques are particularly interesting because of their scalable and low-cost fabrication in comparison with photolithography and etching processes that are commonly employed for Si-based devices. There are examples in the literature where heaters have been manufactured by inkjet printing of silver nanoparticles on polymeric films [14]–[16]. However, they are hindered at higher operation temperatures because of the non-stability due to electromigration and, in addition, their lifetime is limited by chemical degradation [17]. In other works, the use of metal nanowires (MNWs) such as silver (AgNW) and copper (CuNWs) nanowires deposited by spray deposition was reported for the production of transparent heaters [18], [19]. MNWs represent a very promising new material due to their high Figures of Merit (FoM) for the transparency and the sheet resistance that challenges the values for ITO. However, MNW-based heaters face important constraints for their use as robust and durable heaters [20]: *i)* CuNWs oxidize below a temperature of 100 ^{o}C [21], [22]; *ii)* the electromigration for AgNWs is critical at elevated electrical current densities; *iii)*

the fragmentation temperatures for both materials are lowered substantially with regard to the melting points for the bulk counterparts. It should be noted that recently some authors have successfully considered the use of gold (Au) based heaters to enhance the stability at different operating conditions and guarantee bio-compatibility, but the material costs obviously pose a large obstacle for commercial purposes [20]. In detail, Khan *et al.* have reported aerosol jetted heaters based on Au-nanoparticles on a polyimide substrate that cover an area of around 1 mm^2. Their heaters can operate at temperatures up to 250 ^oC with a power demand of 22 mW [23]. These values yield to an increase in temperature over electrical power density of around 102 $^oC\ cm^2/W$, which is lowered by around 22% compared to the value reported in this work.

All the aforementioned examples are based on the deposition of a self-heating layer, and therefore, requiring additional post-processing techniques, such as drying, curing or sintering [24]. In this work, we describe a low-cost and one-step process to integrate heaters directly in polymeric films. In particular, we exploit the fabrication process previously described in Ref. [25], where graphene films with a foam-like morphology (Laser-Induced Graphene, LIG) are produced by the photothermal ablation of Kapton® HN (DuPont™) polyimide using a laser diode driven by a CNC unit. As shown in the previous work, the electrical conductivity of the film can be tailored by adjusting the laser power. This technique offers four main advantages over the existing deposition or printing methods: *i)* high-precision patterns can be defined on the polyimide surface without affecting the unexposed areas and without the need of using lithographic masks; *ii)* the heaters are fabricated directly from the polyimide substrate without the need of any chemical reagent, being, therefore, a clean and environmentally friendly method; *iii)* the process is intrinsically inexpensive and scalable; *iv)* as shown in this work the performance of the heaters is very competitive. In previous works, the laser scribing parameters have been tailored to achieve the best trade-off between sheet resistance and substrate stability, aiming to minimize the variability of the samples, as described in Section V.2.1 and referenced there in. So far, the laser ablation process has been utilized to produce graphene films for various applications such as supercapacitors [26], [27], polymer-written and on-skin electronics [27], oxygen electrocatalysis [28], water oxidation catalysts [29], electrochemical devices [30] and desalination [31]. In this work, we apply for the first time this versatile fabrication technique for the production of flexible heaters developing a comprehensive study of their structural, chemical electrical and mechanical properties. The paper is structured as follows. The fabrication method for the LIG films is briefly described in Section V.2 along with the characterization techniques implemented. In Section V.3, the results are presented starting with the characterization of the structural, chemical, electrical and thermal properties of the laser-scribed heaters, including the modeling of its temperature response. Then, the films are tested as heaters, and the transient thermal response of the devices is investigated and discussed as well as benchmarked with commercial heaters. Finally, the robustness of the heaters is studied with respect to their maximum operating temperature, long-term stability and flexibility in operation and standing idle.

V.2 Materials and Methods

V.2.1 Fabrication of the LIG films

The samples were fabricated using Kapton® HN polyimide films with a thickness of 125 μm from DuPont™ as substrate and raw material. The conductive patterns were obtained through photo-thermal ablation of this polyimide film using an in-house developed CNC-driven laser diode from Q-BAIHE™ (model: 405 ML-300-2290). In particular, the substrate was located in a horizontal holder at a distance of 6 cm from the laser head, allowing a spatial resolution of about 20 μm at a fixed wavelength of 405 nm. As demonstrated in Ref. [25], a laser power of 100 mW that corresponds to a fluence of 18 J/cm^2 constitutes the best trade-off between sheet resistance and the substrate stability in terms of thermal load during the laser treatment. At this power, LIG films with a sheet resistance below 250 $\Omega/sq.$ were produced without inducing a plastic deformation on the substrate. Therefore, all samples were fabricated using this power value. The sheet resistances were measured using a four-point probe head from Jandel connected to a B2901A Keysight source measuring unit (SMU). In order to establish electrical percolation, as shown in Fig. V.4, a constant current of 3 mA was sourced for all measurements.

V.2.2 Measurement of the film morphology

A 3D profile of the LIG film was acquired using a DekTak XT profilometer from Bruker (USA). Field-emission scanning electron microscope (FESEM) images were recorded using an NVision40 from Carl Zeiss (Germany) at an acceleration voltage of 7.0 kV and an extraction voltage of 5.0 kV.

V.2.3 Transient electrical and thermal measurements

For the transient measurements, the LIG films were contacted with copper tape and conductive silver paint. The electrical input powers were applied and the data recorded using a LabVIEW controlled DC power supply 2200-30-5 from Keithley (USA) with a voltage and current resolution of 1 mV and 0.1 mA, respectively. Thermal images were recorded using a 640 × 480 px infrared (IR) camera Testo890 from Testo (Germany). Using the software IRSoft from Testo (Germany) and a MATLAB script, the temperature transients were extracted from processing the IR images. The resulting temperature values represent a mean temperature that was determined by averaging over an area on the heaters of around 2 × 2 mm^2. An accurate emissivity value, ε, for the LIG films with $0 \leq \varepsilon \leq 1$ of 0.75 was determined by placing the LIG samples on a hotplate with a set-point temperature of 75 ^{o}C. Subsequently, the temperature of the LIG film was measured using a contact technique, i.e., a Pt100 thermoresistor, and the emissivity reading of the IR camera was adjusted such that the camera displayed temperature matches the measured one.

V.2.4 Bending test

A custom bending setup was designed and built for the bending tests. The setup consists of a LabVIEW 2016 controlled stepper motor (PD4-N5918M4204) equipped with a precision planetary gear (GPLE60) from Nanotec (Germany) that slides the movable clamp along an aluminum rail. The samples are mounted in the insulating Polyoxymethylene (POM) clamps and connected to a LabVIEW controlled Keithley 2700 multimeter from Keithley (USA). For the bending tests, the bending speed and minimum bending diameter were kept constant at 10 mm/s and 4 mm, respectively.

V.2.5 X-ray photoelectron spectroscopy

X-ray photoelectron spectroscopy (XPS) measurements wereperformed at a base pressure of $5{\cdot}10^{-10}$ mbar with a monochromatic aluminum Kα anode as a x-ray source at an operating power of 350 W. The high resolution spectra were acquired using a SPECS Phoibos hemispherical analyzer at a pass-energy of 20 eV with an energy resolution of 0.05 eV.

V.3 Results and Discussion

In this section, we first show the structural, chemical electrical and thermal properties of the heaters fabricated by laser ablation of polyimide films. After that, the thermal stability of the devices is presented and finally, their response during bending cycles is shown.

V.3.1 Structural, chemical, electrical and thermal properties

Mechanical profilometer scans of the LIG over an area of $1{\times}1$ mm^2 are shown in Fig. V.1 (a) along with the line profiles in (b) x- and(c) y-direction, in accordance with the dashed lines drawn to Fig. 1(a). From the height profile and the optical image in the inset in Fig. V.1 (a), the mesh-like structure of the LIG film can be recognized. A mean height of 18.7 $\pm$ 2.2 mm was determined for the LIG lines after considering the data of the indicated x-y line profiles. The reticulated pattern of the laser scribing process shown in Fig. V.1 (a) and in the SEM-image below in Fig. V.7 (c) is a direct consequence of the mechanical step size of the utilized CNC unit, which is larger than the spot size of the laser focused on the surface. This fact limits the surface coverage and, in turn, the minimum sheet resistance that can be achieved.

Further, the chemical alterations that are induced by the laser ablation process have been studied by X-ray photoelectron spectroscopy (XPS), which allows extracting concentrations for the elements and identifying changes in the carbon-oxygen compounds. Survey scans, as well as high-resolution XPS spectra for the C 1s, N1s and O 1s peaks, are shown in the supporting information in Fig. V.11 and Fig. V.11, respectively. In accordance with the expectation that a graphene material is produced, the laser ablation process leads to an increase of

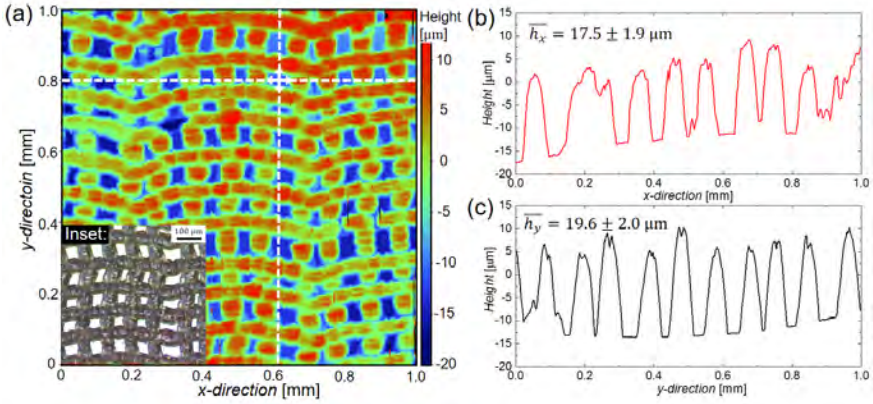

Figure V.1: (a) Profilometer scan for a LIG film on polyimide substrate over an area of 1 × 1 mm^2. The inset shows a microscope image of the same sample. Line profiles in (b) x- and (c) y-direction were drawn in accordance with the arrows and dashed lines indicated in (a).

the relative carbon content from 78% before to 85% after laser ablation, whereas the oxygen content decreases from 18% to 10%. Besides the change in the elemental composition, also a modification of the carbon-oxygen compounds can be observed. To understand this effect, the high-resolution C 1s spectra for the polyimide substrate (Kapton® HN) are depicted in Fig. V.2 (a) before and (b) after laser ablation.

After a careful comparison of the extensive literature for carbon-related XPS spectra [32]–[37] including the few reports on Kapton® HN [38], [39], the C 1s raw spectra were deconvoluted into its different contributions, which are associated with C-C sp^2 hybridized carbon bonds (284.6 eV), C-C sp^3 hybridized carbon bonds (285.6 eV), the carbon-oxygen compounds C-O (286.6 eV), O-C-O (287.6 eV) and O-C=O (289 eV) as well $\pi - \pi^*$ transitions (291 eV). For the untreated polyimide substrate, a large contribution of sp^3 hybridized carbon atoms and carbon-oxygen compounds from the aromatic rings can be seen, in accordance with the structural formula of the polyimide shown in Fig. V.2 (c).

The extracted concentrations before and after ablation for sp^2 and sp^3 hybridized carbon and the carbon-oxygen compounds are summarized in Table V.1. From this summary, it can be concluded that, after ablation, the concentrations of carbon-oxygen compounds and sp^3 hybridized carbon decreased, which goes along with the appearance of a large content of sp^2 hybridized carbon. This formation of sp^2 hybridized carbon is a clear indication for the production of amorphous graphene-derived species [40], [41] and gives rise to the name of the material, i.e., laser-induced graphene. As previously shown, the laser writing breaks the carbon-nitrogen and carbon-oxygen compound bonds, i.e., C-N, C-O-C,and C=O, that are the main contributions for the polyimide substrate [25]. The observed decrease in the portion of oxygen-containing carbon compounds

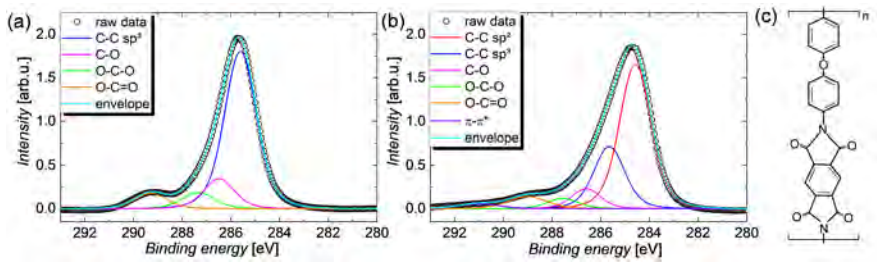

Figure V.2: High-resolution XPS spectra for the C 1s core level (a) before and (b) after laser ablation. (c) Structural formula for the polyimide substrate (Kapton® HN) with the chemical formula $C_{22}H_{11}N_2O_5$.

is also in agreement with the over-all decrease in oxygen species shown in the high-resolution spectra in supplementary Fig. V.12.

Next, the electrical properties of the LIG material are explored. For this, the I-V curves for two LIG heaters with different active areas were recorded and displayed in Fig. V.3 (a). From the relatively constant resistance-current behavior shown in Fig. V.3 (b), it can be recognized that the LIG heaters show an ohmic behavior. Both LIG films were fabricated using the same parameters and show a sheet resistance of around 250 Ω/sq. The difference in resistance of the LIG films arises due to the different electrode dimensions that are formed after contacting with copper tape and conductive silver paint. However, two additional effects can be identified: *i)* the resistance shows a drastic drop for low currents and *ii)* the resistance is slightly and gradually lowered for increasing currents. The first effect can be ascribed to the onset of electrical percolation that requires a finite current density, whereas the latter effect can be explained by the current induced heating of the LIG film. The increase in temperature leads to a reduction in resistance and will be discussed later.

Next, the onset of electrical percolation was studied in more detail; Fig. V.4 shows the resistance of a LIG heater for step-wise increases of the current as a function of time. The first finite resistance of around 328 Ω could be recorded around a current of 0.59 mA, which corresponds to a current density of 5.9 A/m^2. For increasing currents and current densities of 10 mA and 100 A/m^2 respectively, the measured resistance value shows a reduction of around 26% compared to the first recording, leading to a resistance of 243 Ω. The drop in resistance is not ascribed to the resistance-temperature behavior that, for graphitic materials yields to a negative temperature coefficient [42], but to the requirement for a finite current density to establish electrical percolation. This effect has already been observed by Bellew *et al.* [43] who contacted individual silver nanowire junctions and found a current of around 1-10 μA to be required to establish percolation. In their work, this effect was compared with the electroforming process in resistive switching materials that is required to generate an initial conductive state [44].

The transient response of LIG based thin film heaters for increasing powers is shown in Fig. V.5 for (a) the temperature and (b) the resistance. It can be recognized that the resistance response follows the overall trend of the temperature response. The rise in temperature as a function of the effectively heated area of the LIG film/polyimide substrate is illustrated in Fig. V.5 (c) and shows an almost linear behavior with a slope that yields to 131 ± 5 ^{o}C cm^2/W. This value compares well or it is superior to the ones reported for AgNWs 134-179 ^{o}C cm2/W [45], [46], ITO (88-388 ^{o}C cm^2/W) [46]–[48], CNTs (27-212 ^{o}C cm^2/W) [49]–[51], or laser-reduced graphene oxide (200-350 ^{o}C cm^2/W) [52].

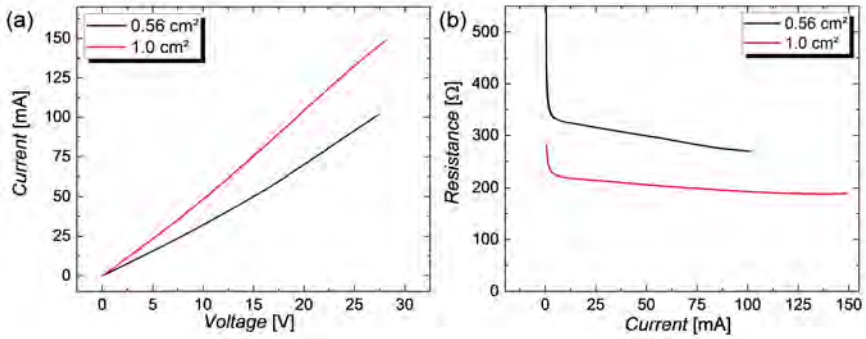

Figure V.3: (a) Current-voltage (I-V) curves for two LIG films with different heated areas on a polyimide substrate. (b) Resistances for the two LIG films as a function of the sourced current.

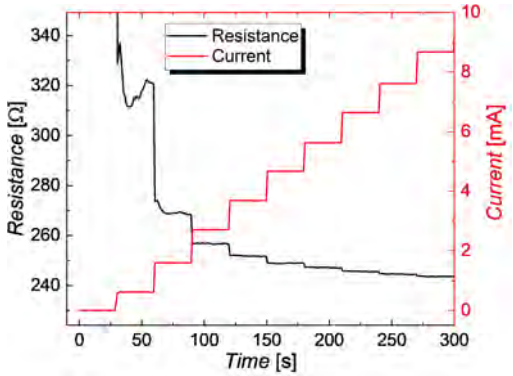

Figure V.4: Resistance and current of a LIG film as a function of the time. The measurement was conducted to study the percolation onset of LIG films at low currents.

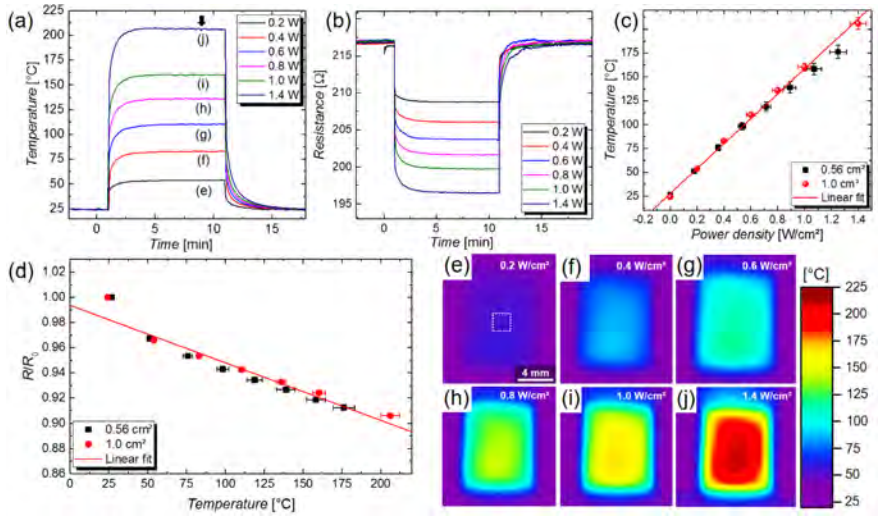

Figure V.5: Transient (a) thermal and (b) resistance curves for a LIG heater on a polyimide substrate. The actively heated area is 1 cm^2. The labels in (a) at the saturation temperatures correspond to the IR-images (e-j) extracted for each power step. (c) Temperature as a function of the applied electrical power density for two LIG heaters. The solid line represents a linear fit to the experimental data. (d) Normalized resistance R/R_0 for two LIG films as a function of the mean temperature of the heated film. The solid line represents a linear fit to the experimental data. IR-images of a LIG film heater with an actively heated area of 1 cm^2 for increasing power densities of (e) 0.2, (f) 0.4, (g) 0.6, (h) 0.8, (i) 1.0 and (j) 1.4 W/cm^2. The area of around 2×2 mm^2 that was used to determine a mean value for the temperature is indicated as dashed white square in (e). The scale bar in (e) also applies to the images (f-j).

Subsequently, the transient thermal response depicted in Fig. V.5 (a) is modeled and the total heat transfer coefficient h is determined. The coefficient h is composed of a convective heat loss h_c and a radiative heat loss h_R coefficient. For simplicity and in agreement with previous works [51], [53], it is assumed that the radiative losses per unit time P_R, which are described by the Stefan-Boltzman law below, can be linearized with regard to the temperature as follows:

$$\begin{aligned} P_R &= \varepsilon \cdot \sigma \cdot A \cdot (T^4 - T_0^4) \\ &= \varepsilon \cdot \sigma \cdot A \cdot (T^2 - T_0^2)(T + T_0)(T - T_0) \\ &= A \cdot h_R (T - T_0) \end{aligned} \tag{V.1}$$

where ε denotes the emissivity, σ the Stefan-Boltzmann constant, A the area of the heater, T the temperature on the heated side, T_0 the ambient temperature and h_R the radiative heat transfer coefficient, respectively. Similarly to previous

publications [45], h_R is considered to be a constant just as the convective heat loss coefficient h_C. This assumption eases the derivation of a simple analytical solution for the differential equation below. The temperature response can be modeled by considering the in- and outgoing heat fluxes at the film-heater/air interface, as sketched in supplementary Fig. V.14, for the ON state ($P_{el} > 0$):

$$c_p \cdot \rho V \cdot dT = P_{el} \cdot dt - 2hA(T - T_0)dt \tag{V.2}$$

where c_p denotes the isobaric specific heat capacity, ρ the mass density and V the volume of the polyimide film, respectively, whereas P_{el} is the electrical input power. For the OFF state, i.e., without electrical input power ($P_{el} = 0$), Eq. V.2 is reduced to:

$$c_p \cdot \rho V \cdot dT = -2hA(T - T_0)dt \tag{V.3}$$

A factor of 2 is included to consider the front and the back sides of the film heater. For Eqs. V.2 and V.3, a simple analytical solution for $P_{el} > 0$ can be derived as follows:

$$\begin{aligned} T(t) &= T_0 + \frac{P_{el}}{2hA}(1 - e^{-\frac{2hA(t-t_{on})}{c_p \rho V}}) \\ &= T_0 + T_{diff}(1 - e^{\frac{(t-t_{on})}{\tau}}) \end{aligned} \tag{V.4}$$

where t_{on} denotes the on-switching time, T_{diff} the increase in temperature due to heating and τ the response time, which is defined as $\tau = 2c_p\rho V/(hA) = 2c_p\rho d/h$, where d denotes the thickness of the heater. For the off-state, the following expression is obtained:

$$T(t) = T_0 + (T_{sat} - T_0)e^{\frac{-(t-t_{off})}{\tau}} \tag{V.5}$$

being t_{off} the off-switching time. Eqs. V.4 and V.5 were used to fit the experimental data for the transient thermal response of the LIG heater shown in Fig. V.5 (a). The results are drawn in supplementary Fig. V.13 as bold red lines (ON state) and dashed red lines (OFF state) for all the electrical powers, and in the inset in Fig. V.6 (b) exemplarily for three different powers. The fitting of the experimental data allows determining τ for the ON and the OFF state of the heater, as plotted in Fig. V.6 (a). τ is defined as the time it takes until the temperature of the heater increases $(e-1)/e = 0.63$ with respect to the absolute temperature increase T_{diff}. From Fig. V.6 (a) it can be concluded that τ_{OFF} stays in a narrow range from 18 s to 22 s for all temperatures, whereas τ_{ON} is gradually decreasing from around 20 s - 8 s, in a temperature range from 50 to 207 ^{o}C. This deviation for τ_{OFF} and τ_{ON} was reported by Ji *et al.* in a previous study on thin-film heaters [46]. It can be attributed to the oversimplified Eqs. V.4 and V.5 that are based on the assumption that the temperature dependence of c_p, ρ, d and h can be neglected. The temperature dependence of the heat loss h shown in Fig. V.6 (b) is solely determined by T_{diff}, in accordance with Eq. V.4. For our heaters, h lies in a range of 35-39 W/m^{2}K and gradually

increases over a temperature range of 50-207 ^{o}C. These values for h compare well to the ones reported in the literature for carbon-based film heaters made of multi-walled CNTs on PET (22 W/m^{2}K) [54], single-walled CNTs on glass (33-100 W/m^{2}K)[50], and CNT/AgNW composite (11-18 W/m^{2}K) [55]. In agreement with Eq. V.4, for a constant electrical power, a low h leads to a higher saturation temperature but a lower heat transfer to the surroundings via radiation or conduction.

The temperature-dependent resistance R normalized with respect to the ambient resistance R_0 at ambient temperature T_0 is illustrated in Fig. V.5 (d). The $R-T$ curve shows a linear dependence from slightly elevated temperatures of around 50 ^{o}C on, which yields to a temperature coefficient of $\alpha = -0.46 \pm 0.04$ m ^{o}C^{-1} that was extracted in accordance with the simple empirical formula:

$$R(T) = R_0 \cdot (1 + \alpha(T - T_0)) \tag{V.6}$$

The extracted temperature coefficient is negative, as reported for polycrystalline graphite below a temperature of 1400 ^{o}C [56], and compares well to the literature values for graphite and graphene of around -0.5 m ^{o}C^{-1} [57], [58], for both materials. At this point, it should not be omitted that the resistance shows a large drop of around 3.3% in the temperature range of 25-50 ^{o}C, which does not fit to the lower and linear decrease for R/R_0 of around 6.5% in the temperature range 50-175 ^{o}C. This behavior is in good agreement with the finding from Fig. V.4, where a minimum current density is required to establish good electrical percolation. The IR-images that are used to produce the transient temperature curves are depicted in Fig. V.5(e-j) for different electrical energy densities up to 1.4 W/cm^2. From these figures, it is evident that the temperature distribution across the actively heated area is relatively homogeneous and shows a drastic drop at the LIG-polyimide transition.

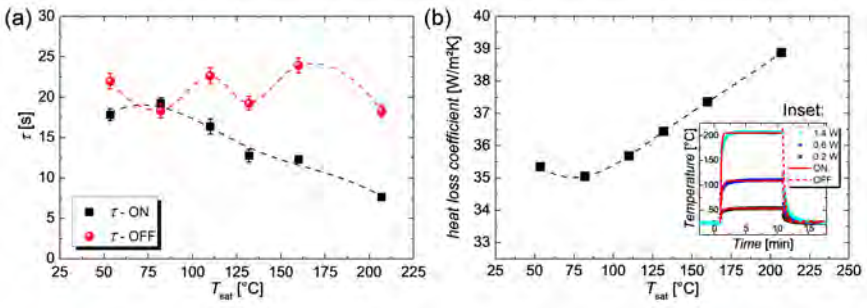

Figure V.6: (a) Response times τ for the ON and the OFF state of the LIG heater shown in Fig. V.5 (a), defined in accordance with Eqs. V.5 and V.6, as a function of the saturation temperatures. (b) Heat loss coefficients for increasing saturation temperatures, extracted from fitting Eq.V.4 to the transient thermal responses illustrated in Fig. V.5 (a). The inset in (b) depicts fits (bold and dashed red lines) of Eqs. V.4 and V.5 to the experimental data.

V.3.2 Thermal stability

After studying the structural, electrical and thermal properties of the LIG heaters, their thermal stability will be investigated with regard to *i)* their maximum operating temperature and *ii)* their stability under prolonged operation for increasing current densities. To study the maximum operating temperature and in turn also the maximum electrical input power density, the normalized resistance R/R_0 shown in Fig. V.7 was recorded as a function of the time. For the change in resistance, two regimes that are indicated in Fig. V.7 (b) can be identified: *i)* an operation regime that can be considered as stable since the resistance shows a step-wise and *ii)* linear decrease in resistance with temperature, in accordance with the temperature coefficient extracted from Fig. V.5 (d). In this region, the temperature and power density range is around 25-200 ^{o}C and 0-2.3 W/cm^2, respectively. For a temperature and power density range of 200-400 ^{o}C and 2.3-4.5 W/cm^2, respectively, the heaters undergo a gradual degradation that is accompanied by an increase in resistance. Around an electrical power density of 4.5 W/cm^2 and a temperature of 400 ^{o}C, R/R_0 shows an abrupt increase and ultimately electrical breakdown for slightly higher power densities. As shown in the SEM-images in Fig. V.7, this breakdown is accompanied by a change in morphology of both (c) the raw substrate and (d) the LIG film. It is evident that the maximum operation temperature is limited by the polyimide substrate, which is reported to be stable up to a temperature range of 300-400 ^{o}C in accordance with the literature [59], [60], and up to 400 ^{o}C according to the manufacturer. In contrast to polyimides, purely carbon-based allotropes exhibit a higher thermal stability. From thermogravimetric (TGA) analysis, graphite has shown to be stable up to a temperature of around 550 ^{o}C, under airflow [61], whereas, from Raman measurements, mono- and bilayer graphene start to show defects around a temperature range of 500-600 ^{o}C [62]. Further, an important difference in the thermal properties is the linear thermal expansion coefficient, which is reported in the range of (32-44)$\cdot 10^{-6}/^o$C for polyimide and -8$\cdot 10^{-6}/^o$C for graphene, both at room temperature [63], [64]. Since, on the one hand, the thermal expansion of the polyimide substrate is at least a factor of 5 higher than for the LIG films; the rupture of the LIG line shown in Fig. V.7 (d) is induced. On the other hand, the robust LIG mesh clings together the expanding polyimide substrate and induces a mechanical stress, which results in the polyimide cracks visible in Fig. V.7 (c). The onset of the electrical breakdown is further studied from the IR-images shown in Fig. V.7 that capture the moment of breakdown with respect to fully the operational device with no change in the heat distribution (Fig. V.7 (e)), 1 min after the onset of rapid degradation, 2 min later and after 3 min (Fig. V.7 (f)-(h), respectively). The LIG film is burnt off on the top section (Fig. V.7 (f)), whereas the overall breakdown occurs on a timescale below 3 min. The maximum operation temperature achieved under ambient conditions of around 400 ^{o}C for the LIG film heaters is superior to the one reported for other novel film heater materials. For example, heaters based on AgNWs show fragmentation in the range 250-300 ^{o}C [18], [65], [66] and those made of CuNWs readily oxidize above 100-150 ^{o}C [19], [21]. In addition,

graphene and its derivatives are known for their high chemical stability, which is comparable to the one of diamond at atmospheric pressure [67].

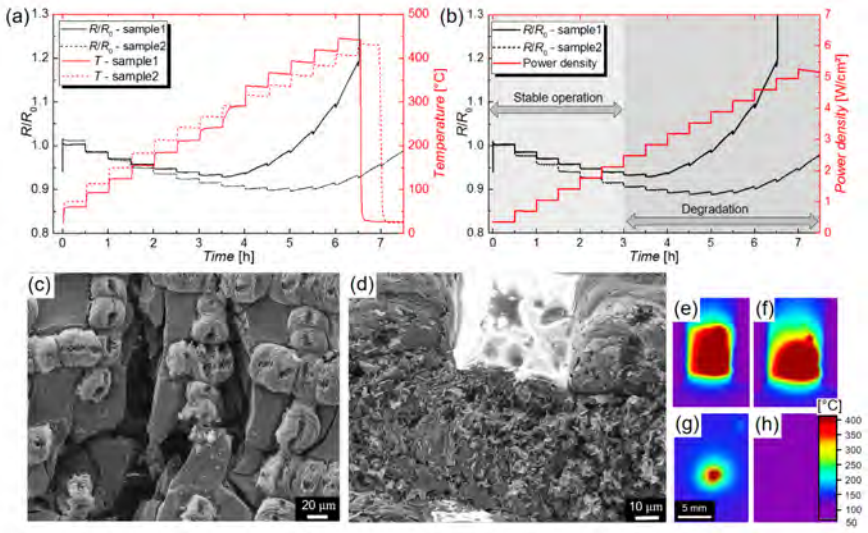

Figure V.7: (a) Normalized resistance R/R_0 and temperature for two LIG film heaters as a function of the time. (b) Normalized resistance R/R_0 and power density for two LIG film heaters as a function of the time. SEM-images for a degraded LIG film heater that show (c) the rupture of the polyimide substrate and (d) the damaging of the LIG lines. (e-h) IR images that depict the moment of breakdown for a LIG film heater in time steps of 1 min between two adjacent images.

Next, the degradation of the LIG films is studied for prolonged operation under current flow, as depicted in Fig. V.8 (a) that shows the resistance of a LIG heater as a function of the operation time for increasing power densities. For each power density, 8 heating steps with a duration of 2 h are followed by cooling steps with a duration of 30 min. The change in resistance after each heating cycle with respect to the initial resistance is shown in Fig. V.8 (b) as a function of the number of cycles for increasing power densities. This plot allows a rough classification of the heater into different degradation regimes. For a power density of up to 1.8 W/cm^2 that corresponds to a temperature of 225 ^{o}C, the change in resistance lies below 4%, whereas, for power densities above 2.7 W/cm^2 corresponding to a temperature of 250-275 ^{o}C, the change is more pronounced, as highlighted by the percentage values in Fig. V.8 (b).

The increase in resistance for prolonged operation of the LIG films can be attributed to two effects: *i)* mechanical and *ii)* chemical degradation. The mechanical degradation is induced by the large thermal expansion coefficient of the polyimide substrate that leads to a rupture of the LIG lines, which is gradually increasing overtime. The chemical degradation is induced by the oxidation of

carbon. The thermal behavior under airflow and elevated temperatures of carbon-based materials such as fullerenes (C60 and C70), diamond, carbon nanotubes and graphene was the subject of previous studies [68]–[73]. In summary, the thermal robustness of those materials can be grouped as follows:

$$Diamond,\ nanotubes > graphene > C60 > C70 \tag{V.7}$$

From TGA measurements, Cataldo *et al.* observed a clear onset of the reactivity between O_2 molecules and graphite in a temperature range of 400-500 ^oC [61]. This range is slightly higher than the temperatures that were investigated for a long-term test in this study. However, it is likely that the carbon atoms in the LIG heaters undergo a slow but gradual chemical degradation even below 400 ^oC.

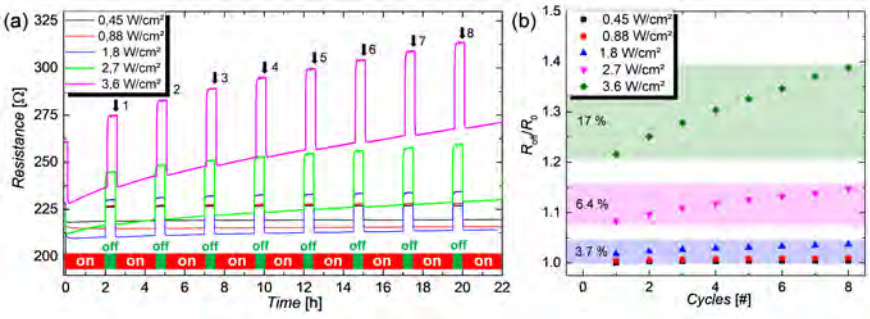

Figure V.8: (a) Long-term stability test for a LIG film heater that is subjected to increasing power densities. In total, 8 cycles with 2 h heating and 0.5 h cooling per cycle were conducted for each power density step. (b) Normalized increase in resistance R_{off}/R_0 for increasing cycles and power densities. R_{off} denotes the resistance in the off state of the film heater after one heating cycle.

V.3.3 Flexibility and adhesion

Flexible heaters can, e.g., be used for wearable electronics such as for wearable articular thermotherapy, as proposed by Choi *et al.* in 2015 [74]. So far, flexible thin-film heaters were fabricated using solution-processed metal nanowires such as AgNWs [75], graphitic materials such as graphene [48], [76] and CNTs as well as composite materials such as AgNWs/CNTs [55] or AgNWs/PEDOT:PSS [46]. In detail, the utilized flexible materials were polyimide [76], PDMS [77], PET [55], PEN [75] and a polyacrylate-based polymer [78]. The novelty in this study is that the heaters are directly produced on a bare polyimide substrate, which inherently guarantees that the active film adapts the shape of the underlying substrate. This circumstance should aid to improve the flexibility of the fabricated devices. It should be noted that, for the presented heaters, it is mainly important to achieve a uniform LIG film and, hence, a uniform heat flux and temperature distribution

across the device. Thus, novel flexible and eventually also semi-transparent heaters are often fabricated by scalable spraying processes. In the case of metal nanowires, this process results in the formation of a random nanowire mesh that uniformly conducts [18], [19], [79]. Besides spray coating, other deposition techniques such as drop casting [78], vacuum filtration [77] or spinning [54] were also reported for the fabrication of self-heating films. However, these techniques possess large drawbacks like the lack of homogeneity and scalability. In the end, it should be emphasized that the versatile CNC-driven fabrication process can also be utilized to form more complex structures such as graphene-based and biocompatible interdigitated electrodes (IDEs) to fabricate biosensors, self-recovering sensors, or environmental and health monitoring systems [80].

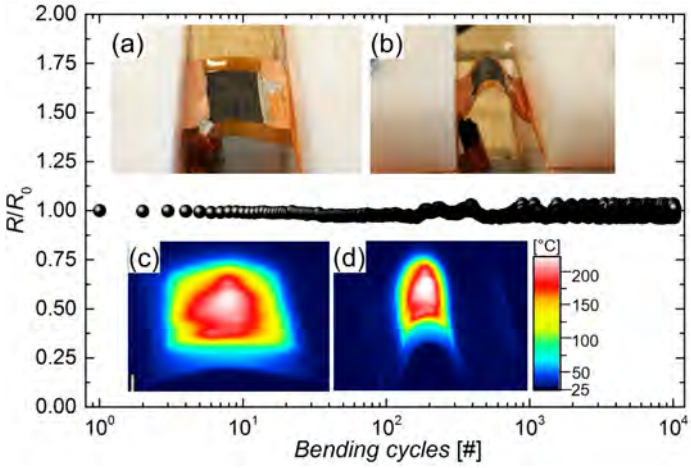

Figure V.9: Change in resistance R with respect to the initial resistance R_0 for an increasing number of bending cycles. The sample under test is bent to a minimum diameter of around 4 mm. For this test, only a small probe current was applied. The inset (a) and (b) show the sample in the relaxed and bent position, whereas the insets (c) and (d) show the infrared images for the LIG heater in the relaxed and bent position, respectively, both subjected to an electrical power of 1 W.

In this work, the flexibility of the presented devices was studied for subsequent bending cycles, as shown in Fig. V.9 that depicts the change in resistance R with respect to the initial resistance R_0 for an increasing number of bending cycles. Photos for (a) the relaxed and (b) the bent state of the film heater with a minimum bending diameter of 4 mm are shown in the inset of Fig. V.9. It can be recognized that even after 10000 bending cycles, the change in the normalized resistance is below 4%. For the multimeter measurement, a probe current of 3 mA was passed through the device to establish a good electrical percolation, in agreement with Fig. V.4. It should be mentioned that there exist enormous future opportunities for flexible heaters such as for wearable devices or

low-cost point-of-care chips, analytical chemistry and for combinatorial studies [81]. Examples of this can be found in the literature, e.g., Bagherifard *et al.* [82] and Tamayol *et al.* [83] used them in flexible dermal patches for on demand drug delivery, while Kim *et al.* [55] used the flexible heater as a conformal patch on the surface of a beaker. However, of interest is also the stability of the devices in operation, i.e., when subjected to high electrical currents or power densities. For this, the same bending experiment was performed at an electrical input power density of 1 W/cm^2, as shown by the IR images in the inset of Fig. V.9 that depicts the LIG heater in (c) the relaxed and (d) the bent state. No increase in resistance or change in the IR-images could be observed after 100 bending cycles (see supporting information Video in this link).

V.4 Commercialization potential

Before concluding our work, we would like to emphasize the commercial potential of the laser-scribing technique in combination with the proposed substrate for manufacturing cost-effective heaters. For this, nanographene heaters with an area of 7×5 = 35 cm^2 were fabricated, as shown in Fig. V.10 (a), and compared with a commercial heater based on metal serpentine-structures that is depicted in Fig. V.10 (b). The patterned areas of the heaters are identical. For both heaters, polyimide was employed as the substrate. Electrical contacts to the nanographene heater were formed by screen printing a solution-based silver paste (Loctite 1010). Next, the two types of heaters are compared with each other with regard to the homogeneity of their heat distribution, which is depicted in Fig. V.10 for (c) the nanographene heater and (d) the commercial heater 3616107 from Thermos Technologies (Germany), at an electrical input power of 3.5 W. From these images, it can be seen that our nanographene heater shows a high uniformity, whereas for the commercial heaters, hot areas are formed. The presented LIG heaters can be fabricated under ambient conditions, whereas common thin film heaters are typically produced under high-vacuum, which is very costly and difficult to realize for larger areas [84], [85]. Besides the homogeneous heat distribution of the nanographene heater and the facile fabrication process, another advantage over the commercial one is its robustness to mechanical stress. For the case that the serpentine-like structure of the commercial heater is interrupted at some position, the heater is broken, whereas the nanographene heater can still be operated with a reduction in uniformity of the heat distribution and, eventually, also an increase in resistance. From an economic point of view, the laser-scribed heaters are also attractive since they are around a factor of 31 cheaper than the commercial ones (see supporting information for this estimation). Finally, despite of the already very promising robustness, it should be mentioned that our heaters are susceptible to scratching. However, we believe that this issue can easily be solved by employing polymer-based coatings such as polymethyl methacrylate (PMMA) [21] or parylene [86], which have widely been reported for encapsulation.

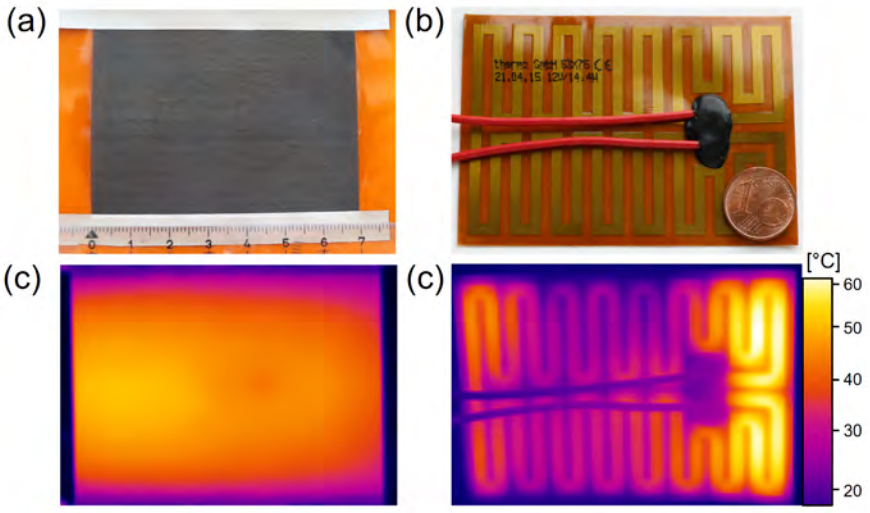

Figure V.10: Photographies of (a) a photothermally scribed nanographene heater with screen printed and silver-based bias electrodes and (b) a commercial polyimide heater. Infrared images for (c) the nanographene and (d) the commercial heater.

V.5 Conclusions

In this paper, we describe the manufacturing of flexible and cost-effective heaters by an innovative and simple laser-scribing process on bare polyimide films. This technique offers a reproducible and easy fabrication process, which modified the electrical properties of such a polyimide. In contrast to commercial flexible heaters, the LIG heaters show a much higher heat uniformity and can be fabricated under ambient conditions. The resulting material shows electrical properties comparable to the ones of graphene, such as the temperature coefficient. In particular, the fabricated heaters can operate up to 400 ^{o}C, only limited by the mechanical stability of the substrate. These devices have a very stable response up to 225 ^{o}C, even while bending them. The temperature response of around 131 W cm^2/^{o}C, when subjected to Joule heating, compares well or is even superior to most values reported in the literature. In addition to an efficient generation of high temperatures at low input powers, an important parameter for sensing applications is also their response time, which is around 8 s for electrical input power densities up to 1.4 W/cm^2. Furthermore, the films are low-cost, environmentally friendly and the flexible heaters can be directly integrated on the substrate by laser-scribing, without requiring any extra fabrication steps such as thermal or photonic sintering. All these features open a wide range of possibilities for the presented devices that can be integrated easily in biosensor systems, environmental and health monitoring applications, reducing fabrication costs and complexity and, at the same time, providing a high performance.

Acknowledgements. This work was supported by the German Research Foundation (DFG) and the Technical University of Munich within the funding program Open Access Publishing and the TUM Graduate School. This work was also partially funded by Spain's Government through project TEC2017-89955-P and pre-doctoral grant FPU16/01451, as well as by the European Union through the fellowship H2020-MSCA-IF-2017 794885-SELFSENS.

References

[1] Catto, A. C., Silva, L. F. da, Ribeiro, C., Bernardini, S., Aguir, K., Longo, E., and Mastelaro, V. R., "An easy method of preparing ozone gas sensors based on ZnO nanorods," *RSC Advances*, vol. 5, no. 25, pp. 19 528–19 533, 2015.

[2] Catto, A. C., Silva, L. F. da, Bernardi, M. I. B., Bernardini, S., Aguir, K., Longo, E., and Mastelaro, V. R., "Local structure and surface properties of CoxZn1–xO thin films for ozone gas sensing," *ACS Applied Materials & Interfaces*, vol. 8, no. 39, pp. 26 066–26 072, Sep. 2016.

[3] Falco, A., Rivadeneyra, A., Loghin, F. C., Salmeron, J. F., Lugli, P., and Abdelhalim, A., "Towards low-power electronics: Self-recovering and flexible gas sensors," *Journal of Materials Chemistry A*, vol. 6, no. 16, pp. 7107–7113, 2018.

[4] Abdelhalim, A., Winkler, M., Loghin, F., Zeiser, C., Lugli, P., and Abdellah, A., "Highly sensitive and selective carbon nanotube-based gas sensor arrays functionalized with different metallic nanoparticles," *Sensors and Actuators B: Chemical*, vol. 220, pp. 1288–1296, Dec. 2015.

[5] Handique, K., "Microfluidic cartridge and method of using sam," US9815057B2, 2004.

[6] Courbat, J., Briand, D., and Rooij, N. de, "Reliability improvement of suspended platinum-based micro-heating elements," *Sensors and Actuators A: Physical*, vol. 142, no. 1, pp. 284–291, Mar. 2008.

[7] Simon, I., Bârsan, N., Bauer, M., and Weimar, U., "Micromachined metal oxide gas sensors: Opportunities to improve sensor performance," *Sensors and Actuators B: Chemical*, vol. 73, no. 1, pp. 1–26, Feb. 2001.

[8] Triantafyllopoulou, R., Chatzandroulis, S., Tsamis, C., and Tserepi, A., "Alternative micro-hotplate design for low power sensor arrays," *Microelectronic Engineering*, vol. 83, no. 4-9, pp. 1189–1191, Apr. 2006.

[9] Chang, W.-Y. and Hsihe, Y.-S., "Multilayer microheater based on glass substrate using MEMS technology," *Microelectronic Engineering*, vol. 149, pp. 25–30, Jan. 2016.

[10] Khan, S., Lorenzelli, L., and Dahiya, R. S., "Technologies for printing sensors and electronics over large flexible substrates: A review," *IEEE Sensors Journal*, vol. 15, no. 6, pp. 3164–3185, Jun. 2015.

[11] Mattana, G. and Briand, D., "Recent advances in printed sensors on foil," *Materials Today*, vol. 19, no. 2, pp. 88–99, Mar. 2016.

[12] Courbat, J., Canonica, M., Teyssieux, D., Briand, D., and Rooij, N. F. de, "Design and fabrication of micro-hotplates made on a polyimide foil: Electrothermal simulation and characterization to achieve power consumption in the low mW range," *Journal of Micromechanics and Microengineering*, vol. 21, no. 1, p. 015 014, Dec. 2010.

[13] Briand, D., Oprea, A., Courbat, J., and Bârsan, N., "Making environmental sensors on plastic foil," *Materials Today*, vol. 14, no. 9, pp. 416–423, Sep. 2011.

[14] Molina-Lopez, F., Briand, D., and Rooij, N. de, "Decreasing the size of printed comb electrodes by the introduction of a dielectric interlayer for capacitive gas sensors on polymeric foil: Modeling and fabrication," *Sensors and Actuators B: Chemical*, vol. 189, pp. 89–96, Dec. 2013.

[15] Danesh, E., Molina-Lopez, F., Camara, M., Bontempi, A., Quintero, A. V., Teyssieux, D., Thiery, L., Briand, D., Rooij, N. F. de, and Persaud, K. C., "Development of a new generation of ammonia sensors on printed polymeric hotplates," *Analytical Chemistry*, vol. 86, no. 18, pp. 8951–8958, Aug. 2014.

[16] Briand, D., Molina-Lopez, F., Quintero, A. V., Ataman, C., Courbat, J., and Rooij, N. F. de, "Why going towards plastic and flexible sensors?" *Procedia Engineering*, vol. 25, pp. 8–15, 2011.

[17] Calata, J. N., Lu, G.-Q., Ngo, K., and Nguyen, L., "Electromigration in sintered nanoscale silver films at elevated temperature," *Journal of Electronic Materials*, vol. 43, no. 1, pp. 109–116, Oct. 2013.

[18] Bobinger, M., Angeli, D., Colasanti, S., Torraca, P. L., Larcher, L., and Lugli, P., "Infrared, transient thermal, and electrical properties of silver nanowire thin films for transparent heaters and energy-efficient coatings," *physica status solidi (a)*, vol. 214, no. 1, p. 1 600 466, Sep. 2016.

[19] Bobinger, M., Mock, J., Torraca, P. L., Becherer, M., Lugli, P., and Larcher, L., "Tailoring the aqueous synthesis and deposition of copper nanowires for transparent electrodes and heaters," *Advanced Materials Interfaces*, vol. 4, no. 20, p. 1 700 568, Aug. 2017.

[20] Camara, M., Breuil, P., Pijolat, C., Viricelle, J., Rooij, N. de, and Briand, D., "Tubular gas preconcentrators based on inkjet printed micro-hotplates on foil," *Sensors and Actuators B: Chemical*, vol. 236, pp. 1111–1117, Nov. 2016.

[21] Zhai, H., Wang, R., Wang, X., Cheng, Y., Shi, L., and Sun, J., "Transparent heaters based on highly stable cu nanowire films," *Nano Research*, vol. 9, no. 12, pp. 3924–3936, Sep. 2016.

[22] Khaligh, H. H. and Goldthorpe, I. A., "Failure of silver nanowire transparent electrodes under current flow," *Nanoscale Research Letters*, vol. 8, no. 1, May 2013.

[23] Khan, S., Nguyen, T., Lubej, M., Thiery, L., Vairac, P., and Briand, D., "Low-power printed micro-hotplates through aerosol jetting of gold on thin polyimide membranes," *Microelectronic Engineering*, vol. 194, pp. 71–78, Jul. 2018.

[24] Albrecht, A., Rivadeneyra, A., Abdellah, A., Lugli, P., and Salmerón, J. F., "Inkjet printing and photonic sintering of silver and copper oxide nanoparticles for ultra-low-cost conductive patterns," *Journal of Materials Chemistry C*, vol. 4, no. 16, pp. 3546–3554, 2016.

[25] Romero, F. J., Rivadeneyra, A., Toral, V., Castillo, E., Garcia-Ruiz, F., Morales, D. P., and Rodriguez, N., "Design guidelines of laser reduced graphene oxide conformal thermistor for IoT applications," *Sensors and Actuators A: Physical*, vol. 274, pp. 148–154, May 2018.

[26] Peng, Z., Lin, J., Ye, R., Samuel, E. L. G., and Tour, J. M., "Flexible and stackable laser-induced graphene supercapacitors," *ACS Applied Materials & Interfaces*, vol. 7, no. 5, pp. 3414–3419, Jan. 2015.

[27] Lin, J., Peng, Z., Liu, Y., Ruiz-Zepeda, F., Ye, R., Samuel, E. L. G., Yacaman, M. J., Yakobson, B. I., and Tour, J. M., "Laser-induced porous graphene films from commercial polymers," *Nature Communications*, vol. 5, no. 1, Dec. 2014.

[28] Zhang, J., Ren, M., Wang, L., Li, Y., Yakobson, B. I., and Tour, J. M., "Oxidized laser-induced graphene for efficient oxygen electrocatalysis," *Advanced Materials*, vol. 30, no. 21, p. 1 707 319, Apr. 2018.

[29] Zhang, J., Ren, M., Li, Y., and Tour, J. M., "In situ synthesis of efficient water oxidation catalysts in laser-induced graphene," *ACS Energy Letters*, vol. 3, no. 3, pp. 677–683, Feb. 2018.

[30] Zhang, Z., Song, M., Hao, J., Wu, K., Li, C., and Hu, C., "Visible light laser-induced graphene from phenolic resin: A new approach for directly writing graphene-based electrochemical devices on various substrates," *Carbon*, vol. 127, pp. 287–296, Feb. 2018.

[31] Tittle, C. M., Yilman, D., Pope, M. A., and Backhouse, C. J., "Robust superhydrophobic laser-induced graphene for desalination applications," *Advanced Materials Technologies*, vol. 3, no. 2, p. 1 700 207, Dec. 2017.

[32] Lascovich, J., Giorgi, R., and Scaglione, S., "Evaluation of the sp2/sp3 ratio in amorphous carbon structure by XPS and XAES," *Applied Surface Science*, vol. 47, no. 1, pp. 17–21, Jan. 1991.

[33] Blyth, R., Buqa, H., Netzer, F., Ramsey, M., Besenhard, J., Golob, P., and Winter, M., "XPS studies of graphite electrode materials for lithium ion batteries," *Applied Surface Science*, vol. 167, no. 1-2, pp. 99–106, Oct. 2000.

[34] Yang, D., Velamakanni, A., Bozoklu, G., Park, S., Stoller, M., Piner, R. D., Stankovich, S., Jung, I., Field, D. A., Ventrice, C. A., and Ruoff, R. S., "Chemical analysis of graphene oxide films after heat and chemical treatments by x-ray photoelectron and micro-raman spectroscopy," *Carbon*, vol. 47, no. 1, pp. 145–152, Jan. 2009.

[35] Ektessabi, A. and Hakamata, S., "XPS study of ion beam modified polyimide films," *Thin Solid Films*, vol. 377-378, pp. 621–625, Dec. 2000.

[36] Jackson, S., "Determining hybridization differences for amorphous carbon from the XPS c 1s envelope," *Applied Surface Science*, vol. 90, no. 2, pp. 195–203, Oct. 1995.

[37] Leiro, J., Heinonen, M., Laiho, T., and Batirev, I., "Core-level XPS spectra of fullerene, highly oriented pyrolitic graphite, and glassy carbon," *Journal of Electron Spectroscopy and Related Phenomena*, vol. 128, no. 2-3, pp. 205–213, Feb. 2003.

[38] Wang, P. S., Wittberg, T. N., and Wolf, J. D., "A characterization of kapton polyimide by x-ray photoelectron spectroscopy and energy dispersive spectroscopy," *Journal of Materials Science*, vol. 23, no. 11, pp. 3987–3991, Nov. 1988.

[39] Huang, X. D., Bhangale, S. M., Moran, P. M., Yakovlev, N. L., and Pan, J., "Surface modification studies of kapton®HN polyimide films," *Polymer International*, vol. 52, no. 7, pp. 1064–1069, Jun. 2003.

[40] Stankovich, S., Dikin, D. A., Dommett, G. H. B., Kohlhaas, K. M., Zimney, E. J., Stach, E. A., Piner, R. D., Nguyen, S. T., and Ruoff, R. S., "Graphene-based composite materials," *Nature*, vol. 442, no. 7100, pp. 282–286, Jul. 2006.

[41] Dominguez-Bajo, A., González-Mayorga, A., López-Dolado, E., and Serrano, M. C., "Graphene-derived materials interfacing the spinal cord: Outstanding in vitro and in vivo findings," *Frontiers in Systems Neuroscience*, vol. 11, Sep. 2017.

[42] Balandin, A. A., "Thermal properties of graphene and nanostructured carbon materials," *Nature Materials*, vol. 10, no. 8, pp. 569–581, Jul. 2011.

[43] Bellew, A. T., Manning, H. G., Rocha, C. G. da, Ferreira, M. S., and Boland, J. J., "Resistance of single ag nanowire junctions and their role in the conductivity of nanowire networks," *ACS Nano*, vol. 9, no. 11, pp. 11 422–11 429, Oct. 2015.

[44] Waser, R., Dittmann, R., Staikov, G., and Szot, K., "Redox-based resistive switching memories - nanoionic mechanisms, prospects, and challenges," *Advanced Materials*, vol. 21, no. 25-26, pp. 2632–2663, Jul. 2009.

[45] Zhang, X., Liu, M., Wang, B., Chen, H., and Wang, Z., "A wide measurement range and fast update rate integrated interface for capacitive sensors array," *IEEE Transactions on Circuits and Systems I: Regular Papers*, vol. 61, no. 1, pp. 2–11, Jan. 2014.

[46] Ji, S., He, W., Wang, K., Ran, Y., and Ye, C., "Thermal response of transparent silver nanowire/PEDOT:PSS film heaters," *Small*, vol. 10, no. 23, pp. 4951–4960, Jul. 2014.

[47] Gainutdinov, I. S., Nesmelov, E. A., Aliakberov, R. D., and Mikhailov, A. V., "Heater elements based on in2o3(sn) layers transparent in the visible region," *Journal of Optical Technology*, vol. 71, no. 10, p. 705, Oct. 2004.

[48] Kang, J., Kim, H., Kim, K. S., Lee, S.-K., Bae, S., Ahn, J.-H., Kim, Y.-J., Choi, J.-B., and Hong, B. H., "High-performance graphene-based transparent flexible heaters," *Nano Letters*, vol. 11, no. 12, pp. 5154–5158, Dec. 2011.

[49] Yoon, Y.-H., Song, J.-W., Kim, D., Kim, J., Park, J.-K., Oh, S.-K., and Han, C.-S., "Transparent film heater using single-walled carbon nanotubes," *Advanced Materials*, vol. 19, no. 23, pp. 4284–4287, Dec. 2007.

[50] Kang, T. J., Kim, T., Seo, S. M., Park, Y. J., and Kim, Y. H., "Thickness-dependent thermal resistance of a transparent glass heater with a single-walled carbon nanotube coating," *Carbon*, vol. 49, no. 4, pp. 1087–1093, Apr. 2011.

[51] Bae, J. J., Lim, S. C., Han, G. H., Jo, Y. W., Doung, D. L., Kim, E. S., Chae, S. J., Huy, T. Q., Luan, N. V., and Lee, Y. H., "Heat dissipation of transparent graphene defoggers," *Advanced Functional Materials*, vol. 22, no. 22, pp. 4819–4826, Jul. 2012.

[52] Lin, S.-Y., Zhang, T.-Y., Lu, Q., Wang, D.-Y., Yang, Y., Wu, X.-M., and Ren, T.-L., "High-performance graphene-based flexible heater for wearable applications," *RSC Advances*, vol. 7, no. 43, pp. 27 001–27 006, 2017.

[53] Kwak, H. S., Kim, K., Shon, B. C., Lee, H., and Han, C.-S., "Thermal characteristics of a transparent film heater using single-walled carbon nanotubes," *Journal of Nanoscience and Nanotechnology*, vol. 10, no. 5, pp. 3512–3515, May 2010.

[54] Jang, H.-S., Jeon, S. K., and Nahm, S. H., "The manufacture of a transparent film heater by spinning multi-walled carbon nanotubes," *Carbon*, vol. 49, no. 1, pp. 111–116, Jan. 2011.

[55] Kim, D., Zhu, L., Jeong, D.-J., Chun, K., Bang, Y.-Y., Kim, S.-R., Kim, J.-H., and Oh, S.-K., "Transparent flexible heater based on hybrid of carbon nanotubes and silver nanowires," *Carbon*, vol. 63, pp. 530–536, Nov. 2013.

[56] Ota, T., Yamai, I., and Takahashi, J., "Positive-temperature-coefficient effect in graphite-cristobalite composites," *Journal of the American Ceramic Society*, vol. 75, no. 7, pp. 1772–1776, Jul. 1992.

[57] Giancoli, D., *Physics : principles with applications*. Upper Saddle River, N.J: Pearson/Prentice Hall, 2005.

[58] Davaji, B., Cho, H. D., Malakoutian, M., Lee, J.-K., Panin, G., Kang, T. W., and Lee, C. H., "A patterned single layer graphene resistance temperature sensor," *Scientific Reports*, vol. 7, no. 1, Aug. 2017.

[59] Dine-Hart, R. A. and Wright, W. W., "Thermal stability of aromatic polyimides: Factors affecting the oxidative stability of poly-n, n′-(4,4′-diphenyl ether) pyromellitimide," *British Polymer Journal*, vol. 3, no. 4, pp. 163–168, Jul. 1971.

[60] B. Kamerbeek G.H. Kroes, W. G., "Thermal degradation of some polyamides," *Soc. Chem. Ind. Monograph*, vol. 13, 1961.

[61] Cataldo, F., "A study on the thermal stability to 1000°c of various carbon allotropes and carbonaceous matter both under nitrogen and in air," *Fullerenes, Nanotubes and Carbon Nanostructures*, vol. 10, no. 4, pp. 293–311, Dec. 2002.

[62] Nan, H. Y., Ni, Z. H., Wang, J., Zafar, Z., Shi, Z. X., and Wang, Y. Y., "The thermal stability of graphene in air investigated by raman spectroscopy," *Journal of Raman Spectroscopy*, vol. 44, no. 7, pp. 1018–1021, Apr. 2013.

[63] Hidnert, P., "Thermal expansion of artificial graphite and carbon," *Journal of Research of the National Bureau of Standards*, vol. 13, no. 1, p. 37, Jul. 1934.

[64] Yoon, D., Son, Y.-W., and Cheong, H., "Negative thermal expansion coefficient of graphene measured by raman spectroscopy," *Nano Letters*, vol. 11, no. 8, pp. 3227–3231, Aug. 2011.

[65] Molares, M. E. T., Balogh, A. G., Cornelius, T. W., Neumann, R., and Trautmann, C., "Fragmentation of nanowires driven by rayleigh instability," *Applied Physics Letters*, vol. 85, no. 22, pp. 5337–5339, Nov. 2004.

[66] Li, Z., Okasinski, J. S., Almer, J. D., Ren, Y., Zuo, X., and Sun, Y., "Quantitative determination of fragmentation kinetics and thermodynamics of colloidal silver nanowires by in situ high-energy synchrotron x-ray diffraction," *Nanoscale*, vol. 6, no. 1, pp. 365–370, 2014.

[67] Kestin, J., *A Course in Thermodynamics*. New York etc: Hemisphere Publ. Corp, 1979.

[68] Ismail, I. M. and Rodgers, S. L., "Comparisons between fullerene and forms of well-known carbons," *Carbon*, vol. 30, no. 2, pp. 229–239, 1992.

[69] Werner, H., Herein, D., Blöcker, J., Henschke, B., Tegtmeyer, U., Schedel-Niedrig, T., Keil, M., Bradshaw, A., and Schlögl, R., "Spectroscopic and chemical characterisation of "fullerene black"," *Chemical Physics Letters*, vol. 194, no. 1-2, pp. 62–66, Jun. 1992.

[70] Kawata, S., Yamauchi, K., Suzuki, S., Kikuchi, K., Shiromaru, H., Katada, M., Saito, K., Ikemoto, I., and Achiba, Y., "The origin of the ESR signal of c60seen in the powder and in benzene solution. the indication of the reaction of c60with oxygen induced by photoexcitation," *Chemistry Letters*, vol. 21, no. 9, pp. 1659–1662, Sep. 1992.

[71] Chibante, L. F., Pan, C., Pierson, M. L., Haufler, R. E., and Heymann, D., "Rate of decomposition of c60 and c70 heated in air and the attempted characterization of the products," *Carbon*, vol. 31, no. 1, pp. 185–193, 1993.

[72] Scanlon, J. C., Brown, J. M., and Ebert, L. B., "Oxidative stability of fullerenes," *The Journal of Physical Chemistry*, vol. 98, no. 15, pp. 3921–3923, Apr. 1994.

[73] Wohlers, M., Werner, H., Herein, D., Schedel-Niedrig, T., Bauer, A., and Schlögl, R., "Reaction of c60 and c70 with molecular oxygen," *Synthetic Metals*, vol. 77, no. 1-3, pp. 299–302, Feb. 1996.

[74] Choi, S., Park, J., Hyun, W., Kim, J., Kim, J., Lee, Y. B., Song, C., Hwang, H. J., Kim, J. H., Hyeon, T., and Kim, D.-H., "Stretchable heater using ligand-exchanged silver nanowire nanocomposite for wearable articular thermotherapy," *ACS Nano*, vol. 9, no. 6, pp. 6626–6633, Jun. 2015.

[75] Celle, C., Mayousse, C., Moreau, E., Basti, H., Carella, A., and Simonato, J.-P., "Highly flexible transparent film heaters based on random networks of silver nanowires," *Nano Research*, vol. 5, no. 6, pp. 427–433, May 2012.

[76] Sui, D., Huang, Y., Huang, L., Liang, J., Ma, Y., and Chen, Y., "Flexible and transparent electrothermal film heaters based on graphene materials," *Small*, vol. 7, no. 22, pp. 3186–3192, Oct. 2011.

[77] Hong, S., Lee, H., Lee, J., Kwon, J., Han, S., Suh, Y. D., Cho, H., Shin, J., Yeo, J., and Ko, S. H., "Highly stretchable and transparent metal nanowire heater for wearable electronics applications," *Advanced Materials*, vol. 27, no. 32, pp. 4744–4751, Jul. 2015.

[78] Li, J., Liang, J., Jian, X., Hu, W., Li, J., and Pei, Q., "A flexible and transparent thin film heater based on a silver nanowire/heat-resistant polymer composite," *Macromolecular Materials and Engineering*, vol. 299, no. 11, pp. 1403–1409, Aug. 2014.

[79] Bobinger, M., Torraca, P. L., Mock, J., Becherer, M., Cattani, L., Angeli, D., Larcher, L., and Lugli, P., "Solution-processing of copper nanowires for transparent heaters and thermo-acoustic loudspeakers," *IEEE Transactions on Nanotechnology*, vol. 17, no. 5, pp. 940–947, Sep. 2018.

[80] Shao, Y., Wang, J., Wu, H., Liu, J., Aksay, I., and Lin, Y., "Graphene based electrochemical sensors and biosensors: A review," *Electroanalysis*, vol. 22, no. 10, pp. 1027–1036, Mar. 2010.

[81] Gupta, R., Rao, K. D. M., Kiruthika, S., and Kulkarni, G. U., "Visibly transparent heaters," *ACS Applied Materials & Interfaces*, vol. 8, no. 20, pp. 12 559–12 575, May 2016.

[82] Bagherifard, S., Tamayol, A., Mostafalu, P., Akbari, M., Comotto, M., Annabi, N., Ghaderi, M., Sonkusale, S., Dokmeci, M. R., and Khademhosseini, A., "Dermal patch with integrated flexible heater for on demand drug delivery," *Advanced Healthcare Materials*, vol. 5, no. 1, pp. 175–184, Oct. 2015.

[83] Tamayol, A., Najafabadi, A. H., Mostafalu, P., Yetisen, A. K., Commotto, M., Aldhahri, M., Abdel-wahab, M. S., Najafabadi, Z. I., Latifi, S., Akbari, M., Annabi, N., Yun, S. H., Memic, A., Dokmeci, M. R., and Khademhosseini, A., "Biodegradable elastic nanofibrous platforms with integrated flexible heaters for on-demand drug delivery," *Scientific Reports*, vol. 7, no. 1, Aug. 2017.

[84] Choi, K., Kim, J., Lee, Y., and Kim, H., "ITO/ag/ITO multilayer films for the application of a very low resistance transparent electrode," *Thin Solid Films*, vol. 341, no. 1-2, pp. 152–155, Mar. 1999.

[85] Guillén, C. and Herrero, J., "ITO/metal/ITO multilayer structures based on ag and cu metal films for high-performance transparent electrodes," *Solar Energy Materials and Solar Cells*, vol. 92, no. 8, pp. 938–941, Aug. 2008.

[86] Wang, J., Gulari, M. N., and Wise, K. D., "A parylene-silicon cochlear electrode array with integrated position sensors," in *2006 International Conference of the IEEE Engineering in Medicine and Biology Society*, IEEE, Aug. 2006.

V.6 Supplementary Information

The XPS survey scans over an area of around 5×5 mm^2 for polyimide substrate (black) before and (red) after laser ablation are depicted in Figure V.11. The C 1s, N 1s and O 1s core level peaks that are associated with the carbon, nitrogen, and oxygen-containing specimen present in the polyimide film can clearly be identified.

XPS high-resolution scans are shown in Figure S2 for the (a) C 1s, (b) O 1s and (c) N 1s peak along with (d) the concentrations for each element. The concentrations were determined by considering the relative sensitivity factors (RSF) for the C 1s, O 1s and N 1s peaks of 0.25, 0.66 and 0.42, respectively. All spectra were normalized by their area and weighted with the determined concentration of the respective element. From table (d) it can be concluded that the concentrations extracted for the polyimide film are in very good agreement with the concentrations expected by considering the chemical formula of polyimide, i.e., $C_{22}H_{11}N_2O_5$. For this estimate, the hydrogen content was neglected since it cannot be resolved by XPS. The experimentally determined concentrations for nitrogen are lower than expected, which can be attributed to residual contamination and a thin water layer that is present on most films. The contamination and water film contribute to an increase in the C 1s and O 1s signal, which in turn leads to a decrease of the N 1s signal.

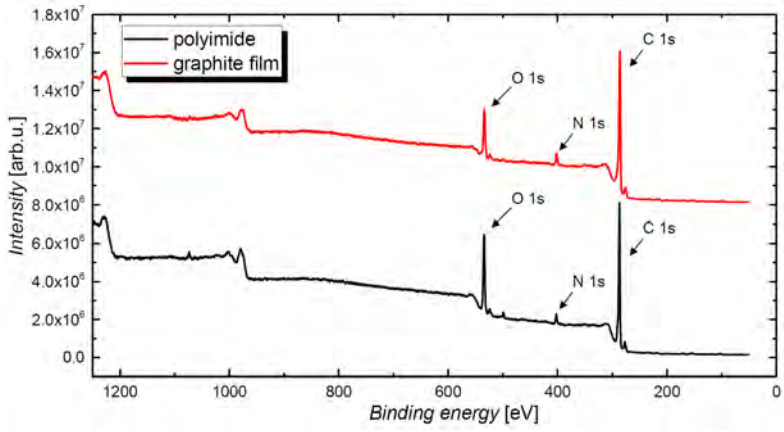

Figure V.11: XPS survey scan for polyimide Kapton® HN (DuPont™) substrate before (black) and after laser ablation (red). The relevant core-level peaks O 1s, N 1s and C 1s that are associated with oxygen, nitrogen, and carbon species are indicated by arrows.

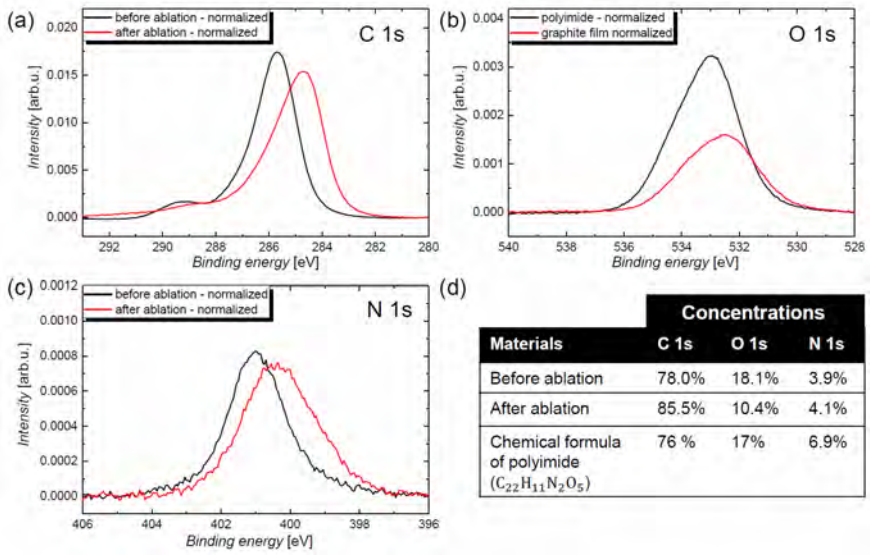

(d)

Materials	Concentrations C 1s	O 1s	N 1s
Before ablation	78.0%	18.1%	3.9%
After ablation	85.5%	10.4%	4.1%
Chemical formula of polyimide ($C_{22}H_{11}N_2O_5$)	76 %	17%	6.9%

Figure V.12: High-resolution XPS spectra for the (a) C 1s, (b) O 1s and (c) N 1s peaks before (black) and after laser ablation (red). (d) Table that summarizes the concentrations for carbon, oxygen and the nitrogen-related specimen in the polyimide sample: *i)* before, *ii)* after ablation and *iii)* expected values in accordance with the chemical formula.

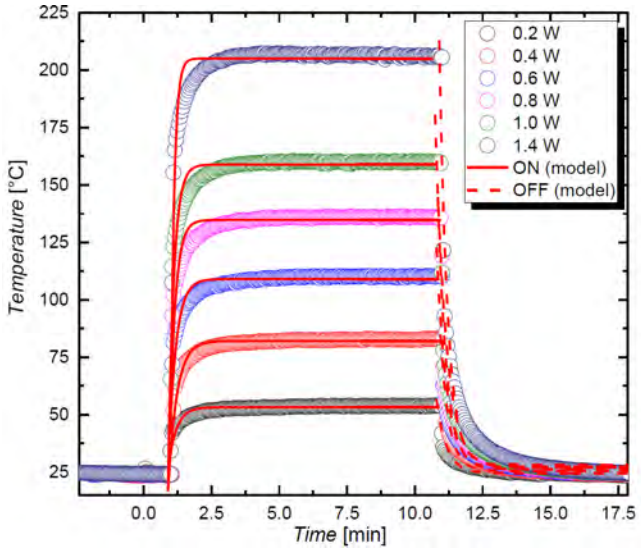

Figure V.13: Transient thermal temperature responses of the LIG heater shown in Figure V.5 (a). In agreement with the Eqs. V.4 and V.4, the analytical expressions of the temperature-time dependence for the ON (bold red line) and the OFF (dashed red line) states were fitted to the experimental data.

Contributions	Polyimide	LIG Film
C-C sp^2 (284.6 eV)	0%	56.6%
C-C sp^3 (285.6 eV)	71.9%	24%
C-O (286.6 eV)	7.6%	7.2%
O-C-O (287.6 eV)	13.4%	4%
O-C=O (289 eV)	7.1%	5.8%
$\pi - \pi^*$ (291 eV)	0%	2.4%

Table V.1: Summary for the different contributions of the deconvoluted C 1s raw spectra.

Estimation of the LIG heater costs. The commercial polyimide heater was purchased from conrad.de (order number: 1594183 - 62) for 20.38 euros. The price for the polyimide foil purchased from shyde.com is around 0.014 euros/cm^2, whereas the CNC unit costs 160 euros. The power consumption can be neglected for a cost estimate. Considering an area of 35 cm^2 for the heaters the fabrication of a total of 10.000 units, the price per heater can be estimated to be 0.65 euros, which is around a factor of 31 lowered than the price for the commercial heater.

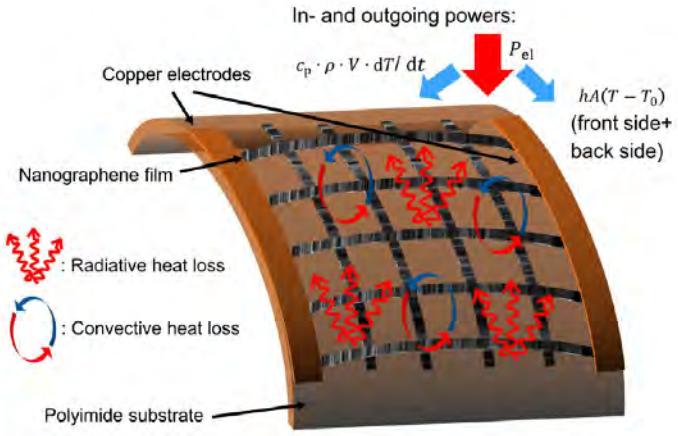

Figure V.14: Schematic of the LIG heater that shows the structure as well as the heat losses composed of radiative and convective losses. The in- and outgoing powers are indicated by the red arrow and the blue arrows, respectively, in agreement with Eq. V.3.

Paper VI

Inexpensive Graphene Oxide Heaters Lithographed by Laser

Francisco J. Romero [1,2,*], Almudena Rivadeneyra [1,2], Inmaculada Ortiz-Gomez [3], Alfonso Salinas-Castillo [3], Andres Godoy [1,2], Diego P. Morales [2,4], Noel Rodriguez [1,2,*]

[1] Pervasive Electronics Advanced Research Laboratory, University of Granada, 18071 Granada, Spain.
[2] Department of Electronics and Computer Technology, University of Granada, 18071 Granada, Spain.
[3] Department of Analytical Chemistry, University of Granada, 18071 Granada, Spain.
[4] Biochemistry and Electronics as Sensing Technologies Group, University of Granada, 18071 Granada, Spain
* Corresponding authors: franromero@ugr.es (F.J.R.) and noel@ugr.es (N.R.)

VI

Published in *Nanomaterials*, Aug 2019, volume 9(9), 1184. DOI: 10.3390/nano9091184. Impact Factor: 4.324. JCR Rank: 42/103 (Q2) in *Nanoscience & Nanotechnology* and 89/314 (Q1) in *Materials Science, Multidisciplinary*.

Abstract

In this paper, we present a simple and inexpensive method for the fabrication of high-performance graphene-based heaters on different large-scale substrates through the laser photothermal reduction of graphene oxide (laser-reduced graphene-oxide, LrGO). This method allows an efficient and localized high level of reduction and therefore a good electrical conductivity of the treated films. The performance of the heaters is studied in terms of steady-state temperature, power consumption, and time response for different substrates and sizes. The results show that the LrGO heaters can achieve stable steady-state temperatures higher than 200 °C when a voltage of 15 V is applied, featuring a time constant of around 4 s and a heat transfer coefficient of ∼200 °C cm^2/W. These characteristics are compared with other technologies in this field, demonstrating that the fabrication approach described in this work is competitive and promising to fabricate large-scale flexible heaters with a very fast response and high steady-state temperatures in a cost-effective way. This technology can be easily combined with other fabrication methods, such as screen printing

or spray-deposition, for the manufacturing of complete sensing systems where the temperature control is required to adjust functionalities or to tune sensitivity or selectivity.

Keywords: flexible electronics, graphene oxide, heater, laser-scribing, thermal response

VI.1 Introduction

In recent years, heaters have attracted a growing interest because of the emergence of a broad spectrum of newly integrated sensing technologies, such as gas sensors or biosensors [1]–[3], which require a certain constant temperature or a programmable sequence of temperatures to operate or to achieve a proper performance [4], [5]. In this regard, heaters are expected to play a notable role in the ubiquitous sensing of environmental and biological parameters. However, the major challenges facing their widespread use are related to the demanding requirements of this kind of application since, apart from the response, the recovery time, and the stability properties, these applications also require flexibility, lightness, low cost, transparency, or biocompatibility [6], [7].

In this context, graphene and graphene related materials have attracted the attention of many researchers as an alternative to the conventional expensive indium tin oxide (ITO) heaters due to their outstanding electrochemical, mechanical, and optical properties [8]. Thus, different approaches for the fabrication of graphene-based heaters can be found in the literature. One of the most commonly used is based on the bottom-up production of graphene by the chemical vapor deposition (CVD) process, as presented by Kang *et al.* [9]. However, this approach suffers from large sheet resistance and therefore requires chemical doping and multiple transfer processes to be applied in large-scale manufacturing. To tackle this issue, other authors such as Lin *et al.* and Kang *et al.* [10], [11] make use of hybrid structures of silver particles mixed with graphene, reducing the sheet resistance and increasing both steady-state temperature and response time. However, although some of these approaches report an adequate performance, the drawbacks of a complex fabrications process, slow thermal response, or high-power consumption limit their integration in end-user applications. For these reasons, a cost-effective and scalable process for the manufacturing of graphene-based heaters is still being sought.

In this work, we present a methodology for the fabrication of high-performance laser-reduced graphene-oxide (LrGO) heaters, which can be applied on different substrates (flexible or not). The laser reduction of GO [12], [13], aiming to increase its conductivity, offers several advantages over other reduction processes, such as chemical or thermal ones [14]: *i)* it does not require chemicals reagents to produce the reduction, making it an environmentally friendly technique, *ii)* it allows the lithography of high-resolution patterns of reduced graphene oxide without the need for masks [15], therefore offering a simpler and more economical

process, and *iii)* it also allows a surface-localized treatment of the GO without affecting the substrate, which increases its versatility, extending the range of suitable supporting materials [16].

SEM, Raman spectroscopy, as well as X-ray photoelectron spectroscopy (XPS) were used to study the quality of the synthesized material, and the electrothermal experiments show promising results in terms of power consumption, response time, and steady-state temperature when compared with other existing technologies. Thus, this fabrication approach paves the way to an extremely simple, inexpensive and eco-friendly fabrication of graphene-based heaters. The paper is structured as follows. The fabrication of the LrGO heaters is described in Section VI.2 along with the materials and the characterization setups used. Section VI.3 presents structural, electrical, and thermal characterization of the LrGO heaters, comparing their key features with other approaches in the literature. Finally, the main conclusions are outlined in Section VI.4.

VI.2 Materials and Methods

VI.2.1 Fabrication of the rGO Films

The samples were fabricated using an in-house prepared GO colloid, GOc, (4 mg/mL) following a modified version of the Hummers and Offerman's method; further details on the GOc synthesis path can be found in [17]. The GOc was deposited at a concentration of $\sim$150 μL/cm^2 on two different outstanding thermal insulators, Kapton® HN polyimide films with a thickness of 125 μm (from DuPont™, Constantine, MI, USA) and mica sheets with a thickness of $\sim$1.5 mm (model HP5M5-1 from ZT Mica, Hubei, China). After drying the deposited GO for at least 24 h at ambient temperature (relative humidity 50%), the resulting $\sim$50 μm layer of GO was photothermally reduced using a CO_2 laser engraving machine (8015 Rayjet-50, Trotec Laser, S.L.U., Barcelona, Spain). The laser-assisted reduction was demonstrated as a fast and scalable approach to obtain conductive patterns of laser reduced graphene-oxide (LrGO) with different lithographic patterns avoiding the use of chemicals or masks [15], [18], [19]. For the fabrication of the LrGO film, a laser power of $\sim$5 W (wavelength: 10.6 μm) was applied at an engraving speed of 300 mm/s, aiming to get low sheet resistance values ($\sim$200 Ω/sq.). The laser fluence applied on the GO was high enough to achieve a high level of reduction of the samples, ensuring the absence of resistive switching effects that appear when GO is partially reduced [20]. Furthermore, this combination of laser power and engraving speed ensured the integrity of the substrates during the photothermal reduction process. Once the surface of the GO was reduced, electrical access to the heater was achieved by means of an Ag-loaded conductive paint (from RS, Corby, UK) mask-coated on its opposed edges. A schematic representation of the resulting devices is shown in Figure VI.1a.

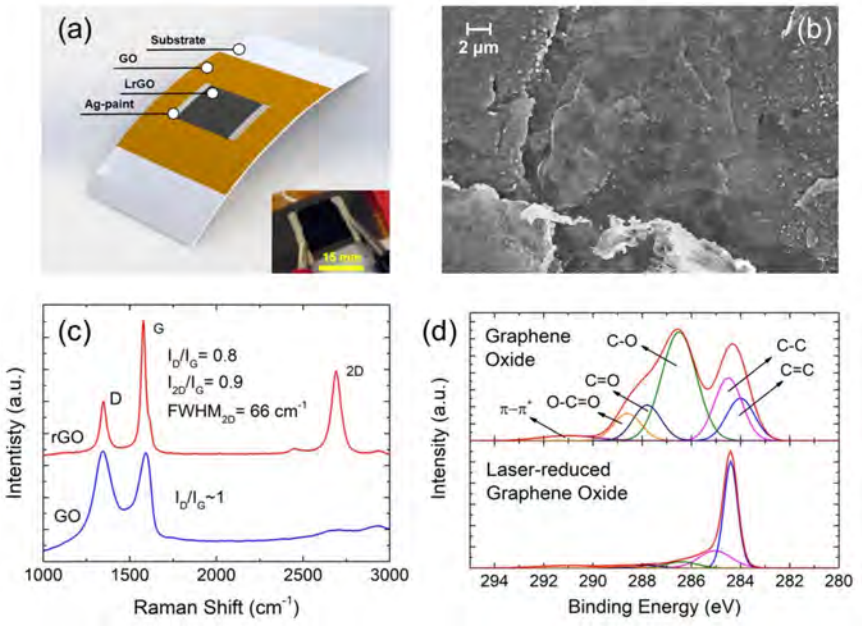

Figure VI.1: (a) Schematic diagram of the laser-reduced graphene-oxide (LrGO) heaters. Inset shows an actual picture of one of the LrGO heater (scale bar: 15 mm). (b), SEM image of a laser-reduced graphene oxide sheet [20]. (c) Raman spectra of both graphene oxide and laser-reduced graphene oxide. (d) X-ray photoelectron spectroscopy (XPS) high-resolution C 1 s peak of the graphene oxide before [20] and after the laser-reduction.

VI.2.2 Structural Characterization

SEM images were recorded with an NVision 40 field-emission scanning electron microscope (from Carl Zeiss, Oberkochen, Germany) at an extraction and acceleration voltage of 5 kV. Raman spectra were acquired with a JASCO 108 NRS-5100 dispersive micro-Raman spectrometer (from JASCO, Inc., Tokio, Japan) with an excitation wavelength of $\lambda = 532$ nm. XPS measurements were performed at a base pressure of 10^{-10} Torr with an Al Kα (hν = 1486.6 eV) excitation at an operating power of 450 W using an Axis Ultra-DLD spectrometer (from Kratos Analytical Ltd., Manchester, UK).

VI.2.3 Transient Electrical and Thermal Characterization

The electrical and the power measurements were performed using a software-controlled low-noise power source (B2962A from Keysight, Santa Rosa, CA USA), while the temperature of the films was recorded using the Fluke TiS75 infrared camera at a sampling rate of 9 Hz and later processed with the SmartView 4.3

software (both from Fluke Corporation, Everett, WA, USA).

VI.3 Results and Discussion

VI.3.1 Structural Properties

The SEM image displayed in Figure VI.1b corresponds to an LrGO sheet [20]. The rGO showed a platelet-like crystalline structure as a result of the partial crystalline restoration of the graphene framework, as was already reported for the LrGO [21], [22] as well as for the reduction of GO by stirring in hot water [23] and by chemical methods [24]. However, the two main challenges in the reduction of graphene oxide were reducing the agglomerated layers in the crystallographic structure and increasing the C/O ratio. Hereafter, we analyzed the quality of the LrGO sheets synthesized in this work.

On the one hand, the crystallographic quality of the samples could be analyzed with the aid of Raman spectroscopy. As can be observed in Figure VI.1c, before the laser treatment, the Raman spectra of the GO was composed of two broad peaks, which corresponded to the D ($\sim$1345 cm^{-1}) and the G peaks ($\sim$1580 cm^{-1}) typically present in graphitic materials. The ratio of these peaks (I_D/I_G) was associated with the number of defects in the crystalline lattice structure of graphene, which increased as the number of defects did. Therefore, based on the Raman spectra of the GO, it was clear that its structure was mainly composed of highly defect-containing graphene flakes as a result of the hydroxyl and the epoxy groups introduced by the oxidization process [25].

Once the GO was laser-reduced, it could be observed how the G peak became higher and narrower than the D peak, which meant a restoration, at least partially, of the hexagonal honeycomb crystal lattice of graphene and the change of carbon atoms from sp^3 to sp^2 hybridization [26]. This fact was also supported by the emergence of the 2D peak at $\sim$2700 cm^{-1}, whose intensity and shape were not only correlated with the number of defects but also with the number of layers of the graphene-based structure [26]. In this case, the intensity and the full width at half maximum of the 2D band relative to the G band indicated that the LrGO obtained was comparable to the few-layered graphene obtained by chemical vapor deposition (CVD) [27].

The chemical alterations induced by the laser photothermal process were also studied by XPS. As was expected, the laser reduction led to a dramatic change in the original carbon–oxygen compounds of the GO layer [28], [29]. Thus, the initial carbon atomic content of $\sim$52% increased up to 90% after the laser reduction process, whereas the oxygen presented a decrease from $\sim$45% before the photothermal process to $\sim$6% after, meaning an increase from $\sim$1 to $\sim$15 of the atomic carbon to oxygen ratio (C/O). This demonstrated that the laser photothermal process was suitable for the production of highly reduced graphene oxide (HRG) with a C/O ratio higher than that presented by other chemical methods [30], [31].

A better understanding of the nature of these changes could be obtained by means of the analysis of high-resolution C 1 s spectra before and after the

laser treatment, whose results are depicted in Figure VI.1d. As can be seen, the laser photothermal process was able to remove most of the oxygen-containing functional groups (hydroxyl, epoxy, and carbonyl) presented as defects in the raw material and turn the hybridization of the carbon domains from sp^3 to sp^2. In addition, these results also indicated that the level of reduction obtained was higher than that obtained for other kinds of lasers that work at lower powers [20]. Therefore, these experiments, together with the Raman results, confirmed the proper reduction of the GO.

VI.3.2 Electrical and Thermal Properties

The electrical properties of the LrGO heaters were studied for different dimensions (150 mm^2, 400 mm^2, and 600 mm^2) using both Kapton® HNand mica as supporting substrates. As presented in Figure VI.2a, the heaters exhibited a linear relationship between voltage and current, indicating a good ohmic behavior in all cases. Note that the different slopes of the samples were associated with the different aspect ratios and the contact resistances ($R_T = \rho_s L/W + 2R_c$). Both sheet resistance (ρ_s) and contact resistance (R_c) were obtained by means of the transmission line model (TLM) [32], whose results for the 150 mm^2 heater are depicted in Figure VI.2b. In this way, we obtained a sheet resistance of around 200 Ω/sq. and a residual contact resistance (R_c) of ∼25 Ω with no dependence on the substrate, which demonstrated a proper tuning of the laser parameters. This demonstrated that an only-laser fabricated LrGO heater could achieve results comparable to those reported for Ag-doped LrGO (158.7 Ω/sq.) [10] and electrochemically exfoliated graphite (159.0 Ω/sq.) [33] in terms of sheet resistance.

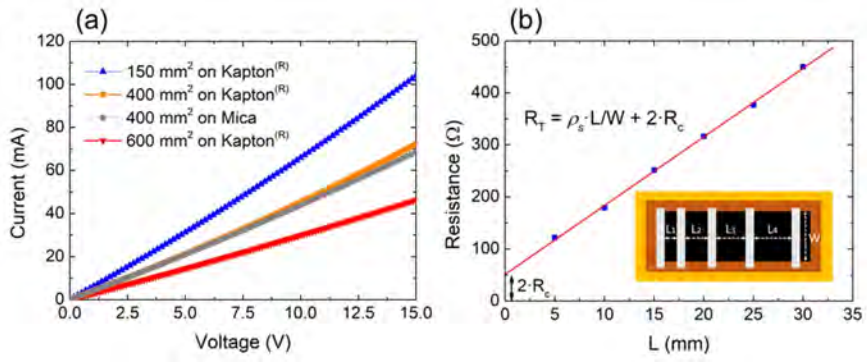

Figure VI.2: (a) Current–voltage (I–V) curves for different LrGO films on flexible substrates: 150 mm^2 (L = 10 mm, W = 15 mm), 400 mm^2 (L = 20 mm, W = 20 mm), 600 mm^2 (L = 30 mm, W = 20 mm). (b) Total resistance (R_T) as a function of the distance between consecutive contacts (L_i) and its relationship with sheet resistance (ρ_s), contact resistance (R_c), and dimensions (L, W).

The time dependence of the electrothermal characteristics of the heaters was also studied at different operation voltages in ambient conditions. For that purpose, we applied different voltage steps (up to 15 V) starting at 10 s and monitoring both current and temperature over time. The results obtained for a rectangular heater with an area of 150 mm^2 are depicted in Figure VI.3. Thus, as can be observed in Figure VI.3a, once the step was applied, the temperature on the surface of the heater started to increase exponentially until reaching a steady-state situation. Besides, the higher the voltage applied to the heater was, the higher the final temperature was, as shown in Figure VI.3b. It is worth mentioning that the parabolicity of the pattern in this figure was interrupted at the higher voltage since radiative losses could be estimated in 0.032 W/cm^2 (>5%) at this temperature according to Stefan–Boltzmann law ($P/A \sim \sigma T4$, with $\sigma = 5.67 \times 10^{-8}$ W/m^2K^4). The relationship between the steady-state temperature and the voltage applied defined the performance of the heaters in terms of transduction of electrical energy into joule heating [11]. Thus, in this case, the heaters presented steady-state temperature of ∼215 ^oC when a voltage of 15 V was applied, demonstrating higher transduction efficiency than those reported by several works in literature, e.g., for electrochemically exfoliated graphene (139 ^oC at 30 V) [33], multi-walled carbon nanotubes (MWCNTs) (65 ^oC at 12 V) [34], or doped graphene (97 ^oC at 12 V) [9], among others.

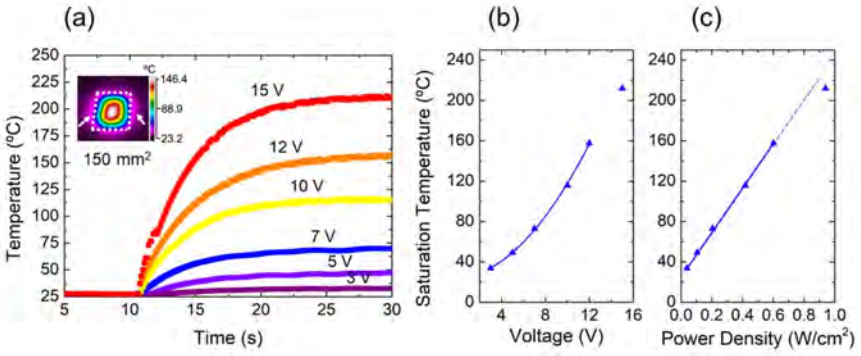

Figure VI.3: Temperature profiles of a 150 mm2 LrGO-based heater on Kapton®. (a) Time dependent characteristic of the heater. Inset shows a thermal image of the LrGO heater (arrows indicate the contacting sides). (b) Saturation temperature as a function of the voltage applied. (c) Saturation temperature as a function of the input power density.

It is also interesting to study the performance of the heaters in terms of power density (W/cm^2) since this factor has special relevance in low-power and portable applications. For that, we analyzed the saturation temperature as a function of the LrGO area of the different heaters considered in this work. In all cases, this characteristic showed an almost linear behavior, as illustrated in Figure VI.3c for the 150 mm^2 heater on Kapton® HN (with the exception

of the last point of the series due to the aforementioned radiative losses) and in Figure VI.4a for two heaters of 400 mm^2 on both mica and Kapton® HN substrates. The heat transfer coefficients obtained were in the range 200–440 ^oC cm^2/W, increasing with the sample area. This meant that the LrGO heaters required less power to achieve the same temperature than those reported for other materials such as laser-induced graphene (131 ^oC cm^2/W) [35] or silver nanowires (134–179 ^oC cm^2/W) [36], [37]. It was also demonstrated that this parameter not only depended on the heat capacity of the conducting film itself but also on the substrate type, as shown in Figure VI.4a. This figure depicts the values of the saturation temperature as functions of the power density of two heaters with the same characteristics in terms of dimension (L = W, L × W = 400 mm^2) and resistivity (∼238 Ω) but on different substrates. It can be noted that the thermal insulation of the heaters on mica (373 ^oC cm^2/W) was higher than that obtained on the Kapton® substrate (311 ^oC cm^2/W). This difference could be attributed to the greater roughness of the mica surface, which stunted the heat losses by means of the air gaps between its surface and the GO deposited layer [38].

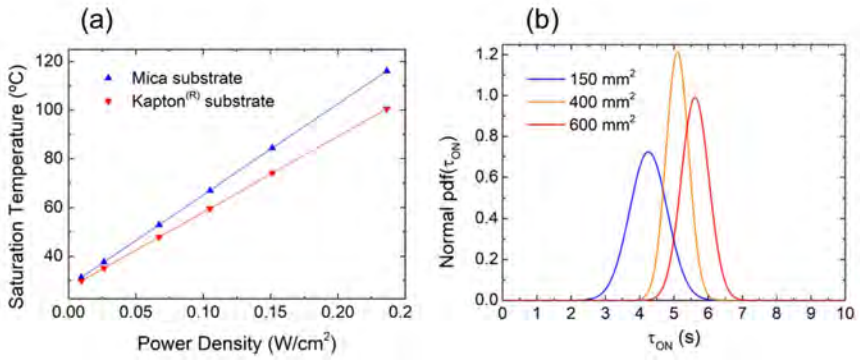

Figure VI.4: (a) Saturation temperature as a function of the input power density for two equal 400 mm^2 LrGO heaters on two different substrates. (b) Probability density function of the response time for different heaters on Kapton®.

Moreover, together with steady-state temperature, operating voltage, and power consumption, the transient thermal characteristic of the heaters is also important since many applications are subjected to strict requirements of response time, as in the case of many gas sensors [39], [40]. Thus, we examined the thermal response of the heaters for different sizes and steady temperatures by means of their time constant, τ, defined as the time required by the heater to increase their temperature to 63% of the total variation [41]. Figure VI.4b shows the probability density function of the time constant obtained from the LrGO on Kapton® heaters by applying increasing voltages up to 15 V (as shown in Figure VI.3a). There are many factors that influence the response time of a heater. It was demonstrated that the heating size had an effect on the time constant

as well as the heat transfer coefficient (which increased with the sample area), the length to width ratio, the sheet resistance, the substrate material, and the substrate thickness [37], [38], [42]. Figure VI.4b shows how the time constant of the LrGO heaters increased from ∼4.3 s to ∼5.7 s when increasing the surface area. In this case, the increment on the response time could be attributed to the increase in both the size and heat transfer coefficients, as reported by Liu *et al.* for their CNT-based heaters [42]. In any case, this range of response time was also very promising when compared with other large-area heaters from the literature, such as the ones presented by Bobinger *et al.* [35] and Vertuccio *et al.*. [43].

Furthermore, when the time constant is studied, many authors consider the heater resistance to be invariable, neglecting the effect of its drift with time. However, this is not necessarily true since two effects may appear with different relevance. On one side, the heating material can present a thermistive effect responsible for relatively fast changes on the conductivity [17]; on the other side (but with more impact, especially when working at high temperatures [37], [44]), the joule annealing in the LrGO film can cause a lowering of the resistance [45] through the modification of the functional groups of the GO in a similar way as the laser reduces the samples. As shown in Figure VI.5, whereas the heater resistance could be considered constant when fixed voltages of either 10 V or 15 V were applied between its terminals; for an input bias of 20 V, it decreased slowly (as compared with the heater time constant). This variation of the resistance influenced the transient response of the heaters, which explained the variability of the time constants when they were subjected to a high thermal stress. Hence, the time constant obtained for the smallest heater, which was the one that reached the higher temperature for the lower input power, presented greater variability than the ones of the bigger samples, as previously reported by Ji *et al.* and Rao *et al.* for their silver nanowire/PEDOT: PSS film haters [37] and Au wire networks-based heaters [44], respectively. Although this fact may pose a drawback for certain applications demanding high heating needs, the power required for the appearance of joule annealing drift on the samples was estimated to be above 1.5 W, which was much higher than that normally required for these kinds of technologies and applications.

Further, we also analyzed the electromechanical stability of the heaters on Kapton® substrate by monitoring the temperature for different conditions of bending. In this way, Figure VI.6 shows the relative variation of temperature $[\Delta T/T_0\ (\%)]$ for a 150 mm^2 heater during 5 min (300 s) of bending with a bending radius and a frequency of 10 mm and 0.5 Hz (150 cycles in total), respectively. The driving voltage was set to 12.5 V to achieve a steady temperature of 145 ^oC, according to the electrothermal experiments shown in Figure VI.3 on a rectangular 150 mm^2 heater. Under these conditions, the maximum changes in temperature reported were below 10 ^oC, resulting in a relative variation of temperature under 10%, following the periodic bending of the substrate (as shown in the inset of Figure VI.6). These results demonstrated good stability under bending since, under these conditions and for an interval of 150 s (even under mechanical stress), the output temperature remained consistent.

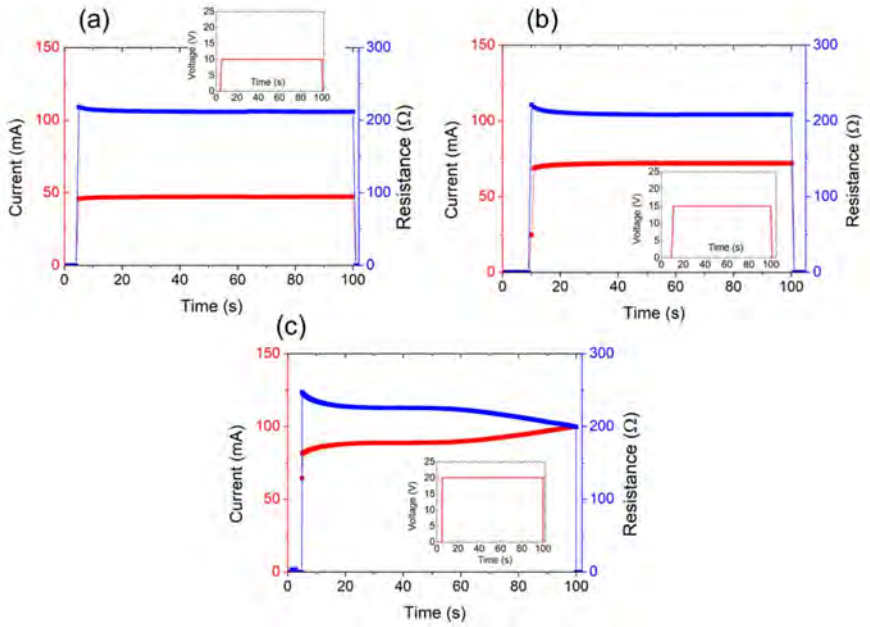

Figure VI.5: Resistance (blue) and current (red) over time of an LrGO-based heater for different step voltages of 10 V (a), 15 V (b), and 20 V (c).

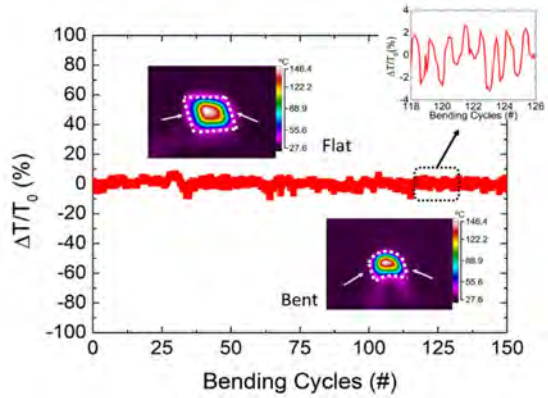

Figure VI.6: Relative change in temperature with respect to the theoretical steady-state temperature for a driving voltage of 12.5 V while bending. The heater (area: 150 mm^2) was bent to a minimum diameter of 10 mm at a bending frequency of 0.5 Hz over 150 cycles (300 s). Insets show the infrared images of both flat and bent states (arrows indicate the contacting sides).

VI.4 Conclusions

Laser-reduced graphene-oxide was studied as a heating element for the fabrication of flexible heaters. We presented a comprehensive study covering aspects from the production and the characterization of the raw material to the electrical and the thermal characterization of LrGO films operating as heaters for different sizes and substrates. The laser photothermal treatment was demonstrated as a fast and simple procedure to obtain conductive patterns of highly reduced graphene-oxide on flexible substrates with a competitive sheet resistance of $\sim$200 Ω/sq. The self-heating effect of the LrGO films when voltage was applied between their terminals was studied in terms of steady-state temperature, transient response, power consumption, and size. The results illustrated that the saturation temperature depended linearly on the input power density, reporting heat transfer coefficients in the range 200–440 ^{o}C cm^2/W. It was also demonstrated that, while the electrical conductivity did not depend on the properties of the substrate, the heat transfer coefficient did, reporting a variation of 62 ^{o}C cm^2/W from the Kapton® substrate to the mica one. The response time for the different steady-state temperatures and sizes was also analyzed, as well as its dependence on the heater area and the resistance variation. Finally, bending experiments demonstrated the stability and the consistency of the heaters when they were operating under mechanical stress. The authors believe that this technology is a big step forward in the cost-effective fabrication of high-performance heaters on large flexible substrates, which could be expanded to multiple ubiquitous applications.

Acknowledgements. This work has been supported by the Spanish Ministry of Education, Culture and Sport (MECD)/FEDER-EU through the project TEC2017-89955-P and the predoctoral grant FPU16/01451; by the European Commission through the fellowship H2020-MSCA-IF-2017-794885-SELFSENS and by Iberdrola Foundation under its 2018 Research Grant Program.

References

[1] Falco, A., Rivadeneyra, A., Loghin, F. C., Salmeron, J. F., Lugli, P., and Abdelhalim, A., "Towards low-power electronics: Self-recovering and flexible gas sensors," *Journal of Materials Chemistry A*, vol. 6, no. 16, pp. 7107–7113, 2018.

[2] Choi, H., Choi, J. S., Kim, J.-S., Choe, J.-H., Chung, K. H., Shin, J.-W., Kim, J. T., Youn, D.-H., Kim, K.-C., Lee, J.-I., Choi, S.-Y., Kim, P., Choi, C.-G., and Yu, Y.-J., "Flexible and transparent gas molecule sensor integrated with sensing and heating graphene layers," *Small*, vol. 10, no. 18, pp. 3685–3691, May 2014.

[3] Biscotti, A., Lazzarini, R., Virgilli, G., Ngatcha, F., Valisi, A., and Rossi, M., "Optimizing a portable biosensor system for bacterial detection in

milk based mix for ice cream," *Sensing and Bio-Sensing Research*, vol. 18, pp. 1–6, Apr. 2018.

[4] Tabraue-Chávez, M., Luque-González, M. A., Marin-Romero, A., Sánchez-Martin, R. M., Escobedo-Araque, P., Pernagallo, S., and Diaz-Mochón, J. J., "A colorimetric strategy based on dynamic chemistry for direct detection of trypanosomatid species," *Scientific Reports*, vol. 9, no. 1, Mar. 2019.

[5] Abdelhalim, A., Winkler, M., Loghin, F., Zeiser, C., Lugli, P., and Abdellah, A., "Highly sensitive and selective carbon nanotube-based gas sensor arrays functionalized with different metallic nanoparticles," *Sensors and Actuators B: Chemical*, vol. 220, pp. 1288–1296, Dec. 2015.

[6] Claramunt, S., Monereo, O., Boix, M., Leghrib, R., Prades, J., Cornet, A., Merino, P., Merino, C., and Cirera, A., "Flexible gas sensor array with an embedded heater based on metal decorated carbon nanofibres," *Sensors and Actuators B: Chemical*, vol. 187, pp. 401–406, Oct. 2013.

[7] Wu, X., Ma, Y., Zhang, G., Chu, Y., Du, J., Zhang, Y., Li, Z., Duan, Y., Fan, Z., and Huang, J., "Thermally stable, biocompatible, and flexible organic field-effect transistors and their application in temperature sensing arrays for artificial skin," *Advanced Functional Materials*, vol. 25, no. 14, pp. 2138–2146, Feb. 2015.

[8] Arvidsson, R., Kushnir, D., Molander, S., and Sandén, B. A., "Energy and resource use assessment of graphene as a substitute for indium tin oxide in transparent electrodes," *Journal of Cleaner Production*, vol. 132, pp. 289–297, Sep. 2016.

[9] Kang, J., Kim, H., Kim, K. S., Lee, S.-K., Bae, S., Ahn, J.-H., Kim, Y.-J., Choi, J.-B., and Hong, B. H., "High-performance graphene-based transparent flexible heaters," *Nano Letters*, vol. 11, no. 12, pp. 5154–5158, Dec. 2011.

[10] Lin, S.-Y., Zhang, T.-Y., Lu, Q., Wang, D.-Y., Yang, Y., Wu, X.-M., and Ren, T.-L., "High-performance graphene-based flexible heater for wearable applications," *RSC Advances*, vol. 7, no. 43, pp. 27 001–27 006, 2017.

[11] Kang, J., Jang, Y., Kim, Y., Cho, S.-H., Suhr, J., Hong, B. H., Choi, J.-B., and Byun, D., "An ag-grid/graphene hybrid structure for large-scale, transparent, flexible heaters," *Nanoscale*, vol. 7, no. 15, pp. 6567–6573, 2015.

[12] El-Kady, M. F., Strong, V., Dubin, S., and Kaner, R. B., "Laser scribing of high-performance and flexible graphene-based electrochemical capacitors," *Science*, vol. 335, no. 6074, pp. 1326–1330, Mar. 2012.

[13] Marquez, C., Rodriguez, N., Ruiz, R., and Gamiz, F., "Electrical characterization and conductivity optimization of laser reduced graphene oxide on insulator using point-contact methods," *RSC Advances*, vol. 6, no. 52, pp. 46 231–46 237, 2016.

[14] Pei, S. and Cheng, H.-M., "The reduction of graphene oxide," *Carbon*, vol. 50, no. 9, pp. 3210–3228, Aug. 2012.

[15] Wan, Z., Streed, E. W., Lobino, M., Wang, S., Sang, R. T., Cole, I. S., Thiel, D. V., and Li, Q., "Laser-reduced graphene: Synthesis, properties, and applications," *Advanced Materials Technologies*, vol. 3, no. 4, p. 1 700 315, Feb. 2018.

[16] Kymakis, E., Petridis, C., Anthopoulos, T. D., and Stratakis, E., "Laser-assisted reduction of graphene oxide for flexible, large-area optoelectronics," *IEEE Journal of Selected Topics in Quantum Electronics*, vol. 20, no. 1, pp. 106–115, Jan. 2014.

[17] Romero, F. J., Rivadeneyra, A., Toral, V., Castillo, E., Garcia-Ruiz, F., Morales, D. P., and Rodriguez, N., "Design guidelines of laser reduced graphene oxide conformal thermistor for IoT applications," *Sensors and Actuators A: Physical*, vol. 274, pp. 148–154, May 2018.

[18] Bhattacharjya, D., Kim, C.-H., Kim, J.-H., You, I.-K., In, J. B., and Lee, S.-M., "Fast and controllable reduction of graphene oxide by low-cost CO2 laser for supercapacitor application," *Applied Surface Science*, vol. 462, pp. 353–361, Dec. 2018.

[19] Gao, W., Singh, N., Song, L., Liu, Z., Reddy, A. L. M., Ci, L., Vajtai, R., Zhang, Q., Wei, B., and Ajayan, P. M., "Direct laser writing of micro-supercapacitors on hydrated graphite oxide films," *Nature Nanotechnology*, vol. 6, no. 8, pp. 496–500, Jul. 2011.

[20] Romero, Toral-Lopez, Ohata, Morales, Ruiz, Godoy, and Rodriguez, "Laser-fabricated reduced graphene oxide memristors," *Nanomaterials*, vol. 9, no. 6, p. 897, Jun. 2019.

[21] Longo, A., Verucchi, R., Aversa, L., Tatti, R., Ambrosio, A., Orabona, E., Coscia, U., Carotenuto, G., and Maddalena, P., "Graphene oxide prepared by graphene nanoplatelets and reduced by laser treatment," *Nanotechnology*, vol. 28, no. 22, p. 224 002, May 2017.

[22] Ghoniem, E., Mori, S., and Abdel-Moniem, A., "Low-cost flexible supercapacitors based on laser reduced graphene oxide supported on polyethylene terephthalate substrate," *Journal of Power Sources*, vol. 324, pp. 272–281, Aug. 2016.

[23] Loryuenyong, V., Totepvimarn, K., Eimburanapravat, P., Boonchompoo, W., and Buasri, A., "Preparation and characterization of reduced graphene oxide sheets via water-based exfoliation and reduction methods," *Advances in Materials Science and Engineering*, vol. 2013, pp. 1–5, 2013.

[24] Pham, V. H., Pham, H. D., Dang, T. T., Hur, S. H., Kim, E. J., Kong, B. S., Kim, S., and Chung, J. S., "Chemical reduction of an aqueous suspension of graphene oxide by nascent hydrogen," *Journal of Materials Chemistry*, vol. 22, no. 21, p. 10 530, 2012.

[25] Sahoo, S., Khurana, G., Barik, S. K., Dussan, S., Barrionuevo, D., and Katiyar, R. S., "In situ raman studies of electrically reduced graphene oxide and its field-emission properties," *The Journal of Physical Chemistry C*, vol. 117, no. 10, pp. 5485–5491, Mar. 2013.

[26] Wu, J.-B., Lin, M.-L., Cong, X., Liu, H.-N., and Tan, P.-H., "Raman spectroscopy of graphene-based materials and its applications in related devices," *Chemical Society Reviews*, vol. 47, no. 5, pp. 1822–1873, 2018.

[27] Gautam, M., Shi, Z., and Jayatissa, A. H., "Graphene films as transparent electrodes for photovoltaic devices based on cadmium sulfide thin films," *Solar Energy Materials and Solar Cells*, vol. 163, pp. 1–8, Apr. 2017.

[28] Wan, Z., Wang, S., Haylock, B., Kaur, J., Tanner, P., Thiel, D., Sang, R., Cole, I. S., Li, X., Lobino, M., and Li, Q., "Tuning the sub-processes in laser reduction of graphene oxide by adjusting the power and scanning speed of laser," *Carbon*, vol. 141, pp. 83–91, Jan. 2019.

[29] Romero, Toral-Lopez, Ohata, Morales, Ruiz, Godoy, and Rodriguez, "Laser-fabricated reduced graphene oxide memristors," *Nanomaterials*, vol. 9, no. 6, p. 897, Jun. 2019.

[30] Pei, S., Zhao, J., Du, J., Ren, W., and Cheng, H.-M., "Direct reduction of graphene oxide films into highly conductive and flexible graphene films by hydrohalic acids," *Carbon*, vol. 48, no. 15, pp. 4466–4474, Dec. 2010.

[31] Shin, H.-J., Kim, K. K., Benayad, A., Yoon, S.-M., Park, H. K., Jung, I.-S., Jin, M. H., Jeong, H.-K., Kim, J. M., Choi, J.-Y., and Lee, Y. H., "Efficient reduction of graphite oxide by sodium borohydride and its effect on electrical conductance," *Advanced Functional Materials*, vol. 19, no. 12, pp. 1987–1992, Jun. 2009.

[32] Romero, F., Salinas-Castillo, A., Rivadeneyra, A., Albrecht, A., Godoy, A., Morales, D., and Rodriguez, N., "In-depth study of laser diode ablation of kapton polyimide for flexible conductive substrates," *Nanomaterials*, vol. 8, no. 7, p. 517, Jul. 2018.

[33] Li, C., Xu, Y.-T., Zhao, B., Jiang, L., Chen, S.-G., Xu, J.-B., Fu, X.-Z., Sun, R., and Wong, C.-P., "Flexible graphene electrothermal films made from electrochemically exfoliated graphite," *Journal of Materials Science*, vol. 51, no. 2, pp. 1043–1051, Sep. 2015.

[34] Jang, H.-S., Jeon, S. K., and Nahm, S. H., "The manufacture of a transparent film heater by spinning multi-walled carbon nanotubes," *Carbon*, vol. 49, no. 1, pp. 111–116, Jan. 2011.

[35] Bobinger, M. R., Romero, F. J., Salinas-Castillo, A., Becherer, M., Lugli, P., Morales, D. P., Rodriguez, N., and Rivadeneyra, A., "Flexible and robust laser-induced graphene heaters photothermally scribed on bare polyimide substrates," *Carbon*, vol. 144, pp. 116–126, Apr. 2019.

[36] Zhang, X., Liu, M., Wang, B., Chen, H., and Wang, Z., "A wide measurement range and fast update rate integrated interface for capacitive sensors array," *IEEE Transactions on Circuits and Systems I: Regular Papers*, vol. 61, no. 1, pp. 2–11, Jan. 2014.

[37] Ji, S., He, W., Wang, K., Ran, Y., and Ye, C., "Thermal response of transparent silver nanowire/PEDOT:PSS film heaters," *Small*, vol. 10, no. 23, pp. 4951–4960, Jul. 2014.

[38] Gupta, R., Rao, K. D. M., Kiruthika, S., and Kulkarni, G. U., "Visibly transparent heaters," *ACS Applied Materials & Interfaces*, vol. 8, no. 20, pp. 12 559–12 575, May 2016.

[39] Hwang, W.-J., Shin, K.-S., Roh, J.-H., Lee, D.-S., and Choa, S.-H., "Development of micro-heaters with optimized temperature compensation design for gas sensors," *Sensors*, vol. 11, no. 3, pp. 2580–2591, Mar. 2011.

[40] Li, Y., Zhang, M., Long, S., Teng, J., Liu, Q., Lv, H., Miranda, E., Suñé, J., and Liu, M., "Investigation on the conductive filament growth dynamics in resistive switching memory via a universal monte carlo simulator," *Scientific Reports*, vol. 7, no. 1, Sep. 2017.

[41] Bae, J. J., Lim, S. C., Han, G. H., Jo, Y. W., Doung, D. L., Kim, E. S., Chae, S. J., Huy, T. Q., Luan, N. V., and Lee, Y. H., "Heat dissipation of transparent graphene defoggers," *Advanced Functional Materials*, vol. 22, no. 22, pp. 4819–4826, Jul. 2012.

[42] Liu, P., Liu, L., Jiang, K., and Fan, S., "Carbon-nanotube-film microheater on a polyethylene terephthalate substrate and its application in thermochromic displays," *Small*, vol. 7, no. 6, pp. 732–736, Feb. 2011.

[43] Vertuccio, L., Santis, F. D., Pantani, R., Lafdi, K., and Guadagno, L., "Effective de-icing skin using graphene-based flexible heater," *Composites Part B: Engineering*, vol. 162, pp. 600–610, Apr. 2019.

[44] Rao, K. D. M. and Kulkarni, G. U., "A highly crystalline single au wire network as a high temperature transparent heater," *Nanoscale*, vol. 6, no. 11, p. 5645, 2014.

[45] Rathi, S., Lee, I., Kang, M., Lim, D., Lee, Y., Yamacli, S., Joh, H.-I., Kim, S., Kim, S.-W., Yun, S. J., Choi, S., and Kim, G.-H., "Observation of negative differential resistance in mesoscopic graphene oxide devices," *Scientific Reports*, vol. 8, no. 1, May 2018.

Paper VII

Screen Printable Electrochemical Capacitors on Flexible Substrates

Francisco J. Romero [1,*], Diego P. Morales [1], Markus Becherer [2], Almudena Rivadeneyra [1], Noel Rodriguez [1]

[1] Department of Electronics and Computer Technology, University of Granada, 18071 Granada, Spain.
[2] Institute for Nanoelectronics, Technische Universität München, 80333, Munich, Germany.
* Corresponding author: franromero@ugr.es

Presented in *The Fifth International Conference on Advances in Sensors, Actuators, Metering and Sensing (ALLSENSORS 2020)*, Valencia, Spain, Nov 2020, pp. 3–7. ISBN: 978-1-61208-766-5.

VII

Abstract

This work presents a novel approach for the fabrication of Electrochemical Capacitors (ECs) based on the screen-printing of a commercial carbon-based conductive ink on flexible substrates. This technique enables the fast and cost-effective production of ECs with high flexibility and outstanding performance over bending states and voltage cycling, as demonstrated by means of cyclic voltammetry and galvanometric charge-discharge measurements. Despite the fact that the specific areal capacitances achieved are lower than the ones obtained using other carbon-based materials ($\sim$22 μF/cm^2), the results show that, as soon as new screen-printable carbon-based pastes become available, this fabrication method will enable the mass production of ECs that can be attached to any surface as a conformal patch, as it is being required by a large number of the emerging technological applications.

Keywords: Carbon, Conductive ink, Electrochemical Capacitor, Flexible Electronics, Screen-printing, Specific Sapacitance.

VII.1 Introduction

In recent years, flexible electronics has attracted the attention of many researches. This technology is expected to cause a disruption in the field of electronics devices, since it arises from the need to fulfill the demands required by novel technological applications, such as wearables or biomedical sensors, which cannot be addressed by means of the traditional silicon-based electronics [1]. Many of the advances in this context come with the emergence of new conductive and flexible materials. Examples of those are Carbon NanoTubes (CNTs) [2], graphene and its derivatives [3]–[5], or silver nanowires (AgNWs) and nanoparticles (AgNPs) [6], [7]. Additionally, alternative fabrication processes enabling the cost-effective processing of these materials on large flexible substrates are targeted. Those processes include printing technologies or laser treatment approaches, among others [8], [9].

Thus, the combination of these two emerging lines of research has resulted in the development of many flexible electronics devices, including sensors [10], [11], Radio Frequency Identification Tags (RFID) [12], [13] and antennas [14], [15]. Besides, apart from these latter, the flexible electronics progress is also requiring of flexible energy storage devices that, combined with energy harvesting technologies, contribute to the development of self-powered devices [16].

Numerous studies have been conducted to examine different materials as electrodes for the fabrication of flexible Electrochemical Capacitors (ECs). Among them, carbon-based materials are the preferred to play this role for several reasons: *i)* exceptionally high surface area, *ii)* relatively high electrical conductivity and *iii)* acceptable cost [17]. Examples of materials studied so far are Laser-Induced Graphene (LIG) [18], [19], reduced Graphene Oxide (rGO) [20] and single walled CNTs [21]. Many researchers agree that carbon-based electrodes will play an important role in the supercapacitor technology and that is why a big effort is being devoted to further optimizing its properties through doping [22] or surface treatments [23]. Besides, the performance of the electrochemical capacitors does not only rely on the material of the electrodes, but also on the electrolyte used. Therefore, it is also important to achieve a proper interaction electrode-electrolyte. Then, different acid/base/salt-Poly(Vinyl Alcohol) (PVA) gel electrolytes have been widely studied for this purpose, being the PVA/phosphoric acid (PVA/H_3PO_4) and the PVA/sulfuric acid (PVA/H_2SO_4) the ones which report the best performance [24], [25].

In this contribution, we present a novel approach for the fabrication of flexible ECs based on the screen-printing of a commercial carbon-based electrically conductive ink using PVA/H_3PO_4 as electrolyte. We have opted for a 2D structure which consists of several InterDigital Electrodes (IDEs) arranged on a flexible substrate, since this configuration offers some advantages over the conventional designs, such as lower thicknesses and smaller distances between electrodes [16]. This paper is organized as follows. Section VII.2 describes the materials and methods used. Section VII.3 presents the performance of the presented ECs and, finally, Section VII.4 addresses the main conclusions.

VII.2 Materials and Methods

VII.2.1 Materials

Transparent polyester films for water-based inks with a thickness of 160 μm (from ColorGATE Digital Output Solutions GmbH, Hannover, Germany) were used as a flexible substrate for the fabrication of the capacitors. The screen-printing carbon-based paste used in this work, product name: C-220, was provided by Applied Ink Solutions (Westborough, MA, USA). Both Poly(vinyl alcohol) (PVA, Mw 31,000-50,000, 98-99% hydrolyzed) and phosphoric acid (H_3PO_4, product name: 1005731000) were acquired from Sigma-Aldrich (St. Louis, MO, USA). Electrical access to the capacitive devices was achieved using a silver nanoparticles (AgNPs) screen printable ink (LOCTITE® ECI 1010 EC from Henkel AG, Düsseldorf, Germany).

VII.2.2 Devices Fabrication

Figure VII.1 shows the scheme for the fabrication of the carbon-based flexible electrochemical capacitors. First, the in-plane interdigital electrodes were printed on the flexible substrate using a 90 Nylon threads per centimeter (T/cm) mesh with a FLAT-DX200 screen printing machine (from Siebdruck-Versand, Magdeburg, Germany), as shown in Figure VII.1a and VII.1b. The capacitive structure considered has the following dimensions (see Figure VII.1c: number of fingers N: 20, width W: 1 mm, spacing S: 1 mm, interspacing i: 1 mm and length L: 1 cm; which results in an effective area of 4 cm^2. Following the manufacturer recommendations, the samples were dried at a temperature of 130 ^{o}C for 3 min to remove all residual solvent using a UF55 oven (from Memmert, Schwabach, Germany). Following the same screen-printing process, electrical contacts were printed using silver ink (Figure VII.1d), and the sample was dried afterwards again (this time at 120 ^{o}C for a duration of 15 min). Furthermore, the gel electrolyte was prepared by dissolving 1 g of PVA in 10 mL of de-ionized water (10 wt%) with stirring at 80 ^{o}C for 2 h using a VWR 12365-382 hot plate stirrer (from VWR International, Radnor, PA, USA). Once the PVA was completely dissolved, 1.2 g of H_3PO_4 was added to the solution and it was stirred for another hour [26]–[28]. The final homogeneous gel solution was drop casted ($\sim$1.5 mL) on the capacitive IDE structure covering all the effective surface area (Figure VII.1e). Finally, once the device is left standing overnight to remove the excess of water, the EC looks as shown in Figure VII.1f.

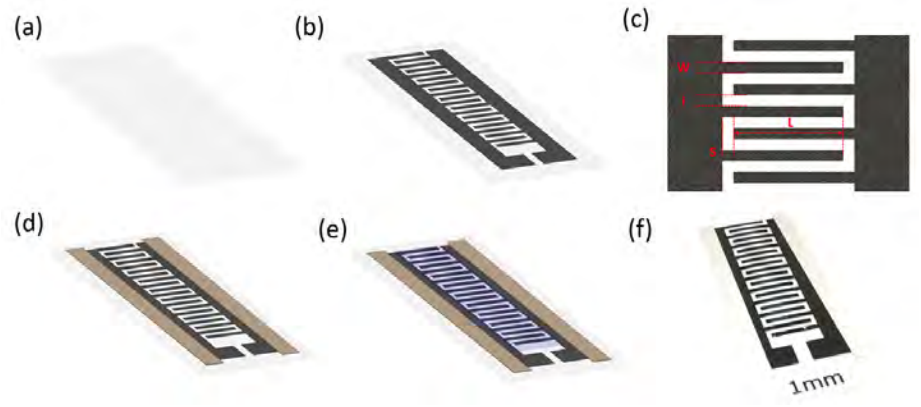

Figure VII.1: Schematic representation of the fabrication process of the flexible EC. (a) Flexible transparent substrate (thickness: 160 μm). (b) Capacitive IDE structure screen-printed on the substrate. (c) Dimmension of the interdigitally arranged electrodes (W: width, i: interspacing, L: length, S: spacing). (d) Silver electrical contacts screen-printed on each electrode. (e) PVA/H_3PO_4 electrolyte drop-casted on top of the IDE structure (blue shadow color has been selected to make the electrolyte visible). (d) Real view of the EC presented in this work.

VII.2.3 Characterization

Microscope pictures were obtained with a ZEISS Axioscope 5 (from Carl Zeiss AG, Oberkochen, Germany). The sheet resistances were measured through the four-point method at a DC current of 100 μA using a probe head from Jandel connected to a B2901A Keysight (Keysight Technologies, Inc., CA, USA) Source Measuring Unit (SMU). Cyclic Voltammetry (CV) and charge-discharge measurements at Constant Current (CC) were performed using a 2602B Keithley SMU from Tektronix Inc. (Beaverton, OR, USA). The impedance of the samples was obtained using the impedance analyzer 4294A (from Keysight Technologies, Inc., CA, USA). The performance of the devices as a function of the temperature was studied using the climate chamber VCL4006 (from Vötsch Industrietechnik GmbH, Balingen, Germany). A custom bending setup was built to perform the bending tests using a PD4-N5918M420 stepper motor together with a GPLE60 precision planetary gear (from Nanotec Electronic GmbH & Co. KG, Feldkirchen, Germany). All the measurement setup was automated using the software LabView 2017 (from National Instruments Corporation, TX, USA).

VII.3 Results and Discussion

Microscope images of the screen-printed electrodes are shown in Figure VII.2. On one hand, Figure VII.2a shows the printing resolution achieved. From the microscope images, it can be obtained that the average electrode width is $W =$

1.168 mm, while its interspacing and separation are found to be $i = 0.892$ mm and $S = 0.902$ mm, respectively, as a consequence of the paste spreading once it is deposited on the substrate. On the other hand, the porous nature of the carbon-based electrodes can be observed in Figure VII.2b. The sheet resistance of these conductive patterns is 503.6 ± 74.4 Ω/sq.

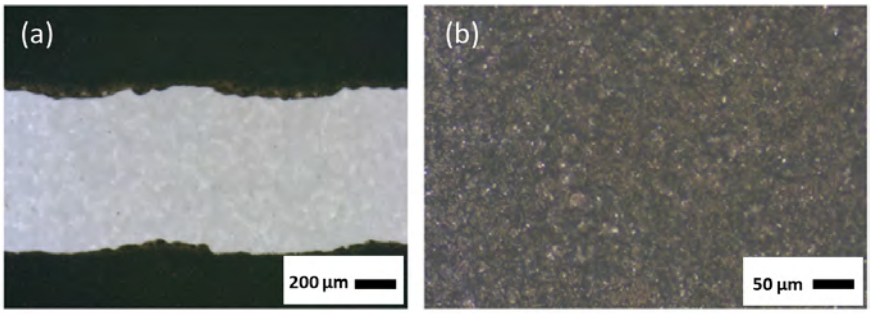

Figure VII.2: Microscope images of the screen-printed electrodes. (a) Interspacing between two consecutive electrodes (scale bar: 200 μm). (b) Electrode surface (scale bar: 50 μm).

First, the electrochemical performance of the ECs was investigated through Cyclic Voltammetry (CV). The experiments were conducted considering a potential window of ΔV = 1 V, from -0.5 V to +0.5 V, at different scanning rates (20 mV/s, 50 mV/s, 90 mV/s and 120 mV/s), as shown in Figure VII.3a. It can be noted that the CV curves maintain the quasi rectangular shape over the increasing scan rates, indicating a good reversible Electrostatic Double-Layer Capacitive (EDLC) behavior [29]. From these curves, the capacitance can be calculated as follows:

$$C_{CV} = \frac{1}{2\Delta V \cdot s} \cdot \left(\int_{-0.5}^{0.5} I(V)dV + \int_{0.5}^{-0.5} I(V)dV \right) \tag{VII.1}$$

where ΔV is the potential window, s the scan rate and $I(V)$ the current response as a function of the voltage [20]. The results, depicted in Figure VII.3b, show an average capacitance of ∼12.5 μF (∼3.1 μF/cm^2). As seen, the capacitance does not suffer from a considerable decrease as the scan rate increases, which indicates a good interaction electrode-electrolyte [30].

Galvanostatic charge-discharge measurements are also commonly used for the characterization of ECs. The resulting curves associated with these measurements are displayed in Figure VII.3c. In this case, the quasi triangular symmetric shape demonstrates a good charge propagation across the carbon electrodes and negligible internal resistances [31]. In the same way, these results can also be used to calculate the specific capacitance by the following equation:

$$C_{CC} = \frac{1}{dV/dt} \tag{VII.2}$$

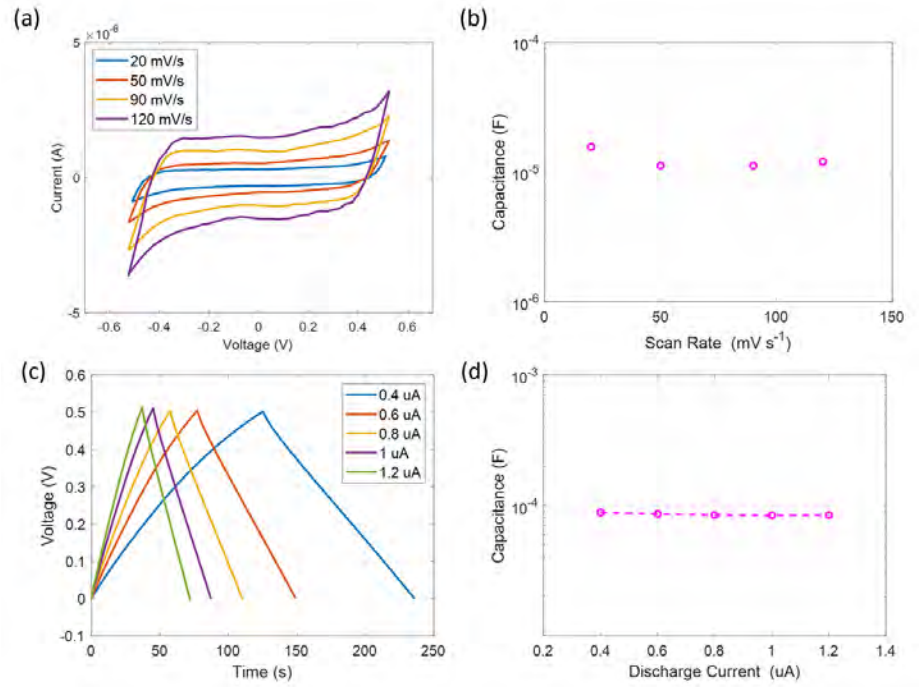

Figure VII.3: Evaluation of the specific capacitance of the ECs under different conditions. (a) Cyclic voltammetry curves at different scan rates. (b) Capacitance as a function of the scan rate extracted from the CV curves. (c) Galvanometric charge-discharge curves at different constant currents. (d) Capacitance as a function of the discharge current extracted from the CC curves.

where I is the discharge current and dV/dt the slope of galvanostatic discharge curve [22]. In this case, the specific capacitance obtained is around 86 μF ($\sim$22 μF/cm^2) with a slight decrease as the discharge current increases ($\Delta C/C_0 = 4.7\%$), see Figure VII.3d. This specific areal capacitance is similar to that obtained with other non-treated carbon materials [32], [33].

The outstanding performance of the ECs under different bending conditions (r = 1.25 cm, 0.75 cm and 0.5 cm) is demonstrated in Figure VII.4. It can be noted how the EC presents almost unchanged CC and CV curves for the different bending states, which would allow to use these ECs in conformal applications with no effect on their electrochemical performance.

The electrochemical cycling durability of the ECs has also been studied. The results, displayed in Figure VII.5, have shown that the capacitors are able to retain their capacitance even after 1000 bending cycles ($\Delta C/C_0 < 1\%$). However, it can also be noticed how the rectangular shape of the CV curves is progressively deformed. This latter can be attributed to the appearance of reversible pseudocapacitive effects, indicating that an increasing number of

continuous cycles boosts the electrosorption, redox and intercalation processes on the surface of the porous electrodes [20], [34], [35].

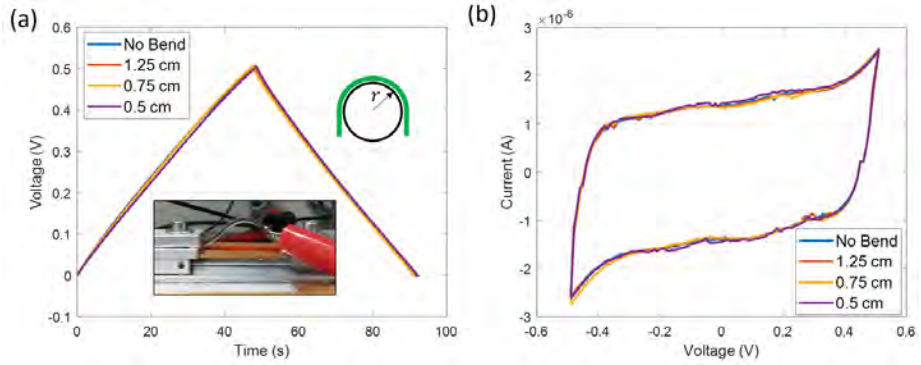

Figure VII.4: ECs performance under different bending conditions. (a) CC curves at the four different states ($I = 1$ μA). Inset shows a bent EC, while the diagram depicts the definition of bend radius. (b) CV curves for the four bending states considered ($s = 100$ mV/s).

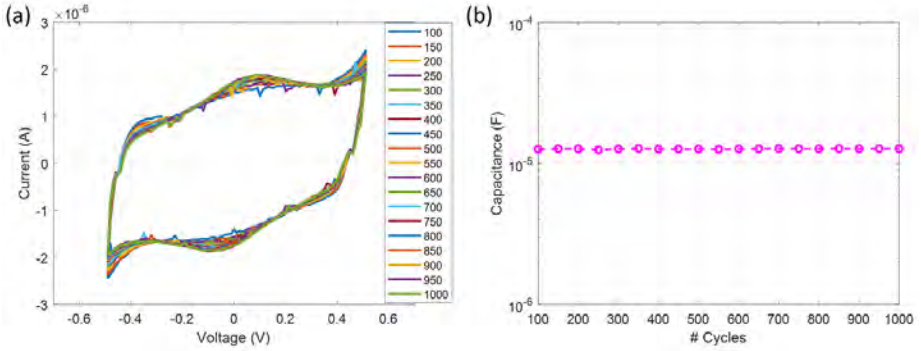

Figure VII.5: Cycle ability experiments. (a) CV curves obtained at the different cycles shown in legend. (b) Specific capacitance as a function of the number of cycles extracted from the CV curves.

The ECs have been further investigated using a Nyquist diagram (Figure VII.6), which shows the capacitive behaviour of the presented ECs as a function of the frequency. At low frequencies, the imaginary part of the impedances against the real one is almost linear (up to ∼65 Hz), then a semicircle appears in the high frequency region indicating the transition between resistance and capacitance behaviors. It should also be noticed that, at this point, the curve faces the real axis at a $\sim 45^o$ angle, which is a common characteristic when a porous electrode is saturated with electrolyte [30], [36], [37]. Moreover, the

interception with the real axis is associated with the Equivalent Series Resistance (ESR), which is estimated to be ∼250 Ω. Lastly, Figure VII.6b and Figure VII.6c show the behaviour of the analyzed ECs if we simplify its model to a capacitance in parallel with a resistance.

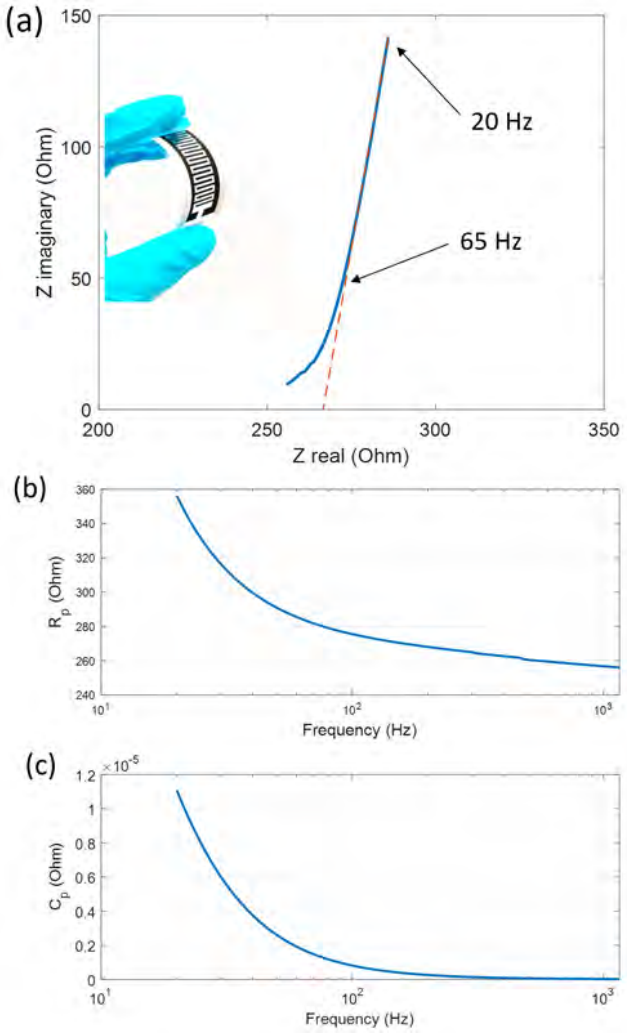

Figure VII.6: Electrochemical Impedance Spectroscopy (EIS) of the presented ECs. (a) Nyquist plot. (b) Equivalent resistance and (c) capacitance considering a simple model based on a R‖C circuit.

Finally, the temperature effect on the performance of the ECs is represented in Figure VII.7. As demonstrated by both CC and CV experiments, the specific capacitance increases as the temperature increases, as it has been demonstrated

for several electrode/electrolyte systems, such as rGO-PVA/H_3PO_4 [37], CNT-PC/TEABF4 [38], among others [39]. This effect has been attributted to changes in the electrolyte, since an increase of the temperature possibly leads to the physisorbtion of the electrolyte ions [37], [38].

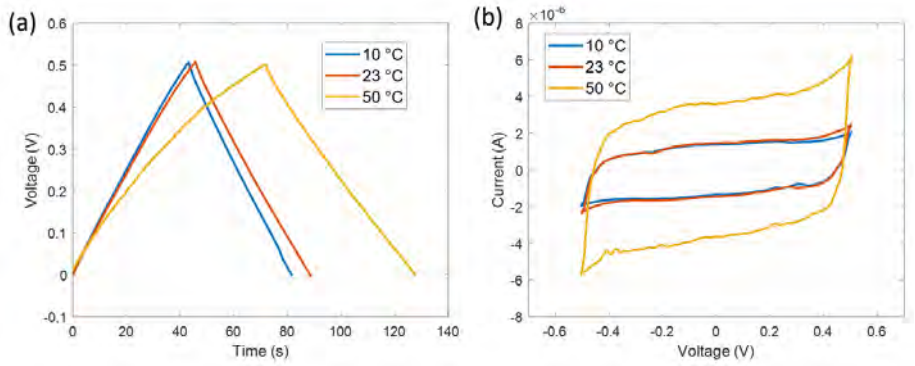

Figure VII.7: ECs performance under different bending conditions. (a) CC curves at the four different states. Inset shows a bent EC, while the diagram depicts the definition of bend radius. (b) CV curves for the four bending states.

VII.4 Conclusions

In summary, we report the fabrication of thin-film flexible electrochemical capacitors trough the screen-printing of a carbon-based conductive ink on a flexible substrate. Using PVA/H_3PO_4 as electrolyte, the devices present good performance as ECDL capacitors, which has been demonstrated trough cyclic voltammetry, charge-discharge experiments and electrochemical impedance spectroscopy. Although the specific capacitances obtained for this electrode material does not achieve those obtained with other carbon-based materials, further studies aim to treat the conductive ink in order to optimize its properties and increase the specific areal capacitance. It has been demonstrated that this method paves the way towards an alternative method for the large-scale and cost-effective fabrication of flexible electrochemical capacitors.

Acknowledgements. This work has been partially supported by the Spanish Ministry of Education, Culture and Sport (MECD) and the European Union through the pre-doctoral grant FPU16/01451, and its mobility program, the project TEC2017-89955-P and fellowship H2020-MSCA-IF-2017794885-SELFSENS.

References

[1] Sun, D.-M., Liu, C., Ren, W.-C., and Cheng, H.-M., "A review of carbon nanotube- and graphene-based flexible thin-film transistors," *Small*, vol. 9, no. 8, pp. 1188–1205, Mar. 2013.

[2] Castillo, E., Salmeron, J. F., Falco, A., Loghin, F. C., Romero, F. J., Lugli, P., Morales, D. P., and Rivadeneyra, A., "An optimized measurement algorithm for gas sensors based on carbon nanotubes: Optimizing sensor performance and hardware resources," *IEEE Internet of Things Journal*, vol. 6, no. 5, pp. 9140–9146, Oct. 2019.

[3] Jang, H., Park, Y. J., Chen, X., Das, T., Kim, M.-S., and Ahn, J.-H., "Graphene-based flexible and stretchable electronics," *Advanced Materials*, vol. 28, no. 22, pp. 4184–4202, Jan. 2016.

[4] Eda, G., Fanchini, G., and Chhowalla, M., "Large-area ultrathin films of reduced graphene oxide as a transparent and flexible electronic material," *Nature Nanotechnology*, vol. 3, no. 5, pp. 270–274, Apr. 2008.

[5] Romero, F. J., Rivadeneyra, A., Toral, V., Castillo, E., Garcia-Ruiz, F., Morales, D. P., and Rodriguez, N., "Design guidelines of laser reduced graphene oxide conformal thermistor for IoT applications," *Sensors and Actuators A: Physical*, vol. 274, pp. 148–154, May 2018.

[6] Langley, D., Giusti, G., Mayousse, C., Celle, C., Bellet, D., and Simonato, J.-P., "Flexible transparent conductive materials based on silver nanowire networks: A review," *Nanotechnology*, vol. 24, no. 45, p. 452 001, Oct. 2013.

[7] Shen, W., Zhang, X., Huang, Q., Xu, Q., and Song, W., "Preparation of solid silver nanoparticles for inkjet printed flexible electronics with high conductivity," *Nanoscale*, vol. 6, no. 3, pp. 1622–1628, 2014.

[8] Khan, S., Lorenzelli, L., and Dahiya, R. S., "Technologies for printing sensors and electronics over large flexible substrates: A review," *IEEE Sensors Journal*, vol. 15, no. 6, pp. 3164–3185, Jun. 2015.

[9] Chang, H. and Wu, H., "Graphene-based nanomaterials: Synthesis, properties, and optical and optoelectronic applications," *Advanced Functional Materials*, vol. 23, no. 16, pp. 1984–1997, Nov. 2012.

[10] Romero, Toral-Lopez, Ohata, Morales, Ruiz, Godoy, and Rodriguez, "Laser-fabricated reduced graphene oxide memristors," *Nanomaterials*, vol. 9, no. 6, p. 897, Jun. 2019.

[11] Salim, A. and Lim, S., "Review of recent inkjet-printed capacitive tactile sensors," *Sensors*, vol. 17, no. 11, p. 2593, Nov. 2017.

[12] Salmerón, J. F., Molina-Lopez, F., Briand, D., Ruan, J. J., Rivadeneyra, A., Carvajal, M. A., Capitán-Vallvey, L. F., Rooij, N. F. de, and Palma, A. J., "Properties and printability of inkjet and screen-printed silver patterns for RFID antennas," *Journal of Electronic Materials*, vol. 43, no. 2, pp. 604–617, Nov. 2013.

[13] Albrecht, A., Salmeron, J. F., Becherer, M., Lugli, P., and Rivadeneyra, A., "Screen-printed chipless wireless temperature sensor," *IEEE Sensors Journal*, vol. 19, no. 24, pp. 12 011–12 015, Dec. 2019.

[14] Goliya, Y., Rivadeneyra, A., Salmeron, J. F., Albrecht, A., Mock, J., Haider, M., Russer, J., Cruz, B., Eschlwech, P., Biebl, E., Becherer, M., and Bobinger, M. R., "Next generation antennas based on screen-printed and transparent silver nanowire films," *Advanced Optical Materials*, vol. 7, no. 21, p. 1 900 995, Aug. 2019.

[15] Lukacs, P., Pietrikova, A., Potencki, J., and Tomaszewski, G., "UWB antenna based on nanoparticles of silver on polyimide substrate," in *2015 38th International Spring Seminar on Electronics Technology (ISSE)*, IEEE, May 2015.

[16] Beidaghi, M. and Gogotsi, Y., "Capacitive energy storage in micro-scale devices: Recent advances in design and fabrication of micro-supercapacitors," *Energy & Environmental Science*, vol. 7, no. 3, p. 867, 2014.

[17] Pandolfo, A. and Hollenkamp, A., "Carbon properties and their role in supercapacitors," *Journal of Power Sources*, vol. 157, no. 1, pp. 11–27, Jun. 2006.

[18] Lamberti, A., Clerici, F., Fontana, M., and Scaltrito, L., "A highly stretchable supercapacitor using laser-induced graphene electrodes onto elastomeric substrate," *Advanced Energy Materials*, vol. 6, no. 10, p. 1 600 050, Mar. 2016.

[19] Peng, Z., Lin, J., Ye, R., Samuel, E. L. G., and Tour, J. M., "Flexible and stackable laser-induced graphene supercapacitors," *ACS Applied Materials & Interfaces*, vol. 7, no. 5, pp. 3414–3419, Jan. 2015.

[20] Chen, Z., Ren, W., Gao, L., Liu, B., Pei, S., and Cheng, H.-M., "Three-dimensional flexible and conductive interconnected graphene networks grown by chemical vapour deposition," *Nature Materials*, vol. 10, no. 6, pp. 424–428, Apr. 2011.

[21] Kaempgen, M., Chan, C. K., Ma, J., Cui, Y., and Gruner, G., "Printable thin film supercapacitors using single-walled carbon nanotubes," *Nano Letters*, vol. 9, no. 5, pp. 1872–1876, May 2009.

[22] Peng, Z., Ye, R., Mann, J. A., Zakhidov, D., Li, Y., Smalley, P. R., Lin, J., and Tour, J. M., "Flexible boron-doped laser-induced graphene microsupercapacitors," *ACS Nano*, vol. 9, no. 6, pp. 5868–5875, May 2015.

[23] Wang, W., Lu, L., Xie, Y., Mei, X., Tang, Y., Wu, W., and Liang, R., "Tailoring the surface morphology and nanoparticle distribution of laser-induced graphene/co3o4 for high-performance flexible microsupercapacitors," *Applied Surface Science*, vol. 504, p. 144 487, Feb. 2020.

[24] Chen, Q., Li, X., Zang, X., Cao, Y., He, Y., Li, P., Wang, K., Wei, J., Wu, D., and Zhu, H., "Effect of different gel electrolytes on graphene-based solid-state supercapacitors," *RSC Adv.*, vol. 4, no. 68, pp. 36 253–36 256, 2014.

[25] Zhou, J., Anjum, D. H., Chen, L., Xu, X., Ventura, I. A., Jiang, L., and Lubineau, G., "The temperature-dependent microstructure of PEDOT/PSS films: Insights from morphological, mechanical and electrical analyses," *J. Mater. Chem. C*, vol. 2, no. 46, pp. 9903–9910, 2014.

[26] He, D., Marsden, A. J., Li, Z., Zhao, R., Xue, W., and Bissett, M. A., "Fabrication of a graphene-based paper-like electrode for flexible solid-state supercapacitor devices," *Journal of The Electrochemical Society*, vol. 165, no. 14, A3481–A3486, 2018.

[27] Shieh, J.-Y., Zhang, S.-H., Wu, C.-H., and Yu, H. H., "A facile method to prepare a high performance solid-state flexible paper-based supercapacitor," *Applied Surface Science*, vol. 313, pp. 704–710, Sep. 2014.

[28] Singh, R. and Tripathi, C. C., "Electrochemical exfoliation of graphite into graphene for flexible supercapacitor application," *Materials Today: Proceedings*, vol. 5, no. 1, pp. 1125–1130, 2018.

[29] Lee, J.-S. M., Briggs, M. E., Hu, C.-C., and Cooper, A. I., "Controlling electric double-layer capacitance and pseudocapacitance in heteroatom-doped carbons derived from hypercrosslinked microporous polymers," *Nano Energy*, vol. 46, pp. 277–289, Apr. 2018.

[30] Ali, G. A., Tan, L. L., Jose, R., Yusoff, M. M., and Chong, K. F., "Electrochemical performance studies of MnO 2 nanoflowers recovered from spent battery," *Materials Research Bulletin*, vol. 60, pp. 5–9, Dec. 2014.

[31] Luo, J., Fan, F. R., Jiang, T., Wang, Z., Tang, W., Zhang, C., Liu, M., Cao, G., and Wang, Z. L., "Integration of micro-supercapacitors with triboelectric nanogenerators for a flexible self-charging power unit," *Nano Research*, vol. 8, no. 12, pp. 3934–3943, Nov. 2015.

[32] Zang, X., Li, P., Chen, Q., Wang, K., Wei, J., Wu, D., and Zhu, H., "Evaluation of layer-by-layer graphene structures as supercapacitor electrode materials," *Journal of Applied Physics*, vol. 115, no. 2, p. 024 305, Jan. 2014.

[33] Yoo, J. J., Balakrishnan, K., Huang, J., Meunier, V., Sumpter, B. G., Srivastava, A., Conway, M., Reddy, A. L. M., Yu, J., Vajtai, R., and Ajayan, P. M., "Ultrathin planar graphene supercapacitors," *Nano Letters*, vol. 11, no. 4, pp. 1423–1427, Apr. 2011.

[34] Zhu, J., Sun, W., Yang, D., Zhang, Y., Hoon, H. H., Zhang, H., and Yan, Q., "Multifunctional architectures constructing of PANI nanoneedle arrays on MoS2thin nanosheets for high-energy supercapacitors," *Small*, vol. 11, no. 33, pp. 4123–4129, Jun. 2015.

[35] You, D.-J., Yin, Z., Ahn, Y.-k., Lee, S.-H., Yoo, J., and Kim, Y. S., "Redox-active ionic liquid electrolyte with multi energy storage mechanism for high energy density supercapacitor," *RSC Advances*, vol. 7, no. 88, pp. 55 702–55 708, 2017.

[36] El-Kady, M. F., Strong, V., Dubin, S., and Kaner, R. B., "Laser scribing of high-performance and flexible graphene-based electrochemical capacitors," *Science*, vol. 335, no. 6074, pp. 1326–1330, Mar. 2012.

[37] Wang, L., Yang, C., Wen, J., Gai, S., and Peng, Y., "Overview of emerging memristor families from resistive memristor to spintronic memristor," *Journal of Materials Science: Materials in Electronics*, vol. 26, no. 7, pp. 4618–4628, Mar. 2015.

[38] Masarapu, C., Zeng, H. F., Hung, K. H., and Wei, B., "Effect of temperature on the capacitance of carbon nanotube supercapacitors," *ACS Nano*, vol. 3, no. 8, pp. 2199–2206, Jul. 2009.

[39] Jung, H.-C., Moon, J.-H., Baek, D.-H., Lee, J.-H., Choi, Y.-Y., Hong, J.-S., and Lee, S.-H., "CNT/PDMS composite flexible dry electrodesfor long-term ECG monitoring," *IEEE Transactions on Biomedical Engineering*, vol. 59, no. 5, pp. 1472–1479, May 2012.

Paper VIII

Inexpensive and Flexible Nanographene-Based Electrodes for Ubiquitous Electrocardiogram Monitoring

Francisco J. Romero [1,2,*], Encarnacion Castillo [1], Almudena Rivadeneyra [1,2], Alejandro Toral-Lopez [1,2], Markus Becherer [3], Francisco G. Ruiz [1,2], Noel Rodriguez [1,2], Diego P. Morales [2,4]

[1] Pervasive Electronics Advanced Research Laboratory, University of Granada, 18071 Granada, Spain.
[2] Department of Electronics and Computer Technology, University of Granada, 18071 Granada, Spain.
[3] Institute for Nanoelectronics, Technische Universität München, 80333, Munich, Germany.
[4] Biochemistry and Electronics as Sensing Technologies Group, University of Granada, 18071 Granada, Spain
* Corresponding authors: franromero@ugr.es (F.J.R.)

Published in *npj Flexible Electronics*, Jun 2019, volume 3, 12. DOI: 10.1038/s41528-019-0056-2.

VIII

Abstract

Flexible electronics is one of the fundamental technologies for the development of electronic skin, implant wearables, or ubiquitous biosensing. In this context, graphene-derived materials have attracted a great interest due to their unique properties to fulfill the demands of these applications. Here we report a simple one-step method for the fabrication of electrophysical electrodes based on the photothermal production of porous nanographene structures on the surface of flexible polyimide substrates. This approach constitutes an inexpensive alternative to the commercial medical electrodes, leading to a lower and much more stable skin–electrode contact resistance and providing comparable signal transduction. This technology has been framed inside the IoT paradigm through the development of a denoising and signal classification clustering algorithm suitable for

its implementation in wearable devices. The experiments have shown promising achievements regarding noise reduction, increasing the crest factor ∼3.7 dB, as well as for the over 90% heart rate-monitoring accuracy.

VIII.1 Introduction

Cardiovascular diseases (CVDs) are the most common cause of death in the world [1]. This has led to assign great efforts to their early diagnosis, prevention, and treatment. According to the European Heart Network (EHN), overall CVDs are estimated to cost the EU economy 210 billion a year, of which around 53% (111 billion) are intended to the health costs [2], [3]. Electrocardiography (ECG) is the most common method to diagnose abnormalities in the cardiac activity and to extract the information that might reveal CVDs in advance [4]. So far, this technique was traditionally limited to the hospital environment; however, the emergence of new technological paradigms, such as the Internet of Things (IoT), the flexible electronic devices and the electronic textiles (e-textiles), are shifting the "in-hospital care" towards the ubiquitous health-monitoring [5]–[7].

Metals such as silver (Ag) or copper (Cu) are currently the most used materials for the biosignal transduction [8]–[10]. There is no doubt that these materials have offered high performance in this kind of applications and have contributed to the process of medical diagnosis. However, wearable health-monitoring systems (WHMS) also require of inexpensive, lightweight, and biocompatible conductive materials. Following these premises, flexible electronics and carbon-based materials are a symbiosis expected to play an important role in the next generation of WHMS [11]–[14]. On this basis, Celik *et al.* presented an electrode fabricated by chemical vapor deposition coating of graphene on top of a Ag-based electrode [15]; whereas, chemically reduced graphene oxide on polyethylene terephthalate (PET) and porous textile substrates have been also studied by Lou *et al.* and Karim *et al.*, respectively [16], [17]. Moreover, Jung *et al.* also proposed a carbon-nanotube (CNT) on polydimethylsiloxane (PDMS) composite-based electrode for the ECG monitoring [18]. All these proposed electrodes, in addition of being biocompatible, are suitable for long-term monitoring due to their "dry" nature, since they do not require of the use of adhesive or conductive gels, in contrast to the Ag/AgCl ones [6]. However, they are subjected to manufacturing processes with multiple stages, and therefore high production costs. In addition, the signal transduction capability of the electrodes must be good enough for the subsequent processing of the recorded signals. It is also important to keep in mind that wearables devices are subjected to significant restrictions of size, computational capabilities and power consumption. Therefore, it is necessary to ensure a compromise between both the raw biosignal quality and the optimization of the processing algorithms to obtain accurate results.

In this article, we propose the use of a low-power laser diode to produce a foam of porous graphene (PG) on a flexible substrate; this structure is applied

to the fabrication of electrodes for the continuous and ubiquitous monitoring of ECG signals. As reported by previous works, PG with high electrical conductivity can be induced on the surface of diverse carbon-rich materials by a photothermal process [19]. Recently, we presented an in-depth study of the laser-induction of PG on a flexible Kapton® substrate under ambient conditions by using a laser diode [20]. This approach offers the advantage of defining high-precision conductive patterns of laser-induced nanographene aggregates (LINA) on flexible substrates without the need for lithographic masks or the deposition of any material before the laser treatment (such as occurs for the laser-reduced graphene oxide (laser-rGO) [21]). This one-step technique is also compatible with roll-to-roll methods, enabling an inexpensive mass-production of samples. The feasibility of the proposed electrodes for recording electrophysiological signals is demonstrated by monitoring the heart rate through a clustering algorithm intended to be implemented in portable hardware, such as wearables. This algorithm performs, on one side, the artifact removal from the ECG signal (baseline wandering (BW), tremor artifacts, etc.) and, on the other side, the extraction of the heart beat from the QRS-complexes by means of the classification of the peaks in different clusters. Thus, the classification is much more robust against noise and amplitude variations, since it is based on similarities instead of on fixed values as in the case of threshold-based methods. The results have shown that the proposed electrodes, in combination with data analysis techniques, pave the way for the inexpensive and simple fabrication of electrodes for a new generation of wearable monitoring devices.

VIII.2 Results and discussion

VIII.2.1 Electrode design and fabrication

Figure VIII.1a illustrates a schematic of the structure of the developed electrodes, fabricated following the basis of the laser-scribing procedure proposed in our previous work [20]. The Kapton® HN tape was cut into squares (20 mm × 20 mm), then a circumference with a diameter of 10 mm was photothermally patterned on its surface using a computer numerical control (CNC)-driven laser diode. The electrode was laser-scribed at a fluence of 20 J cm−2 (laser spot diameter: 20 μm) and at an excursion rate of 3 min cm^{-2} in two perpendicular passes (one for X-axis and one for Y-axis), ensuring the carbonization process and the integrity of the substrate in terms of thermal dissipation [22]. Next, a planar wire was connected to the LINA electrode using Ag-based conductive paint. This electrical connection approach provides a low contact resistance due to the increase of the contact area resulting from the high porosity of the nanographene-induced patterns [20]. Most common commercial electrodes are based on Ag/AgCl composites, being the surface of contact between the skin and the electrode of 78.5 mm^2. Therefore, the whole structure was isolated using laminating pouches (as shown in Fig. 1a) leaving the access to the LINA circumference free in order to establish an appropriate comparison between our electrodes and the commercial ones (Supplementary Fig. VIII.4). An adhesive

skin patch with a transparent polyurethane (PU) film and a polyacrylate adhesive was used to attach the electrodes safely on the skin, as shown in Fig. VIII.1b.

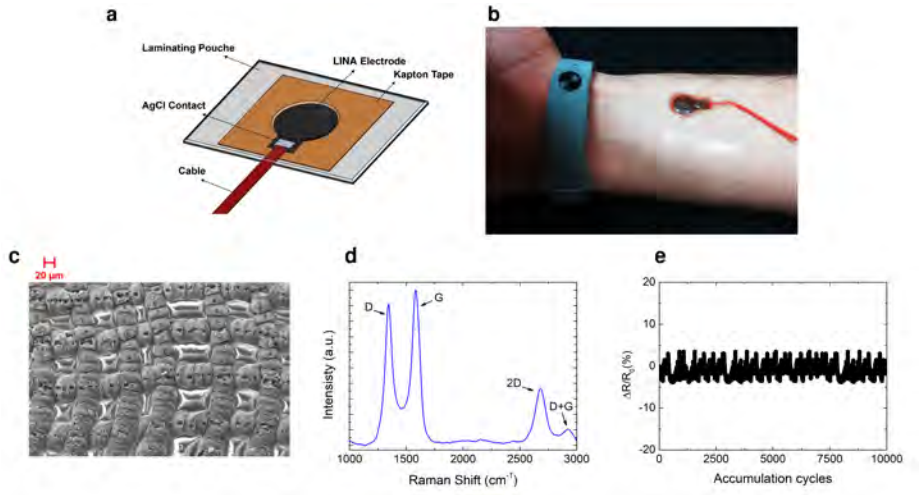

Figure VIII.1: Electrode fabrication and material characterization. (a) Schematic of the flexible electrode. (b) Flexible electrode attached to the forearm of a person. (c) SEM-image of the laser patterned surface (scale bar: 20 μm). The bright areas corresponds to the non-irradiated surface, while the dark ones are that of laser-induced nanographene aggregate. (d) Raman spectrum of the laser-induced porous nanographene aggregates. (e) Percentage of change in resistance ($R/R_0(\%)$) for a increasing number of bending cycles, being R_0 the initial resistance and R the resistance measured after each bending cycle.

VIII.2.2 Electrode characterization

A SEM image of the patterned area of the flexible polyimide substrate is shown in Fig. VIII.1c. As can be observed, the laser-induced nanographene patterns show a mesh-like structure as a consequence of the mechanical resolution of the CNC unit ($\sim$40 μm). Besides, the ablated surface (non-bright areas) exhibits a high porosity, which is a distinctive feature of the laser-induced porous nanographene [23]. The LINA increases substantially the porosity of the polyimide, resulting in an increase of the thickness of 18.7 $\pm$2.2 μm over its surface, which enhances the overall contact interface. The nanographene nature of the induced patterns is confirmed by the Raman spectrum (Fig. VIII.1d), which is composed of three main peaks (D peak: $\sim$135 cm^{-1}, G peak: $\sim$158 cm^{-1}, 2D peak: $\sim$270 cm^{-1}). However, it is far from achieving the single-layer pristine graphene structure, since the ratio $I_D/I_G \simeq 1$ indicates that the sp^2-hybridized carbonous systems which compose the surface present defects in their crystalline structure, while the I_{2D}/I_G ratio reflects the 3D nature of PG [24].

Furthermore, XPS results demonstrate the structure alterations induced by the photothermal process (Supplementary Fig. VIII.5). The initial relative content of carbon (∼75%), present as C-C sp^3 hybridized bonds, is increased up to ∼85% after the laser ablation, more than a half corresponding to C-C sp^2 hybridized carbon. The increase of the relative content of carbon is the outcome of the release of the nitrogen and oxygen as gases from the polyimide substrate. Thus, both oxygen and nitrogen relative contents are reduced by more than 10% and 5%, respectively, as a result of the photothermal process.

In addition to the chemical alterations, the LINA-induced patterns also present a great enhancement of the electrical conductivity with respect to the precursor substrate. The four-wire sensing experiments demonstrate that, through the photothermal ablation process, the sheet resistance of the samples can be reduced down to values closed to 250 Ω sq^{-1}. The bending dependence of the sheet resistance was also investigated to demonstrate the feasibility of the flexible electrodes for a long-term monitoring. Figure VIII.1e shows the normalized change in the resistance of an electrode ($\Delta R/R_0(\%)$) as a function of the bending cycles accumulated. The results have confirmed that the difference in the electrode resistance between the initial state and the state after 10^4 bending cycles are negligible (<4%). Further, we compared the skin-electrode contact impedance of the fabricated electrodes with two different commercial wet electrodes (see the section "Materials") aiming to compare their frequency response, which is normally modeled as the association of parallel connections of resistors and capacitors [25]. Results have shown promising values of skin-electrode impedance as a function of the frequency when compared with the commercial electrodes, as depicted in Fig. VIII.2a. On one hand, the commercial electrodes show a contact impedance more than 15 times higher than that of the electrodes presented in this work at low frequencies (∼1 kΩ). On the other hand, the frequency response of the contact impedance of the LINA electrodes stands out for its lower ratio of change in frequency (2.33 Ω Hz^{-1}), while the commercial electrodes present a deviation with respect to the frequency of 66.52 and 37.84 Ω Hz^{-1}, respectively, due to the higher impact of the parasitic capacitance when the frequency increases. The notable achievement of the LINA electrodes is attributed to the high porosity of the material, which enhances the specific contact area of the interface skin-electrode decreasing both the resistance and the capacitance seen from the body to the electrodes.

VIII.2.3 ECG and heart rate monitoring with LINA electrodes

The raw signals recorded from both the commercial and the flexible electrodes developed are comparable in terms of amplitude and signal-to-noise ratio. Figure VIII.2b shows an extract of 3.5 s from two simultaneous ECG recordings where the P-QRS-T complexes can be clearly distinguished [26]. The measuring electrodes were placed on a volunteer according to the Lead I Einthoven's triangle scheme [27]. Thus, the positive electrode was placed on the left wrist, the negative electrode was placed on the right wrist and the reference one on the left ankle. Under the configurations parameters of the ECG acquisition system

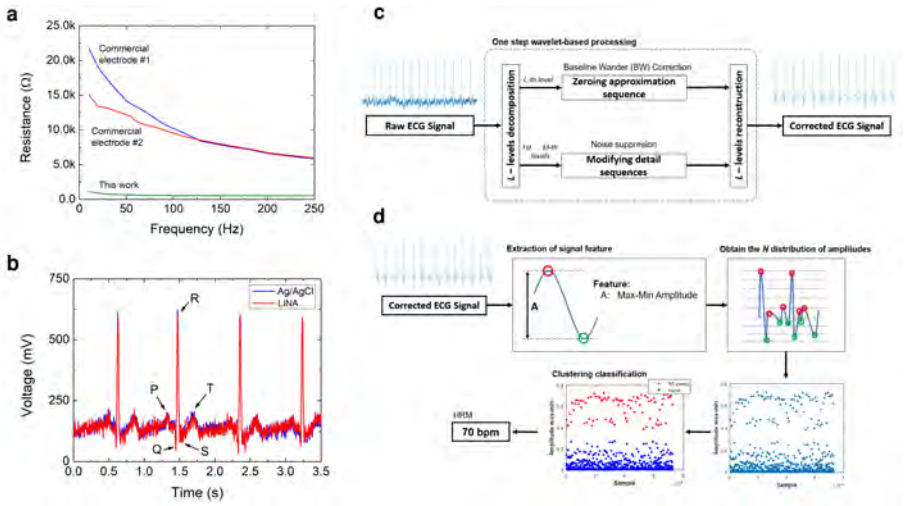

Figure VIII.2: Electrocardiography recording and processing methods. (a) Comparison of the skin-electrode contact resistance as a function of the frequency for two commercial electrodes (Ambu® BlueSensor VL and Biopac EL503, respectively) and the LINA electrode. (b) ECG recordings carried out simultaneously with the LINA electrodes (in red) and the Ag/AgCl commercial electrodes (in blue). (c) One step wavelet-preprocessing method for the baseline wandering and noise correction. (d) Clustering-based method for the heart rate monitoring based on the max-min amplitude.

(see the section "Materials and methods"), the signals present an average R-peak amplitude of ∼467 mV with a crest factor (peak-to-RMS ratio) of 11.40 and 11.47 dB for the Ag-based electrodes and the LINA ones, respectively.

The feasibility of the proposed electrodes for the WHMS paradigm is further demonstrated combining them with an algorithm that can be applied not only for filtering and preprocessing the signal obtained from the LINA electrodes, but also to extract the heart rate [28]. This algorithm can be divided in two main blocks, as schematized in Fig. VIII.2c and Fig. VIII.2d. First, we apply a modified version of the discrete wavelet transform (DWT) optimized for portable hardware implementations to reduce the BW and noise of the recorded ECG signals produced by the motion artifacts (see the section "Materials and methods").

The resulting signal after the baseline wander correction and noise suppression is shown in Fig. VIII.3b, where the crest factor has been increased up to 15.24 dB. After that, a clustering-based method, depicted in Fig. VIII.2d and described in the section "Materials and methods", is applied to the preprocessed signal for the heart rate monitoring. This method allows the extraction of the heart rate from the RS-peaks frequency by means of the classification of the different peaks (RS-peaks and others) which compose the ECG signal, using the distance

between a local maximum followed by a local minimum (amplitude Max-Min) as the feature for clustering (depicted in Fig. VIII.3c). Then, the results of the classification allow the high accuracy detection of the R-peaks (Fig. VIII.3d). As can be seen, this method, applied to an extract of 60 s from a signal recorded with the LINA electrodes, yields a 94.3% of accuracy, since it allows to detect 66 R-peaks from a total of 70 R-peaks (four false negatives), which is comparable to that obtained for commercial electrodes.

Finally, the frequency of the RS-peaks is used to extract the instantaneous heart rate as shown in Fig. VIII.3e, where the outliers resulting of the false negatives can also be appreciated. Future studies aim to include a next stage to correct these false negatives, as well as to consider alternative machine/deep learning techniques to automatically extract features from ECG signals. For instance, the approach proposed by Xia *et al.* [29], which combines a stacked denoising autoencoder with a softmax regression for the feature extraction and its subsequent classification to detect cardiac arrhythmia, or the one proposed by Zhang *et al.* [30], which is based on convolutional neural networks. Alternatively, we aim to combine the electrodes proposed in this work with our recently presented wearable system for biosignals acquisition [31].

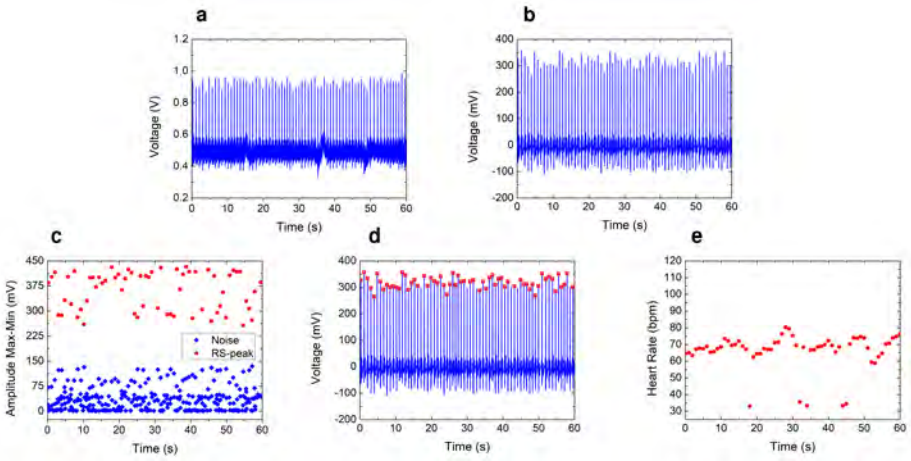

Figure VIII.3: Electrodes performance in electrocardiography and heart rate monitoring. (a) Raw ECG signal recording with some motion artifacts performed with the LINA-based electrodes. (b) Resulting signal after the baseline correction and noise suppression using the proposed DWT-based method. (c) Two-clusters classification (RS-peaks and noise) of the peaks which compose the ECG signal. (d) Identification of the RS-peaks along the 60 s signal from the clustering algorithm results. (e) Evolution of the heart rate over time extracted from the RS-peaks frequency.

VIII.3 Materials and Methods

VIII.3.1 Materials

Flexible Kapton® HN films with a thickness of 125 μm obtained from DuPont™ were used as raw material for LINA production in our experiments. Ag-based conductive paint was acquired from RS Pro. Two Comercial silver/silver chloride (Ag/AgCl) ECG electrodes were used for comparison, the Ambu® BlueSensor VL (VL-00-S/25, from Ambu A/S) and the EL503 general purpose electrode (from Biopac Systems Inc.), together with the SIGNAGEL® electrolyte gel (15–25 from Parker Laboratories Inc). The laminating pouches Capture125 acquired from Fellowes Inc. were used to seal and isolate the LIG electrodes. Moreover, the photothermal process was carried out using a DIY CNC laser engraver (λ = 405 nm) with adjustable laser power and laser spot size.

VIII.3.2 Material characterization

The morphology and structural properties of the LINA layer were analyzed by scanning electron microscopy (SEM), Raman spectroscopy, and X-ray photoelectron spectroscopy (XPS). SEM-images were recorded using a NVision 40 field-emission scanning electron microscope (from Carl Zeiss) at an extraction and acceleration voltage of 5 kV and a working distance of 6 mm. Raman-spectra were acquired using a JASCO NRS-5100 dispersive micro-Raman spectrometer with an Elforlight G4-30 green diode (λ = 532 nm) as excitation source [32]. XPS experiments were performed on a Katros Axis Ultra-DLD spectrometer with an X-ray power of 450 W in a vacuum chamber with a pressure 10^{-10} Torr. CasaXPS software (from Casa Software Ltd.) was used for the C1s spectra decomposition. A 3D profile was also acquired using a DekTak XT profilometer from Bruker. For the electrical characterization of the samples we used the four-point-contact method based on a probe head from Jandel connected to a B2901A source measuring unit (from Keysight) with a constant current of 0.5 mA. The bending tests were automated using a LabVIEW 2016 (from National Instruments) software controlled setup with a bending speed of 10 mm s^{-1} and a minimum bending diameter of 4 mm.

VIII.3.3 Measurement of the skin–electrode contact resistance

The contact resistance of the skin-electrode interface was extracted following a modified version of the setup proposed by Spach *et al.* [33] (Supplementary Fig. VIII.6a) for both commercial wet Ag/AgCl and LINA electrodes. Three electrodes were placed on the forearm (ventral side) of a person at a distance of 5 cm from each other. For this particular implementation, we used an input voltage of 1 V with a frequency range from 1 to 250 Hz referenced to the first electrode. The contact resistance (R_c) was calculated using the equation below, where the input current (i_{in}) was monitored through the voltage drop (v_{12}) on

the reference resistor (r), while v_{23} corresponds to the the voltage drop in the contact resistance (considering an ideal differential amplifier).

$$R_c = \frac{v_{23}}{i_{in}} = \frac{v_{23} \cdot r}{v_{12}} = \frac{G_1 \cdot v_{o_2} \cdot r}{G_2 \cdot v_{o_1}} \tag{VIII.1}$$

Due to the inherent variability of the signals recorded from one person to another and the signal amplitude variations associated with the use of the different kinds of electrodes, the monitoring stage (differential amplifiers, gains G_1 and G_2, and high-frequency noise suppression) was implemented using a reconfigurable field programmable analog array (FPAA) from Anadigm (AN221E04, Anadigm, Inc.) to obtain a reliable and adaptive analog conditioning signal for each case. In this way, the conditioning electronics is simplified within the FPAA device as depicted in Supplementary Fig. VIII.6b.

VIII.3.4 ECG electrodes performance evaluation

ECG signals were acquired using the wearable body sensing platform Biosignals Researcher Kit (from PLUX wireless biosignals S.A.) combined with an ECG local differential three-lead electrode (also from PLUX wireless biosignals S.A.) with 16-bit resolution and 1 kHz sampling rate. This wearable device has Bluetooth streaming capability which allowed to send the signals to a computer for their analysis. To compare the performance of both commercial and proposed LINA electrodes, we analyzed the crest factor of each P–QRS–T complex of the raw recorded signals using the following equation [34]:

$$CF(dB) = 20log_{10}\left(\frac{|S_{peak}|}{S_{rms}}\right) \tag{VIII.2}$$

being S_{peak} the peak amplitude of the ECG signal (R peak) and S_{rms} the RMS value of the signal along the P–QRS–T complex.

The main sources of noise of the electrocardiogram signals are the power line interference (50 or 60 Hz) and the motion artifacts [35]. For the noise suppression of the ECG signals we have applied an algorithm based on DWT digital processing techniques proposed by Castillo *et al.* [36], which is widely used to reduce the BW and noise in ECG signals [37], [38]. Moreover, the advantage of the custom algorithm proposed by Castillo *et al.* lies on its feasibility to be used in portable devices, such as wearables. The algorithm, which has been coded in Matlab® (from The MathWorks, Inc.), follows the scheme shown in Fig. VIII.2c. Then, to obtain the noiseless ECG signal, the raw signal is decomposed into L frequency bands ($L < \lceil log_2(F_s/2) \rceil$), being F_s the sampling frequency) to, on one hand, remove the BW by the zeroing approximation of the lowest frequencies and, on the other hand, denoise the signal by the modification of the details of levels 1 to M (with $M < L$). The frequency details subbands of levels $M + 1$ to L, where most of the spectral energy should lie, are preserved to avoid losing possible clinically important components of the signal [39]. Thus, the BW corrected and denoised ECG signal is reconstructed using the modified details

of the levels 1 to M, the original details of levels $M + 1$ to L and the zeroing approximation of the coefficients of level L. For this particular implementation we have decomposed the recorded signal (Fig. VIII.3a) into nine frequency levels ($L = 9$), using the first five levels for the noise suppression ($M = 5$). Therefore, the BW correction is applied to the 9^{th} level, which captures frequencies from 0 to 0.9765 Hz, while the adaptive filtering is applied to the first five levels (range from 15.625 to 500 Hz) [39]. Thus, from 0.9765 to 15.625 Hz the signal is unaltered to preserve the information of the QRS low-frequency bands [40]. The results of the BW and noise correction in the frequency domain are shown in Supplementary Fig. VIII.7.

Together with the implementation of the DWT detailed above, we have applied a clustering-based method to the recorded signals for the heart rate monitoring. This method is an adaptation of the method recently proposed by Castillo *et al.* devoted to the extraction of the fetal heart rate from mother's abdominal ECG signal [28]. In this case, the heart rate is extracted from the RS-peaks frequency of the P–QRS–T complexes following the procedure shown in Fig. VIII.2d. The RS-peak wave morphology shows a local maximum followed by a local minimum, therefore this pattern is localized along the denoised signal and assigned to one of the N intervals according to the maximum to minimum amplitude. The data is then classified into two different clusters (noise and RS-peaks) using the squared Euclidean distance $D^2(x_i, x_j) = (x_i - x_j)^2$ and the $k - medoids{+}{+}$ algorithm, which ensures a highly accurate classification and a better performance over threshold-based methods, as it has already been demonstrated in our previous work [28].

Acknowledgements. This work has been partially supported by the Spanish Ministry of Education, Culture and Sport (MECD) and the European Union through the project TEC2017-89955-P, the predoctoral grants FPU16/01451 and FPU16/04043, and the fellowship H2020-MSCA-IF-2017 794885-SELFSENS. Additionally, this work was also supported by the German Research Foundation (DFG) and the Technical University of Munich.

References

[1] Domanski, M. J., Fuster, V., Diaz-Mitoma, F., Grundy, S., Lloyd-Jones, D., Mamdani, M., Roberts, R., Thorpe, K., Hall, J., Udell, J. A., and Farkouh, M. E., "Next steps in primary prevention of coronary heart disease," *Journal of the American College of Cardiology*, vol. 66, no. 16, pp. 1828–1836, Oct. 2015.

[2] Buse, J. B., Ginsberg, H. N., Bakris, G. L., Clark, N. G., Costa, F., Eckel, R., Fonseca, V., Gerstein, H. C., Grundy, S., Nesto, R. W., Pignone, M. P., Plutzky, J., Porte, D., Redberg, R., Stitzel, K. F., and Stone, N. J., "Primary prevention of cardiovascular diseases in people with diabetes mellitus," *Circulation*, vol. 115, no. 1, pp. 114–126, Jan. 2007.

[3] Wilkins, E., Wilson, L., Wickramasinghe, K., Bhatnagar, P., Leal, J., Luengo-Fernandez, R., Burns, R., Rayner, M., and Townsend, N., *European Cardiovascular Disease Statistics 2017*. European Heart Network, 2017.

[4] Bacquer, D. D., Backer, G. D., Kornitzer, M., and Blackburn, H., "Prognostic value of ECG findings for total, cardiovascular disease, and coronary heart disease death in men and women," *Heart*, vol. 80, no. 6, pp. 570–577, Dec. 1998.

[5] Kenry, Yeo, J. C., and Lim, C. T., "Emerging flexible and wearable physical sensing platforms for healthcare and biomedical applications," *Microsystems & Nanoengineering*, vol. 2, no. 1, Sep. 2016.

[6] Majumder, S., Mondal, T., and Deen, M., "Wearable sensors for remote health monitoring," *Sensors*, vol. 17, no. 12, p. 130, Jan. 2017.

[7] Castano, L. M. and Flatau, A. B., "Smart fabric sensors and e-textile technologies: A review," *Smart Materials and Structures*, vol. 23, no. 5, p. 053 001, Apr. 2014.

[8] Zama, T. and Shimada, S., "Simultaneous measurement of electroencephalography and near-infrared spectroscopy during voluntary motor preparation," *Scientific Reports*, vol. 5, no. 1, Nov. 2015.

[9] Baek, J.-Y., An, J.-H., Choi, J.-M., Park, K.-S., and Lee, S.-H., "Flexible polymeric dry electrodes for the long-term monitoring of ECG," *Sensors and Actuators A: Physical*, vol. 143, no. 2, pp. 423–429, May 2008.

[10] Gruetzmann, A., Hansen, S., and Müller, J., "Novel dry electrodes for ECG monitoring," *Physiological Measurement*, vol. 28, no. 11, pp. 1375–1390, Oct. 2007.

[11] Takei, K., Honda, W., Harada, S., Arie, T., and Akita, S., "Toward flexible and wearable human-interactive health-monitoring devices," *Advanced Healthcare Materials*, vol. 4, no. 4, pp. 487–500, Nov. 2014.

[12] Misra, V., Bozkurt, A., Calhoun, B., Jackson, T., Jur, J., Lach, J., Lee, B., Muth, J., Oralkan, O., Ozturk, M., Trolier-McKinstry, S., Vashaee, D., Wentzloff, D., and Zhu, Y., "Flexible technologies for self-powered wearable health and environmental sensing," *Proceedings of the IEEE*, vol. 103, no. 4, pp. 665–681, Apr. 2015.

[13] Liu, L., Yu, Y., Yan, C., Li, K., and Zheng, Z., "Wearable energy-dense and power-dense supercapacitor yarns enabled by scalable graphene–metallic textile composite electrodes," *Nature Communications*, vol. 6, no. 1, Jun. 2015.

[14] Vargas-Quesada, B., Chinchilla-Rodriguez, Z., and Rodriguez, N., "Identification and visualization of the intellectual structure in graphene research," *Frontiers in Research Metrics and Analytics*, vol. 2, Oct. 2017.

[15] Celik, N., Manivannan, N., Strudwick, A., and Balachandran, W., "Graphene-enabled electrodes for electrocardiogram monitoring," *Nanomaterials*, vol. 6, no. 9, p. 156, Aug. 2016.

[16] Lou, C., Li, R., Li, Z., Liang, T., Wei, Z., Run, M., Yan, X., and Liu, X., "Flexible graphene electrodes for prolonged dynamic ECG monitoring," *Sensors*, vol. 16, no. 11, p. 1833, Nov. 2016.

[17] Karim, N., Afroj, S., Malandraki, A., Butterworth, S., Beach, C., Rigout, M., Novoselov, K. S., Casson, A. J., and Yeates, S. G., "All inkjet-printed graphene-based conductive patterns for wearable e-textile applications," *Journal of Materials Chemistry C*, vol. 5, no. 44, pp. 11 640–11 648, 2017.

[18] Jung, H.-C., Moon, J.-H., Baek, D.-H., Lee, J.-H., Choi, Y.-Y., Hong, J.-S., and Lee, S.-H., "CNT/PDMS composite flexible dry electrodesfor long-term ECG monitoring," *IEEE Transactions on Biomedical Engineering*, vol. 59, no. 5, pp. 1472–1479, May 2012.

[19] Jiao, L., Chua, Z., Moon, S., Song, J., Bi, G., Zheng, H., Lee, B., and Koo, J., "Laser-induced graphene on additive manufacturing parts," *Nanomaterials*, vol. 9, no. 1, p. 90, Jan. 2019.

[20] Romero, F. J., Rivadeneyra, A., Toral, V., Castillo, E., Garcia-Ruiz, F., Morales, D. P., and Rodriguez, N., "Design guidelines of laser reduced graphene oxide conformal thermistor for IoT applications," *Sensors and Actuators A: Physical*, vol. 274, pp. 148–154, May 2018.

[21] Romero, F., Salinas-Castillo, A., Rivadeneyra, A., Albrecht, A., Godoy, A., Morales, D., and Rodriguez, N., "In-depth study of laser diode ablation of kapton polyimide for flexible conductive substrates," *Nanomaterials*, vol. 8, no. 7, p. 517, Jul. 2018.

[22] Duy, L. X., Peng, Z., Li, Y., Zhang, J., Ji, Y., and Tour, J. M., "Laser-induced graphene fibers," *Carbon*, vol. 126, pp. 472–479, Jan. 2018.

[23] Lin, J., Peng, Z., Liu, Y., Ruiz-Zepeda, F., Ye, R., Samuel, E. L. G., Yacaman, M. J., Yakobson, B. I., and Tour, J. M., "Laser-induced porous graphene films from commercial polymers," *Nature Communications*, vol. 5, no. 1, Dec. 2014.

[24] Wu, J.-B., Lin, M.-L., Cong, X., Liu, H.-N., and Tan, P.-H., "Raman spectroscopy of graphene-based materials and its applications in related devices," *Chemical Society Reviews*, vol. 47, no. 5, pp. 1822–1873, 2018.

[25] Meziane, N., Webster, J. G., Attari, M., and Nimunkar, A. J., "Dry electrodes for electrocardiography," *Physiological Measurement*, vol. 34, no. 9, R47–R69, Aug. 2013.

[26] Elgendi, M., Mohamed, A., and Ward, R., "Efficient ECG compression and QRS detection for e-health applications," *Scientific Reports*, vol. 7, no. 1, Mar. 2017.

[27] Barold, S. S., "Willem einthoven and the birth of clinical electrocardiography a hundred years ago," *Cardiac Electrophysiology Review*, vol. 7, no. 1, pp. 99–104, 2003.

[28] Castillo, E., Morales, D. P., Garcia, A., Parrilla, L., Ruiz, V. U., and Alvarez-Bermejo, J. A., "A clustering-based method for single-channel fetal heart rate monitoring," *PLOS ONE*, vol. 13, no. 6, Tolkacheva, E. G., Ed., e0199308, Jun. 2018.

[29] Xia, Y., Zhang, H., Xu, L., Gao, Z., Zhang, H., Liu, H., and Li, S., "An automatic cardiac arrhythmia classification system with wearable electrocardiogram," *IEEE Access*, vol. 6, pp. 16 529–16 538, 2018.

[30] Zhang, X., Liu, S., Zhao, X., Wu, F., Wu, Q., Wang, W., Cao, R., Fang, Y., Lv, H., Long, S., Liu, Q., and Liu, M., "Emulating short-term and long-term plasticity of bio-synapse based on cu/a-si/pt memristor," *IEEE Electron Device Letters*, vol. 38, no. 9, pp. 1208–1211, Sep. 2017.

[31] Toral, V., Garcia, A., Romero, F., Morales, D., Castillo, E., Parrilla, L., Gomez-Campos, F., Morillas, A., and Sanchez, A., "Wearable system for biosignal acquisition and monitoring based on reconfigurable technologies," *Sensors*, vol. 19, no. 7, p. 1590, Apr. 2019.

[32] Ferrari, A. C. and Basko, D. M., "Raman spectroscopy as a versatile tool for studying the properties of graphene," *Nature Nanotechnology*, vol. 8, no. 4, pp. 235–246, Apr. 2013.

[33] SPACH, M. S., BARR, R. C., HAVSTAD, J. W., and LONG, E. C., "Skin-electrode impedance and its effect on recording cardiac potentials," *Circulation*, vol. 34, no. 4, pp. 649–656, Oct. 1966.

[34] Takamatsu, S., Lonjaret, T., Crisp, D., Badier, J.-M., Malliaras, G. G., and Ismailova, E., "Direct patterning of organic conductors on knitted textiles for long-term electrocardiography," *Scientific Reports*, vol. 5, no. 1, Oct. 2015.

[35] Satija, U., Ramkumar, B., and Manikandan, M. S., "Automated ECG noise detection and classification system for unsupervised healthcare monitoring," *IEEE Journal of Biomedical and Health Informatics*, vol. 22, no. 3, pp. 722–732, May 2018.

[36] Castillo, E., Morales, D., Botella, G., Garcia, A., Parrilla, L., and Palma, A., "Efficient wavelet-based ECG processing for single-lead FHR extraction," *Digital Signal Processing*, vol. 23, no. 6, pp. 1897–1909, Dec. 2013.

[37] Mamaghanian, H., Khaled, N., Atienza, D., and Vandergheynst, P., "Compressed sensing for real-time energy-efficient ECG compression on wireless body sensor nodes," *IEEE Transactions on Biomedical Engineering*, vol. 58, no. 9, pp. 2456–2466, Sep. 2011.

[38] Sharma, L., Dandapat, S., and Mahanta, A., "ECG signal denoising using higher order statistics in wavelet subbands," *Biomedical Signal Processing and Control*, vol. 5, no. 3, pp. 214–222, Jul. 2010.

[39] Castillo, E., Morales, D. P., Garcia, A., Martinez-Marti, F., Parrilla, L., and Palma, A. J., "Noise suppression in ECG signals through efficient one-step wavelet processing techniques," *Journal of Applied Mathematics*, vol. 2013, pp. 1–13, 2013.

[40] Zidelmal, Z., Amirou, A., Adnane, M., and Belouchrani, A., "QRS detection based on wavelet coefficients," *Computer Methods and Programs in Biomedicine*, vol. 107, no. 3, pp. 490–496, Sep. 2012.

VIII.4 Supplementary Information

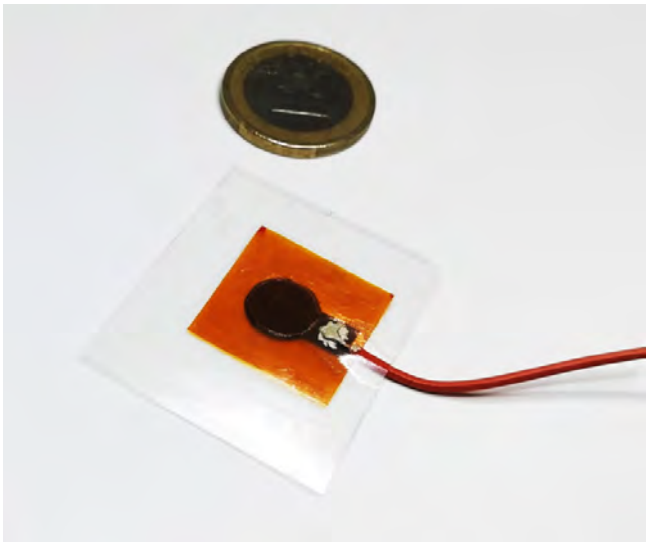

Figure VIII.4: Actual view of the ECG electrode including the connection of the wire and a thermal sealing to avoid undesired contacts.

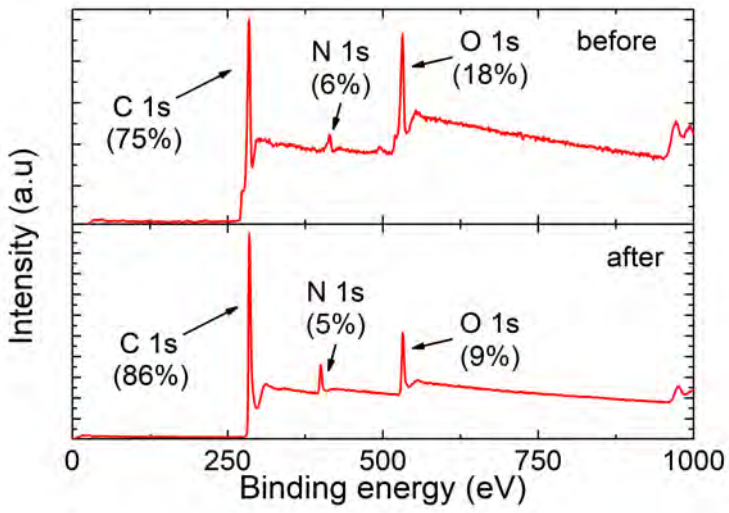

Figure VIII.5: Comparison of wide XPS spectra for Kapton® polyimide before and after the laser assisted photothermal process. The peaks correspond to the carbon (C 1s), nitrogen (N 1s) and oxygen (O 1s) species present in the chemical structure of these materials. Values in parentheses indicate the atomic concentrations of carbon, oxygen and nitrogen for both cases.

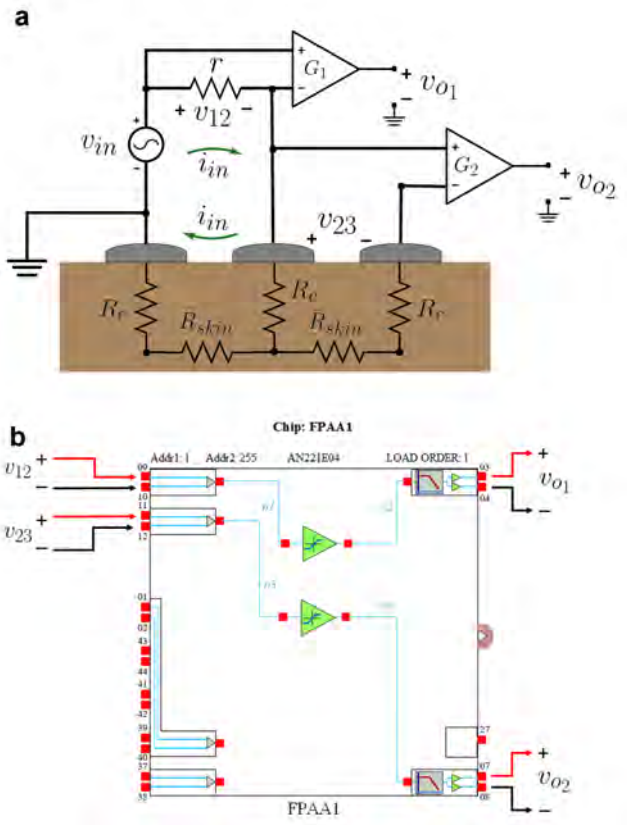

Figure VIII.6: (a) Model of the equivalent electrical circuit for three consecutive electrodes (R_c: contact resistance, R_{skin}: skin resistance). The contact resistance is obtained relating the voltage drop v_{23} and the input current i_{in}, which can be obtained from the voltage drop across the resistor r (v_{12}). v_{o1} and v_{o2} correspond to the voltages v_{12} and v_{23} amplified by a factor G_1 and G_2, respectively. (b) Anadigm IDE implementation of the measuring circuit shown in (a) for the Dynamic Reconfigurable Field-Programmable Analog Array FPAA AN221E04. A resistor r is externally connected to pins 09 and 10. The gains G_1 and G_2 of the differential amplifiers (green blocks) can be updated just by changing the FPAA firmware.

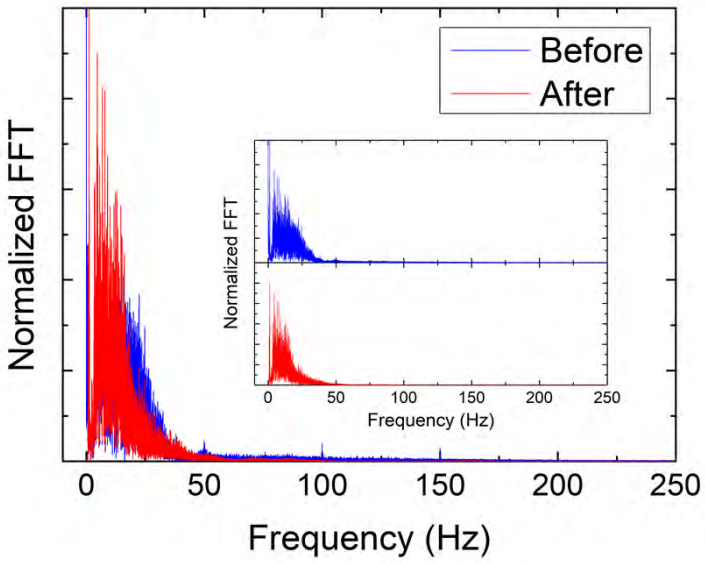

Figure VIII.7: Normalized module of the Fast Fourier Transform of an ECG signal before and after both baseline correction and denoising processes ($L = 9$, $M = 5$).

Paper IX

Laser-Fabricated Reduced Graphene Oxide Memristors

Francisco J. Romero [1,2,*], Alejandro Toral-Lopez [1,2], Akiko Ohata [3], Diego P. Morales [2,4], Francisco G. Ruiz [1,2], Andres Godoy [1,2], Noel Rodriguez [1,2]

[1] Pervasive Electronics Advanced Research Laboratory, University of Granada, 18071 Granada, Spain.
[2] Department of Electronics and Computer Technology, University of Granada, 18071 Granada, Spain.
[3] Institute of Space and Astronautical Science, Japan Aerospace Exploration Agency, Kanagawa 252-5210, Japan.
[4] Biochemistry and Electronics as Sensing Technologies Group, University of Granada, 18071 Granada, Spain.
* Corresponding author: franromero@ugr.es

Published in *Nanomaterials*, Jan 2019, volume 9(6), 897. DOI: 10.3390/nano9060897. Impact Factor: 4.324. JCR Rank: 42/103 (Q2) in *Nanoscience & Nanotechnology* and 89/314 (Q1) in *Materials Science, Multidisciplinary*.

Abstract

Finding an inexpensive and scalable method for the mass production of memristors will be one of the key aspects for their implementation in end-user computing applications. Herein, we report a pioneering research on the fabrication of laser-lithographed graphene oxide memristors. The devices have been surface-fabricated through a graphene oxide coating on a polyethylene terephthalate substrate followed by a localized laser-assisted photo-thermal partial reduction. When the laser fluence is appropriately tuned during the fabrication process, the devices present a characteristic pinched closed-loop in the current-voltage relation revealing the unique fingerprint of the memristive hysteresis. Combined structural and electrical experiments have been conducted to characterize the raw material and the devices that aim to establish a path for optimization. Electrical measurements have demonstrated a clear distinction between the resistive states, as well as stable memory performance, indicating the potential of laser-fabricated graphene oxide memristors in resistive

IX

switching applications.

Keywords: memristor, graphene oxide, laser-scribing, neuromorphic, flexible electronics.

IX.1 Introduction

The memristor (memory-resistor) is the fourth element needed to complete the relationships between the four fundamental electrical magnitudes (voltage, v; current, i; charge, q, and flux, ϕ), which establishes the missing link between charge and flux [1]. The memristor was predicted almost 50 years ago, fundamentally as a theoretical device [2], and then remained forgotten until the last decade when it was physically implemented [3]. Since then, the interest and research devoted to this electrical element have experienced an exponential rise [4]–[7]. On one side, it has become one of the most promising candidates for the so-called storage class memories in the form of resistive random access memories (ReRAMs) [8]–[11]. On the other side, memristors are devices able to mimic the behavior of biological synapses, opening the path for the future development of artificial intelligence in the emerging field of neuromorphic electronics [12]–[14]. The spike-timing-dependent plasticity (STDP) is the key characteristic in the development of neuromorphic computing circuits [4]; the conductance can be changed by the input pulses (related to the input charge injected into the device), in such a way, that they behave like solid-state artificial electronic synapses [15]. Moreover, memristor-based synapses are simpler and energetically more efficient than those based on complementary metal-oxide-semiconductor (CMOS) emulation circuits, allowing them to pave the way for the next generation of computing and human-machine interfaces.

In contrast to the other existing electrical elements, memristors present a unique voltage-current relationship determined by a closed hysteresis loop pinched in the origin. This characteristic can be considered as the electrical signature of memristors to the point that any device presenting this electrical behavior can be assimilated as one of them. Memristors present an intrinsic non-volatile memory effect because their resistance depends on the history of the device according to a certain state equation [2]: their state of resistance (typically high resistance state, HRS, or low resistance state, LRS) remains unaltered even in the absence of any energy supply. This memory effect has already reached the market and is being used in commercial digital applications [16].

One of the crucial issues that science needs to address concerning the rise of memristive electronics, especially for neuromorphic applications, is the selection of the best technology for the fabrication of the memristors. Memristors are commonly classified into four categories depending on the physico-chemical mechanism responsible for the memristive hysteresis: nanoionics, phase-change, electronics (ferroelectrics and those based on charge trapping/detrapping), and nanomechanics [4]. Experimentally, any device from these first three categories

applies to neuromorphic electronics due to its "analog" memristive behavior. It has been demonstrated that a large number of solids present analog memristive switching characteristics, including solid electrolytes (such as GeSe or Ag_2S), perovskites (e.g., $SrZrO_3$), transitions oxides (such as NiO or TiO_2), organic materials, or even amorphous silicon [4]. However, despite the large spectrum of existing memristive materials, there is not yet a real competitor for traditional Silicon-CMOS technologies that support the digital von-Neumann computational archetype. Research on memristive circuits needs to investigate differential advantages over silicon to gather pace within the field of electronics. This means that, apart from demonstrating their particular functionalities, memristors should be based on a cost-effective fabrication approach that avoids the use of scarce materials.

With the rise of graphene and related nanomaterials [17], a new path for the development of inexpensive resistive-switching devices has been opened. Graphene derivatives are being considered for both the application at the electrodes of the memristors [18] and as part of active memristive materials [19]. The reader can find a comprehensive review of the state of the art of graphene and transition metal dichalcogenides (TMDs) based resistive switching devices in reference [20]. This new family of memristors can benefit from the intrinsic characteristics of graphene-related materials (i.e., abundant raw materials, structural flexibility and transparency). Among these emerging candidates, it is graphene oxide (GO), a non-stoichiometric polycrystalline form of nanographene decorated with oxygen-containing functional groups [21], where most of the research interest is focused due to its easy processability and low cost. GO-incorporating memristors can be fabricated with a wide range of techniques, from the deposition of the pristine material [22] to reduced versions of it synthesized by chemical, electrochemical, thermal annealing, microwave irradiation, or photothermal treatments [23]. Among all the aforementioned techniques, the use of high-precision lasers to reduce GO is one of the most attractive alternatives since it allows for the combination of lithography and conductivity modulation in one single environmentally friendly step [24].

The application of laser-reduced graphene oxide for the fabrication of resistive switching devices was introduced first in 2014 by Tian *et al.* [25]. In that work, the authors presented a low-cost approach targeting the production of random-access memory using laser-reduced graphene oxide as the bottom electrode of a GO-HfO_x-Ag memristive stack. However, Tian *et al.* concentrated on achieving a high-conductivity GO-based electrode while the active memristive material remained as the HfO_x itself. In this work, for the first time, we introduce the development of laser-fabricated GO memristors that fully rely on the laser-reduction process to create the active switching element. This new process for the fabrication of memristors takes an inexpensive graphene oxide colloid as the precursor material. A computer numerical control (CNC) driven laser is used to photothermally reduce the GO, altering its nanostructure and leading, under appropriate laser-scribing conditions, to memristive behavior. This fabrication approach is extremely simple, which allows for an intrinsic lithography of the devices. The results have shown that the devices present a promising and

stable memristance which is correlated with the formation of low-resistance conductive paths originated by oxidation-reduction reactions within the GO body. The paper is structured as follows: the materials, experimental setup, and fabrication process are described in Section IX.2. Section IX.3 presents results on the structural and electrical characterization of the laser-fabricated memristors, showing that these devices point to potential applications not only in non-volatile memory storage but also in analog computing since they present, both, clear discrimination between the resistive states and stable memory performance. Section IX.4 includes a discussion of the origin of the memristance of the reduced-GO elements, and, finally, the main conclusions are highlighted in Section IX.5.

IX.2 Materials and Methods

IX.2.1 Materials

The precursor material for the fabrication of the memristors was an in-house prepared graphene oxide colloid (4 mg/mL). We followed a modified version of the Hummers and Offerman's method [26] starting with the oxidation of graphite for about two hours in an ice bath, using concentrated sulfuric acid (H_2SO_4), sodium nitrate ($NaNO_3$), and potassium permanganate ($KMnO_4$) as functionalization and oxidizing reagents (from Sigma-Aldrich Corp., St. Louis, MO, USA). The oxidized graphite is filtered (HCl) and washed (H_2O) to remove remaining ions. Then, with the aid of sonication (30 min) and due to the increased interlayer distance caused by the introduction of the functional groups, water molecules can easily penetrate in the layers producing layer splitting leading to the GO colloid. Further details on the production of the GO colloid can be found in [24]. Polyethylene terephthalate films (PET) (3M, St. Paul, MN, USA) were used as supporting substrates for the samples. Electrical access to the memristors was achieved by applying micro-drops of conductive carbon-based paste (Bare Conductive Electric Paint, London, UK), or Ag-loaded conductive paint (RS, Corby, UK).

IX.2.2 Experimental Setup

The CNC driving the laser used for laser-scribing the devices was partially developed in our group. This system allows the patterning of surfaces located in a horizontal holder at 6 cm from the exposure source. The laser excursion speed was fixed at 3 min/cm^2. The 405 nm laser head was acquired from Q-BAIHETM, model 405ML-300-2290 (Shenzhen, China) using a laser diode as an exposure source (Figure IX.1a). The power of the laser can be modulated from 10 mW to 300 mW. The 3D-shaker (Seoulin Bioscience, South Korea) used for the GO homogenization during the water evaporation process was set to an orbital speed of 0.3 rps Scanning electron microscopy (SEM) images were acquired by a field-emission scanning electron microscope (NVision40 from Carl Zeiss, Oberkochen, Germany) set at an extraction and acceleration voltage of 5

kV. Raman spectra were recorded with a dispersive micro-Raman spectrometer (JASCO NRS-5100, Easton, PA, USA) with a green diode as the excitation source (Elforlight G4-30; Nd:YAG, $\lambda = 532$ nm). The X-ray photoelectron spectroscopy (XPS) experiments were carried out on a Kratos Axis Ultra-DLD (Manchester, UK), using an X-ray (Al Kα, h$\upsilon = 1486.6$ eV) power of 450 W in a vacuum chamber where the pressure was kept below 10^{-10} Torr. The Casa-XPS® software (Teignmouth, UK) was used for the XPS spectra deconvolution. Attenuated total reflectance Fourier transform infrared (ATR-FTIR) spectroscopy was carried out using a Bruker Tensor 27 spectrometer (MA, USA). The electrical measurements were performed by a Keysight® B2902A precision source-measure unit controlled by Easy-Expert® software (CA, USA). Samples were located on an Everbeing® C-series analytical probe station (Taiwan).

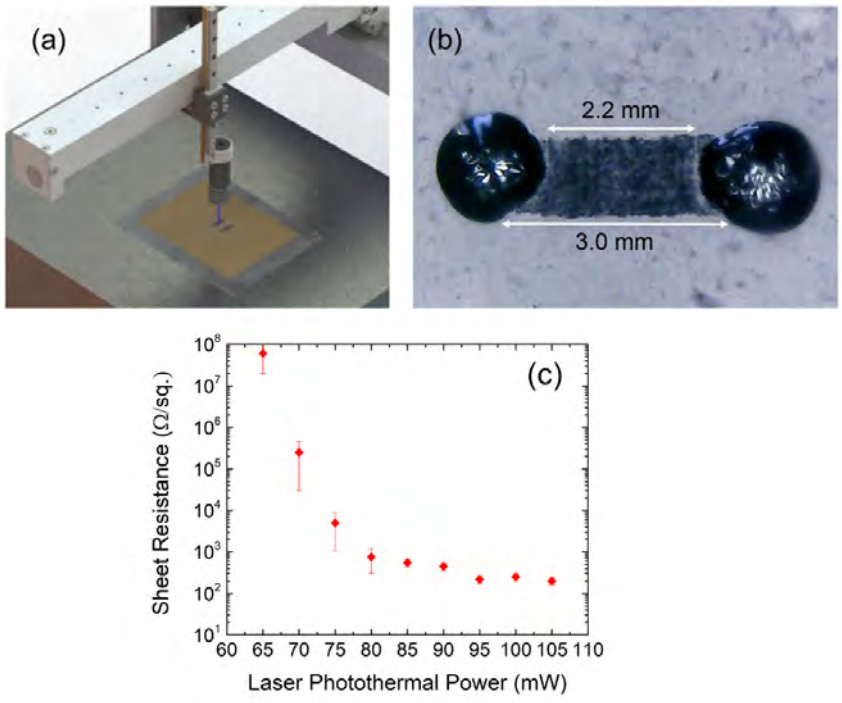

Figure IX.1: (a) Schematic of the CNC-driven laser used for the fabrication of rGO memristors. The spatial resolution of the system used in this work is 10 μm. (b) Actual picture of one of the laser-fabricated memristors ($L = 2.2$ mm, $W = 1$ mm) using microdrops of bare conductive electric paint™ as contacting electrodes. (c) Sheet resistance of laser-reduced graphene oxide samples (4 mg/mL) on PET treated at different laser powers ($\lambda = 405$ nm) extracted by the transmission line method (TLM) [27]. Error bars were calculated as the standard deviation of 15 different samples for each laser power.

IX.2.3 Laser-Reduced Memristor Fabrication

The raw film for the fabrication of the memristors was prepared by drop-casting the GO colloid on PET films (0.5 mL/cm^2). Next, they were placed on a 3D-shaker for 48 h at room temperature (relative humidity 50%) until the water was fully evaporated. According to the Kelvin measurements, the resulting GO layer was essentially an electrical insulator ($\rho_s > 10$ MΩ/sq.) with an approximate thickness of 200 μm according to the optical profilometry results.

The memristors were fabricated by laser-scribing the surface of the GO film (Figure IX.1a). The laser is only used for the fabrication of the samples and it is not involved in the electrical measurements carried out for the characterization of the resistive switching of the devices. Starting with the bare GO film, the laser triggers a photothermal reduction process that removes oxygen-containing functional groups (increasing the atomic percentage of carbon) and partially recovers the sp^2 hybridized carbon-carbon bonds, increasing the conductivity of the nanographene flakes according to the laser power [28]. The laser power can be adjusted to modulate the conductivity of the samples leading to different levels of reduction. The dependence of the sheet resistance of the laser-reduced GO as a function of the photothermal power was investigated. The results, summarized in Figure IX.1c, show that an increase of the laser power results in a dramatic decrease of sheet resistance (from >MΩ/sq. to <kΩ/sq.) for a relatively narrow power window, reflecting the progressive reduction of the GO sample. It is also possible to observe that, for a laser power below 85 mW, the variability of the sheet resistance increases partly due to the appearance of the resistive switching. For a laser power over 85 mW, the improvement of the conductance (decrease of the sheet-resistance) tends to saturate.

For the purpose of the experiments, memristors with a macroscopic rectangular size of $L = 3$ mm, $W = 1$ mm, were fabricated at a laser power ranging from 40 mW to 100 mW. The laser-scribing process was performed at room temperature with a controlled relative humidity of 50% and a constant airflow forced by a fume extractor system. These conditions avoid any intentional doping during the lithographic process; however, the intentional doping/functionalization of the devices by setting an appropriate environment during the laser-scribing process [28], [29] constitutes a path to be explored for boosting the performance of this type of devices. Micro drops of bare conductive electric paint^{TM} or Ag-based conductive paint were placed as electrodes to define the electrical access and to avoid any damage on the active GO material when contacting the devices with probes. This contact approach led to a reduction of the effective length of the devices of about 0.8 mm, resulting in an effective dimension of L = 2.2 mm, W = 1.0 mm (Figure IX.1b). As observed, the edges of the final device present a slight roughness consequence of the mechanical limitations of the experimental setup. However, this fact should not represent any constraint for scaling down the device if a more sophisticated positioning system is used (i.e., a galvanometric positioning allows a linewidth of 10 μm and a repeatability of 1 μm).

IX.3 Results

IX.3.1 Structural Characterization

We investigated the changes induced by the laser photothermal process in the chemical structure of the GO (Figure IX.2) by SEM, Raman spectroscopy, XPS, and ATR-FTIR spectroscopy.

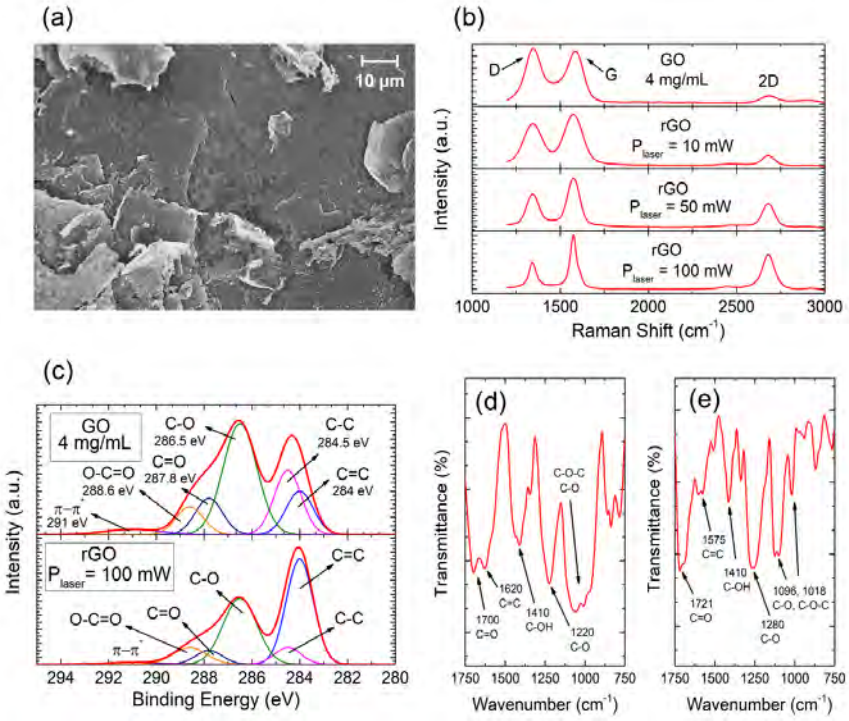

Figure IX.2: Structural characterization. (a) SEM image of laser-reduced graphene oxide at 70 mW (initial GO colloid concentration 0.5 mL/cm^2). (b) Raman spectra acquired from the GO film before and after the laser-assisted reduction for different laser powers. (c) Comparison of the C1s peak from the XPS spectrum of both GO (top) and laser-reduced GO (bottom) samples. (d) ATR-FTIR spectra of unreduced GO. (e) ATR-FTIR spectra of 100 mW laser-reduced GO.

Figure IX.2a shows an SEM image of a laser-reduced GO area. The laser-treated surface is characterized by a large roughness and porosity as a consequence of the spontaneous and violent release of oxygen-containing functional groups during the photothermal process.

The Raman spectroscopy provided information about the lattice structure of the sp^2 hybridized carbon systems. It is worth mentioning that the spectra were

acquired with special caution to avoid any undesired photothermal reduction of the GO by the laser stimulation source itself [30]. In particular, the laser power was set to 5.3 mW with an 80% attenuation and acquisition time of 15 s. As can be seen in Figure IX.2b, the Raman spectra of the bare GO and laser-reduced GO samples are composed of three main peaks at approximately 1350 cm^{-1} (D), 1620 cm^{-1} (G) and 2700 cm^{-1} (2D). The presence of disorders in the sp^2 structure is evaluated through the relative intensity of the I_G/I_D ratio, while the intensity of the 2D band gives information about the number of layers of the graphene-derived structure (which may range from the one single layer of pristine graphene to the multilayer structure of graphite) [31], [32]. Thus, Figure IX.2b shows the evolution of defects in the graphene-based samples as well as the changes in their layer structure as the photothermal power of the laser increases. For the raw GO, the prominent intensity and area of the D peak, with respect to the G peak, is a consequence of the structural imperfections created by the oxidation process of the graphite. Besides, the almost nonexistent 2D band indicates the multilayer and defective nature of the GO sample. When the laser-scribing process is applied on the surface, the photothermal reduction takes place, and as the laser power increases, the G and D peaks become narrower and the I_G/I_D ratio increases, demonstrating the decrease of the number of defects, and therefore the reduction of the GO. Moreover, the gradual restoration of the crystallographic structure is also manifested by the decrease of the I_G/I_{2D} ratio along the photothermal process [24].

XPS experiments were performed for a better understanding of the nature of the defects. The results showed that the initial atomic percentages of ∼52% and ∼45% for both carbon and oxygen species of GO became ∼72% (C) and ∼26% (O) after the reduction at a laser power of 100 mW. Furthermore, Figure IX.2c shows the C1s XPS high-resolution spectra of the GO film before and after the laser treatment and their deconvolution. The defects in the structure of the sp^2 hybridized carbon bonds (284 eV) are associated to C-C sp^3 bonds (284.5 eV), carbon-oxygen compounds (C-O, 286.5 eV) present as hydroxyl (C-OH) and epoxy (C-O-C) groups, carbonyl groups (C=O, 287.8 eV) as well as O-C=O (288.6 eV) and $\pi - \pi^*$ transitions (291 eV) [33], [34]. Therefore, the GO film presents a large contribution of sp^3 hybridized carbon bonds and different carbon-oxygen compounds as a consequence of the oxidation process. The laser treatment turns a large portion of sp^3 carbon into sp^2 hybridized carbon, which is a clear indication of a graphene-based composite material [35], and removes a significant portion of the defects introduced by carbon-oxygen compounds, as it was reflected in the Raman results.

All these results are also consistent with those achieved from the ATR-FTIR experiments, shown in Figure IX.2d,e. In the GO spectrum (Figure IX.2d), the different oxygen-containing functional groups can be observed at the broad peaks located at 1700 cm^{-1} (C=O stretching vibrations in carbonyl and carboxyl groups), 1410 cm^{-1} (C-OH hydroxyl), as well as at 1220 cm^{-1} and at the band from 968 cm^{-1} to 1060 cm^{-1} associated with epoxy and other C-O groups. Moreover, one band at 1620 cm^{-1} due to the skeletal vibrations of unoxidized sp^2 hybridized carbon bonds is also observed [36]–[38]. After the laser photothermal

reduction (Figure IX.2e), the sp^2 hybridized carbon domain is also present but shifted to 1575 cm^{-1} [39]. Besides, a significant reduction of the bands associated with the oxygen-containing groups is detected, which is a clear evidence of the successful laser-reduction of the GO.

IX.3.2 Electrical Characterization

The laser-reduced graphene oxide memristors were initially characterized by cyclically applying a triangular voltage bias at the two surface electrodes [-3.5, 3.5] V and simultaneously monitoring the driven current using a source-measure unit (SMU), as the inset of Figure IX.3a shows. Unless otherwise specified, the experiments presented hereinafter were performed using bare conductive electric paint^{TM} as contacting electrodes. Representative results of the current-voltage characteristics are shown in Figure IX.3a for a memristor lithographed at a laser power of 70 mW. As can be observed, the device presents the unequivocal fingerprint of a bipolar memristor [40], corresponding to a closed pinched hysteresis loop collapsed in the origin in its current-voltage characteristic. In Figure IX.3a, the two resistive states of the device are identified presenting a resistance, in the initial cycle, of R = 896 kΩ and R = 75 kΩ at the HRS and LRS, respectively. These resistances have been measured within the voltage range [-1, 1] V. All the fabricated devices presented a forming-free resistive switching [23]. The top inset of Figure IX.3a shows an example of another device contacted with Ag-loaded conductive paint. As observed, the device presents similar memristive hysteresis. This contact independence of the memristance allows elucidating the underlying mechanisms responsible for the resistive switching, as discussed in detail in Section IX.4, and opens this technology to the investigation of a large variety of contact approaches.

As it is the case of some other reported symmetric memristors [41]–[43], the polarity of the device can only be determined after the first cycle of its current-voltage characteristic. Prospective studies are to be conducted to disclose if it is possible to induce a specific polarity during the fabrication process or by using an electrical approach. The memristive behavior of the devices (i.e., the pinched hysteresis loop, as shown in Figure IX.3a) was investigated for different values of the laser power. The results, summarized as the ratio between the resistive states, are shown in Figure IX.3b. As observed, the largest hysteresis was spotted for the devices laser-fabricated from 65 mW to 75 mW. Whereas, for the devices reduced at a laser power below 60 mW, the memristance was not observable. This does not mean that resistive switching effects were not taking place in the structures but rather that they were fully masked by the high resistance of the material. At the opposite end of the scale, we did not observe any memristance for devices reduced at a laser power over 80 mW. We speculate that the number of oxygen-containing functional groups resulting after the laser treatment was too small to appreciate any hysteresis effect on the current-voltage characteristic (see Section IX.4 for further discussion).

The stability of the resistive states has been assessed by continuous device cycling. Results represented in Figure IX.4a show that after 10 complete up and

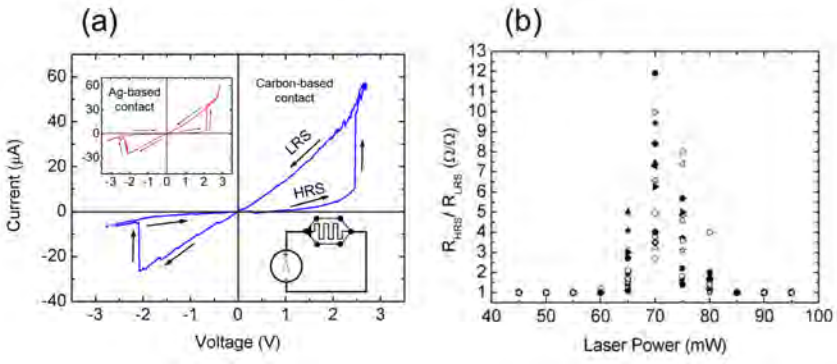

Figure IX.3: Electrical performance of a laser-reduced GO memristor (P_{laser} = 70 mW, L = 2.2 mm, W = 1 mm). (a) Current-voltage characteristic of a memristor showing the characteristic signature of memristance. The voltage has been scanned from -3 V to 3 V with a voltage step of 10 mV. The scanning rate was adjusted to 2 V/s. The top inset of the figure shows an example of another device fabricated with Ag-based contacts. (b) Ratio of the resistance measured in the high resistance state (HRS) and low resistance state (LRS) of a set of laser-lithographed graphene oxide memristors fabricated at different laser power (15 devices for each laser power). The resistance was extracted in the range [-1,1] V of the current-voltage characteristics. The memristors were of identical dimensions with an effective length of 2.2 mm and width of 1 mm.

down voltage excursions, without establishing any current compliance during the measurements, the states remain reasonably stable with a tolerance <30% and the average values of high and low resistance states $<R_{HRS}>$ = 900 kΩ and $<R_{LRS}>$ = 84 kΩ, respectively. After the cycling of the device, there is neither a significant degradation in the performance nor an overlap between the HRS and LRS. The devices can safely be cycled further if the current compliance is set to 20 μA, limiting the power dissipated and preventing irreversible resistive switching. As shown in Figure IX.4b, under these requisites it is possible to achieve 100 cycles. These values, despite still well below the endurance values of better established inorganic memristor technologies [44], are comparable with other GO-based memristors. For example, in [45] the endurance properties of Al/GO/ITO devices were evaluated during 100 switching cycles, showing that the HRS and LRS values and its ratio maintained stable values. In a recent work [46], the authors make clear statements about the lack of research efforts in organic devices compared with their inorganic counterparts. They specifically highlight that problems arise from insufficient reproducibility, endurance, stability, scalability, and low switching speed. In their Table S1 (Supplementary Materials) they present a comprehensive comparison between the state of the art of both organic and inorganic oxide memristors. The data presented for the reduced-GO material indicates an endurance of 250 cycles, which is far below (orders of magnitude)

the values already demonstrated for other materials shown in Table S2 of the same work. Specifically, they refer to [47] where a metal/rGO/metal memory device was fabricated and characterized. In that work, after 250 cycles, the HRS and LRS values show a noticeable degradation, as depicted in its Figure 8a. In Ref. [48], a Pt/GO/ITO device was fabricated and characterized, which demonstrates good retention characteristics up to 100 cycles.

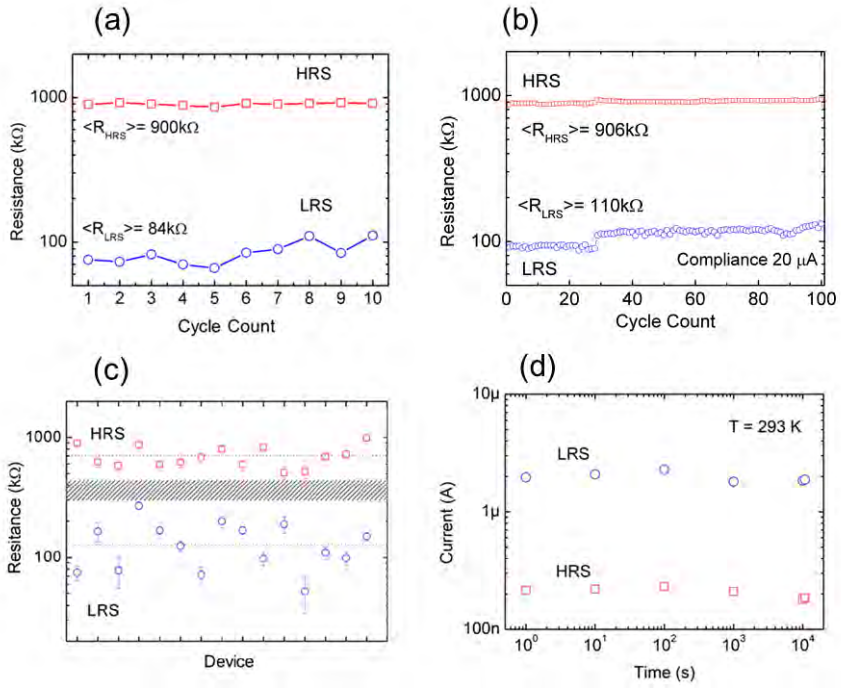

Figure IX.4: (a) Resistance values obtained from successive programming/erasing cycles without current compliance. Average values of the resistance at the HRS and LRS are included. (b) Resistance values obtained from successive device cycling demonstrating up to 100 cycles. The experiments were carried out by establishing a current compliance of 20 μA. (c) Resistance values obtained from 15 different memristors at the HRS and LRS states. Error bars illustrate the resistance variability of the device during 10 cycles. (d) Retention characteristic of laser-reduced graphene oxide memristor at room temperature (same device for LRS and HRS states). The state of the device is read with 0.2 V pulses during 50 ms.

Figure IX.4c shows statistical results of the HRS and LRS states of 15 laser-fabricated graphene oxide memristors (lithographed at 70 mW). The variability, especially that of the LRS state, is relatively high; however, there is no overlap in the distributions of states. Furthermore, the resistance ratio between the states remains around a factor of 6, which can be considered a promising achievement

given the early stage of development of the devices (best ratio = 11.9, worst ratio = 3.2). Finally, Figure IX.4d shows results on the characterization of the retention time of a memristor at room temperature. The current at the HRS and LRS was monitored periodically (every time-decade) applying 0.2 V/50 ms pulses during 4 hours after programming the HRS or LRS exemplifying the non-volatility of the states. A low reading voltage (0.2 V) was selected to avoid device disturbance given that in this experiment it was only necessary to discriminate the states.

IX.4 Discussion

An in-depth understanding of the physical mechanisms of the resistive switching-process in GO and reduced-GO is yet a subject under study and not exempt from controversy [49]. Two main models have been proposed to explain the formation of conductive paths involved in the resistive switching of GO. In one of the theories, the conductivity of the GO layer is modified according to redox reactions of the electrodes at the interface between GO and metals [50]. Our results have shown equivalent memristive behavior under different contact approaches (see Figure IX.3a), making us rule out this process as the origin of the memristance. This is specifically supported because, in the case of the devices contacted with bare conductive electric paint^{TM}, there are no metallic agents in the composite (water, natural resin, conductive carbon, humectant agent, diazolidinyl urea, and preservative agents [51]).

The other model to explain the resistive switching in GO films proposes that the conductive path is caused by transforming insulating sp^3 domains to conducting sp^2 bonds (oxygen vacancies) based on the detachment of oxygen groups under the action of an electric field [49], [52]. Several works based on first principles and statistical calculations have demonstrated the tendency of the oxygen functionalities to agglomerate and form highly oxidized domains surrounded by areas of pristine graphene [53], [54]. In Ref. [55], the authors studied the reversible oxidation of graphene oxide by DFT. Their studies show that although the bonding between oxygen and carbon atoms is strong, the migration barrier of oxygen atoms is below 0.8 eV. These values are further corroborated in [53], which estimates an energy of 0.6 eV (on average) for those endothermic reactions.

This second model is likely to explain the switch of the resistance of laser-fabricated graphene oxide memristors. Thus, the memristance relates to a bulk phenomenon involving the drift of oxygen ions and oxygen-containing groups inducing local changes in the level of reduction of the GO, hence turning it into a more conductive state [23], [56], [57]. This statement is also supported by estimating the energy involved during the resistive switching process. In our devices, the transitions HRS to LRS are typically occurring at a current of 10 μA (Figure IX.3a) and a resistance (HRS) of 1 MΩ (Figure IX.4a). Therefore, the power involved in the transition is about $\sim$0.1 mW. The transition time cannot be determined precisely due to the large time constant of the devices

which masks the actual physical phenomenon somewhere below 20 ms. However, we do not expect this device to achieve the sub-ms transitions of more scaled technologies [58]. Therefore, we elucidate that this transition is in the range from 1 ms to 10 ms. According to this, the energy supplied to the device is above 10^12 eV, consistent enough to trigger a significant percentage of the migration and recombination of oxygen ions and functional groups across the basal plane [53], since the number of surface sp^3 C-O bonds can be roughly estimated in the order of $\sim 10^13$ C atoms ($\sim 10^19$ C atoms cm^{-2} in the graphitic structure [59], and 60% of carbon sp^3-hybridized with oxygen-containing functional groups according to the XPS experiments).

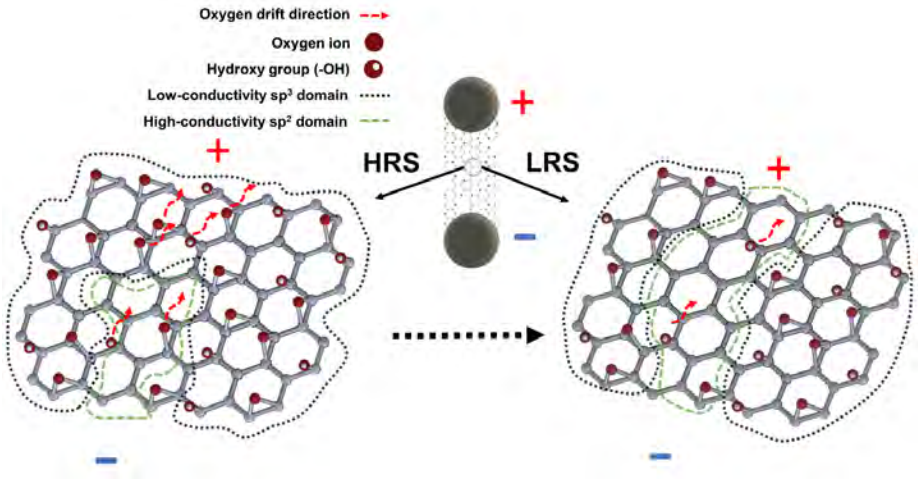

Figure IX.5: Conceptual model of the origin of the resistive switching of laser-fabricated graphene oxide memristors illustrating the transition from HRS to LRS. Starting from an HRS state, under the action the current flow, the electrostatic potential is mostly applied on the non-conductive sp^3 domains resulting in large local electric fields. The sp^2 based conductive domain (area surrounded by the green dashed line) is extended by the field-assisted migration of oxygen ions, creating a local high conductivity path leading to an LRS state.

Figure IX.5 illustrates the process of resistive switching. The non-uniformity in the number and location of the functional groups of the partially reduced graphene oxide [60]–[62] is responsible for the creation of different conductive domains. sp^2 high-conductive domains are interrupted by low-conductive ones (sp^3) at a nanoscale level. When a current is flowing, the electrostatic potential is mostly applied on those non-conductive regions resulting in large local electric fields. sp^2-based conductive paths are set up under the action of the current flow leading to an LRS state. The hypothesis of the formation of interconnected high-conductivity domains does not mean that the high conductivity state is related to a homogeneously distributed conduction medium, but rather the LRS

is correlated with a confined effect associated to the formation of a percolation path (or paths) of highly reduced GO by the energy accumulated in the device. Under reversed polarity, a partial recombination of the oxygen vacancies and mobile ions is possibly resulting in the recovery of the HRS. According to [49], this recombination can also be triggered by thermal effects resulting in degradation of the LRS or even in a retention failure when it is produced spontaneously. This latter statement is in agreement with our need to limit the current driven at the LRS (Figure IX.4b) when performing multiple cycles to avoid the collapse of the current hysteresis.

IX.5 Conclusions

This work addressed the fabrication of organic memristors based on the laser-assisted reduction of graphene oxide. This technique has been demonstrated as a fast and reliable approach for fabricating the devices with a clear advantage in its simplicity and intrinsic lithography. The results have proved that after tuning the photothermal intensity of the ablation process, the devices feature a prominent and stable memristance. Therefore, this fabrication technique may constitute a new high throughput approach for the advent of memristive circuits. According to our experiments and existing theories, the resistive switching of the devices is attributed to oxygen-containing functional groups drift modifying the local stoichiometry of the reduced-graphene oxide layer. Low-resistance conductive paths are formed in the bulk of the material when sp^3 domains are tuned into sp^2 domains (oxygen vacancies). The sp^3 domains can be recovered by reverse polarity and these mechanisms are likely to be triggered by dissipative effects and assisted by the electric field.

Acknowledgements. This work has been supported by the Spanish Ministry of Science, Innovation and Universities/FEDER-EU through the project TEC2017-89955-P, Iberdrola Foundation under its 2018 Research Grant Program, the pre-doctoral grants FPU16/01451, FPU16/04043, and the JSPS KAKENHI through grant number JP18k04275.

References

[1] Chua, L., "Memristor-the missing circuit element," *IEEE Transactions on Circuit Theory*, vol. 18, no. 5, pp. 507–519, 1971.

[2] Chua, L. and Kang, S. M., "Memristive devices and systems," *Proceedings of the IEEE*, vol. 64, no. 2, pp. 209–223, 1976.

[3] Strukov, D. B., Snider, G. S., Stewart, D. R., and Williams, R. S., "The missing memristor found," *Nature*, vol. 453, no. 7191, pp. 80–83, May 2008.

[4] Tetzlaff, R., *Memristors and Memristive Systems*, Tetzlaff, R., Ed. Springer-Verlag GmbH, Jan. 1, 2014.

[5] Wang, L., Yang, C., Wen, J., Gai, S., and Peng, Y., "Overview of emerging memristor families from resistive memristor to spintronic memristor," *Journal of Materials Science: Materials in Electronics*, vol. 26, no. 7, pp. 4618–4628, Mar. 2015.

[6] Hu, S. G., Wu, S. Y., Jia, W. W., Yu, Q., Deng, L. J., Fu, Y. Q., Liu, Y., and Chen, T. P., "Review of nanostructured resistive switching memristor and its applications," *Nanoscience and Nanotechnology Letters*, vol. 6, no. 9, pp. 729–757, Sep. 2014.

[7] Rehn, D. A. and Reed, E. J., "Memristors with distorted structures," *Nature Materials*, vol. 18, no. 1, pp. 8–9, Dec. 2018.

[8] Gonzalez-Rosillo, J. C., Ortega-Hernandez, R., Jareño-Cerulla, J., Miranda, E., Suñe, J., Granados, X., Obradors, X., Palau, A., and Puig, T., "Volume resistive switching in metallic perovskite oxides driven by the metal-insulator transition," *Journal of Electroceramics*, vol. 39, no. 1-4, pp. 185–196, Jul. 2017.

[9] Gale, E., "TiO2-based memristors and ReRAM: Materials, mechanisms and models (a review)," *Semiconductor Science and Technology*, vol. 29, no. 10, p. 104 004, Sep. 2014.

[10] Rodriguez-Fernandez, A., Aldana, S., Campabadal, F., Sune, J., Miranda, E., Jimenez-Molinos, F., Roldan, J. B., and Gonzalez, M. B., "Resistive switching with self-rectifying tunability and influence of the oxide layer thickness in ni/HfO2/n+-si RRAM devices," *IEEE Transactions on Electron Devices*, vol. 64, no. 8, pp. 3159–3166, Aug. 2017.

[11] Lanza, M., Wong, H.-S. P., Pop, E., Ielmini, D., Strukov, D., Regan, B. C., Larcher, L., Villena, M. A., Yang, J. J., Goux, L., Belmonte, A., Yang, Y., Puglisi, F. M., Kang, J., Magyari-Köpe, B., Yalon, E., Kenyon, A., Buckwell, M., Mehonic, A., Shluger, A., Li, H., Hou, T.-H., Hudec, B., Akinwande, D., Ge, R., Ambrogio, S., Roldan, J. B., Miranda, E., Suñe, J., Pey, K. L., Wu, X., Raghavan, N., Wu, E., Lu, W. D., Navarro, G., Zhang, W., Wu, H., Li, R., Holleitner, A., Wurstbauer, U., Lemme, M. C., Liu, M., Long, S., Liu, Q., Lv, H., Padovani, A., Pavan, P., Valov, I., Jing, X., Han, T., Zhu, K., Chen, S., Hui, F., and Shi, Y., "Recommended methods to study resistive switching devices," *Advanced Electronic Materials*, vol. 5, no. 1, p. 1 800 143, Sep. 2018.

[12] Wang, S., Xu, J., Wang, W., Wang, G.-J. N., Rastak, R., Molina-Lopez, F., Chung, J. W., Niu, S., Feig, V. R., Lopez, J., Lei, T., Kwon, S.-K., Kim, Y., Foudeh, A. M., Ehrlich, A., Gasperini, A., Yun, Y., Murmann, B., Tok, J. B.-H., and Bao, Z., "Skin electronics from scalable fabrication of an intrinsically stretchable transistor array," *Nature*, vol. 555, no. 7694, pp. 83–88, Feb. 2018.

[13] Jo, S. H., Chang, T., Ebong, I., Bhadviya, B. B., Mazumder, P., and Lu, W., "Nanoscale memristor device as synapse in neuromorphic systems," *Nano Letters*, vol. 10, no. 4, pp. 1297–1301, Apr. 2010.

[14] Zhang, X., Liu, S., Zhao, X., Wu, F., Wu, Q., Wang, W., Cao, R., Fang, Y., Lv, H., Long, S., Liu, Q., and Liu, M., "Emulating short-term and long-term plasticity of bio-synapse based on cu/a-si/pt memristor," *IEEE Electron Device Letters*, vol. 38, no. 9, pp. 1208–1211, Sep. 2017.

[15] Indiveri, G., Linares-Barranco, B., Legenstein, R., Deligeorgis, G., and Prodromakis, T., "Integration of nanoscale memristor synapses in neuromorphic computing architectures," *Nanotechnology*, vol. 24, no. 38, p. 384 010, Sep. 2013.

[16] Kelion, L. (Jul. 2015). "3d xpoint memory: Faster-than-flash storage unveiled," BBC News, [Online]. Available: https://www.bbc.com/news/technology-33675734.

[17] Geim, A. K. and Novoselov, K. S., "The rise of graphene," *Nature Materials*, vol. 6, no. 3, pp. 183–191, Mar. 2007.

[18] Yao, J., Lin, J., Dai, Y., Ruan, G., Yan, Z., Li, L., Zhong, L., Natelson, D., and Tour, J. M., "Highly transparent nonvolatile resistive memory devices from silicon oxide and graphene," *Nature Communications*, vol. 3, no. 1, Jan. 2012.

[19] Wu, C., Li, F., and Guo, T., "Efficient tristable resistive memory based on single layer graphene/insulating polymer multi-stacking layer," *Applied Physics Letters*, vol. 104, no. 18, p. 183 105, May 2014.

[20] Hui, F., Grustan-Gutierrez, E., Long, S., Liu, Q., Ott, A. K., Ferrari, A. C., and Lanza, M., "Graphene and related materials for resistive random access memories," *Advanced Electronic Materials*, vol. 3, no. 8, p. 1 600 195, May 2017.

[21] Dreyer, D. R., Park, S., Bielawski, C. W., and Ruoff, R. S., "The chemistry of graphene oxide," *Chem. Soc. Rev.*, vol. 39, no. 1, pp. 228–240, 2010.

[22] Porro, S., Accornero, E., Pirri, C. F., and Ricciardi, C., "Memristive devices based on graphene oxide," *Carbon*, vol. 85, pp. 383–396, Apr. 2015.

[23] Porro, S. and Ricciardi, C., "Memristive behaviour in inkjet printed graphene oxide thin layers," *RSC Advances*, vol. 5, no. 84, pp. 68 565–68 570, 2015.

[24] Romero, F. J., Rivadeneyra, A., Toral, V., Castillo, E., Garcia-Ruiz, F., Morales, D. P., and Rodriguez, N., "Design guidelines of laser reduced graphene oxide conformal thermistor for IoT applications," *Sensors and Actuators A: Physical*, vol. 274, pp. 148–154, May 2018.

[25] Tian, H., Chen, H.-Y., Ren, T.-L., Li, C., Xue, Q.-T., Mohammad, M. A., Wu, C., Yang, Y., and Wong, H.-S. P., "Cost-effective, transfer-free, flexible resistive random access memory using laser-scribed reduced graphene oxide patterning technology," *Nano Letters*, vol. 14, no. 6, pp. 3214–3219, May 2014.

[26] Hummers, W. S. and Offeman, R. E., "Preparation of graphitic oxide," *Journal of the American Chemical Society*, vol. 80, no. 6, pp. 1339–1339, Mar. 1958.

[27] Romero, F., Salinas-Castillo, A., Rivadeneyra, A., Albrecht, A., Godoy, A., Morales, D., and Rodriguez, N., "In-depth study of laser diode ablation of kapton polyimide for flexible conductive substrates," *Nanomaterials*, vol. 8, no. 7, p. 517, Jul. 2018.

[28] Wan, Z., Wang, S., Haylock, B., Kaur, J., Tanner, P., Thiel, D., Sang, R., Cole, I. S., Li, X., Lobino, M., and Li, Q., "Tuning the sub-processes in laser reduction of graphene oxide by adjusting the power and scanning speed of laser," *Carbon*, vol. 141, pp. 83–91, Jan. 2019.

[29] Guan, Y. C., Fang, Y. W., Lim, G. C., Zheng, H. Y., and Hong, M. H., "Fabrication of laser-reduced graphene oxide in liquid nitrogen environment," *Scientific Reports*, vol. 6, no. 1, Jun. 2016.

[30] Amato, G., Milano, G., Vignolo, U., and Vittone, E., "Kinetics of defect formation in chemically vapor deposited (CVD) graphene during laser irradiation: The case of raman investigation," *Nano Research*, vol. 8, no. 12, pp. 3972–3981, Oct. 2015.

[31] Wu, J.-B., Lin, M.-L., Cong, X., Liu, H.-N., and Tan, P.-H., "Raman spectroscopy of graphene-based materials and its applications in related devices," *Chemical Society Reviews*, vol. 47, no. 5, pp. 1822–1873, 2018.

[32] Hao, Y., Wang, Y., Wang, L., Ni, Z., Wang, Z., Wang, R., Koo, C. K., Shen, Z., and Thong, J. T. L., "Probing layer number and stacking order of few-layer graphene by raman spectroscopy," *Small*, vol. 6, no. 2, pp. 195–200, Jan. 2010.

[33] Huang, Y.-L., Tien, H.-W., Ma, C.-C. M., Yang, S.-Y., Wu, S.-Y., Liu, H.-Y., and Mai, Y.-W., "Effect of extended polymer chains on properties of transparent graphene nanosheets conductive film," *Journal of Materials Chemistry*, vol. 21, no. 45, p. 18 236, 2011.

[34] Bobinger, M. R., Romero, F. J., Salinas-Castillo, A., Becherer, M., Lugli, P., Morales, D. P., Rodriguez, N., and Rivadeneyra, A., "Flexible and robust laser-induced graphene heaters photothermally scribed on bare polyimide substrates," *Carbon*, vol. 144, pp. 116–126, Apr. 2019.

[35] Stankovich, S., Dikin, D. A., Dommett, G. H. B., Kohlhaas, K. M., Zimney, E. J., Stach, E. A., Piner, R. D., Nguyen, S. T., and Ruoff, R. S., "Graphene-based composite materials," *Nature*, vol. 442, no. 7100, pp. 282–286, Jul. 2006.

[36] Mei, X., Yan, Q., Lu, P., Wang, J., Cui, Y., Nie, Y., Umar, A., and Wang, Q., "Synthesis of pt/k2co3/MgAlOx–reduced graphene oxide hybrids as promising NOx storage–reduction catalysts with superior catalytic performance," *Scientific Reports*, vol. 7, no. 1, Feb. 2017.

[37] Piovesan, J. V., Santana, E. R., and Spinelli, A., "Reduced graphene oxide/gold nanoparticles nanocomposite-modified glassy carbon electrode for determination of endocrine disruptor methylparaben," *Journal of Electroanalytical Chemistry*, vol. 813, pp. 163–170, Mar. 2018.

[38] Aragaw, B. A., Su, W.-N., Rick, J., and Hwang, B.-J., "Highly efficient synthesis of reduced graphene oxide–nafion nanocomposites with strong coupling for enhanced proton and electron conduction," *RSC Advances*, vol. 3, no. 45, p. 23 212, 2013.

[39] Abdali, H. and Ajji, A., "Preparation of electrospun nanocomposite nanofibers of polyaniline/poly(methyl methacrylate) with amino-functionalized graphene," *Polymers*, vol. 9, no. 12, p. 453, Sep. 2017.

[40] Sakharov, Y. V., "Investigation of memristor effect on basis of thin-film oxide dielectrics modified by carbon," *IOP Conference Series: Materials Science and Engineering*, vol. 498, p. 012 029, Apr. 2019.

[41] Venugopal, G. and Kim, S.-J., "Observation of nonvolatile resistive memory switching characteristics in ag/graphene-oxide/ag devices," *Journal of Nanoscience and Nanotechnology*, vol. 12, no. 11, pp. 8522–8525, Nov. 2012.

[42] Panin, G. N., Kapitanova, O. O., Lee, S. W., Baranov, A. N., and Kang, T. W., "Resistive switching in al/graphene oxide/al structure," *Japanese Journal of Applied Physics*, vol. 50, no. 7, p. 070 110, Jul. 2011.

[43] Cheng, P. and Hu, Y. H., "Novel design for the odd-symmetric memristor from asymmetric switches," *Journal of Materials Chemistry C*, vol. 3, no. 12, pp. 2768–2772, 2015.

[44] Lee, M.-J., Lee, C. B., Lee, D., Lee, S. R., Chang, M., Hur, J. H., Kim, Y.-B., Kim, C.-J., Seo, D. H., Seo, S., Chung, U.-I., Yoo, I.-K., and Kim, K., "A fast, high-endurance and scalable non-volatile memory device made from asymmetric ta2o5-x/TaO2-x bilayer structures," *Nature Materials*, vol. 10, no. 8, pp. 625–630, Jul. 2011.

[45] Hong, S. K., Kim, J. E., Kim, S. O., Choi, S.-Y., and Cho, B. J., "Flexible resistive switching memory device based on graphene oxide," *IEEE Electron Device Letters*, vol. 31, no. 9, pp. 1005–1007, Sep. 2010.

[46] Goswami, S., Matula, A. J., Rath, S. P., Hedström, S., Saha, S., Annamalai, M., Sengupta, D., Patra, A., Ghosh, S., Jani, H., Sarkar, S., Motapothula, M. R., Nijhuis, C. A., Martin, J., Goswami, S., Batista, V. S., and Venkatesan, T., "Robust resistive memory devices using solution-processable metal-coordinated azo aromatics," *Nature Materials*, vol. 16, no. 12, pp. 1216–1224, Oct. 2017.

[47] Pradhan, S. K., Xiao, B., Mishra, S., Killam, A., and Pradhan, A. K., "Resistive switching behavior of reduced graphene oxide memory cells for low power nonvolatile device application," *Scientific Reports*, vol. 6, no. 1, May 2016.

[48] Khurana, G., Misra, P., and Katiyar, R. S., "Forming free resistive switching in graphene oxide thin film for thermally stable nonvolatile memory applications," *Journal of Applied Physics*, vol. 114, no. 12, p. 124 508, Sep. 2013.

[49] Qi, M., Bai, L., Xu, H., Wang, Z., Kang, Z., Zhao, X., Liu, W., Ma, J., and Liu, Y., "Oxidized carbon quantum dot–graphene oxide nanocomposites for improving data retention of resistive switching memory," *Journal of Materials Chemistry C*, vol. 6, no. 8, pp. 2026–2033, 2018.

[50] Jeong, H. Y., Kim, J. Y., Kim, J. W., Hwang, J. O., Kim, J.-E., Lee, J. Y., Yoon, T. H., Cho, B. J., Kim, S. O., Ruoff, R. S., and Choi, S.-Y., "Graphene oxide thin films for flexible nonvolatile memory applications," *Nano Letters*, vol. 10, no. 11, pp. 4381–4386, Nov. 2010.

[51] *Bare conductive ltd. electric paint®: Safety data sheet.* 2015.

[52] Abunahla, H., Mohammad, B., Homouz, D., and Okelly, C. J., "Modeling valance change memristor device: Oxide thickness, material type, and temperature effects," *IEEE Transactions on Circuits and Systems I: Regular Papers*, vol. 63, no. 12, pp. 2139–2148, Dec. 2016.

[53] Zhou, S. and Bongiorno, A., "Origin of the chemical and kinetic stability of graphene oxide," *Scientific Reports*, vol. 3, no. 1, Aug. 2013.

[54] Kim, S., Zhou, S., Hu, Y., Acik, M., Chabal, Y. J., Berger, C., Heer, W. de, Bongiorno, A., and Riedo, E., "Room-temperature metastability of multilayer graphene oxide films," *Nature Materials*, vol. 11, no. 6, pp. 544–549, May 2012.

[55] Dai, Y., Ni, S., Li, Z., and Yang, J., "Diffusion and desorption of oxygen atoms on graphene," *Journal of Physics: Condensed Matter*, vol. 25, no. 40, p. 405 301, Sep. 2013.

[56] Wei, H. Q., Zhou, P., Sun, Q. Q., Wang, L. H., Geng, Y., Zhang, D. W., and Wang, X. B., "The nano-scale resistive memory effect of graphene oxide," in *2012 IEEE Nanotechnology Materials and Devices Conference (NMDC2012)*, IEEE, Oct. 2012.

[57] Mativetsky, J. M., Treossi, E., Orgiu, E., Melucci, M., Veronese, G. P., Samori, P., and Palermo, V., "Local current mapping and patterning of reduced graphene oxide," *Journal of the American Chemical Society*, vol. 132, no. 40, pp. 14 130–14 136, Oct. 2010.

[58] Wang,
Zhang, D. W., "The mechanism of the asymmetric SET and RESET speed of graphene oxide based flexible resistive switching memories," *Applied Physics Letters*, vol. 100, no. 6, p. 063 509, Feb. 2012.

[59] Bizao, R. A., Machado, L. D., Sousa, J. M. de, Pugno, N. M., and Galvao, D. S., "Scale effects on the ballistic penetration of graphene sheets," *Scientific Reports*, vol. 8, no. 1, Apr. 2018.

[60] He, H., Klinowski, J., Forster, M., and Lerf, A., "A new structural model for graphite oxide," *Chemical Physics Letters*, vol. 287, no. 1-2, pp. 53–56, Apr. 1998.

[61] Jiang, L., Wu, B., Liu, H., Huang, Y., Chen, J., Geng, D., Gao, H., and Liu, Y., "A general approach for fast detection of charge carrier type and conductivity difference in nanoscale materials," *Advanced Materials*, vol. 25, no. 48, pp. 7015–7019, Oct. 2013.

[62] Loh, K. P., Bao, Q., Eda, G., and Chhowalla, M., "Graphene oxide as a chemically tunable platform for optical applications," *Nature Chemistry*, vol. 2, no. 12, pp. 1015–1024, Nov. 2010.

Paper X

Memcapacitor Emulator based on the Miller Effect

Francisco J. Romero [1,2,*], Diego P. Morales [2], Andres Godoy [1,2], Francisco G. Ruiz [1,2], Isabel M. Tienda-Luna [1,2], Akiko Ohata [3], Noel Rodriguez [1,2]

[1] Pervasive Electronics Advanced Research Laboratory, University of Granada, 18071 Granada, Spain.
[2] Department of Electronics and Computer Technology, University of Granada, 18071 Granada, Spain.
[3] Institute of Space and AstronauticalScience (ISAS), Japan AerospaceExploration Agency (JAXA), Sagamihara, Japan
* Corresponding author: franromero@ugr.es (F.J.R.)

Published in *International Journal of Circuit Theory and Applications*, Feb 2019, volume 47(4), pp. 572–579. DOI: 10.1002/cta.2604. Impact Factor: 1.581. JCR Rank: 174/266 (Q3) in *Engineering, Electrical & Electronics*.

Abstract

This work provides the guidelines to design and implement an elemental memcapacitor circuit emulator based on the relation between memcapacitance and the Miller effect in voltage amplifiers. The emulator is presented theoretically in a top-down approach, from the circuit behavior to the foundations of the constitutive equations of the memcapacitance and the electrical mutation of a memristor. Then, a practical and simple circuit implementation is demonstrated by SPICE computer simulations, circumventing the solid-state memristor by a two-state flux-dependent resistor, which modulates the gain of the amplifier in consonance to the flux of the input signal. Further electrical properties of the system are extracted from its physical implementation in a field-programmable analog array. The work is concluded illustrating the functionality of the memcapacitor emulator to study neuromorphic applications with a long-term potentiation example.

Keywords: feedback, memcapacitor, memristor, Miller effect, mutator.

X

X.1 Introduction

In 1971, Professor L. Chua completed the electrical relationships between the fundamental electrical magnitudes voltage (v), current (i), flux (φ), and charge (q) introducing the memristor [1]: a new passive element presenting a memory effect manifested through a closed pinched loop in the current–voltage characteristic. For almost four decades, the memristor only remained consigned to the circuit theory; until 2008, when Hewlett-Packard Labs (HP) developed a device that followed the equations of the memristor [2]. In this way, and not exempt of controversy [3], it became the first solid-state demonstrator of the elusive device. Since then, the memristor has gained an exponential interest whether for the implementation of new storage-class memories, logic gates and crossbar classifiers, or for the development of synaptic devices in neuromorphic computing applications [4]–[8]. In 2009, the concept of passive memory devices was revisited [9], proposing the memcapacitor and meminductor as a part of a larger essential family of circuit elements for developing a rigorous mathematical theory of nonlinear circuits [10]. The memcapacitance (memory capacitance), C_M, that will be the objective of this work, establishes the electrical relation between the time integral of the charge (σ) and the time integral of the voltage (i.e., flux, φ; see Figure X.1):

$$C_M = \frac{d\sigma}{d\varphi} \tag{X.1}$$

C_M has dimensional units of charge divided by voltage and evidences, to some extent, a sort of capacitance. Note that the flux, φ, does not necessarily have an electromagnetic meaning (in the sense of the electromagnetic flux), so the notation $[V \cdot s]$ will be used as its units instead of $[Wb]$ to highlight this difference.

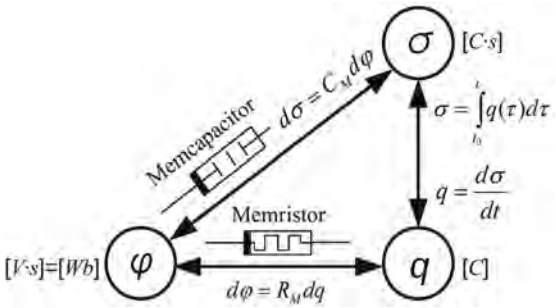

Figure X.1: Mem-elements relating the charge (q) with the time integral of the voltage (φ), (memristor), and the time integral of the charge (σ) with the time integral of the voltage, (memcapacitor). Units are presented in brackets.

From Equation X.1, a general voltage-controlled memcapacitive system is defined by the two following expressions[9]:

$$q(t) = C_M(x_1, x_2, ..., x_N, v, t)v(t) \tag{X.2}$$

$$\frac{d\vec{x_N}(t)}{dt} = \xi(\vec{x_N}, v, t) \tag{X.3}$$

where t is the time, and $\vec{x_N}(t) = (x_1, x_2, ..., x_N, v, t)$ represents the N-components vector defining the N state variables of the system ($N \geq 1$). The resulting $q - v$ characteristic curve of the memcapacitive system presents a pinched hysteresis loop through the origin since, according to Equation X.2, the charge is zero whenever the voltage is zero. A particular case of this general definition is a memcapacitive system with only one single state variable leading to the so-called voltage-controlled memcapacitor [11]:

$$q(t) = C_M\varphi v(t) \tag{X.4}$$

with $\varphi = \int_{t_0}^{t} v(\tau)d\tau$ as long as $\varphi = \int_{-\infty}^{t_0} v(\tau)d\tau = 0$.

In contrast to memristors, which are called to be a cornerstone for the development of the future of electronics [12], memcapacitors (as well as meminductors) are still in their earliest stage of development: their properties and applications needto be fully understood, and solid-state demonstrators must be found [13]. Most of the works dealing with memcapacitors still need to be focused on circuital emulators that enable the assessment of their properties and applications in actual circuits, especially to develop their full potential for the neuromorphic electronics field [11]. Examples of these emulator circuits can be found in the study of Pershin and Ventra [14], where a memcapacitor is implemented transforming memristance into memcapacitance (mutator); in the study of Sah *et al.* [15], a memcapacitor is emulated with off-the-shelf devices. The concept is further developed in the study of Yu *et al.* [16], where a full-floating memcapacitor is developed without grounded restrictions. All these works are fairly based on a bottom-up approach: designing the circuits from which a similarity transformation is achieved, and the constitutive relations of memcapacitance are satisfied.

This work introduces a new and simple approach for memcapacitance emulation relating the memcapacitance with the Miller effect, which is present in amplifiers with a parasitic or physically implemented capacitance connecting both input and output terminals. After this introduction, the paper is divided in four Sections. Section X.2 introduces the relationship between the Miller effect and the memcapacitance. Section X.3 proposes a design for memcapacitor emulator based on the Miller effect and provides SPICE simulations demonstrating its functionality. The circuit is implemented on a field-programmable analog array for its electrical characterization in Section X.4. Finally, Section X.5 exemplifies the potential of this emulator for studying neuromorphic applications, in particular, a long-term potentiation (LTP).

X.2 The Miller Effect and the Memcapacitance

The Miller effect, originally identified in triode vacuum tubes, accounts for the increase in the equivalent input capacitance connected between the input and another node of a circuit exhibiting gain. This effect is typically observed in voltage amplifiers with inverting output [17]. Thus, the capacitor in the circuit of Figure X.2 is affected by the Miller effect. For its analysis, we assume that the memristor is characterized by its memristance at a given instant of time (R_M). This memristance intrinsically depends on the electrical history of the device [1]. The output voltage of the circuit is related to the input voltage by the amplifier gain ($v_{out}(t) = -Av_{IN}(t)$), with $A > 0$), and therefore, the impedance seen at the input terminal of the circuit can be calculated as follows:

$$Z_{IN} = \frac{V_{IN}}{I_{IN}} = \frac{V_{IN}}{j\omega C(V_{IN} - V_{OUT})} = \frac{1}{j\omega C(1+A)} \tag{X.5}$$

which yields an equivalent input capacitance $(1 + A)$ times the value of the original feedback capacitor C (Miller effect).

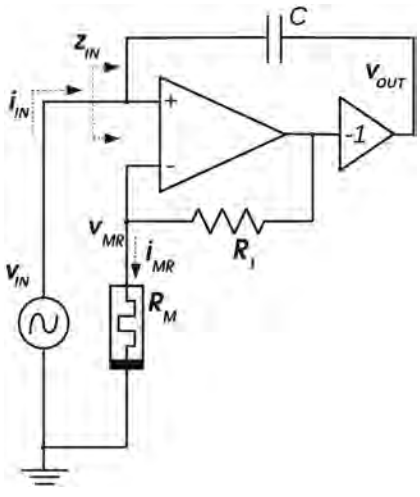

Figure X.2: Schematic of the memcapacitor emulator based on the Miller effect over feedback capacitor C. The gain of the amplifier, $(-A)$, is modulated according to the flux of the input signal, v_{IN}, by means of the memristor.

This gain dependence of the input capacitance can be connected directly with the memcapacitance. In the circuit of Figure X.2, the derivative of σ_{IN}, i.e., the input charge, can be related to the voltage across the feedback capacitor C and therefore to the gain of the amplifier through the following expression:

$$\begin{aligned}\frac{d\sigma_{IN}(t)}{dt} = q_{IN}(t) &= \int i_{IN}(t) \\ &= \int C\frac{dv_C(t)}{dt} = Cv_C(t) = C(1+A)v_{IN}(t)\end{aligned} \tag{X.6}$$

The first term of Equation X.6 can be further developed introducing the input flux (i.e., the flux on the equivalent input capacitance):

$$\frac{d\sigma_{IN}(t)}{dt} = \frac{d\sigma_{IN}(t)}{d\varphi_{IN}(t)} \cdot \frac{d\varphi_{IN}(t)}{dt} \tag{X.7}$$

Combining the definition of memcapacitance (Equation X.1), with Equations X.6 and X.7, the resulting memcapacitance seen at the input of the circuit is derived as follows:

$$\begin{aligned}C_M = \frac{d\sigma_{IN}(t)}{d\varphi_{IN}(t))} &= \frac{C(1+A)v_{IN}(t))}{d\varphi_{IN}(t)/dt} \\ &= \frac{C(1+A)v_{IN}(t))}{v_{IN}(t)} = C(1+A)\end{aligned} \tag{X.8}$$

Considering a close to ideal operational amplifier, the voltage across the memristor (inverting terminal) follows concomitantly the input voltage applied to the circuit (non-inverting terminal), and therefore, the input flux and the flux in the memristor are equal ($\varphi_{IN} = \varphi_{MR}$). This latter flux, through the electrical action of the memristor, controls the gain of the amplifier $C_M = C(1 + A_{\varphi_{MR}})$. Therefore, substituting the gain of the amplifier of Figure X.2 in Equation X.8, the resulting memcapacitance is given by:

$$C_M = C\left(2 + \frac{R_1}{R_M}\right) \tag{X.9}$$

The circuit in Figure X.2 can be considered as an electrical mutator circuit since, according to Equation X.9, it transforms a memristor with a certain constitutive relation $f_{MR}(\varphi, q)$ into a memcapacitor with its own constitutive relation $f_{MR}(\sigma, \varphi)$.

X.3 Miller Effect Memcapacitor Circuit Demonstrator

We have developed a simple Miller effect-based memcapacitor demonstrator to study its electrical behavior based on the general schematic of Figure X.2. The schematic of the circuit is shown in Figure X.3. To avoid the use of a solid-state memristor, we substituted it by a flux-controlled resistor (that actually behaves as a two-state bipolar memristor [18]), represented inside the dotted box in Figure X.3. This simplification ultimately yields a two-state memcapacitor instead of a continuous transition of capacitance that would be produced by

using, for example, an analog solid-state TiO_2 memristor [2]. In the circuit of Figure X.3, the value of the flux, φ, is obtained by integrating the voltage of the inverting terminal of the operational amplifier (which is identical to the input voltage). If this value is lower or equal to the triggering flux value, Φ (set in the comparator), the resistor R_3 is not connected in the feedback loop, and the amplifier presents the low value of gain ($A = 1 + R_1/R_2$). In any other case ($\varphi > \Phi$), R_3 is connected in parallel to R_2, and the gain takes a larger value ($A = 1 + R_1/(R_2 \| R_3)$). Considering an off-the-shelf application, the integrator can be implemented by an op-amp integrator with a feedback resistor behaving as an inverting active low-pass filter with a very low cut-off frequency (setting a feedback resistance much larger than the resistance connected to the negative terminal) followed by an inverting amplifier stage to recover the polarity of the signal and a final level comparator.

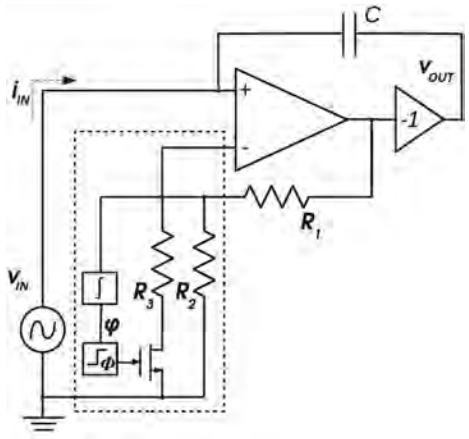

Figure X.3: Schematic circuit of the memcapacitor emulator based on the Miller Effect. The elements inside the dotted rectangle emulate a two-state memristor. The total resistance of the feedback loop (determining the gain) is modified between two values depending on the input flux, φ, and the triggering flux value of the comparator, Φ. For the sake of clarity, the circuits corresponding to the inverter, integrator, and comparator are not detailed.

From the input equivalent capacitance perspective of Equation X.9, the piecewise definition of the feedback resistance depending on the input flux yields the following capacitance values:

$$C_M(\varphi) = \begin{cases} C_{low} = C(2 + R_1/R_2) & \text{if } \varphi \leq \Phi \\ C_{high} = C(2 + R_1/(R_2 \,||\, R_3)) & \text{if } \varphi \geq \Phi \end{cases} \tag{X.10}$$

The time-domain impedance of a time-dependent capacitor ($Z_C(t) = v_{IN}(t)/i_{IN}(t)$) can be determined from the fundamental relationship between charge and capacitance:

$$q(t) = C(t)v_{IN}(t) \tag{X.11}$$

The current can be obtained as the derivative of Equation X.11:

$$i_{IN}(t) = \frac{dC(t)}{dt}v_{IN}(t) + C(t)\frac{dv_{IN}(t)}{dt} \tag{X.12}$$

which produces the following time-domain impedance:

$$Z_C(t) = \frac{v_{IN}(t)}{\frac{dC(t)}{dt}v_{IN}(t) + C(t)\frac{dv_{IN}(t)}{dt}} \tag{X.13}$$

If the input voltage is of a sinusoidal form ($v_{IN}(t) = V_m sin(\omega t)$), and the capacitance is characterized by two discrete values depending on the history of the system (flux, φ), then Equation X.13 yields:

$$Z_C(t) = \frac{1}{\omega C_i}tan(\omega t) \tag{X.14}$$

where C_i will take the low and high capacitance values according to Equation X.10. The circuit in Figure X.3 has been first simulated with SPICE to confirm the memcapacitive behavior of the input impedance. The results shown in Figure X.4A confirm the characteristic behaviour of the flux dependent gain. For this particular example we selected: C = 10 nF, R_1 = 4 kΩ, R_2 = 4kΩ, R_3 = 1.33kΩ, and Φ = 0 V·s for the triggering value of the flux. The input signal was sinusoidal with 1 V of amplitude and an oscillation frequency of 50 Hz. The resulting values of the gain are A = −2 V/V for $\varphi \leq \Phi$, and A = −5 V/V for $\varphi > \Phi$. The time-domain impedance, shown in Figure X.4B, reproduces the analytical time-domain input impedance of the circuit given by Equation X.14. The extracted values of capacitance are C = 30 nF ($\varphi \leq \Phi$) and C = 60 nF ($\varphi > \Phi$), matching perfectly the predicted values according to Equation X.10. Additional results showing the response of the circuit to a triangular input signal are shown in Figure X.4C.

X.4 Field Programmable Analog Array Implementation

The circuit shown in Figure X.3 can be implemented easily with off-the-shelf devices, but for the purpose of integration, we tested it in a dynamic reconfigurable Field-Programmable Analog Array (FPAA, Anadigm AN221E04) [19]. This platform allows the implementation of complex analog functions using configurable analog modules (CAMs) [20], which are optimized in terms of sensitivity to parasitic effects. The user-interface modular view of the Anadigm workspace, where the circuit is designed, is shown in Figure X.5A. The integrator, comparator, and controlled-gain amplifier CAMs simplify considerably the implementation of the circuit shown in Figure X.3. Pins 11 and 12 are set as the positive and negative memcapacitor terminals. The input signal is integrated and compared with the triggering flux value, defining a piecewise gain in the amplifier

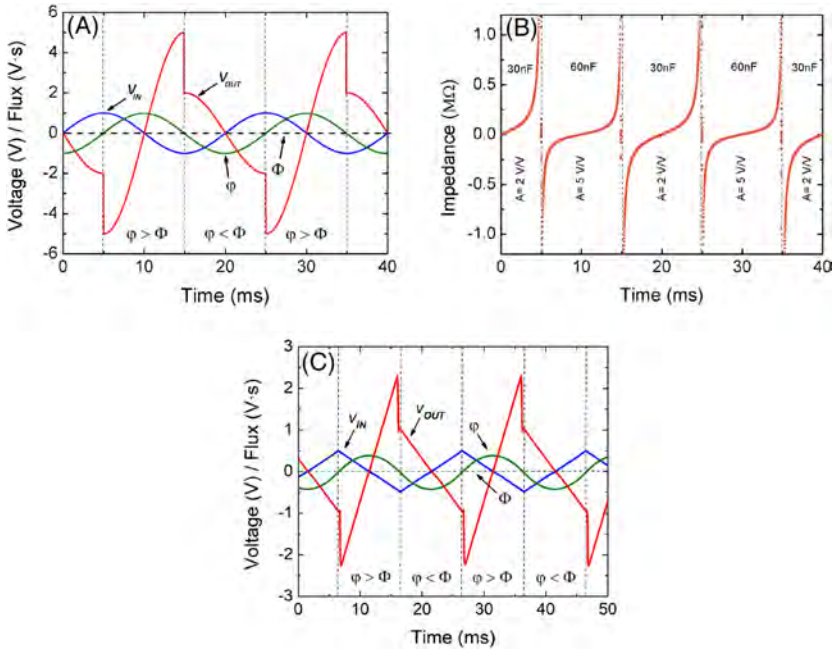

Figure X.4: (A) SPICE simulation, the output voltage and the input flux for a sinusoidal input signal ($V_m = 1$ V, $f = 50$ Hz) of the circuit implemented in Figure X.3. $R_1 = 4$ kΩ, $R_2 = 4$ kΩ, $R_3 = 1.33$ kΩ, $C = 10$ nF. (B) Real-time impedance measured at the input of the circuit of Figure X.3 when the sinusoidal stimulus in (A) is applied to the input. The results agree with the theoretical values of Equation X.13, characterized by two values of capacitance depending on the history of the memcapacitor. (C) Simulation results of the output voltage and the input flux for a triangular input signal.

($G_1 = -2$ V/V when $\varphi_{IN} \leq \Phi$, and $G_2 = -5$ V/V when $\varphi_{IN} > \Phi$). Then, the output signal of the amplifier is sampled and filtered internally before being directed to pin 7. A feedback capacitor of 9.4 nF, responsible for the Miller effect (not shown), is connected between pins 7 and 11. This capacitance is several orders of magnitude larger than the maximum input parasitic capacitance of the Anadigm AN221E04, which is in the range of ~ 5 pF [19]. The inherent electrical signature of the memcapacitor is manifested on the experimental charge-voltage plot (Figure X.5B), where the triggering flux was varied taking the values Φ = {0,250,450} mV·s. The input charge, determined from the integral of the input current (corresponding to the memcapacitor charge), describes a closed pinched loop passing through the origin when represented against the input voltage (corresponding to a sinusoidal waveform in this figure). The positive and negative lobes enclose the same area, resulting in a purely reactive memcapacitor. As shown, the use of a two-state bipolar memristor in Figure X.3, yields a two-

state bipolar memcapacitor (Figure X.5B). Moreover, Figure X.5C shows the corresponding two-state input capacitance (memcapacitance) values extracted from the charge-voltage plot.

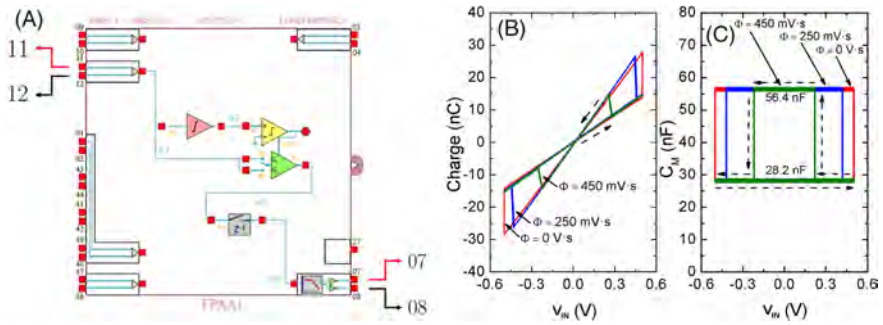

Figure X.5: (A) Anadigm workspace implementation of the memcapacitor emulator of Figure X.3 in the dynamic reconfigurable field-programmable analog array FPAA, AN221E04. A 9.4 nF capacitor is connected between the input and output terminals of the amplifier: pins 11 and 7. (B) Closed pinched hysteresis loops of the charge-voltage curve of the emulated memcapacitor for different values of the triggering flux (Φ) when the circuit is driven with a 50 Hz, 0.5 V sinusoidal waveform. (C) Measured input capacitance of the memcapacitor emulator for the same stimulus of (B).

X.5 Long-Term Potentiation Application

In this last section of the work, we would like to highlight the suitability of the memcapacitor emulator to study and design neuromorphic circuits provided with synaptic plasticity. In particular, a LTP example is illustrated. This principle, inside the neuroscience field, conforms a persistent strengthening of synapses based on recent patterns of activity, and it is assumed to be one of the major mechanisms that underlies learning and memory [21]. The neural stimuli are modelled by successive voltage spikes that are applied to the memcapacitor emulator with positive sign, corresponding to a pre-synaptic stimulus, or negative sign corresponding to a postsynaptic stimulus (Figure X.6A). The initial presynaptic spikes progressively increase the input flux of the device (Figure X.6B). This situation corresponds to the potentiation of the device. When the triggering flux (Φ=150mV $\cdot$ s) is surpassed, after 10 voltage spikes in this case, the input capacitance (C_M) increases and therefore so does the input current ($i_{IN}(t) = C_M \frac{dv_{IN}(t)}{dt}$), Figure X.6C. The confirmation of the learning process of the device can also be recognized in the charge that the device stores and removes during each spike (Figure X.6D).

Similarly to the learning process, the device can forget its training, emulating a long-term depression (LTD) process by applying postsynaptic voltage spikes.

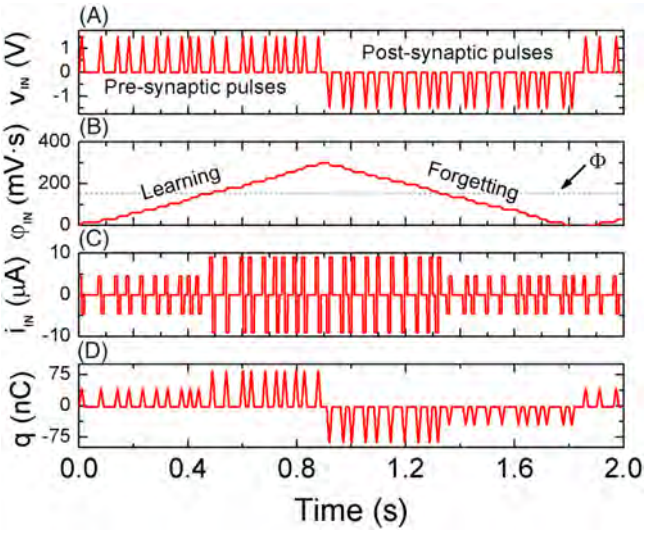

Figure X.6: (A) Pre-synaptic (v_{IN}>0) and post-synaptic (v_{IN}<0) voltage spikes applied to the Miller effect memcapacitor, emulating neural stimuli. (B) Input flux (φ_{IN}) of the device; the triggering flux is set to Φ = 150 mV·s. (C) Input current reflecting the change in the memory state. (D) Evolution of the memcapacitor charge during the train of stimuli.

These negative stimuli (above 0.9 s in Figure X.6) progressively decrease the input flux (φ_{IN}) ending up with the depression of the memory action that recovers its initial pretrained state.

X.6 Conclusions

The Miller effect has been suited as a simple approach to build memcapacitor emulators from memristor electrical mutation. The designed circuit is general and can be implemented using an actual memristor, or from pure off-the-shelf devices. The electrical properties of the circuit have been tested both by SPICE simulations and by implementing it using a field-programmable analog array. Finally, its potential functionality to study neuromorphic applications has been illustrated through a LTP example.

Acknowledgements. This work has been done with the support of the Spanish Government through Project TEC2017-89955-P (MINECO, FEDER) and the grant FPU16/01451 held by F. Romero. The authors would also like to thank the support of the JSPS KAKENHI through the grant number JP18K04275.

References

[1] Chua, L., "Memristor-the missing circuit element," *IEEE Transactions on Circuit Theory*, vol. 18, no. 5, pp. 507–519, 1971.

[2] Strukov, D. B., Snider, G. S., Stewart, D. R., and Williams, R. S., "The missing memristor found," *Nature*, vol. 453, no. 7191, pp. 80–83, May 2008.

[3] Vongehr, S. and Meng, X., "The missing memristor has not been found," *Scientific Reports*, vol. 5, no. 1, Jun. 2015.

[4] Xu, C., Dong, X., Jouppi, N. P., and Xie, Y., "Design implications of memristor-based RRAM cross-point structures," in *2011 Design, Automation & Test in Europe*, IEEE, Mar. 2011.

[5] Corinto, F., Gilli, M., and Forti, M., "Flux-charge description of circuits with non-volatile switching memristor devices," *IEEE Transactions on Circuits and Systems II: Express Briefs*, vol. 65, no. 5, pp. 642–646, May 2018.

[6] Tran, D. and Teuscher, C., "Memcapacitive devices in logic and crossbar applications," Apr. 19, 2017. arXiv: 1704.05921 [cs.ET].

[7] Prezioso, M., Merrikh-Bayat, F., Hoskins, B. D., Adam, G. C., Likharev, K. K., and Strukov, D. B., "Training and operation of an integrated neuromorphic network based on metal-oxide memristors," *Nature*, vol. 521, no. 7550, pp. 61–64, May 2015.

[8] Azghadi, M. R., Linares-Barranco, B., Abbott, D., and Leong, P. H. W., "A hybrid CMOS-memristor neuromorphic synapse," *IEEE Transactions on Biomedical Circuits and Systems*, vol. 11, no. 2, pp. 434–445, Apr. 2017.

[9] Ventra, M. D., Pershin, Y. V., and Chua, L. O., "Circuit elements with memory: Memristors, memcapacitors, and meminductors," *Proceedings of the IEEE*, vol. 97, no. 10, pp. 1717–1724, Oct. 2009.

[10] Tetzlaff, R., Ed., *Memristors and Memristive Systems*. Springer New York, 2014.

[11] Radwan, A. G. and Fouda, M. E., *On the Mathematical Modeling of Memristor, Memcapacitor, and Meminductor*. Springer International Publishing, 2015.

[12] Zidan, M. A., Strachan, J. P., and Lu, W. D., "The future of electronics based on memristive systems," *Nature Electronics*, vol. 1, no. 1, pp. 22–29, Jan. 2018.

[13] Kim, Y., Park, K. H., Chung, T. H., Bark, H. J., Yi, J.-Y., Choi, W. C., Kim, E. K., Lee, J. W., and Lee, J. Y., "Ultralarge capacitance–voltage hysteresis and charge retention characteristics in metal oxide semiconductor structure containing nanocrystals deposited by ion-beam-assisted electron beam deposition," *Applied Physics Letters*, vol. 78, no. 7, pp. 934–936, Feb. 2001.

[14] Pershin, Y. and Ventra, M. D., "Memristive circuits simulate memcapacitors and meminductors," *Electronics Letters*, vol. 46, no. 7, p. 517, 2010.

[15] Sah, M. P., Yang, C., Budhathoki, R. K., Kim, H., and Yoo, H. J., "Implementation of a memcapacitor emulator with off-the-shelf devices," *Electronics and Electrical Engineering*, vol. 19, no. 8, Oct. 2013.

[16] Yu, D. S., Liang, Y., Chen, H., and Iu, H. H. C., "Design of a practical memcapacitor emulator without grounded restriction," *IEEE Transactions on Circuits and Systems II: Express Briefs*, vol. 60, no. 4, pp. 207–211, Apr. 2013.

[17] Miller, J. M., "The dependence of the input impedance of a three-electrode vacuum tube upon the load in the plate circuit," *Journal of the Franklin Institute*, vol. 188, no. 6, p. 814, Dec. 1919.

[18] Wald, N., Amrani, E., Drori, A., and Kvatinsky, S., "Logic with unipolar memristors – circuits and design methodology," in *IFIP Advances in Information and Communication Technology*, Springer International Publishing, 2017, pp. 24–40.

[19] Anadigm®, I., "An221e04 datasheet – dynamically reconfigurable fpaa with enhanced i/o," Tech. Rep., 2021.

[20] Fonseca, P. J. R. and Barbosa, R. S., "Realization of PID controllers in analog reconfigurable hardware," in *Lecture Notes in Electrical Engineering*, Springer International Publishing, Sep. 2016, pp. 809–820.

[21] Cooke, S. F., "Plasticity in the human central nervous system," *Brain*, vol. 129, no. 7, pp. 1659–1673, Jul. 2006.

Paper XI

Meminductor Emulator Based on a Modified Antoniou's Gyrator Circuit

Francisco J. Romero [1,*], Manuel Escudero [2], Alfredo Medina-Garcia [3], Diego P. Morales [1], Noel Rodriguez [1]

[1] Department of Electronics and Computer Technology, University of Granada, 18071 Granada, Spain.
[2] Infineon Technologies Austria AG, 9500 Villach, Austria [3] Infineon Technologies AG, 85579 Neubiberg, Germany
* Corresponding author: franromero@ugr.es (F.J.R.)

Published in *Electronics*, Sep 2020, volume 9(9), 1407. DOI: 10.3390/electronics9091407. Impact Factor: 2.412. JCR Rank: 125/266 (Q2) in *Engineering, Electrical & Electronic*.

Abstract

In this work, we presented the design and simulation of a new flux-controlled meminductor emulator based on a modified version of the well-known Antoniou's inductor simulator circuit. The constitutive theoretical equations of meminductance are presented and subsequently correlated with the electrical behavior of Antoniou's circuit, hence illustrating its practical meminductive behavior with a proper selection of feedback impedances. After that, the feasibility of a practical implementation using off-the-shelf devices is illustrated firstly for a two-state meminductor and secondly for a continuous-state meminductor by means of SPICE simulations. It was also demonstrated that this emulator can operate at different frequencies and input signals constituting one of the simplest and most versatile meminductor emulators to date.

Keywords: circuit theory, emulator, feedback, gyrator, memdevice, meminductor.

XI

XI.1 Introduction

Prof. L. Chua first presented the notion of a memristor (memory-resistor) in 1971, defining a new circuit element which established the relationship between flux (ϕ, time-integral of the voltage) and charge (q) [1]. The memristor produces a non-linear relation between the current (i) and voltage (v), where the memory effect is manifested through a characteristic pinched hysteresis loop in its $i-v$ curve. In recent times, with the advent of actual physical memristors [2]–[5], the topic of passive memory devices has raised a high interest for researches and it has generated transversal studies involving different science and technologies areas such as chaotic and logic circuits [6], [7], or neuromorphic computing [8], [9]. Nearly 40 years later, the concept of passive memory-devices (memdevices) was generalized, again by Chua, for capacitive and inductive non-linear systems [10], expanding the relation between the different physical magnitudes schematized in Figure XI.1. Thus, the memcapacitance (C_M, memory-capacitance) established the electrical relation between the time-integral of the charge (σ) and the flux (ϕ), whereas the relation between the charge (q) and the time-integral of the flux (ρ) was defined by the meminductance (L_M, memory-inductance).

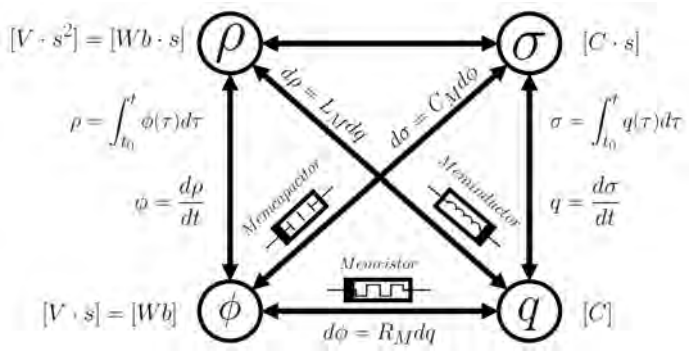

Figure XI.1: Mem-elements defined from the relations between the charge (q) and the time-integral of the voltage (ϕ), (memristor); the time-integral of the charge (σ) and the time-integral of the voltage (ϕ), (memcapacitor); the time-integral of the flux (ρ) and the charge (q), (meminductor). Units are presented in brackets.

Because of their inherent memory and dynamic storage ability, these devices are expected to play an important role in diverse fields of science and technology, such as non-volatile memories and simulations of learning, adaptive, and spontaneous behavior circuits [11]. In the particular case of meminductors, several works have reported promising results for future electronic circuits, e.g., adaptative filters [12], chaotic circuits for encryption [13] or neuromorphic computation [14]. However, the solid-state implementation of these latter devices (memcapacitor and meminductor), in contrast to memristors, presents a challenge due to the yet elusive nature of their physical existence. For this reason, the emulators of these devices are leading the way to envisage real-

practical implementations until single-device solid-state demonstrators become available. Thus, different examples of memcapacitor and meminductor emulators implemented with off-the-shelf devices or based on mutator approaches have been presented in the literature [15]–[21], all of them following the same principle, the designing of a circuit which satisfies the constitutive equations of the emulated device. Following this principle, in this work we addressed a simple approach to emulate a meminductor based on one of the most famous inductor electrical simulators: the gyrator circuit proposed by Antoniou almost 50 years ago [22] which, using two op-amps and five passive elements, has been widely used in the literature to emulate different systems, such as Chua's circuit: a simple electronic circuit that exhibits classic chaotic behavior [23]. Thus, the emulator proposed in this work, in contrast to the aforementioned approaches collected in the literature, presents the advantage of not requiring any four-quadrant analog multipliers, current conveyors or memristive devices, which make it one of the simplest and cheapest meminductor emulators to date. The manuscript is structured as follows: after this introduction, Section 2 presents the analytical relations between the modified Antoniou's circuit and meminductance. Section 3 proposes a design valid for emulating a two-state meminductor as well as a continuous transition of inductances together with their electrical characterization. Section 4 illustrates the feasibility of the meminductor emulator to study neuromorphic applications with a long-term potentiation example, and finally, the main conclusions are drawn in Section 5.

XI.2 Meminductance and Antoniou's Circuit

The canonical meminductor definition from Figure XI.1 can be generalized to a more general meminductance (L_M) concept which establishes a non-linear n^{th}-order relation between the current (i) and the flux (ϕ) that can be expressed in terms of a current-controlled meminductive system [10]:

$$\phi(t) = L_M(\vec{x_n}, i, t)i(t) \tag{XI.1}$$

$$\frac{d\vec{x_n}}{dt} = f_M(\vec{x_n}, i, t) \tag{XI.2}$$

or a flux-controlled meminductive system:

$$i(t) = L_M^{-1}(\vec{x_n}, \phi, t)\phi(t) \tag{XI.3}$$

$$\frac{d\vec{x_n}}{dt} = f_M(\vec{x_n}, \phi, t) \tag{XI.4}$$

where t is the time and $\vec{x_N}$ the history (n^{th}-order state-vector) of the system.

The first-order meminductive system whose inductance only depends on the time-integral of the input flux (TIF, ρ) is also known as flux-controlled meminductor and its definition is reduced to Equation XI.5:

$$i(t) = L_M^{-1}(\rho)\phi(t) \tag{XI.5}$$

with $\rho = \int_{t_0}^{t} \phi(\tau)d\tau$, proved that $\int_{-\infty}^{t_0} \phi(\tau)d\tau = 0$.

Therefore, as Equation XI.5 indicates, the $i-\phi$ characteristic of meminductors is given by a pinched hysteresis loop, the current being zero whenever the input flux is zero. In the case of flux-controlled meminductors, Equation Equation XI.5 can be expressed as

$$i(t) = L_M^{-1}\left(\int_{t_0}^{t}\int_{t_0}^{\tau} v(\tau)d\tau d\tau\right)\phi(t) \tag{XI.6}$$

On this basis, hereinafter we demonstrate that the circuit proposed in this work, shown in Figure XI.2, can be modeled by Equation XI.6 when its different passive elements are properly selected, and therefore it can be used to emulate a grounded meminductor.

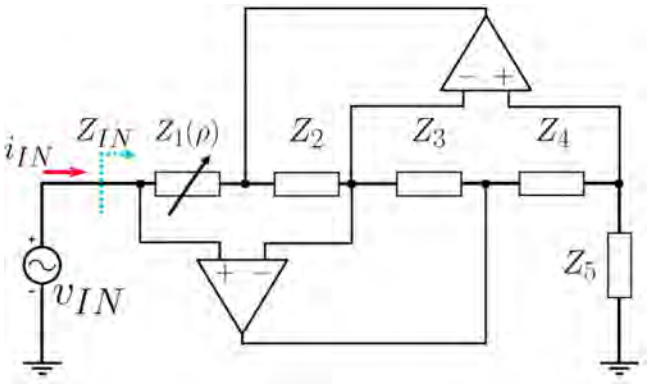

Figure XI.2: Schematic of the meminductor emulator based on Antoniou's circuit. The different passive elements are represented by their impedance (Z_i; $i = 1, ..., 4$). $Z(\rho)$ represents a time integral of the flux (TIF)-dependent impedance, while v_{IN}, i_{IN} and Z_{IN} represent the input voltage, current and impedance, respectively.

Antoniou's simulator is widely described in the literature and it is considered one of the best options to simulate grounded inductors since it is very tolerant to the nonideal properties of the op-amps [24]. In addition, this configuration requires neither actual inductors (with the potential advantage of reduced form-factor, lower losses and cost) nor memristor for its implementation. In this case, to implement the meminductor emulator we drew on the equivalent input impedance (Z_{IN}) of the circuit, considering the original Z_1 as a TIF-dependent impedance, $Z_1(\rho)$, then:

$$Z_{IN} = \frac{v_{IN}}{i_{IN}} = \frac{Z_1(\rho)Z_3Z_5}{Z_2Z_4} \tag{XI.7}$$

From this basic circuit, a flux-controlled inductor could be modelled replacing Z_1 by a TIF-dependent resistor (controlled by the time-integral of the input flux), Z_4 by a capacitor C_4 and finally, Z_2, Z_3 and Z_5 by the resistors R_2, R_3 and R_5, respectively. Therefore, Equation XI.7 can be expressed as:

$$Z_{IN} = \frac{v_{IN}}{i_{IN}} = j\omega \frac{R_1(\rho) R_3 C_4 R_5}{R_2} \tag{XI.8}$$

which corresponds to the impedance of a flux-controlled meminductor given by the following expression:

$$L(\rho) = \frac{C_4 R_3 R_5}{R_2} R_1(\rho) \tag{XI.9}$$

Moreover, this meminductor can be connected directly with the meminductance by means of the constitutive equation of the inductor:

$$v_{IN} = \frac{d}{dt}(L(\rho) i_{IN}(t)) \tag{XI.10}$$

which can also be expressed as:

$$\frac{d\rho_{IN}(t)}{dt} = \varphi_{IN}(t) = \int v_{IN}(t)dt = L(\rho) i_{IN}(t) \tag{XI.11}$$

The first term of Equation XI.11 can be further developed introducing the input charge (i.e., the charge circulating through the equivalent inductor):

$$\frac{d\rho_{IN}(t)}{dt} = \frac{d\rho_q(t)}{dq} \frac{dq(t)}{dt} \tag{XI.12}$$

Combining the definition of flux-controlled meminductance (Equation XI.5) with Equations XI.11 and XI.12, the resulting meminductance seen at the input of the circuit is derived as follows:

$$L_M = \frac{d\rho_q(t)}{dq} = \frac{L(\rho) i_{IN}(t)}{dq/dt} = \frac{C_4 R_3 R_5 R_1(\rho) i_{IN}(t)}{R_2 i_{IN}(t)} = L(\rho) \tag{XI.13}$$

XI.3 Meminductor Circuit Demonstrator

Aiming to illustrate the feasibility of this circuit, we developed a simple two-state meminductor demonstrator to study its electrical behavior based on the general schematic of Figure XI.2. In this circuit, $R(\rho)$ takes two different values depending on the time-integral of the input flux (ρ) and the triggering value of the switch (triggering value of the TIF, ρ_{TH}). The double integrator circuit was simulated by means of two Miller integrators in cascade, considering that in a practical implementation a resistor should be used in the feedback loop to provide a DC feedback path, reducing the low frequency gain of the op-amp and hence avoiding the saturation of the output signal [24].

Therefore, as indicated in Equation XI.14, this particularized circuit yields a two-state meminductor. If the TIF is lower or equal to the triggering value (ρ_{TH}), then R_6 is not connected in the feedback loop, otherwise R_6 is connected in parallel with R_1. Thus, according to Equation XI.13, the equivalent meminductance seen from the input terminal takes the following values:

$$L_M(\rho) = \begin{cases} L_{high} = \frac{R_1 R_3 C_4 R_5}{R_2} & \text{if } \rho \leq \rho_{TH} \\ L_{low} = \frac{(R_1 || R_6) R_3 C_4 R_5}{R_2} & \text{if } \rho > \rho_{TH} \end{cases} \quad \text{(XI.14)}$$

The circuit of Figure XI.3 has been simulated with SPICE to confirm its meminductive behavior. For this, we considered the following values for the discrete components: $R_1 = R_2 = R_3 = R_5 = R_6 = 1k\Omega$, $C = 47$ nF and $\rho_{TH} = 0$ V·s^2, while the input was a sinusoidal signal, $V_m sin(2\pi ft)$, with $V_m = 1$ V considering two different frequencies, $f = 1$ kHz and $f = 10$ kHz. Thus, the resulting values of meminductance, according to Equation XI.14, would be $L_M = 47$ mH for $\rho \leq \rho_{TH}$ and $L_M = 23.5$ mH for $\rho > \rho_{TH}$.

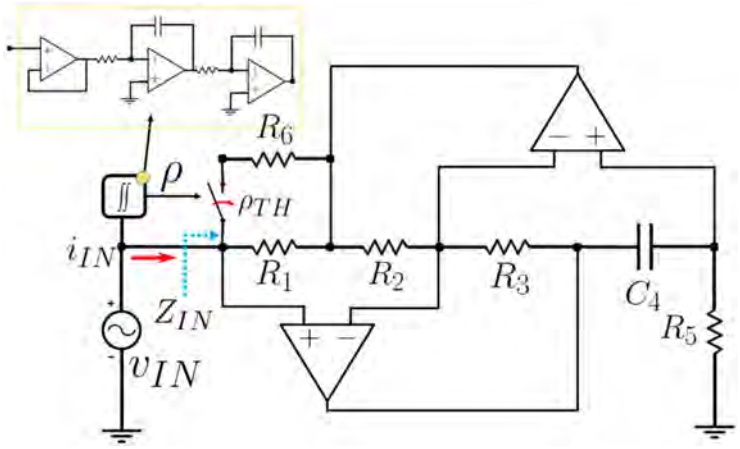

Figure XI.3: Schematic circuit of the two-state meminductor emulator.

The results shown in Figure XI.4 corroborate the two-state meminductive behavior of the proposed circuit. On the one hand, Figure XI.4a depicts the relevant signals of the circuit implemented. As seen, and in agreement with Equation XI.5, the input current takes the same waveform that the input flux (ϕ) but modulated according to the two values of meminductance as a function of its time time-integral (ρ). On the other hand, the $i - \phi$ plot, represented in Figure XI.4b, depicts the closed pinched hysteresis loop passing through the origin, which is the signature of meminductors [10]. It can also be noted that, as expected and as occurs for memristor and memcapacitors, the hysteresis collapses with increasing frequency [10], [25], [26].

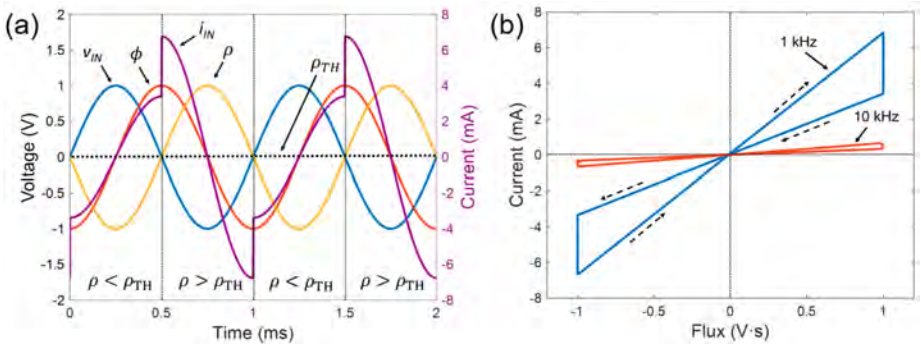

Figure XI.4: Simulation results of the two-state meminductor. (a) Signals extracted from the circuit of Figure XI.3 for a sinusoidal input signal ($V_m = 1$ V, $f = 1$ kHz) with $R_1 = R_2 = R_3 = R_5 = R_6 = 1k\Omega$, $C = 47$ nF and $\rho_{TH} = 0$ V·s^2. (b) Closed pinched hysteresis loop of the flux–current curve for different frequencies ($f = 1$ kHz and $f = 10$ kHz).

The time-domain impedance of a time-dependent inductor ($Z_L(t) = v_L(t)/i_L(t)$) can be determined from the fundamental relationship between flux and inductance:

$$\phi_L(t) = L(t)i_L(t) \tag{XI.15}$$

which, considering a sinusoidal input voltage ($V_L = V_m sin(\omega t)$) and a TIF-dependent inductance, produces the following time-domain impedance:

$$Z_L(t) = \frac{v_L(t)}{i_L(t)} = \frac{v_L(t)}{\phi_L(t)}L(\rho) = \frac{v_L(t)}{\int v_L(t)dt}L(\rho) = -\omega L(\rho)tan(\omega t) \tag{XI.16}$$

This equation matches with the results obtained for the time-domain input impedance extracted from the simulations presented above, as shown in Figure XI.5. It can be noted that the input impedance corresponds to two different values of inductance according to the time-integral of the input-flux and both Equations XI.14 and XI.16.

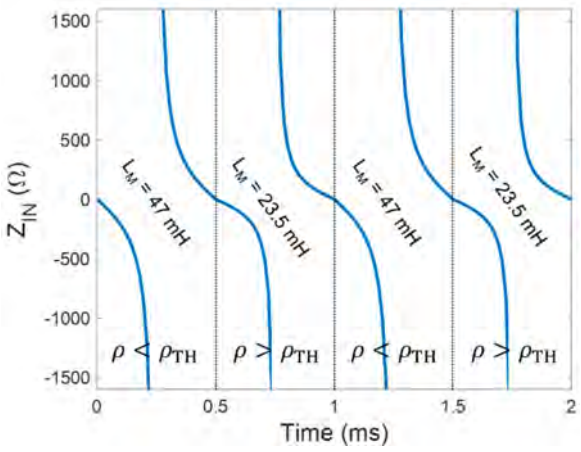

Figure XI.5: Time-domain input impedance extracted using a sinusoidal input signal under the configuration presented in Figure XI.3.

Once the operation of the circuit has been exposed, hereafter we demonstrate that this circuit could also be further extended to a continuous transition of inductances (instead of discrete states) using the configuration shown in Figure XI.6. For that, we considered Z_1 as a TIF-controlled resistor whose values are given by Equation XI.17, while the rest of the components remain unchanged with respect to the previous configuration.

$$R_1(\rho) = R_0 + K\rho \tag{XI.17}$$

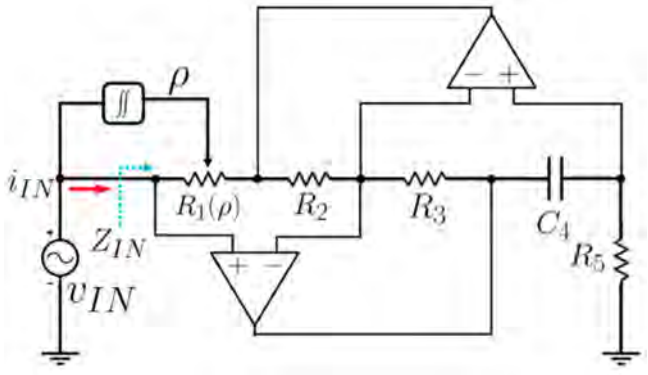

Figure XI.6: Schematic circuit for the continuous states meminductor emulator.

For the simulations we considered $R_0 = 2$ kΩ and the constant factor $K = 1$ kΩ to satisfy that $R_{1_{max}} = 3$ kΩ and $R_{1_{min}} = 1$ kΩ, given that ρ was normalized as $|\rho| \leq 1$. Under this configuration, and as represented in Figure

XI.7a,b, the circuit shown in Figure XI.6 also fulfills the constitutive equations of meminductors, but in this case, the behavior of the meminductor emulator does not present discrete transitions between states but rather continuous ones, since $R_1(\rho)$ is a continuous function of ρ, as indicated in Equation XI.17.

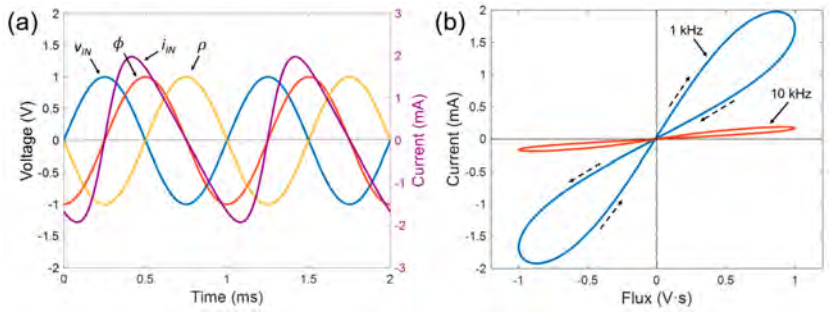

Figure XI.7: Simulation results of the continuous-state meminductor. (a) Signals extracted from the circuit of Figure XI.6 for a sinusoidal input signal ($V_m = 1$ V, $f = 1$ kHz) with $R_2 = R_3 = R_5 = R_6 = 1$ kΩ, $C = 47$ nF and $R_1(\rho)$ as indicated in Equation (17). (b) Closed pinched hysteresis loop of the flux–current curve for different frequencies ($f = 1$ kHz and $f = 10$ kHz).

Moreover, to round up the flexibility of the proposed emulator, we present in Figure XI.8 the operation of the circuit shown in Figure XI.6 with a more complex excitation signal. In this particular example, we used the same continuous meminductance transition given by Equation XI.17, but considering a square input signal with a peak-to-peak amplitude of $V_{pp} = 1$ V and a frequency of 1 kHz.

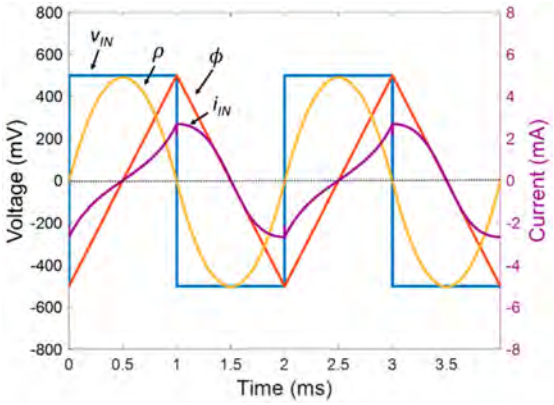

Figure XI.8: Signals extracted from the simulation results of the continuous-state meminductor using a square input signal with an amplitude peak-to-peak of 1 V and a frequency of 1 kHz.

Finally, we present a design of the continuous-states meminductor using commercial off-the-shelf devices. In this case, the TIF-controlled resistor is implemented by means of a photoresistive opto-isolator (which consists of an LED input optically coupled to a photocell, such as the model NSL-32 by Advanced Photonix [27]), as shown in Figure XI.9. With this particular optocoupler, we can achieve resistances from 40 Ω to 500 kΩ. A constant DC voltage (V_{offset}) is added to the TIF to prevent the LED turning off (since it would reduce the current thorough R_1 down to values close to zero) as well as to work in the light-dependent resistor's linear region [28].

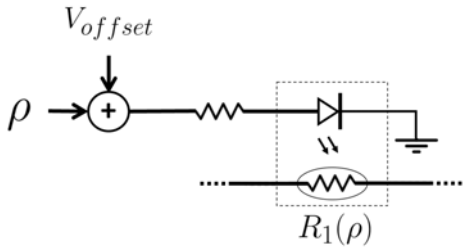

Figure XI.9: TIF-controlled resistor implemented by means of a photoresistive opto-isolator. The schematic of both summing amplifier and double integrator circuit is not shown for simplicity.

The proper working of this approach using the same configuration as the previous examples with a $V_{offset} = 3$ V is demonstrated in Figure XI.10, where it can be appreciated that the circuit behaves as a continuous-state meminductor as a consequence of the change in $R_1(\rho)$ according to the TIF (taking values from ∼60 Ω to ∼150 Ω).

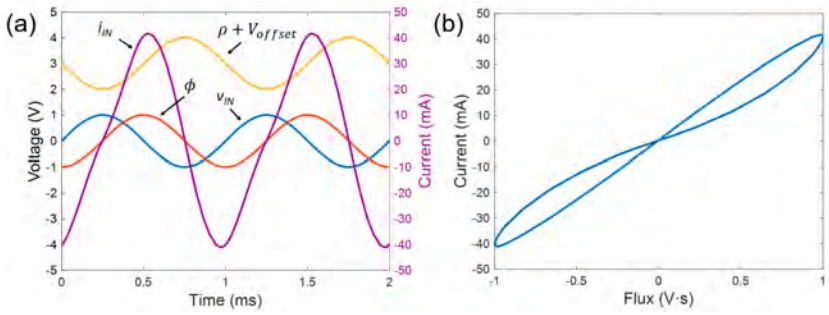

Figure XI.10: (a) Signals extracted from the simulation results of the continuous-state meminductor using a photoresistive opto-isolator as time-integral of the input flux (TIF)-controlled resistor. (b) Closed pinched hysteresis loop of the flux–current curve for an input frequency of $f = 1$ kHz.

XI.4 Long-Term Potentiation Example

In this last section, we demonstrated that this circuit is also feasible for the emulation of neuromorphic circuits. In neural activity, neurons act as signal spike generators to pass an electrical signal to another neuron, and synapses are the means by which they do so [29]. Then, in particular, we show in Figure XI.11a long-term potentiation (LTP) and long-term depression (LTD) example, which emulates the long-term memory in biological systems. For that, we firstly applied pre-synaptic stimuli, modeled by successive current spikes with positive sign, progressively increasing the TIF of the device (potentiation). After that, a series of current spikes of negative value, acting as post-synaptic stimuli, induced the depression of the device, hence progressively reducing the TIF.

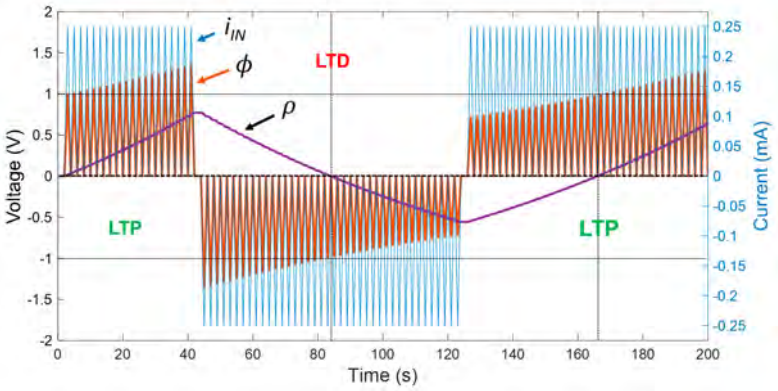

Figure XI.11: Pre-synaptic ($i_{IN} > 0$) and post-synaptic ($i_{IN} < 0$) current spikes applied to the meminductor, emulating neural stimuli. Long-term potentiation (LTP) and long-term depression (LTD) are reflected by the progressive increase and decrease in the TIF, respectively. Input flux (ϕ) reflects the change in the memory state.

The confirmation of the learning/forgetting processes of the device can be recognized in the flux that the device stores and removes during each spike, reflecting an increase and decrease in the meminductance during the potentiation and depression, respectively. Thus, the repeated application of these pulses produces LTP or LTD behavior, in which the flux does not recover its pre-pulses value over a long period of time, and therefore neither does the meminductance.

XI.5 Conclusions

In this work, a modified version of Antoniou's inductor simulator was suited to implement the emulation of meminductive devices. It has been demonstrated that this approach can be used to simulate both discrete-state and continuous-state meminductors for different input signals and frequencies. The designed circuit

is also general and can be implemented using off-the-shelf devices, which make it suitable for simple practical implementations in a wide range of applications, such as chaotic circuits or neuromorphic applications, as it has been illustrated by LTP and LTD examples.

Acknowledgements. This work was supported by the Spanish Ministry of Education, Culture, and Sport (MECD)/FEDER-EU through the grant FPU16/01451 and the project TEC2017-89955-P.

References

[1] Chua, L., "Memristor-the missing circuit element," *IEEE Transactions on Circuit Theory*, vol. 18, no. 5, pp. 507–519, 1971.

[2] Strukov, D. B., Snider, G. S., Stewart, D. R., and Williams, R. S., "The missing memristor found," *Nature*, vol. 453, no. 7191, pp. 80–83, May 2008.

[3] Romero, Toral-Lopez, Ohata, Morales, Ruiz, Godoy, and Rodriguez, "Laser-fabricated reduced graphene oxide memristors," *Nanomaterials*, vol. 9, no. 6, p. 897, Jun. 2019.

[4] Villena, M. A., Hui, F., Liang, X., Shi, Y., Yuan, B., Jing, X., Zhu, K., Chen, S., and Lanza, M., "Variability of metal/h-BN/metal memristors grown via chemical vapor deposition on different materials," *Microelectronics Reliability*, vol. 102, p. 113 410, Nov. 2019.

[5] Zhu, K., Liang, X., Yuan, B., Villena, M. A., Wen, C., Wang, T., Chen, S., Hui, F., Shi, Y., and Lanza, M., "Graphene–boron nitride–graphene cross-point memristors with three stable resistive states," *ACS Applied Materials & Interfaces*, vol. 11, no. 41, pp. 37 999–38 005, Sep. 2019.

[6] Iu, H. H. C., Yu, D. S., Fitch, A. L., Sreeram, V., and Chen, H., "Controlling chaos in a memristor based circuit using a twin-t notch filter," *IEEE Transactions on Circuits and Systems I: Regular Papers*, vol. 58, no. 6, pp. 1337–1344, Jun. 2011.

[7] Xia, Q., Robinett, W., Cumbie, M. W., Banerjee, N., Cardinali, T. J., Yang, J. J., Wu, W., Li, X., Tong, W. M., Strukov, D. B., Snider, G. S., Medeiros-Ribeiro, G., and Williams, R. S., "Memristor-CMOS hybrid integrated circuits for reconfigurable logic," *Nano Letters*, vol. 9, no. 10, pp. 3640–3645, Oct. 2009.

[8] Prezioso, M., Merrikh-Bayat, F., Hoskins, B. D., Adam, G. C., Likharev, K. K., and Strukov, D. B., "Training and operation of an integrated neuromorphic network based on metal-oxide memristors," *Nature*, vol. 521, no. 7550, pp. 61–64, May 2015.

[9] Azghadi, M. R., Linares-Barranco, B., Abbott, D., and Leong, P. H. W., "A hybrid CMOS-memristor neuromorphic synapse," *IEEE Transactions on Biomedical Circuits and Systems*, vol. 11, no. 2, pp. 434–445, Apr. 2017.

[10] Ventra, M. D., Pershin, Y. V., and Chua, L. O., "Circuit elements with memory: Memristors, memcapacitors, and meminductors," *Proceedings of the IEEE*, vol. 97, no. 10, pp. 1717–1724, Oct. 2009.

[11] Wang, Z., Joshi, S., Savel'ev, S. E., Jiang, H., Midya, R., Lin, P., Hu, M., Ge, N., Strachan, J. P., Li, Z., Wu, Q., Barnell, M., Li, G.-L., Xin, H. L., Williams, R. S., Xia, Q., and Yang, J. J., "Memristors with diffusive dynamics as synaptic emulators for neuromorphic computing," *Nature Materials*, vol. 16, no. 1, pp. 101–108, Sep. 2016.

[12] Driscoll, T., Quinn, J., Klein, S., Kim, H. T., Kim, B. J., Pershin, Y. V., Ventra, M. D., and Basov, D. N., "Memristive adaptive filters," *Applied Physics Letters*, vol. 97, no. 9, p. 093 502, Aug. 2010.

[13] Yuan, F., Wang, G., Jin, P., Wang, X., and Ma, G., "Chaos in a meminductor-based circuit," *International Journal of Bifurcation and Chaos*, vol. 26, no. 08, p. 1 650 130, Jul. 2016.

[14] Pershin, Y. V. and Ventra, M. D., "Neuromorphic, digital, and quantum computation with memory circuit elements," *Proceedings of the IEEE*, vol. 100, no. 6, pp. 2071–2080, Jun. 2012.

[15] Yu, D. S., Liang, Y., Chen, H., and Iu, H. H. C., "Design of a practical memcapacitor emulator without grounded restriction," *IEEE Transactions on Circuits and Systems II: Express Briefs*, vol. 60, no. 4, pp. 207–211, Apr. 2013.

[16] Romero, Toral-Lopez, Ohata, Morales, Ruiz, Godoy, and Rodriguez, "Laser-fabricated reduced graphene oxide memristors," *Nanomaterials*, vol. 9, no. 6, p. 897, Jun. 2019.

[17] Sah, M. P., Yang, C., Budhathoki, R. K., Kim, H., and Yoo, H. J., "Implementation of a memcapacitor emulator with off-the-shelf devices," *Electronics and Electrical Engineering*, vol. 19, no. 8, Oct. 2013.

[18] Sah, M. P., Budhathoki, R. K., Yang, C., and Kim, H., "A mutator-based meminductor emulator circuit," in *2014 IEEE International Symposium on Circuits and Systems (ISCAS)*, IEEE, Jun. 2014.

[19] Yu, W., Sisi, L., Haiyan, Y., and Jie, L., "Progress in the functional modification of graphene/graphene oxide: A review," *RSC Advances*, vol. 10, no. 26, pp. 15 328–15 345, 2020.

[20] Sozen, H. and Cam, U., "A novel floating/grounded meminductor emulator," *Journal of Circuits, Systems and Computers*, vol. 29, no. 15, p. 2 050 247, May 2020.

[21] Zhao, Q., Wang, C., and Zhang, X., "A universal emulator for memristor, memcapacitor, and meminductor and its chaotic circuit," *Chaos: An Interdisciplinary Journal of Nonlinear Science*, vol. 29, no. 1, p. 013 141, Jan. 2019.

[22] Kumar, U., Shukla, S. K., and Amiete, "Analytical study of inductor simulation circuits," *Active and Passive Electronic Components*, vol. 13, no. 4, pp. 211–227, 1989.

[23] Torres, L. and Aguirre, L., "Inductorless chua's circuit," *Electronics Letters*, vol. 36, no. 23, p. 1915, 2000.

[24] Sedra, A., *Microelectronic circuits*. New York: Oxford University Press, 2004.

[25] Yuan, F., Deng, Y., Li, Y., and Wang, G., "The amplitude, frequency and parameter space boosting in a memristor–meminductor-based circuit," *Nonlinear Dynamics*, vol. 96, no. 1, pp. 389–405, Jan. 2019.

[26] Fouda, M. E. and Radwan, A. G., "Meminductor response under periodic current excitations," *Circuits, Systems, and Signal Processing*, vol. 33, no. 5, pp. 1573–1583, Dec. 2013.

[27] Inc, L. O. (2016). "Optocoupler nsl-32 datasheet," [Online]. Available: https://www.digikey.es/htmldatasheets/production/1699360/0/0/1/nsl-32-datasheet.html.

[28] Fitch, A., Iu, H., Wang, X., Sreeram, V., and Qi, W., "Realization of an analog model of memristor based on light dependent resistor," in *2012 IEEE International Symposium on Circuits and Systems*, IEEE, May 2012.

[29] Majumdar, S., Tan, H., Qin, Q. H., and Dijken, S. van, "Energy-efficient organic ferroelectric tunnel junction memristors for neuromorphic computing," *Advanced Electronic Materials*, vol. 5, no. 3, p. 1 800 795, Jan. 2019.

Paper XII

Design and Implementation of a Floating Meminductor Emulator upon Riordan Gyrator

Francisco J. Romero [1,*], Alfredo Medina-Garcia [2], Manuel Escudero [3], Diego P. Morales [1], Noel Rodriguez [1]

[1] Department of Electronics and Computer Technology, University of Granada, 18071 Granada, Spain.
[2] Infineon Technologies AG, 85579 Neubiberg, Germany
[3] Infineon Technologies Austria AG, 9500 Villach, Austria
* Corresponding author: franromero@ugr.es (F.J.R.)

Published in *AEU - International Journal of Electronics and Communications*, May 2020, volume 133, 153671. DOI: 10.1016/j.aeue.2021.153671. Impact Factor: 2.924. JCR Rank: 99/266 (Q2) in *Engineering, Electrical & Electronic* and 38/90 (Q2) in *Telecommunications*.

Abstract

In this communication we present the design, simulation and implementation of a floating flux-controlled meminductor emulator based on the Riordan gyrator. Firstly, the circuit is presented theoretically, from its original version to emulate inductors to its adaptation for floating meminductors. Once its theoretical equations are presented, using SPICE simulations, we demonstrate the feasibility of this implementation by means of off-the-shelf components and a memristor, or a memristor emulator, for different inputs signals and frequencies in both grounded and floating configurations. Finally, a low-frequency breadboard-level implementation is included to prove its practicality.

Keywords: Circuit theory, emulator, feedback, gyrator, meminductor, memristor.

XII. Design and Implementation of a Floating Meminductor Emulator upon Riordan Gyrator

XII.1 Introduction

Nearly 50 years ago, Prof. Leon Chua presented for the first time the passive circuit element which established the relation between flux (ϕ, time-integral of the input-voltage) and charge (q) [1]. This element was called memristor (memory-resistor) since it demonstrated that, for a given voltage, its resistance at an instant $t = t_1$ depends not only on the current at t_1, but also on the current through the device from $t = -\infty$ to $t = t_1$, hence presenting a memory characteristic. However, it was not until 2008 that a group of researchers from Hewlett-Packard Labs (HP) reported the first solid-state device exhibiting memristive behavior [2]. It was then when the concept of memristor ushered in unprecedented electronic devices and applications, extending from ReRAMs (Resistive Random-Access Memory) to realistic neural networks [3]. Thus, the memristor, and its non-volatile memory effect, has raised as one of the more substantial revolutions in the field of electronic circuit theory since the invention of the transistor [4].

In 2009, after the great interest aroused by memristive devices, M. Di Ventra, Y.V. Pershin and L. Chua generalized the concept of memory devices to capacitors and inductors, thus defining the memcapacitor and the meminductor [5]. In these devices, both capacitance and inductance, as in the case of memristors, present a non-volatile memory effect which depends not only on its present state but also on the history of the device. In this way, apart from the definition of memristor (R_M, Eq. XII.1), they defined the concepts of memcapacitor (C_M, Eq. XII.2), as the n^{th}-order system that establishes a nonlinear relation between the charge (q) of the device and its voltage (V); and the meminductor (L_M, Eq. XII.3), as the nth-order system which establishes the nonlinear relation between current (I) and flux (ϕ) [6].

$$V(t) = R_M(\vec{x_N}, I, t)I(t) \tag{XII.1}$$

$$q(t) = C_M(\vec{x_N}, V, t)V(t) \tag{XII.2}$$

$$\phi(t) = L_M(\vec{x_N}, I, t)I(t) \tag{XII.3}$$

being $\vec{x_N}$ a vector representing the n internal state variables of the system.

These devices, memcapacitor and meminductor, are expected to cause a disruption in the field of electronics, which has led to several studies on diverse applications, such as neuromorphic and quantum computation [7], [8], logic gates [9], [10], self-adaptative filters [11]–[13] or chaotic circuits [14]–[18]. However, in contrast to memristors, which can be already fabricated relying on different materials and resistive switching mechanisms [2], [19]–[21], solid-state memcapacitors and meminductors are yet elusive.

For this reason, in recent years many SPICE models as well as some practical implementations of memcapacitors and meminductors emulators have been proposed. These circuits follow different alternatives to achieve the same goal:

satisfying the constitutive equations of the emulated device. These alternatives can be grouped into two main groups; *i)* those using another mem-device (in particular a memristor) to mutate its behavior to the desired mem-device and *ii)* those not based on mem-devices. Thus, many of the different memcapacitors and meminductors emulators use a memristor (or a memristor emulator) to transform its constitutive equations into the constitutive relation of the mem-device emulated [22]–[28], as it is done in this work, while the rest of them make use of classical voltage-mode op-amps (VOAs), current feedback operational amplifiers (CFOAs), operational transconductance amplifier (OTAs) and/or current conveyors to emulate the desired mem-device [14], [29]–[36].

However, the implementation of most of these circuits limits the emulated device to grounded configurations, hence reducing their potential applications. In order to avoid this, in this work we present a simple and low-cost floating meminductor emulator based on a modification of the Riordan gyrator, typically used to emulate floating inductors and with a design based on classical op-amps [37].

The manuscript is structured as follows: after this introduction, Section XII.2 presents the theoretical modifications over the Riordan gyrator to achieve a meminductive behavior, together with SPICE simulations demonstrating the feasibility of the proposed circuit for floating and grounded configurations. After that, a simple low-frequency breadboard-level implementation using off-the-shelf components is presented in Section XII.3 and, finally, the main conclusions are drawn in Section XII.4.

XII.2 Meminductance and the modified Riordan gyrator

As defined by Chua [6], the meminductive systems can be either current-controlled or flux-controlled depending on the relation of the meminductance with these parameters. This work is focused on flux-controlled meminductive systems, which are described by the following equations:

$$I(t) = L_M^{-1}(x_1, x_2, ..., x_N, \phi, t)\phi(t) \tag{XII.4}$$

$$\frac{\vec{x_N}}{dt} = f(\vec{x_N}, \phi, t) \tag{XII.5}$$

being t the time, $\vec{x_N}$ the N-component vector defining the n state variables of the system and f a continuous $\mathrm{n^{TM}}$-dimensional vector function.

A particular case of this general definition is the flux-controlled meminductor, a meminductive system with one single state variable whose meminductance depends only on the input flux. In that case, Eq. XII.4 and Eq. XII.5 can be reduced to Eq. XII.6 [6]:

$$I(t) = L_M^{-1}\left[\int_{t_0}^{t} \phi(\tau)d\tau\right]\phi(t) \tag{XII.6}$$

provided that $\int_{-\infty}^{t_0} \phi(\tau)d\tau = 0$. Note that a flux-controlled meminductor is not only an inductor whose inductance depends on the time integral of the input flux, but also whose current–flux characteristic presents a pinched hysteresis loop (in which the current is zero whenever the flux is zero) [6].

On this basis, here we demonstrate that the Riordan gyrator [37], [38], after certain modifications (see Fig. XII.1), is suitable for the emulation of floating flux-controlled meminductors.

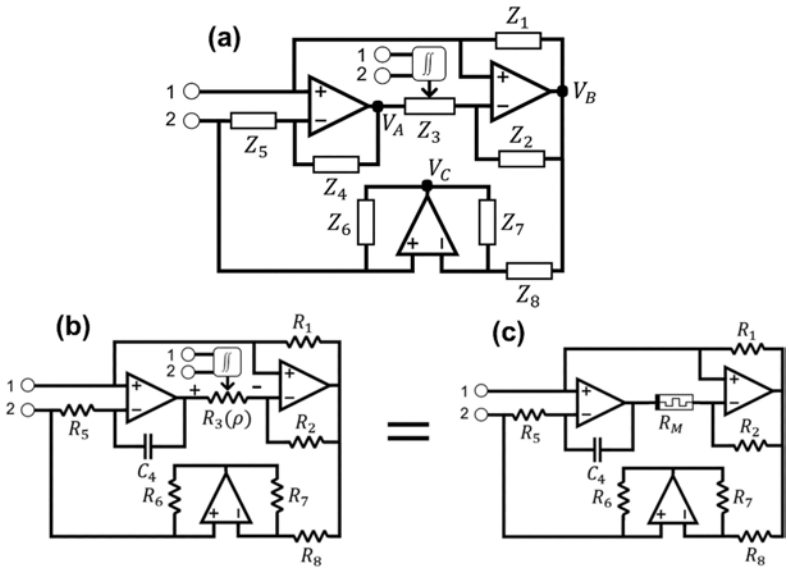

Figure XII.1: (a) Modified Riordan gyrator using an impedance Z_3 whose value depends on the double time integral of the input voltage. (b) Adaptation of the circuit shown in (a) to emulate flux-controlled meminductors. (c) Circuit equivalent to the one shown in (b).

Firstly, for a floating impedance, the input current at terminal one must be equal to the output current of terminal two:

$$I_1 = -I_2 \tag{XII.7}$$

Neglecting the input bias current of the op amps, the input current at terminal one corresponds to the current through the impedance Z_1, and therefore, it can be obtained as indicated in Eq. XII.8.

$$I_1 = \frac{V_{IN_1} - V_B}{Z_1} = (V_{IN_1} - V_{IN_2})\frac{Z_2 Z_4}{Z_1 Z_3 Z_5} = V_{IN}\frac{Z_2 Z_4}{Z_1 Z_3 Z_5} \tag{XII.8}$$

In the same way, the current at terminal two corresponds to the sum of the current through Z_6 and Z_5, which can be derived as expressed in Eq. XII.9.

$$I_2 = \frac{V_{IN_1} - V_{IN_2}}{Z_5} + \frac{V_{IN_2} - V_C}{Z_6} = V_{IN}\left(\frac{Z_7}{Z_8 Z_6} + \frac{Z_2 Z_4 Z_7}{Z_3 Z_5 Z_6 Z_8} - \frac{1}{Z_5}\right) \quad \text{(XII.9)}$$

Thus, in order to satisfy Eq. XII.7, the circuit shown in Fig. XII.1a needs to fulfill the following condition:

$$\frac{1}{Z_5} = \frac{1}{Z_1} = \frac{Z_7}{Z_6 Z_8} \quad \text{(XII.10)}$$

In that case, and considering Z_3 as a flux-controlled impedance, the value of the lossless floating flux-controlled input impedance of the circuit can be expressed as indicated in Eq. XII.11 in Laplace's domain.

$$Z_{1\longrightarrow 2}(\rho(s)) = \frac{Z_1 Z_3(\frac{\phi(s)}{s}) Z_5}{Z_2 Z_4} \quad \text{(XII.11)}$$

This impedance, after the substitutions shown in Fig. XII.1b, can be directly related to a flux-controlled inductance (see Eq. XII.12) considering $R_1 = R_2 = R_5 = R_6 = R_7 = R_8 = R$, and a resistance $R_3(\rho)$ controlled by the time integral of the flux (ρ).

$$Z_{1\longrightarrow 2}(\rho(s)) = sRC_4 R_3(\frac{\phi(s)}{s}) = sL(\frac{\phi(s)}{s}) \quad \text{(XII.12)}$$

This also makes feasible that the circuit of Fig. XII.1b satisfies the constitutive equation of a meminductor, given that:

$$I_1 = \frac{1}{RC_4 R_3(\frac{\phi(s)}{s})} \cdot \frac{V_{IN}}{s} \longrightarrow I_1(t) = \frac{\phi(t)}{L(\rho)} \quad \text{(XII.13)}$$

Moreover, if we further analyze this circuit considering close to ideal operational amplifiers, it can be derived that the voltage across $R_3(\rho)$ can be expressed as a function of the input flux (ϕ) (Eq. XII.14).

$$\begin{aligned} V_{R_3}(t) = V_{R_3^+} - V_{R_3^-} &= \frac{1}{R_5 C_4}\int (V_{in_1}(t) - V_{in_2}(t))dt \\ &= \frac{1}{R_5 C_4}\int (V_{in}(t))dt = \frac{\phi(t)}{R_5 C_4} \end{aligned} \quad \text{(XII.14)}$$

Therefore, given that the resistance $R_3(\rho)$ changes its value according to the time-integral of the input flux (ρ), it is really changing its value as a function of the time-integral of its own input, hence behaving as a voltage-controlled memristor [6]. On this basis, $R_3(\rho)$ could be replaced by a voltage-controlled memristor, as illustrated in Fig. XII.1c, which would allow to formulate Eq. XII.12 in terms of memristance, as indicated in Eq. XII.15.

$$Z_{1\longrightarrow 2}(\rho(s)) = sRC_4 R_M = sL(s) \quad \text{(XII.15)}$$

XII. Design and Implementation of a Floating Meminductor Emulator upon Riordan Gyrator

To prove the feasibility of the circuit to emulate a meminductor, we have considered the simple two-states meminductor implementation depicted in Fig. XII.2.

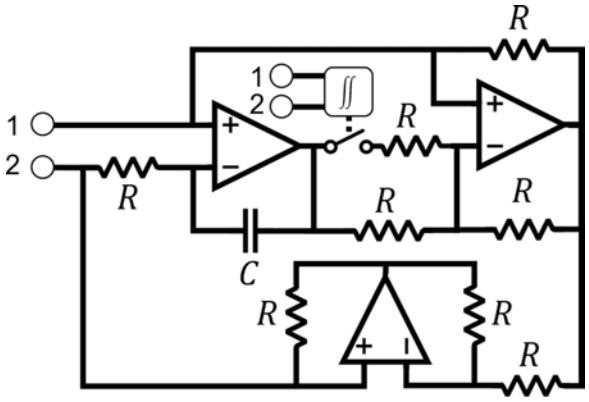

Figure XII.2: Two-states meminductor emulator based on the Riordan gyrator.

In the circuit of Fig. XII.2, the value of the time integral of the input flux is obtained by integrating the input voltage twice (e.g., using differential op-amp voltage-mode integrators [39]). This value is then used to control a voltage-controlled switch that will connect (or not) the additional resistor to the feedback loop. Under this configuration, the flux-controlled inductance given in Eq. XII.12 can be expressed as follows:

$$L(\rho) = \begin{cases} R^2C & \text{if } \rho < \rho_{TH} \\ R^2C/2 & \text{if } \rho \geq \rho_{TH} \end{cases} \tag{XII.16}$$

where p_{TH} is the defined threshold value which triggers the switch.

This bistable configuration has been simulated with SPICE in order to confirm its meminductive behavior. For that, we considered the following configuration: $R = 1$ kΩ, $C = 47$ nF and $\rho_{TH} = 0$ V·s^2, which results in the following values of inductance according to Eq. XII.16: $L(\rho) = 47$ mH for $\rho < 0$ and $L(\rho) = 23.5$ mH for $\rho \geq 0$.

The results shown in Fig. XII.3 demonstrate that the circuit proposed behaves as a two-states meminductor regardless of the input signal. As seen, the emulator satisfies the constitutive equation of the meminductor (Eq. XII.16), since the input current is zero whenever the input flux is zero and its waveform is a function of the input flux and the state of inductance (which in turn depends on the time-integral of the input flux as indicated by Eq. XII.16). In the same way, the meminductive behavior is also manifested in the closed pinched hysteresis loop of its $i - \phi$ characteristic (Fig. XII.4), which has been obtained using a sinusoidal input signal with different frequencies (1 kHz and 10 kHz). In addition, the $i - v$ characteristic of R_3 (inset of Fig. XII.4) also proves that

the voltage-controlled resistor behaves as a memristor, hence demonstrating the feasibility of the implementation shown in Fig. XII.1c.

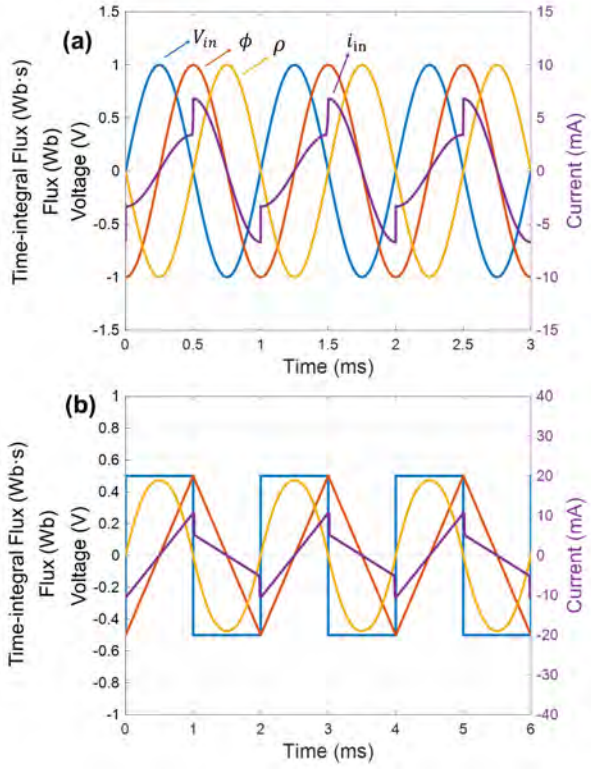

Figure XII.3: Simulation of the two-states meminductor emulator using a sinusoidal input signal with a frequency of 1 kHz (a) and a square input signal of 500 Hz (a).

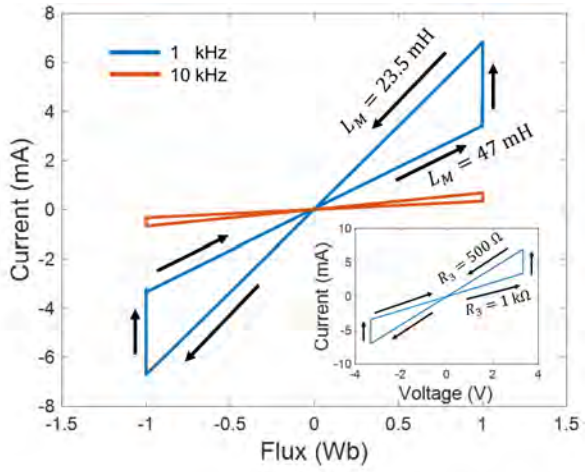

Figure XII.4: Closed pinched hysteresis loop of the $i-\phi$ characteristic obtained using a sinusoidal input signal at different frequencies. Inset shows the closed pinched hysteresis loop in the $i-v$ characteristic of the voltage-controlled resistor.

XII.3 Example in a floating configuration

In order to probe de feasibility of the proposed meminductor emulator to be used in floating configurations, in this section we show a simple low-pass filter based on the circuit shown in Fig. XII.5.

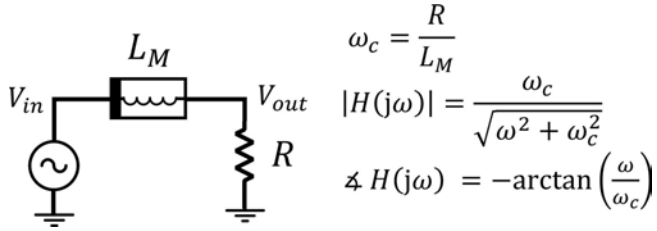

Figure XII.5: Low-pass filter based on a meminductor and a resistor connected in series. Equations correspond to the cutoff frequency (ω_c) and both modulus ($|H(j\omega)|$ and phase ($\measuredangle H(j\omega)$) of the transfer function in the frequency domain.

For this implementation we have considered the same circuit as the one used in the previous sections but replacing the two-states memristor by a continuous states memristor (R_M) described by Eq. XII.17, where $R_0 = 1$ kΩ, and $k = 500$ Ω is a scale factor of the double integration of the voltage between the meminductor's terminals.

$$R_M = R_0 + k \cdot \rho \tag{XII.17}$$

The circuit was simulated using a $R = 1$ kΩ and an input signal with a frequency of 1 kHz, thus obtaining directly from the meminductor emulator the signals shown in Fig. XII.6a. Note that under this configuration, the emulator also behaves as a meminductor, although in this case as a continuous-states meminductor, as the pinched hysteresis loop of Fig. XII.6b indicates.

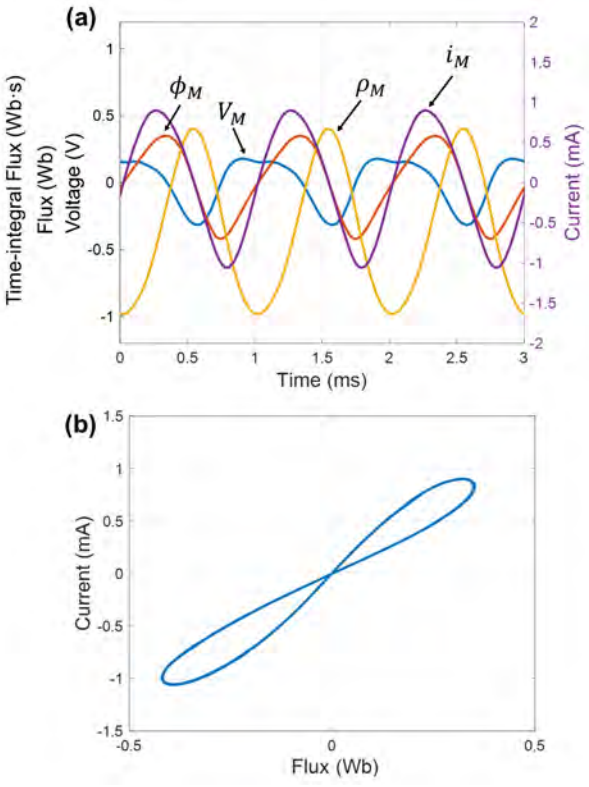

Figure XII.6: (a) Meminductor signals and (b) closed-pinched hysteresis loop of the $i - \phi$ characteristic under the low-pass filter configuration.

Therefore, according to Eq. XII.15 and Eq. XII.17, the meminductance takes continuous values in the range $L_M = [24, 56.5]$ mH as a function of the time-integral of the input-flux (Fig. XII.7a). The continuous change in the meminductance, in turn, makes that the cut-off frequency of the low pass filter changes over time (see Fig. XII.7a), indicating that both magnitude and phase of the output signal will depend not only on the amplitude and frequency of the input signal, but also on the instantaneous value of meminductance. This effect is represented in Fig. XII.7b, where it can be seen how the delay between both input and output signals increases as the cut-off frequency decreases.

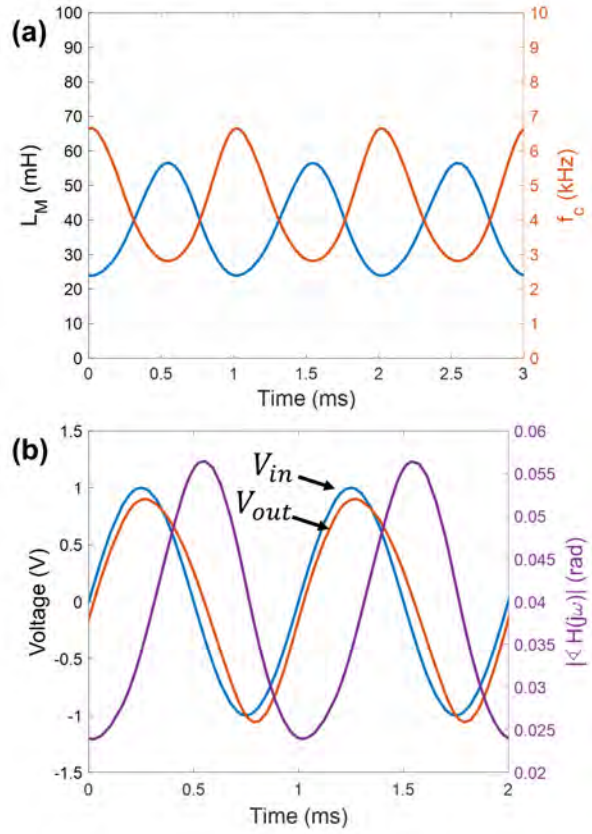

Figure XII.7: (a) Meminductance and cut-off frequency of the filter over time. (b) Input and output signals and delay between them over time.

XII.4 Experimental results

A simple breadboard-level implementation has been carried out in order to demonstrate the feasibility of this circuit by means of experimental results. For the sake of simplicity, to obtain the double time integral of the input voltage, we have considered the implementation shown in Fig. XII.8, which allows to test the meminductor emulator for sinusoidal input signals (if the waveform of the input is of the type sin(ωt), then the waveform of its double time integral corresponds to the type -sin(ωt)).

In this case, the voltage-controlled resistance was implemented using a LED optically coupled to a photo resistance, as shown in the inset of Fig. XII.8. Under this configuration, the brightness of the LED changes according to the time integral of the input flux, and therefore so does the resistance R_3. Moreover, V_{offset} must be set to ensure that the LED never turns off, hence avoiding that

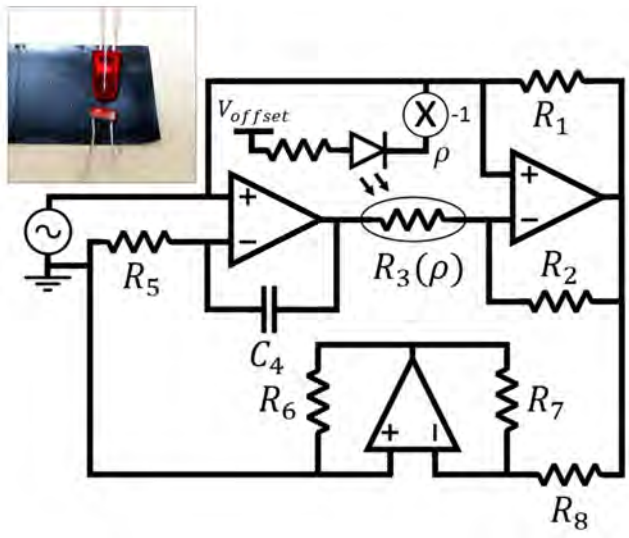

Figure XII.8: Meminductor emulator based on the Riordan gyrator for sinusoidal input signals. Inset shows the in-house voltage-controlled resistance used for this implementation.

the current through R_3 takes values close to zero [36], [40].

The values of the passive circuit elements were chosen as follows: $R_1 = R_2 = R_5 = R_6 = R_7 = R_8 = 10$ kΩ and C = 47 nF, besides, LM-741 were used to implement all op-amps configurations. A sinusoidal signal was applied to the input of the circuit with an amplitude of 50 mV and a frequency of 13 Hz (to ensure the proper response of the photoresistor), whereas V_{offset} was set to 1.8 V.

Fig. 9 shows the experimental signals extracted from the meminductor emulator under the configuration previously described. In this case, the input voltage corresponds to V_{R1}^{+}, whereas V_{R1}^{-} helps to obtain the meminductor input current (neglecting the input bias current of the op-amps).

The input flux can also be derived from the input voltage. Since this latter follows a sin(ωt) function, its integral waveform will correspond to the type -cos(ωt), or in other words, the input flux will have a delay of $-\pi/2$ rad with respect to the input voltage (which corresponds to a time delay of δ = -0.02 s for the frequency used). On this basis, it is possible to plot the input current as a function of the input flux, as shown in Fig. XII.10, demonstrating that the meminductor emulator of Fig. XII.8 presents a continuous closed pinched hysteresis loop in its $i - \phi$ characteristic, and hence proving its meminductive behavior.

XII. Design and Implementation of a Floating Meminductor Emulator upon Riordan Gyrator

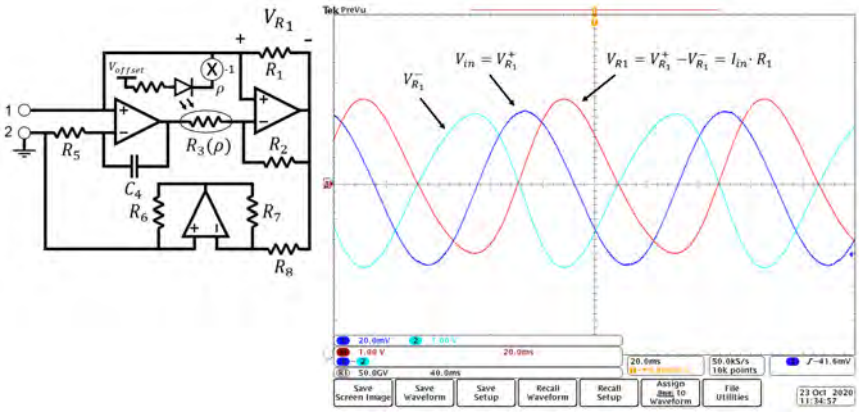

Figure XII.9: Experimental results of the meminductor emulator for an input signal with an amplitude of 50 mV and a frequency of 13 Hz. Signals were acquired with a Tektronix MSO 4104 mixed signal oscilloscope in high-resolution mode with a record length of 10 k point (sampling rate: 50 kSamples/s).

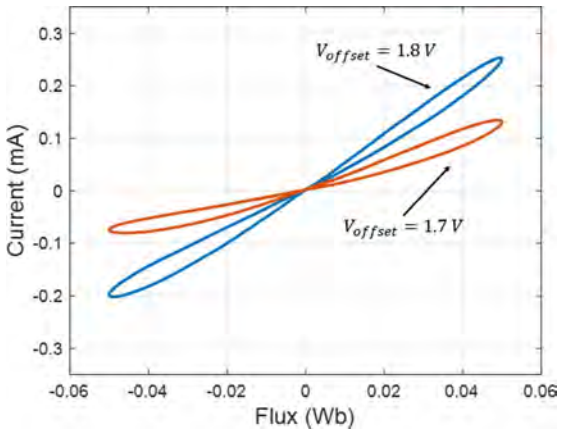

Figure XII.10: Experimental closed pinched hysteresis loop of the $i - \phi$ characteristic of the meminductor emulator for different values of V_{offset}.

Finally, the same experiments were performed using a V_{offset} of 1.7 V instead of 1.8 V, as also shown in Fig. XII.10. Note that in that case the current through the LED is lower than in the previous case, resulting in a lower brightness, and therefore, in higher values of R_3. Since R_3 takes higher values, so does the meminductance (see Eq. (XII.9)), which in turn produces a decrease of the input current with respect to the input flux, as defined by the constitutive equation of the meminductor (Eq. (XII.6)).

XII.5 Conclusions

In this communication the feasibility of a modified version of the Riordan gyrator to emulate floating meminductive systems has been demonstrated. The proposed circuit has been firstly described theoretically, from the modifications on the classical Riordan gyrator to its connection with the constitutive equations of flux-controlled meminductors. The theoretical approach has been supported with SPICE simulations using different inputs signals and frequencies for a simple two-states meminductor implementation as well as for a meminductor-based low-pass filter. Finally, a breadboard-level implementation of a continuous states meminductor demonstrates the simplicity, practicality and versatility of the emulator designed.

Acknowledgements. This work was supported by the Spanish Ministry of Education, Culture, and Sport (MECD)/FEDER-EU through the grant FPU16/01451 and the project TEC2017-89955-P.

References

[1] Chua, L., "Memristor-the missing circuit element," *IEEE Transactions on Circuit Theory*, vol. 18, no. 5, pp. 507–519, 1971.

[2] Strukov, D. B., Snider, G. S., Stewart, D. R., and Williams, R. S., "The missing memristor found," *Nature*, vol. 453, no. 7191, pp. 80–83, May 2008.

[3] Adee, S. (May 2008). "The mysterious memristor," IEEE Spectrum, [Online]. Available: http://www.ann.ece.ufl.edu/courses/eel6935_09spr/memristor.pdf.

[4] Johnson, R. C. (2020). "Eetimes - will memristors prove irresistible?" [Online]. Available: https://www.eetimes.com/will-memristors-prove-irresistible-2/.

[5] Ventra, M. D., Pershin, Y., and Chua, L., "Putting memory into circuit elements: Memristors, memcapacitors, and meminductors [point of view]," *Proceedings of the IEEE*, vol. 97, no. 8, pp. 1371–1372, Aug. 2009.

[6] Ventra, M. D., Pershin, Y. V., and Chua, L. O., "Circuit elements with memory: Memristors, memcapacitors, and meminductors," *Proceedings of the IEEE*, vol. 97, no. 10, pp. 1717–1724, Oct. 2009.

[7] Pershin, Y. V. and Ventra, M. D., "Neuromorphic, digital, and quantum computation with memory circuit elements," *Proceedings of the IEEE*, vol. 100, no. 6, pp. 2071–2080, Jun. 2012.

[8] Chen, C., Bao, H., Chen, M., Xu, Q., and Bao, B., "Non-ideal memristor synapse-coupled bi-neuron hopfield neural network: Numerical simulations and breadboard experiments," *AEU - International Journal of Electronics and Communications*, vol. 111, p. 152 894, Nov. 2019.

[9] Kvatinsky, S., Belousov, D., Liman, S., Satat, G., Wald, N., Friedman, E. G., Kolodny, A., and Weiser, U. C., "Magic-memristor-aided logic," *IEEE Transactions on Circuits and Systems II: Express Briefs*, vol. 61, no. 11, pp. 895–899, Nov. 2014.

[10] Kvatinsky, S., Wald, N., Satat, G., Kolodny, A., Weiser, U. C., and Friedman, E. G., "Mrl - memristor ratioed logic," in *2012 13th International Workshop on Cellular Nanoscale Networks and their Applications*, IEEE, Aug. 2012.

[11] Yang, W., Broski, A., Wu, J., Fan, Q. H., and Li, W., "Characteristics of transparent, PEDOT:PSS-coated indium-tin-oxide (ITO) microelectrodes," *IEEE Transactions on Nanotechnology*, vol. 17, no. 4, pp. 701–704, Jul. 2018.

[12] Gan, H., Yu, D., Li, D., and Cheng, H., "Binary memcapacitor based first-order active filter," *Circuit World*, vol. 46, no. 2, pp. 117–124, Jan. 2020.

[13] Wang, M., Yu, Y., Yang, N., Yang, C., and Ma, H., "New band-pass and band-stop filters with three memory devices," in *2019 14th IEEE Conference on Industrial Electronics and Applications (ICIEA)*, IEEE, Jun. 2019.

[14] Zhao, Q., Wang, C., and Zhang, X., "A universal emulator for memristor, memcapacitor, and meminductor and its chaotic circuit," *Chaos: An Interdisciplinary Journal of Nonlinear Science*, vol. 29, no. 1, p. 013 141, Jan. 2019.

[15] Yuan, F., Deng, Y., Li, Y., and Wang, G., "The amplitude, frequency and parameter space boosting in a memristor–meminductor-based circuit," *Nonlinear Dynamics*, vol. 96, no. 1, pp. 389–405, Jan. 2019.

[16] Yuan, F., Wang, G., and Wang, X., "Chaotic oscillator containing memcapacitor and meminductor and its dimensionality reduction analysis," *Chaos: An Interdisciplinary Journal of Nonlinear Science*, vol. 27, no. 3, p. 033 103, Mar. 2017.

[17] Wang, X., Yu, J., Jin, C., Iu, H. H. C., and Yu, S., "Chaotic oscillator based on memcapacitor and meminductor," *Nonlinear Dynamics*, vol. 96, no. 1, pp. 161–173, Jan. 2019.

[18] Yildirim, M. and Kacar, F., "Chaotic circuit with OTA based memristor on image cryptology," *AEU - International Journal of Electronics and Communications*, vol. 127, p. 153 490, Dec. 2020.

[19] Gale, E., "TiO2-based memristors and ReRAM: Materials, mechanisms and models (a review)," *Semiconductor Science and Technology*, vol. 29, no. 10, p. 104 004, Sep. 2014.

[20] Romero, Toral-Lopez, Ohata, Morales, Ruiz, Godoy, and Rodriguez, "Laser-fabricated reduced graphene oxide memristors," *Nanomaterials*, vol. 9, no. 6, p. 897, Jun. 2019.

[21] Romero, F. J., Toral, A., Medina-Rull, A., Moraila-Martinez, C. L., Morales, D. P., Ohata, A., Godoy, A., Ruiz, F. G., and Rodriguez, N., "Resistive switching in graphene oxide," *Frontiers in Materials*, vol. 7, Jan. 2020.

[22] Biolek, D. and Biolkova, V., "Mutator for transforming memristor into memcapacitor," *Electronics Letters*, vol. 46, no. 21, p. 1428, 2010.

[23] SAH, M. P., BUDHATHOKI, R. K., YANG, C., and KIM, H., "EXPANDABLE CIRCUITS OF MUTATOR-BASED MEMCAPACITOR EMULATOR," *International Journal of Bifurcation and Chaos*, vol. 23, no. 05, p. 1 330 017, May 2013.

[24] Wang,
Zhang, D. W., "The mechanism of the asymmetric SET and RESET speed of graphene oxide based flexible resistive switching memories," *Applied Physics Letters*, vol. 100, no. 6, p. 063 509, Feb. 2012.

[25] Yu, D. S., Liang, Y., Chen, H., and Iu, H. H. C., "Design of a practical memcapacitor emulator without grounded restriction," *IEEE Transactions on Circuits and Systems II: Express Briefs*, vol. 60, no. 4, pp. 207–211, Apr. 2013.

[26] Pershin, Y. and Ventra, M. D., "Memristive circuits simulate memcapacitors and meminductors," *Electronics Letters*, vol. 46, no. 7, p. 517, 2010.

[27] Yu, D.-S., Liang, Y., Iu, H. H. C., and Hu, Y.-H., "Mutator for transferring a memristor emulator into meminductive and memcapacitive circuits," *Chinese Physics B*, vol. 23, no. 7, p. 070 702, Jul. 2014.

[28] Wang, Z., Joshi, S., Savel'ev, S. E., Jiang, H., Midya, R., Lin, P., Hu, M., Ge, N., Strachan, J. P., Li, Z., Wu, Q., Barnell, M., Li, G.-L., Xin, H. L., Williams, R. S., Xia, Q., and Yang, J. J., "Memristors with diffusive dynamics as synaptic emulators for neuromorphic computing," *Nature Materials*, vol. 16, no. 1, pp. 101–108, Sep. 2016.

[29] Yuan, F., Jin, Y., and Li, Y., "Self-reproducing chaos and bursting oscillation analysis in a meminductor-based conservative system," *Chaos: An Interdisciplinary Journal of Nonlinear Science*, vol. 30, no. 5, p. 053 127, May 2020.

[30] Romero, Toral-Lopez, Ohata, Morales, Ruiz, Godoy, and Rodriguez, "Laser-fabricated reduced graphene oxide memristors," *Nanomaterials*, vol. 9, no. 6, p. 897, Jun. 2019.

[31] Fouda, M. and Radwan, A., "Charge controlled memristor-less memcapacitor emulator," *Electronics Letters*, vol. 48, no. 23, p. 1454, 2012.

[32] Yan, L., Dong-Sheng, Y., and Hao, C., "A novel meminductor emulator based on analog circuits," *Acta Physica Sinica*, vol. 62, no. 15, p. 158 501, 2013.

[33] Konal, M. and Kacar, F., "Electronically tunable meminductor based on OTA," *AEU - International Journal of Electronics and Communications*, vol. 126, p. 153 391, Nov. 2020.

[34] Fouda, M. E. and Radwan, A. G., "Memristor-less current- and voltage-controlled meminductor emulators," in *2014 21st IEEE International Conference on Electronics, Circuits and Systems (ICECS)*, IEEE, Dec. 2014.

[35] Fouda, M. E. and Radwan, A. G., "Meminductor response under periodic current excitations," *Circuits, Systems, and Signal Processing*, vol. 33, no. 5, pp. 1573–1583, Dec. 2013.

[36] Romero, F. J., Escudero, M., Medina-Garcia, A., Morales, D. P., and Rodriguez, N., "Meminductor emulator based on a modified antoniou's gyrator circuit," *Electronics*, vol. 9, no. 9, p. 1407, Sep. 2020.

[37] Riordan, R., "Simulated inductors using differential amplifiers," *Electronics Letters*, vol. 3, no. 2, p. 50, 1967.

[38] Senani, R., Bhaskar, D. R., Singh, A. K., and Singh, V. K., "Simulation of inductors and other types of impedances using CFOAs," in *Analog Circuits and Signal Processing*, Springer New York, 2013, pp. 49–80.

[39] Kamath, D. V., "Overview of OPAMP and OTA based integrators," *IJIREEICE*, vol. 3, no. 9, pp. 74–79, Sep. 2015.

[40] Wang, X.-Y., Fitch, A. L., Iu, H. H. C., Sreeram, V., and Qi, W.-G., "Implementation of an analogue model of a memristor based on a light-dependent resistor," *Chinese Physics B*, vol. 21, no. 10, p. 108 501, Oct. 2012.

Conclusions

This research has focused on the design, development and characterization of different flexible devices based on the use of laser-synthesis processes on flexible substrates as the key fabrication method. Below is included a summary of the main conclusions drawn:

1. The laser-synthesis of graphene-derived materials by means of laser assisted processes has been studied in detail. In particular, we have considered the synthesis of laser-reduced graphene oxide (LrGO) and laser-induced graphene (LIG) on flexible substrates. On one hand, for the synthesis of LrGO, flexible substrates were covered with graphene oxide (GO) and, after a drying process, the GO was turned into rGO through a laser photothermal process. On the other hand, LIG patterns were obtained directly by the laser ablation of the surface of flexible polyimide films. In addition, two different kinds of laser were used for this purpose, a CO_2 laser with an infrared wavelength of $\lambda = 10.6$ μm, and a *do it yourself* low-power UV laser ($\lambda = 405$ nm). It was demonstrated that the quality of the graphene-derived sheets, and therefore their sheet resistance, improves as the laser fluence increases, and that the laser power must be adjusted for each case in order to maintain the integrity of the substrate in terms of thermal dissipation. In addition, it was also demonstrated that the sheet resistance is also highly associated with both laser-mechanical resolution and laser spot size, since the uniformity of the laser-scribed patterns will depend on these latter parameters.

2. The temperature dependence of the LrGO resistance has been studied and exploited for the development of flexible temperature sensors. Given the highly linearity dependence of the sheet resistance of the LrGO with respect to the temperature and its almost non-existent hysteresis, this material was postulated as a perfect candidate for the development of resistive temperature sensors. In this regard, we have presented the design guidelines for the fabrication of flexible temperature sensors based on LrGO. These sensors, whose resistance decreases almost linearly as the temperature increases, presents a relative sensitivity of 0.489 %/K in the range (243 - 308) K. In addition, the practicability of these sensors were

demonstrated by their integration in a wireless node for the long-term monitoring of the ambient temperature.

3. This thesis also addressed the fabrication of capacitive flexible humidity sensors. Firstly, we studied the use of LIG and LrGO as electrode material for the development of capacitive humidity sensors. For that, we synthesized the graphene-derived capacitive structures over flexible polyimide films whose dielectric constant depends on the relative humidity and compared their performance with the obtained using silver-based electrodes as reference. The results, which can be found in Paper III, demonstrated that the LrGO-based capacitors were much more sensitive to humidity changes than those based on LIG and Ag-ink as a consequence of the remaining GO layer in-between their electrodes (up to 100 and 30 times higher at 1 kHz, respectively). However, the use of LrGO electrodes also increases the thermal drift of these sensors, hence hindering the definition of their calibration curve. Because of this, in Paper IV we decided to combine printed silver-based electrodes with a sensitive layer of GO, reporting a sensitivity of 0.23 nF/% RH at 1 kHz in an area less than 30 mm^2. In addition, this paper also showed that the presence of the PEDOT:PSS within the GO structure is able to modify the electrical properties of the sensitive film, improving the overall performance of the sensors. For instance, their sensitivity can be increased up to 1.22 nF/% RH at 1 kHz with a GO/PEDOT:PSS(10%) composite as a result of the combination of the active region of both GO and PEDOT:PSS materials.

4. The use of screen-printed cabon-based materials for the fabrication of flexible electrochemical capacitors was also studied in this work. For that, we screen-printed a interdigitated electrodes (IDEs) structure using a conductive carbon-based paste on a flexible substrate. These IDEs were characterized in combination with PVA/H_3PO_4 electrolyte as electrochemical capacitors in Paper VII, demonstrating that the porous nature of this material results in a electrochemical double-layer capacitive behaviour. The results demonstrated that, although the specific capacitances achieved with these electrodes are lower than the ones obtained using other carbon-based materials ($\sim$22 $\mu F/cm^2$), as soon as high performance carbon-based pastes become available this method would pave the way towards an alternative method for the large-scale and cost-effective fabrication of flexible electrochemical capacitors.

5. Both LIG and LrGO were also used for the fabrication of flexible electrical heaters in Paper V and Paper VI, respectively. In contrast to commercial flexible heaters, we have demonstrated that the laser-synthesized heaters show a much higher heat uniformity and can be fabricated under ambient conditions following a simple, scalable and environmental-friendly fabrication process. In particular, we have reported that the LIG heaters can operate up to 400 ^oC (only limited by the mechanical stability of the substrate), while in the case of the LrGO

heaters this maximum operating temperature is around 200 ^{o}C (limited by the apparition of joule annealing drift effects). Despite this, the heat transfer coefficients obtained with the LrGO heaters (200–440 ^{o}C cm^2/W) indicated that they require less power to achieve the same temperature than the LIG-based ones (131 ^{o}C cm^2/W), with the additional advantage of also requiring less time to get the steady-state temperature, as reported in Paper VI.

6. We have also demonstrated the feasibility of the LIG to fabricate flexible electrodes for medical devices. Thanks to the inherent high porosity of this material, which helps to reduce the skin–electrode contact resistance, it has been postulated as an inexpensive and bio-compatible alternative to commercial Ag-based ECG electrodes. Thus, in Paper VIII we demonstrated that these electrodes provide a comparable signal transduction when compared with commercial electrodes, together with their feasibility to be used inside the IoT paradigm by means of their integration with a commercial wearable and custom signal processing techniques intended to monitor the heart rate.

7. The memristive behavior of LrGO was also a subject matter of this thesis. In our laser-reduction experiments we observed that LrGO patterns with an intermediate level of reduction presented resistive switching. This led us to further explore this effect, which results in Paper IX, where we reported laser-fabricated GO memristors that fully rely on the laser-reduction process to create the active switching element. It was demonstrated that in partially reduced GO, the high concentration of oxygen-containing functional groups on the GO structure is responsible of modifying the local stoichiometry of the reduced-graphene oxide layer, and hence of its memristive behavior. In this work we concluded that low-resistance conductive paths are formed in the bulk of the material when these sp^3 domains are tuned into sp^2 domains (oxygen vacancies) under the action of a bias current and that, once the polarity is reversed, these sp^3 domains are recovered again returning to a high resistance state. In addition, we have also explored the use of memristors for the implementation of electrical mutators in oder to emulate memcapacitors and meminductors in both grounded and floating configurations, as demonstrated in last three chapters of this thesis.

8. Finally, in this thesis we have also addressed the use of reconfigurable electronics for the development of the prototype presented in Paper I, as well as other prototypes and devices developed during the course of this work. We rely on the use of these technology since their inherent reconfigurable analog and digital domains are ideal for handling with the variability in the output from one to another physical sensor, hence reducing the necessity of implementing custom readout circuits for each sensor fabricated. Moreover, the use of this technology, in addition to save both resources and time when designing and implementing an electronics

device, is postulated as an alternative to tackle the issue of Waste Electrical and Electronic Equipment (WEEE).